Tropical Transport and the Seasonal Variability of the Subtropical "Edges" in the Stratosphere

by

Jessica L. Neu

B.S., Meteorology, Texas A&M University (1995)

Submitted to the Department of Earth, Atmospheric, and Planetary Sciences
in partial fulfillment of the requirements for the degree of

Doctor of Philosophy

at the

MASSACHUSETTS INSTITUTE OF TECHNOLOGY

February 2001

Signature of Author .....
Department of Earth, Atmospheric, and Planetary Sciences
January 12, 2001

Certified by .....
R. Alan Plumb
Professor of Meteorology
Thesis Supervisor

Accepted by .....
Ronald G. Prinn
Chairman, Department of Earth, Atmospheric, and Planetary Sciences

Tropical Transport and the Seasonal Variability of the Subtropical "Edges" in the Stratosphere

by

Jessica L. Neu

Submitted to the Department of Earth, Atmospheric, and Planetary Sciences
on January 12, 2001, in partial fulfillment of the
requirements for the degree of
Doctor of Philosophy

Abstract

The chemistry of the stratosphere, in particular the balance between ozone production and loss, is very sensitive to transport into and out of the tropical stratosphere. There is a great deal of evidence that tropical air remains relatively isolated from extratropical air over timescales that are long compared to typical midlatitude mixing timescales. However, there are significant questions regarding the extent to which the tropics may be considered isolated, the mechanisms and variability of this isolation, and the implications of tropical isolation for global-scale transport. We address some of these issues using three very different tools: a simple model of stratospheric transport, which allows us to investigate the role of tropical transport in determining global transport timescales, satellite observations of long–lived tracers, which allow us to diagnose the seasonal variability of the tracer gradients that mark the transition between tropical and extratropical air, and a shallow water model, which allows us to investigate the mechanisms of tropical isolation in the simplest relevant dynamical framework.

We first discuss the characteristics of analytical solutions for the mean age of air, a measure of the mean timescale for transport by large-scale processes in the stratosphere, in a simple, one-dimensional conceptual model of stratospheric transport. In this "leaky pipe" model, the stratosphere is divided into three regions: the tropics and the Northern and Southern extratropics. We examine the dependence of the mean age on advection, diffusive mixing, and quasi-horizontal transport between the tropics and the extratropics. This work provides insight into the role of the tropics in global chemical transport under the assumption of at least some degree of tropical isolation.

We next examine the seasonal variability of the subtropical tracer gradients which mark the transition between tropical and extratropical air from both a diagnostic and a mechanistic standpoint. We use probability distribution functions of satellite measurements of long-lived tracers to define the transition regions, which are commonly called the subtropical "edges". We examine six and a half years of measurements and identify the central latitude, and in some cases the area, of these edges at eight pressure levels on quasi-monthly timescales. We compare the seasonal variability of the subtropical edges to the variability in several transport parameters and thus increase our understanding of the mechanisms of tropical isolation from a diagnostic standpoint.

We then use a shallow water model, which represents many of the properties of the flow between two isentropic surfaces, to examine the mechanisms of the formation of the subtropical

edges during each season. We include the effects of diabatic heating and cooling as well as planetary-scale wave propagation and examine the role of these processes in the formation of potential vorticity gradients that behave in much the same way as the observed subtropical tracer gradients.

Our results indicate that the winter subtropical edge marks a mixing barrier. The rapid stirring in the winter hemisphere that results from planetary-scale wave breaking is generally confined to the midlatitudes, and the strong tracer and potential vorticity gradients in the winter subtropics likely result from "stripping" processes, as filaments of material are occasionally pulled out of the tropics by this midlatitude stirring. The summer subtropical edge, however, does not mark a mixing barrier in the middle and upper stratosphere. Rather, it is likely that the strong subtropical tracer and potential vorticity gradients in the summer hemisphere result purely from the action of the residual circulation, which tends to increase potential vorticity and tracer values in the tropics and decrease them at high latitudes (for tracers with tropospheric sources and photochemical sinks) over the course of the summer. We show that the seasonal variability of the edges can, in some cases, contribute significantly to the mass budgets in simple "leaky pipe"-type models, but find that it is difficult to assess the role of this seasonal variability in tracer transport.

Thesis Supervisor: R. Alan Plumb
Title: Professor of Meteorology

Results! Why, man, I have gotten a lot of results.
I know several thousand things that won't work.

-Thomas Edison

Dedicated to my parents, who never pushed me too hard and never allowed me to give up too easily. Thank you for everything. And in memory of Constantine Giannitsis, who died too young and without reason. You are missed.

Acknowledgments.

The quality of graduate advising is a frequent topic of conversation at MIT, and there is often little good news to be heard in these conversations. However, throughout my time here, I have found myself in the incredibly fortunate position of being able to talk about my experience as an example of how graduate advising ought to work. I am extremely indebted to my advisor, Alan Plumb, for providing me not only with invaluable scientific guidance and insight, but also with career advice, encouragement, and an acknowledgment of my life outside of MIT. I think the most important scientific lesson that I have learned from Alan is that the first step should always be to draw a picture. Whether attempting to work through a set of equations that I don't quite understand or trying to find the right way to explain something to others, I always think of Alan and his hastily drawn squiggles as we discuss things in his office or his well thought-out schematics that he sprinkles throughout his talks and his papers to make his points ever so much clearer. Alan has taught me that pictures are the things that bring science and math together and that communicate ideas to others in the most direct way possible. While I could go on forever about how much I've learned from Alan and how much I admire him as a scientist, these things are only part of what make him a great advisor. Much of the rest of it lies in the simple fact that he treated me as an individual. His management style was flexible and responsive to my changing needs throughout my time as a graduate student. And he somehow managed to force me to think for myself without ever letting me feel that I was completely adrift on my own. But I think the most important thing to me was the fact that he occasionally asked about the other things in my life: soccer, skiing, my family, all of the things that so many graduate students have to pretend don't exist because they take time away from the lab or the computer room. It is such a simple thing, to acknowledge a life, and yet whenever there is a conversation about graduate advising at MIT, it is one of the first things that comes up. So thank you, Alan, for giving me so many good things to say.

The other person to whom I owe much of my success as a graduate student is Lynn Sparling. I met Lynn at a critical point in my graduate career; I had to successfully defend my thesis proposal or leave the program. Lynn's ideas on new ways of looking at data using relatively simple statistical methods led to most of the work in Chapter 3 and have revolutionized the way I and many others look at data. Her scientific input and moral support have helped me

enormously since the day I met her. Lynn constantly reminds me and everyone around her how important it is to be excited about science, and she provides much needed reality checks when science and graduate school start to take over your life. It is entirely possible that I would not have made it through graduate school if I had not met Lynn when I did. I was questioning both my abilities as a scientist and the personal toll that graduate school was taking on me, and my conversations with Lynn were largely what convinced me to stay. Thank you Lynn, for being everything: advisor, mentor, role model, and friend.

The other members of my committee have also been wonderful to work with, both scientifically and personally. Steve Wofsy was enormously helpful in defining the project and I benefited greatly from discussions with him about the simple conceptual model presented in Chapter 2 as well as many of the tracer observations discussed throughout the thesis, in particular the carbon dioxide measurements used as a proxy for the mean age in the stratosphere. Glenn Flierl was instrumental in ensuring that my goals were well-defined and properly stated within the context of the "big picture" and provided me with many valuable comments, particularly regarding the dynamical aspects of the thesis. Reg Newell may be the only person who will ever read every single word of my thesis, and he has provided me with many observational references that I would otherwise have been unaware of.

Other people who have provided valuable advice and discussions about the thesis include Lorenzo Polvani and John Methven, who helped me with the shallow water model simulations, Darryn Waugh, who provided a great deal of useful feedback on every aspect of the thesis, Darin Toohey and Linnea Avallone, who taught me most of what I know about atmospheric chemistry and who have been a great source of moral support throughout my time at MIT, and Doug Allen, who provided me with the equivalent length calculations shown in Chapter 3 and interesting discussions about the relationship between those calculations and the subtropical edges.

Our group has had the great fortune to have two amazing administrative assistants during my time here. Jane McNabb gave almost her entire life to the service of this department, and was a great help as well as a good friend to me through my first two years. Her humor and dedication to the students seemed impossible to match, but Mary Elliff has done a wonderful job of carrying the torch. She has gone far beyond the role of administrator and does so much

to enrich the lives of all of us on the 17th floor. Her office is a lovely haven from the stresses of graduate school and her smile can brighten up even the toughest of days. Our custodian, too, is a member of that rare breed that always has something nice to say and manages to touch the lives of everyone he comes in contact with. Late nights working can be incredibly lonely, but I have always looked forward to Tony's pass through the floor and the occasional treats he would bring with him. I don't know where he buys his Italian pastries, but they are just about the best in the world.

Graduate school is a time of enormous ups and downs. The deadlines are so few and far between that it is easy to lose the sense of daily accomplishment that carries most people through their lives. Everyone carries around the sneaking suspicion that they somehow slipped through the screening process; that they don't really belong in the program. The metamorphosis from someone who learns and regurgitates knowledge to someone who initiates research can be incredibly painful. And yet you are in a place where, for the first time ever, you can make nerdy jokes and people will laugh. There are parties and dinners and trips that are incredibly fun and enriching. And there are the uncommon bonds that come from the fact that everyone is experiencing the same fears and the same stresses as you are. There are two people, in particular, who are responsible for the best times I've had at MIT and who got me through the worst times: Will Heres and Veronique Bugnion. Will is our system administrator, and without him, I would still be sitting in the same seat as I was on my first day here, trying to figure out how to log in. I honestly don't know how I ever would have been able to process my data, run my models, and for that matter, print my thesis, if it hadn't been for Will. But more than that, Will is one of my best friends and a reason to come into work even on days that I can't face doing any work. He was much more than a shoulder to lean on; there were days that he virtually carried me. Thank you Will, for everything. Veronique is my some-time officemate, and she and I shared the additional bond of being women in a male world, not just in science, but also in climbing, skiing, triathlon, mountain biking, etc. I've had more fun and shared more pain with her than with anyone else in the world. How can I possibly say enough?

There are so many other friends that have touched my life over the years here, and I can't possibly mention all of them or thank them in the way that they deserve to be thanked. There is April, my best friend, whose phone calls gave me a much-needed connection to life outside of

Building 54 and who provided unconditional love always. There is Eric, who shared all of the stress of thesis writing with me and who reminded me that life is to be enjoyed. Thank you for all of the fun, friendship, and love. There are Kerim, Karen, and Helen, who are some of the most fun people in the world and who always provided a respite from the stress. There is Chris, who introduced me to so much of Boston and Cambridge and who enriched my life in so many ways. There is my roommate, Cindy, who washed my dishes more than once when I was writing up, and who has been a great friend through it all. There is Scott, who introduced me to the Outing Club and so many fun things like climbing and kayaking, and who gave me one of the best years of my life. Thanks for all the ice cream . . .There is my Graduate Women's Group, who taught me so much and helped me to grow in so many ways.

There are so many people that I have missed and so many more things that I could say, but it would take as many pages as my thesis. So I will just say that I will never forget my time at MIT and the people who touched my life while I was there. I owe the person that I have become, both scientifically and personally, to all of you.

Contents

Chapter 1

Introduction

Much of the research on chemical transport in the stratosphere in recent years has focused on the tropics, where most air enters the stratosphere through the upwelling branch of the large-scale residual circulation (Brewer, 1949; Dobson, 1956). There is an abundance of evidence that the air in the tropics remains relatively isolated from midlatitude air as it travels upward, but there are still significant questions regarding the details of the timescales and mechanisms of horizontal transport into and out of the tropics. The accurate representation of tropical transport in large-scale models of the stratosphere is particularly important because photochemistry acts very efficiently in the tropics both to produce ozone and to convert anthropogenic gases into the reactive compounds that destroy ozone (Ko et al., 1989), so that ozone chemistry throughout the stratosphere is particularly dependent on tropical transport. For example, the response of stratospheric ozone to anthropogenic chemicals produced by aircraft exhaust in the lower midlatitude stratosphere depends critically on the rate at which these chemicals are transported from the midlatitudes into the tropics, upward, and back out into the midlatitudes of the middle and upper stratosphere, where they can have the greatest impact on ozone chemistry (e.g. AESA, 1994). This thesis addresses two issues related to transport in the tropical stratosphere. The first is the dependence of the "mean age", which is a measure of the mean timescale for transport by large-scale processes in the stratosphere, on various transport parameters, including transport rates into and out of the tropics, under the assumption of at least some degree of tropical isolation. The second is the seasonal variability of the subtropical "edges", which mark the transition between tropical air and midlatitude air, including an extensive

diagnosis of this variability using satellite measurements of long-lived chemical tracers and an examination of the mechanisms that lead to the formation of these edges during each season in a shallow water model.

1.1 Evidence for Tropical Isolation

Some of the first evidence that the air in the tropics is relatively isolated came from observations of radioactive debris from nuclear explosions in the tropics as well as aerosols from tropical volcanic eruptions (e.g. Feely and Spar, 1960; Trepte and Hitchman, 1992; McCormick and Vega, 1992; Grant et al., 1996). These observations showed that once material is injected into the tropical stratosphere, the maximum concentrations remain in the tropics for several years, with transport into the midlatitudes occurring mainly through episodic "wave breaking" events (McIntyre and Palmer, 1983) during the winter, in which filaments of tropical air are pulled into the midlatitudes (McCormick and Vega, 1992; Trepte et al., 1993). Measurements of water vapor mixing ratios also indicate a lack of rapid communication between the tropics and midlatitudes. Mote et al. (1996) presented an analysis of water vapor and "total hydrogen" ($2CH_4+H_2O$) mixing ratios in the tropics as measured by the Microwave Limb Sounder (MLS) and Halogen Occultation Experiment (HALOE) instruments on the Upper Atmosphere Research Sounder (UARS) satellite. There is an annual cycle in water vapor mixing ratios at the tropical tropopause because of the annual cycle in tropopause temperature. Mote et al. (1996) showed that the annual cycle in both water vapor and total hydrogen is damped somewhat in the region just above the tropopause, but then propagates upward through the tropics with very little attenuation over periods of 18 months or more. No annual cycle in water vapor is observed in the midlatitudes, except in the lowest few kilometers of the stratosphere (Hyson, 1983). Thus, mixing in the midlatitudes must be rapid enough to homogenize the signal, which implies mixing timescales of one to two months (Boering et al., 1996), but mixing across the subtropics must be slow enough to prevent homogenization of the tropical signal.

As further evidence of inhibited mixing between the tropics and midlatitudes, we can look at the shape of the mixing ratio isopleths of long-lived chemical species in the stratosphere, which tell us a great deal about transport processes. Figures 1-1 a) and b) show zonal mean methane

(CH_4) and hydrofluoric acid (HF) mixing ratios as measured by the HALOE instrument during the period September 21 to October 15, 1992. CH_4 has a tropospheric source and a weak photochemical sink at high altitudes. Its lifetime ranges from centuries in the lower stratosphere to about 90 days in the upper stratosphere. Hydrofluoric acid is a product of the photochemical breakdown of chlorofluorocarbons (CFCs) and is extremely stable in the stratosphere. As seen in Figure 1-1, the mixing ratio isopleths of these species share a characteristic shape: they bulge upward in the tropics and then slope steeply downward in the subtropics. In the Southern hemisphere, the isopleths are relatively flat in the midlatitudes and then slope steeply again at the edge of the polar vortex. In the Northern hemisphere, the isopleths are less steep in the subtropics than in the Southern hemisphere, and gradually flatten out at high latitudes. Although these particular observations were taken near the equinox, the Southern hemisphere tracer distribution is characteristic of the winter hemisphere and the Northern hemisphere distribution is characteristic of the summer hemisphere. Similar winter and summer distributions are observed for all long-lived tracers with weak photochemical sinks. The fact that the isopleths of different species share the same shape indicates that their distributions are controlled mainly by transport process. The persistence of sharp gradients in the mixing ratios of these species is an indication of restricted mixing between regions. Figure 1-2 is a schematic of the relationship between stratospheric transport processes and the slope of mixing ratio isopleths. In Figure 1-2 a), the slope of the isopleths results from a balance between the residual circulation, which carries air upward in the tropics and downward at the poles and therefore tends to steepen the mixing ratio isopleths, and rapid quasi-horizontal mixing, which acts to flatten out tracer isopleths. If the quasi-horizontal mixing is global and rapid compared to the chemical and advective timescales then the slope of the mixing ratio isopleths will be small (Plumb and Ko, 1992). In Figure 1-2 b), the rapid quasi-horizontal mixing is restricted to the midlatitudes, where it flattens the mixing ratio isopleths, thus leading to steepened isopleths and strong gradients at the edges of the mixed region. We shall see that the situation depicted in Figure 1-2 b) is relevant mainly to the winter hemisphere, but strong tracer gradients could not persist in the summer subtropics if there were rapid mixing throughout the summer hemisphere. Thus, the summer subtropical tracer gradients are indicative at least of a lack of rapid mixing between the summer high latitudes and the tropics (though not necessarily of rapid mixing

within the summer high latitudes).

Tracer-tracer correlation diagrams, which are scatter plots of measurements of one chemical species versus another, provide additional evidence of tropical isolation. Measurements of long-lived chemical species in the stratosphere tend to lie along simple, compact correlation curves since their distributions are controlled by the same transport processes and their mixing ratio isopleths coincide with one another, as discussed above (Plumb and Ko, 1992). However, measurements taken in the tropics tend to lie along a different curve than those taken in the midlatitudes (Murphy et al., 1993; Goldan et al., 1980; Michelsen et al., 1998). Paradoxically, this indicates both a lack of rapid mixing between the tropics and midlatitudes and the presence of some mixing between them (Waugh et al., 1997; Plumb et al., 2000). If there were rapid mixing throughout the hemisphere, then mixing ratio isopleths would be surfaces of rapid mixing, and measurements taken in the midlatitudes would be indistinguishable from those taken in the tropics. In contrast, Figure 1-3 is a schematic which shows the impact of a subtropical mixing barrier on a tracer-tracer correlation. The bottom frame represents a correlation diagram for two species with slightly different chemical lifetimes. For example, tracer A could represent CH_4, whose lifetime is about 90 days in the upper stratosphere, and tracer B could represent nitrous oxide (N_2O), whose lifetime is about 50 days in the upper stratosphere. Since photochemical destruction is strongly altitude dependent, the mixing ratio of both species will decrease as air rises in the tropics, but the air will become depleted in tracer B more rapidly than tracer A. If the air enters the stratosphere with the mixing ratios denoted by the square, the tropical correlation will proceed downward in tracer-tracer space as the air rises. The curvature of the correlation will depend on the difference in chemical lifetimes (Plumb and Ko, 1992). If there is no mixing across the subtropical barrier, and the air simply rises and then descends in the midlatitudes, and if we assume that most photochemistry takes place in the high altitude tropical stratosphere, then as the air descends in midlatitudes, it will lie at a single point in tracer-tracer space, which is denoted by the circle in the bottom frame. However, if there is some mixing across the subtropical barrier, then air with the tropical correlation will be mixed in at each height, and the midlatitude correlation will become a "pursuit curve" from the circle back to the square.

Finally, Sparling (2000) showed that the probability distribution function (PDF) of the long-

lived tracer N_2O, as measured by the Cryogenic Limb Array Etalon Spectrometer (CLAES) satellite instrument, is tri-modal in the winter hemisphere, with modes corresponding to air in the tropics, "surf zone" (which will be discussed below), and polar vortex, and bimodal in the summer hemisphere, with modes corresponding to air in the tropics and the summer high latitudes. Minima in the PDF correspond to transition regions between these air masses, and are used in Chapter 3 to diagnose the seasonal variability of the subtropical edges. Rapid communication between regions would destroy the multi-modal structure of the PDF, so that the persistence of minima in the subtropics indicates that the tropics remain relatively isolated from midlatitude air and thus retain a distinct chemical signature.

1.2 Brief Overview of Stratospheric Transport Processes

Thus far, we have discussed the effects of the residual circulation, rapid quasi-horizontal mixing, and the confinement of that mixing on the distribution of long-lived chemical species, without considering the mechanisms behind these transport processes. Rapid quasi-horizontal mixing in the stratosphere occurs mainly in the winter hemisphere, where westerly winds permit the propagation of planetary-scale waves (Charney and Drazin, 1961). Planetary-scale waves with quasi-stationary phase speeds dominate the winter stratosphere, and they propagate upward and equatorward along the potential vorticity (PV) gradients on isentropic surfaces until they reach a region in which the zonal winds are weak and thus match the phase speed of the waves. In this region, the waves "break" and are dissipated (McIntyre and Palmer, 1983) in a highly nonlinear process that resembles the dynamics of a nonlinear critical layer (Stewartson, 1978; Warn and Warn, 1978; Haynes, 1985). This wave breaking results in large-scale isentropic stirring and the stretching and folding of material contours (McIntyre and Palmer, 1983). The cascade of enstrophy to small scales then results in mixing and the homogenization of both potential vorticity and chemical tracers.

Wave breaking is generally confined to the winter midlatitude "surf zone". At high latitudes during the winter, there are large zonal wind speeds in the westerly jet, while in the tropics the zonal winds are generally easterly (ignoring the effects of the quasi-biennial oscillation (QBO), which will be addressed in the thesis). Most of the planetary-scale waves that propagate into

the stratosphere have near-zero or small westerly phase speeds. Thus, they tend to break where the winds are weak and westerly: between the polar jet and the tropical easterlies.

The dissipation of planetary-scale waves in the surf zone and the resulting drag on the flow are largely responsible for the large-scale residual meridional circulation in the stratosphere, which carries air upward in the tropics, poleward, and then downward at mid- and high latitudes (Dickinson, 1971; Haynes et al., 1991). This stress-driven circulation results in diabatic heating in the tropics and cooling at mid- and high latitudes (Brewer, 1949; Dobson, 1956). However, if the wave drag is truly confined to the midlatitudes, then it can not be entirely responsible for the observed tropical upwelling, which reaches into the summer subtropics, unless there is some mechanism which allows non-conservation of angular momentum in the tropics (Plumb and Eluszkiewicz, 1999). Even in the absence of such a mechanism, direct diabatic heating may contribute somewhat to the tropical upwelling (Plumb and Eluszkiewicz, 1999; Semeniuk and Shepard, 2001).

The summer stratosphere is not as well understood as the winter stratosphere. The zonal winds in the summer stratosphere are generally easterly, though there are often very weak westerlies in the lower stratosphere. Recent studies have shown evidence of stirring similar to that of the winter hemisphere in the lower summer stratosphere and have attributed this stirring to two sources: the penetration of baroclinic eddies into the lower stratosphere and the propagation and breaking of planetary-scale waves in the weak westerly winds (Wagner and Bowman, 1999; Haynes and Shuckburgh, 2000). There is little evidence for any such stirring in the middle and upper stratosphere (Allen and Nakamura, 2000; Haynes and Shuckburgh, 2000). Because the wave forcing is weak in the summer hemisphere, there is only a weak overturning residual circulation, with maximum mass fluxes below 10 mb.

1.3 The Subtropical "Edges"

As discussed in Section 1.1, a confined region of quasi-horizontal mixing can lead to enhanced tracer gradients at the edges of the mixing region. If the mixing region spreads with time, as depicted in Figure 1-4, the tracer gradients at its edges will continue to increase as a result of the erosion process. Thus, while the presence of a strong tracer gradient is, in this case,

indicative of a mixing barrier, the gradients are actually enhanced if the mixing occasionally strips material out of the barrier (e.g. Sobel et al., 1997). Observations, as well as studies with high-resolution shallow water models, indicate that the stirring of the winter hemisphere surf zone does indeed occasionally reach into the tropics and the polar vortex and pull out filaments of material which are then stretched and folded in the surf zone until they reach sufficiently small scales for mixing to occur (e.g. McIntyre and Palmer, 1984; Randel et al., 1993; Juckes and McIntyre, 1987; Polvani et al., 1995). In models, this irreversible mass transport leads to a tightening not just of tracer contours, but also of potential vorticity contours, at the subtropical and polar vortex edges of the surf zone (e.g. Juckes and McIntyre, 1987; Norton, 1994; Polvani et al., 1995). Potential vorticity maps calculated from observations also show very strong PV gradients that coincide with the tracer gradients at the vortex edge (McIntyre and Palmer, 1984), but, unfortunately, these calculations are very unreliable in the tropics. The tightening of potential vorticity contours in addition to tracer contours indicates that the enhanced tracer gradients result from material transport and that there must be a net export of mass out of the regions in which the gradients form.

The term "subtropical edge" is often used to refer to the strong tracer gradients in the subtropics that were discussed in Section 1.1. The term was originally used to refer to the subtropical edge of the surf zone (Polvani et al., 1995), i.e., to the latitude at which the equatorward encroachment of the surf zone ends. This implies that a mixing barrier lies at the subtropical edge. As discussed above, the winter subtropical tracer gradients do, indeed, correspond to the mixing barrier at the edge of the surf zone. In addition, aircraft observations indicate that the winter subtropical tracer gradient is, in fact, very "edge-like". While accumulated zonal mean satellite measurements such as the ones shown in Figure 1-1 provide a highly averaged view of an edge that undulates with time, aircraft measurements provide an instantaneous, local view of the edge. Aircraft measurements presented in Strahan et. al., (1999) and Murphy et al. (1993) show that the winter subtropical tracer gradient is, in reality, much steeper than in the satellite observations in Figure 1-1, with changes of 30 to 40 percent of the total hemispheric gradient over a few degrees of latitude. However, the summer subtropical tracer gradient is also often referred to as a subtropical edge. This is a misnomer in the sense that, at least in the middle and upper stratosphere, the subtropical tracer gradient does not mark the edge of

a mixed region. It is also not particularly "edge-like". In fact, we shall show in Chapter 3 that the summer subtropical tracer gradient may occupy as much as 60 percent of the area of the summer hemisphere. However, we present evidence in Chapter 4 that the summer edge is, like the winter edge, a region in which the nonconservative mass flux is divergent. Thus, we consider it to be an "edge region", which separates two regions of convergent mass flux: the tropics (where the vertical mass flux is convergent) and the summer high latitudes (where the horizontal mass flux is convergent), and we refer to both the summer and winter subtropical tracer gradients as edges.

1.4 Overview

In Chapter 2, we examine the behavior of analytical solutions for the "mean age" of air, a measure of the mean transit time from the tropopause to any given location in the stratosphere, in a simple model of stratospheric transport. In this simple model, we divide the stratosphere into three regions: the tropics and the Northern and Southern midlatitudes, and allow communication between them via an entrainment flux. The purpose of the work is to assess the implications of tropical isolation in terms of global transport timescales in the simplest relevant framework.

In Chapter 3, we use the methods of Sparling (2000) to identify the subtropical edges from the minima in the PDFs of the long-lived tracers N_2O and CH_4. We examine six and a half years of measurements and identify the latitude, and in some cases the area, of the edges at eight pressure levels on quasi-monthly timescales. We thus build a picture of the seasonal variability of the edges throughout much of the stratosphere. We then compare this seasonal variability to variability in several transport parameters in order to further our understanding of the interaction between transport mechanisms and the subtropical edges from a diagnostic standpoint.

In Chapter 4, we examine the formation of both the winter and summer subtropical edges in a shallow water model, which represents many of the properties of the flow between two isentropic surfaces. We include the effects of diabatic heating and cooling through a mass source, and the effects of wave propagation through topography. We present perpetual solstice

simulations as well as a seasonal cycle simulation in which the mass source is varied with time to mimic the annual cycle in diabatic heating. The purpose of the work is to examine the role of large-scale stirring and diabatic processes in irreversible transport out of the edge regions.

In Chapter 5, we discuss the implications of our findings in Chapters 3 and 4 in terms of idealized models of transport such as the one discussed in Chapter 2, and in Chapter 6 we summarize the important results of the thesis.

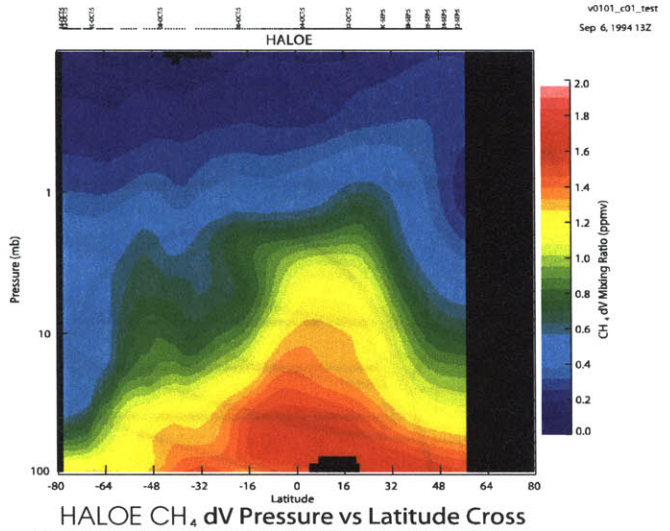

HALOE CH_4 dV Pressure vs Latitude Cross Section, Sunset on 22-SEP to 15-OCT-1992

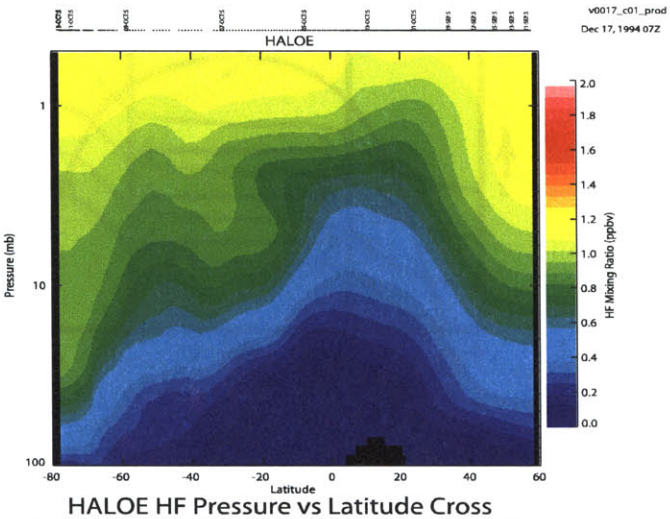

HALOE HF Pressure vs Latitude Cross Section, Sunset on 21-SEP to 15-OCT-1992

Figure 1-1: a) CH_4 and b) HF measurements from the HALOE satellite instrument, accumulated over September 22 to October 15, 1992. (from the HALOE web site: http://haloedata.larc.nasa.gov (J.M. Russell III and E. E. Remsberg))

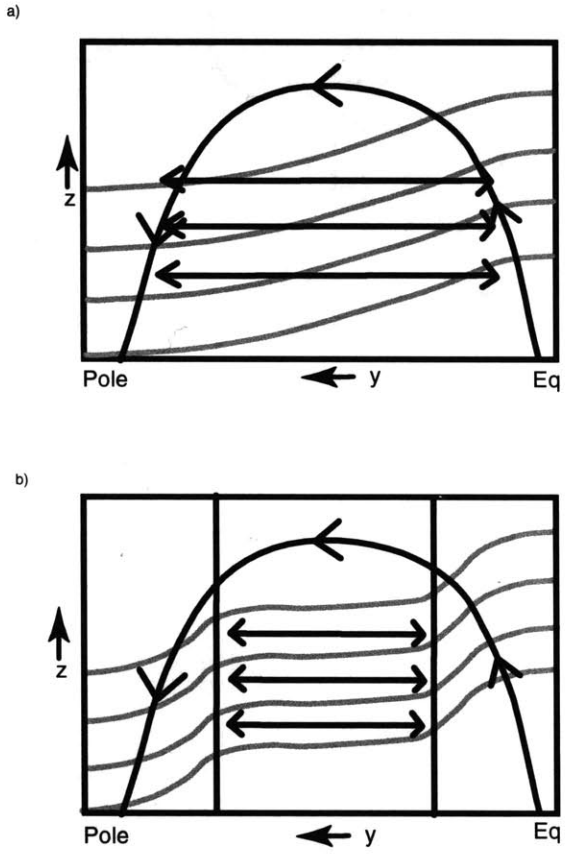

Figure 1-2: a) A representation of the effects of the meridional circulation (arching arrow) and rapid quasi-horizontal mixing (horizontal arrows) on the mixing ratio isopleths of a hypothetical tracer (gray lines). b) A representation of the effects of mixing barriers which confine the quasi-horizontal mixing.

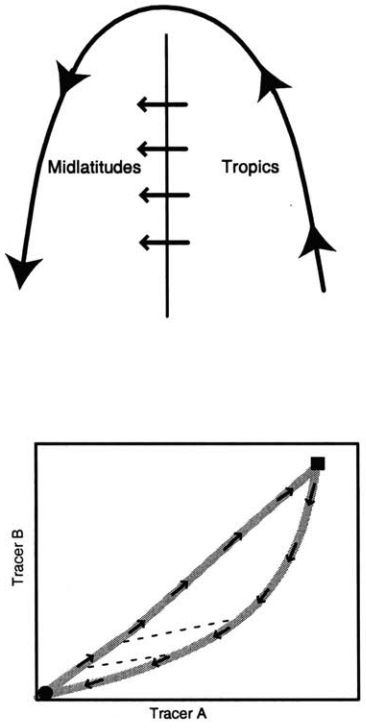

Figure 1-3: A schematic representing the effects of a mixing barrier on a tracer-tracer correlation. See text for discussion.

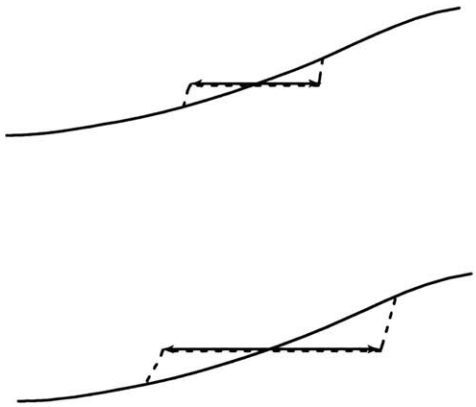

Figure 1-4: The top schematic represents the effects of a mixing region on a mixing ratio isopleth. The mixing, denoted by the arrow, homogenizes the tracer in the mixed region, thus producing enhanced gradients at the edges of the mixed region (dashed line). The bottom schematic represents the effects of spreading of the mixed region, which erodes and sharpens the tracer gradients.

Chapter 2

The Age of Air in a "Leaky Pipe" Model of Stratospheric Transport

2.1 Introduction

The age of air has become a valuable tool for investigating stratospheric transport. Age here refers to the statistical mean age, defined by Hall and Plumb (1994) as the mean transit time for air that has traveled from the tropopause to a given location in the stratosphere. Since the mean age depends purely on transport, and not on chemistry, it provides a powerful test of model performance. Hall et al. (1999) summarized the results of the age experiments from NASA's Models and Measurements II (MMII) model intercomparison. They compared mean ages from more than 20 two- and three-dimensional models to mean ages derived from in situ observations of carbon dioxide (CO_2) and sulfur hexafluoride (SF_6). Since these tracers are nearly conserved in the stratosphere and have been undergoing near-linear increases in their tropospheric concentrations over the past several years, their stratospheric concentration is a proxy for age (e.g., Bischoff et al., 1985; Hall and Plumb, 1994). Hall et al. (1999) found large discrepancies in the mean age between models and observations as well as between individual models. Figure 5 a) of Hall et al. (1999) compares latitudinal profiles of the mean age from the MMII models to mean ages derived from CO_2 and SF_6 at a height of 20 km. In general, the modeled mean ages are younger everywhere than observed mean ages, in some cases by a factor of 2. In addition, the magnitude of the latitudinal age gradient is smaller than the observed

gradient in all but three of the models.

Hall et al. (1999) showed that the mean age is important not only because it is a direct test of model transport, but also because there is a strong correlation between the mean age and the abundance of photochemically active trace species in the MMII models. Thus our understanding of the chemistry of the stratosphere and its response to perturbations depends critically on our understanding of transport. Since the models in the MMII study vary widely in their transport formulations, it is difficult to diagnose reasons for disagreement among models as well as between models and measurements. We have used the "leaky pipe" model, an extension of the Plumb (1996) tropical pipe model, to examine the role of various first-order transport processes in determining the mean age. This work was largely motivated by the fact that the mean age at a given location depends mainly on how efficiently the atmosphere transports air from the tropical tropopause to that location, so that we expect the age to be particularly sensitive to exchange between the tropics and midlatitudes.

We begin by discussing the formulation of the leaky pipe model and its relation to previous simple models of tracer transport. We then review the mathematical definition of the mean age and discuss the characteristics of analytical solutions for the mean age in the leaky pipe model. We also discuss the behavior of these solutions in limiting cases. Finally, we summarize our results and discuss their relevance to the issue of age and transport.

2.2 Model

The leaky pipe model is shown schematically in Figure 2-1. As in the tropical pipe model, the stratosphere is divided into three regions: the tropical region (TR), the northern surf zone (NSZ), and the southern surf zone (SSZ). This is an annually averaged view of the stratosphere in which we assume that polar vortex air is isolated only temporarily during the winter and that the strong mixing of the surf zones extends all the way to the poles in the annual average. The tropical region is bounded by interfaces I_N and I_S at latitudes φ_N and φ_S, which represent the subtropical edges of the northern and southern surf zones, respectively. We assume that the timescale for mixing across these interfaces is slow compared to the timescale for quasi-horizontal mixing within each surf zone. In the tropical pipe model, Plumb (1996) assumed

that mixing across the tropical interfaces was unidirectional, that is, that surf zone turbulence entrains material outward from the tropics into midlatitudes. Here we also allow midlatitude air to be mixed into the tropics across the tropical interfaces. This difference is based on studies such as Avallone and Prather (1996), Volk et al. (1996), and Minschwaner et al. (1996) which indicate that a significant amount (between 33 and 50%) of air in the tropics is of extratropical origin.

The details of the model formulation are given in Appendix A, where it is shown that the modified "leaky pipe" model yields the following one-dimensional tracer budgets for each region:

$$M_N \frac{\partial \sigma_N}{\partial t} - S_N = \frac{\partial}{\partial Z}\left(M_N K_N \frac{\partial \sigma_N}{\partial Z}\right) - M_N W_N \frac{\partial \sigma_N}{\partial Z} + M_N \left(1+\varepsilon_N\right)\lambda_N \left(\sigma_T - \sigma_N\right) \ ,$$

$$M_S \frac{\partial \sigma_S}{\partial t} - S_S = \frac{\partial}{\partial Z}\left(M_S K_S \frac{\partial \sigma_S}{\partial Z}\right) - M_S W_S \frac{\partial \sigma_S}{\partial Z} + M_S \left(1+\varepsilon_S\right)\lambda_S \left(\sigma_T - \sigma_S\right) \ ,$$

$$\begin{aligned} M_T \frac{\partial \sigma_T}{\partial t} - S_T = \frac{\partial}{\partial Z}\left(M_T K_T \frac{\partial \sigma_T}{\partial Z}\right) - M_T W_T \frac{\partial \sigma_T}{\partial Z} \\ -M_T \varepsilon_N \lambda_N \frac{M_N}{M_T}\left(\sigma_T - \sigma_N\right) - M_T \varepsilon_S \lambda_S \frac{M_S}{M_T}\left(\sigma_T - \sigma_S\right) \ , \end{aligned}$$

where σ is the mixing ratio and the subscripts N, S, and T refer to the NSZ, SSZ, and TR, respectively. Here, Z is the equivalent height, which is the height of a given mixing ratio isopleth at the tropical interface within each region, M is the integrated mass per unit equivalent height, and S is the net source per unit equivalent height along a mixing ratio isopleth. K is the diffusivity across the mixing ratio isopleths. In the tropics, K is the vertical diffusion coefficient, while in midlatitudes, it is the projection of the isentropic diffusion coefficient perpendicular to the mixing ratio isopleths. The vertical velocity W is the mean advection by the residual circulation through the mixing ratio isopleths in each region. The entrainment coefficients ε and λ are defined as

$$\lambda_N = \frac{\mu_{N\mathrm{net}}}{M_N} \ , \quad \lambda_S = \frac{\mu_{S\mathrm{net}}}{M_S} \ ,$$

$$\varepsilon_N = \frac{\mu_{N\mathrm{de}}}{\mu_{N\mathrm{net}}} \ , \quad \varepsilon_S = \frac{\mu_{S\mathrm{de}}}{\mu_{S\mathrm{net}}} \ ,$$

where $\mu_{N\mathrm{net}}$ and $\mu_{S\mathrm{net}}$ are the net entrainment mass fluxes into NSZ and SSZ, respectively,

and $\mu_{N\mathrm{de}}$ and $\mu_{S\mathrm{de}}$ are the detrainment mass flux from NSZ and SSZ into the tropics. The net entrainment mass flux is defined here as the difference between the entrainment mass flux out of the tropics into the surf zone and the detrainment mass flux from the surf zone into the tropics. The net entrainment mass flux is determined from mass continuity, which gives the constraint that the net entrainment into each hemisphere is balanced by the divergence of the mass flux in that hemisphere and that the total net entrainment balances the convergence of the mass flux in the tropics. In other words,

$$\mu_{N\mathrm{net}} = \frac{\partial}{\partial Z}(M_N W_N) \ ,$$

$$\mu_{S\mathrm{net}} = \frac{\partial}{\partial Z}(M_S W_S) \ ,$$

$$\mu_{N\mathrm{net}} + \mu_{S\mathrm{net}} = \frac{\partial}{\partial Z}(M_T W_T) \ .$$

The coefficient λ acts as an effective rate coefficient for the net entrainment; that is, λ^{-1} gives the timescale over which entrainment acts to change the mixing ratio in each region. The parameter ε is the ratio of detrainment from the surf zones into the tropics to the net entrainment. While λ is constrained by the mass flux, ε is a free parameter which can vary between 0 and ∞. This allows us to explore the entire range between Plumb's (1996) tropical pipe model with $\varepsilon = 0$, in which there is no detrainment from the surf zones into the tropics, and Plumb and Ko's (1992) global diffuser model with $\varepsilon = \infty$, in which the entrainment and detrainment across the tropical interface are equal, that is, there is no barrier to mixing in the subtropics.

2.3 Analytical Solutions for Age

2.3.1 Mathematical Construct for Age

Following Hall and Plumb (1994), we define an "age tracer" A, which is passive, conserved, and has a linearly growing boundary condition at the tropopause. The continuity equation for this

age tracer in pressure coordinates is given by

$$\frac{\partial A}{\partial t} + \mathcal{L}(A) = 0 \, ,$$

where $\mathcal{L}$ is used to denote the linear transport operator that includes both advection and diffusion. Thus, $\mathcal{L}$ is the divergence of the flux of A, $\vec{F}_A$, divided by the air density ρ:

$$\mathcal{L}(A) \equiv \frac{1}{\rho} \nabla \cdot \vec{F}_A \, . \tag{2.1}$$

Throughout this Chapter, we will neglect seasonal variations; thus, we assume here that $\mathcal{L}$ is steady. The boundary condition for A is

$$A(\overrightarrow{x}_o, t) = \gamma t \quad t \geq 0 \, ,$$

where γ is a constant and $\overrightarrow{x}_o$ is taken to be the tropopause. The solution for A can be written in terms of the Green's function for the continuity equation. In the long-time limit, this solution becomes

$$A(\overrightarrow{x}, t) = \gamma \left[t - \Gamma(\overrightarrow{x}) \right] \, ,$$

where Γ is the mean age. If we substitute the solution back into the continuity equation, we can solve directly for the mean age, which is given by the steady-state solution to the tracer continuity equation with a uniform, steady source of 1 year^{-1} and boundary condition of zero age at the tropopause (Bryan and Holland, 1989; Boering et al., 1996):

$$\begin{aligned} \mathcal{L}(\Gamma) &= 1 \, , \\ \Gamma(\overrightarrow{x}_o) &= 0 \quad t \geq 0 \, . \end{aligned} \tag{2.2}$$

2.3.2 Age in the Leaky Pipe Model

In order to derive an analytical solution for the mean age in the leaky pipe model, we make several simplifying assumptions. We assume that there is symmetry about the equator, that

the mass in each region decreases exponentially over a constant scale height H, and that the vertical ascent rates and effective vertical diffusion coefficients are constant. The leaky pipe equations for the mean age then become

$$-K_M \frac{\partial^2 \Gamma_M}{\partial Z^2} + \left(\frac{K_M}{H} - \alpha W_T \right) \frac{\partial \Gamma_M}{\partial Z} - (1+\varepsilon)\lambda(\Gamma_T - \Gamma_M) = 1 \,, \tag{2.3}$$

$$-K_T \frac{\partial^2 \Gamma_T}{\partial Z^2} + \left(\frac{K_T}{H} + W_T \right) \frac{\partial \Gamma_T}{\partial Z} + \frac{\varepsilon\lambda}{\alpha}(\Gamma_T - \Gamma_M) = 1 \,, \tag{2.4}$$

where the subscripts M and T refer to the midlatitudes and tropics, respectively, and $\alpha = M_T/(2M_M)$ is the ratio of the mass contained in the tropics to that contained in the midlatitudes. The bottom boundary conditions are given by

$$\Gamma_M(Z=0) = 0 \,,$$

$$\Gamma_T(Z=Z_T) = 0 \,,$$

where Z=0 is taken to be the equivalent height of the tropopause in midlatitudes and Z=Z_T to be the equivalent height of the tropical tropopause. We assume that the tropical air below Z_T is well mixed and has zero age. The upper boundary conditions are invoked in the following way: The homogeneous solutions to (2.3) and (2.4) are of the form $e^{r_i Z}$, where r_i represents the four roots of the homogeneous problem, one of which is zero, one of which is negative, and two of which are positive. The two positive roots correspond to unbounded exponential growth, and so are eliminated on physical grounds. The elimination of these solutions corresponds to requiring boundedness for the difference $\Gamma_M - \Gamma_T$ as $Z \to \infty$.

The solutions for this set of equations are then

$$\Gamma_M = A(Be^{-rZ} - e^{-rZ_T}) + C(Z - Z_T) + D \,, \tag{2.5}$$

$$\Gamma_T = A(e^{-rZ} - e^{-rZ_T}) + C(Z - Z_T) \,, \tag{2.6}$$

where

$$A = \frac{D - CZ_T}{e^{-rZ_T} - B} \,,$$

$$B = 1 - \frac{\alpha r}{\varepsilon\lambda}\left(\frac{K_T}{H} + W_T + rK_T\right) ,$$

$$C = \frac{\alpha + \varepsilon(\alpha+1)}{\alpha(1+\varepsilon)(K_T/H + W_T) + \varepsilon(K_M/H - \alpha W_T)} ,$$

$$D = \frac{\alpha(K_T/H + W_T) - \alpha(K_M/H - \alpha W_T)}{\alpha(1+\varepsilon)\lambda(K_T/H + W_T) + \varepsilon\lambda(K_M/H - \alpha W_T)} ,$$

and $-r$ is the negative root of the homogeneous problem.

The first ($\sim e^{-rZ}$) term of the solution in each region largely describes the effects of diffusion. This is most transparent when we consider the scaling constraint $K_M \ll W_M H$, which is discussed in the appendix. Under this scaling, a solution to the homogeneous problem exists for which (2.3) becomes dominated by the first two terms on the left-hand side, whence

$$\Gamma_M \sim e^{\{[W_M + (K_M/H)]/K_M\}Z} .$$

Since $W_M < 0$, this is a bounded solution which decays with height scale $h_D = K_M/\left[W_M + (K_m/H)\right]$ $\cong K_M/W_M << H$ above the tropopause. Thus this component of the solution manifests itself as a thin boundary layer above the tropopause, within which the solution adjusts to the boundary condition of zero age at the tropopause. (It is within this layer that tropospheric air diffuses "upward" (the way in which this model represents isentropic diffusion across the tropopause) into the lower stratosphere.) In the tropics, $W_T > 0$, so there is no similar solution corresponding to this balance for (2.4). However, the exponentially decreasing term in the tropical solution represents the communication of the decaying midlatitude solution to the tropics by in-mixing of midlatitude air.

Close inspection shows that the second ($\sim e^{-rZ_T}$) term of the solution ((2.5) and (2.6)) in each region vanishes in the limit $K_M, K_T \to 0$, and is a negative contribution to the age throughout the parameter range we explore. The remaining terms are the particular solutions, which dominate the behavior of Γ_T and Γ_M. The third term in each region gives a linear increase with equivalent height, as we would expect from the equivalence between age and a tracer whose boundary condition grows linearly with time. The fourth term in the midlatitude solution is a constant offset between the tropical and midlatitude ages, which reflects the fact that the mixing ratio, or in this case the age, is not continuous across the tropical interface on

a surface of constant equivalent height.

Figures 2-2 a) and 2-2 b) show the mean age as a function of equivalent height Z and the entrainment parameter ε for the tropics and midlatitudes, respectively. The midlatitude age shown is the age at the tropical interface. The age at a given equivalent height at other latitudes in the surf zones depends on the slope of the age isopleths. Figure 2-2 c) shows the difference between the midlatitude and tropical ages ($\Delta\Gamma = \Gamma_M - \Gamma_T$). For reference, $\varepsilon = 0$ corresponds to mixing out of the tropics into the surf zones only (the tropical pipe limit), while $\varepsilon = 1$ corresponds to twice as much mixing out of the tropics as into them. We have assumed that each region contains 1/3 of the total stratospheric mass at all equivalent heights, so that $M_T/M_M = 1$ and $\alpha = 1/2$. This implies that the edges of the tropical region are near 20^o, close to the position determined by both Grant et al. (1994, 1996) and Waugh (1996). These solutions were calculated using

$$W_T = 0.3 \text{ mm s}^{-1} ,$$

$$H = 7 \text{ km} ,$$

$$K_T = 0.01 \text{ m}^2 \text{ s}^{-1} ,$$

$$K_M = 0.5 \text{ m}^2 \text{ s}^{-1} ,$$

$$Z_T = 0 .$$

The values for W_T and K_T were taken from Hall and Waugh (1997), who derived them by fitting solutions from a tropical transport model to tracer observations. The value for K_M was chosen to be as large as possible, so that it only marginally satisfies the constraint that $K_M/H << W_M$ (in fact, $K_M/(HW_M) \cong 0.47$ for these numbers; the height scale is $h_D \cong 2.27$ km). Since we later look at the limit in which the vertical diffusion becomes negligible, we chose this value in order to explore an upper limit for the effects of diffusion. The tropical tropopause was taken to be at the same equivalent height as the midlatitude tropopause in this case to allow easier interpretation of the results. The solution for an elevated tropical tropopause will be discussed later.

As ε increases, the age in both the tropics and midlatitudes increases except in the diffusive boundary layer near the tropopause (in $Z \lesssim h_D$). Throughout much of this boundary layer

the midlatitude age is approximately constant with ε. The tropical age is also constant with ε for a short distance above the tropopause. Above the boundary layer the age in each region grows approximately linearly with equivalent height, and the difference between them becomes constant with equivalent height. Note that the behavior of the solution is dominated by the particular solution.

Physically, this behavior can be understood as follows. Air enters the stratosphere at the tropical tropopause and ages as it rises in the tropics. At the same time, air is exchanged between the tropics and the surf zones at a rate which maintains mass balance. In the surf zones, air continues to age as it descends. Thus, at any given equivalent height the midlatitude air is older than the tropical air. Near the midlatitude tropopause, zero age (tropospheric) air enters the midlatitudes by isentropic mixing into the boundary layer. This boundary layer is then communicated to the tropics through the exchange of air across the tropical barrier. Note that for ε=0, the tropical age is linear everywhere despite the fact that the midlatitude age is nonlinear in the boundary layer. Without transport of air from the midlatitudes into the tropics the tropical age is unaffected by the presence of the diffusive boundary layer in midlatitudes. As ε increases, the ratio of detrainment to the net entrainment increases, while the net entrainment remains constant because of mass continuity constraints. Thus, as ε increases, both the entrainment from the tropics into the surf zones and the detrainment from the surf zones into the tropics increase. Air from the midlatitudes can reenter the tropics, increasing the mean age in the tropics. Since the tropical air is then older than it would have been without the input of midlatitude air, it in turn increases the mean age in midlatitudes relative to the ε=0 case as it is entrained into midlatitudes. In other words, air parcels can make multiple circuits between the tropics and midlatitudes, increasing the mean age in both regions as they do. The difference between the tropical and midlatitude ages decreases as ε increases. However, as we will later show, this is not the case when vertical diffusion is neglected.

Figures 2-3 a), 2-3 b), and 2-3 c) show the tropical mean age, the midlatitude mean age, and the difference between them when the height of the tropical tropopause is taken to be half a scale height above the midlatitude tropopause (Z_T=3.5 km). We assume that the air in the tropics below the tropopause is well mixed and has zero age so that entrainment from the tropics into midlatitudes below the tropical tropopause mixes zero age air into midlatitudes.

Since increasing ε leads to greater entrainment as well as detrainment, more zero age air is mixed into the boundary layer above the midlatitude tropopause. Since this acts to decrease the gradient between the older air in midlatitudes and the tropospheric air which is mixing isentropically across the midlatitude tropopause, the diffusive boundary layer is destroyed as ε increases. It is interesting to note that stratospheric mean ages derived from carbon dioxide observations also show very young air above the midlatitude tropopause (Boering et al., 1996). The origin of this young air (i.e., whether it is entrained horizontally from the tropics or mixed across the midlatitude tropopause) remains an open question.

2.3.3 Age in the Global Diffuser Limit

As noted in section 2.2, the limit $\varepsilon \to \infty$ represents equal entrainment and detrainment across the subtropical edge, that is, the absence of a mixing barrier in the subtropics. If we take K_T=K_M in this limit, we should recover the global diffuser model of Plumb and Ko (1992). We assume that $\Gamma_T \approx \Gamma_M$ so that the mixing ratio isopleths are approximately continuous between the tropics and midlatitudes (as we would expect in the global diffuser model) and then define an overall mean age, $\overline{\Gamma} = (\Gamma_M + \alpha\Gamma_T) / (1+\alpha)$, and an age difference, $\delta\Gamma = \Gamma_T - \Gamma_M$, so that $\delta\Gamma \ll \overline{\Gamma}$. The equations for the tropics and midlatitudes then combine to become

$$-K\frac{\partial^2\overline{\Gamma}}{\partial Z^2} + \frac{K}{H}\frac{\partial\overline{\Gamma}}{\partial Z} = 1 \, .$$

This is, in fact, the equation used by Plumb and Ko (1992) (for the case where density is exponentially decreasing). The solution for age in the global diffuser model (assuming Z_T=0) is thus

$$\overline{\Gamma} = \frac{H}{K}Z \, .$$

Figure 2-4 a) shows the age in the global diffuser model for our values of H and K_M. Looking at the slope above the boundary layer for the leaky pipe solution, we find

$$\lim_{\varepsilon\to\infty}\left(\frac{\alpha+\varepsilon(\alpha+1)}{\alpha(1+\varepsilon)\left(\frac{K}{H}+W_T\right)+\varepsilon\left(\frac{K}{H}-\alpha W_T\right)}\right) = \frac{H}{K} \, .$$

For large values of ε the slope is

$$\frac{H}{K}\left[1-\left(\frac{\alpha WH}{(\alpha+1)K}\right)\frac{1}{\varepsilon}+O\left(\frac{1}{\varepsilon^2}\right)\right],$$

so that the first-order error involved in assuming the global diffuser limit is $\sim \frac{\alpha WH}{(\alpha+1)K}(1/\varepsilon)$. Figure 2-4 b) shows our analytical solution, using the same parameters as in Figure 2-2 (except $K_T = K_M = 0.5$ m^2 s^{-1}) for $\varepsilon = 2$, $\varepsilon = 20$, and $\varepsilon = 200$. The difference between the tropical and midlatitude ages is small even for $\varepsilon = 2$, and the age for $\varepsilon = 200$ is very close to the global diffuser limit.

2.3.4 Age in the Nondiffusive Limit

As discussed previously, the assumptions of the leaky pipe model lead to the scaling $K/H \ll W$. Thus, the terms $(K/H)\left[(\partial\Gamma)/(\partial Z)\right]$ and $K\left[\left(\partial^2\Gamma\right)/\left(\partial Z^2\right)\right]$ are small compared to $W\left[(\partial\Gamma)/(\partial Z)\right]$ and we can investigate the behavior of the solution when cross-isopleth (near-vertical) diffusion is neglected. Since $K_T < K_M$ in the previous calculations, and $|W_T| > |W_M|$, we can expect that neglecting vertical diffusion in the tropics will have less of an impact on the solution than neglecting the effective vertical diffusion in midlatitudes. In fact, when we neglect the terms involving K_T, the age becomes slightly older (on the order of 1%) in both the tropics and the midlatitudes, but the behavior of the solution does not change (not shown here).

In the surf zones, neglecting the cross-isopleth diffusion is equivalent to assuming that the mixing ratio isopleths lie along the isentropes, that is , that the slope equilibrium balance is dominated by quasi-horizontal mixing by Rossby waves. When both K_T and K_M are neglected, the solution becomes

$$\Gamma_M = \left(\frac{\alpha+\varepsilon(\alpha+1)}{\alpha W_T}\right)(Z-Z_T)+\frac{(1+\alpha)}{\lambda}, \tag{2.7}$$

$$\Gamma_T = \left(\frac{\alpha+\varepsilon(\alpha+1)}{\alpha W_T}\right)(Z-Z_T). \tag{2.8}$$

Figures 2-5 a), 2-5 b), and 2-5 c) show the solutions for Γ_T, Γ_M, and the difference between them for the non-diffusive system (using the same values for α, W_T, and Z_T as in Figure 2-2). The midlatitude boundary layer is infinitesimally thin, so that the age is no longer zero at the

midlatitude tropopause. Both the tropical and midlatitude mean ages are linear functions of the equivalent height everywhere, as well as linear functions of the entrainment parameter ε. The difference between the tropical and midlatitude ages does not depend on ε, but only on the net entrainment rate, which is constant under our assumptions of constant scale height and constant vertical velocity.

The solutions for the nondiffusive system of equations are similar to those for the full system, especially for small values of ε. Except in the midlatitude boundary layer, the full system of equations has solutions that depart only weakly from linear dependence on Z and ε. Thus we can gain an understanding of the dependence of age on our transport parameters from the nondiffusive system as long as we are mindful of the additional complexity introduced by diffusion. Further, there is some evidence that the nondiffusive limit is at least somewhat relevant to the real stratosphere. Sparling et al. (1997) estimated that the vertical diffusivity K_{ZZ} of the midlatitude stratosphere is approximately 0.1-0.2 m^2 s^{-1} for diffusive mixing that results from the variability of diabatic heating along isentropic surfaces. It is likely that this is a lower bound for the vertical diffusion coefficient, but the magnitude of other contributions is largely unknown. Sparling et al. (1997) quotes estimates of vertical diffusivity ranging from 0.01 to 1 m^2 s^{-1} for diffusive mixing associated with thin turbulent layers. Figures 2-6 a) and 2-6 b) show the tropical and midlatitude ages for the full system of equations for the same parameters as Figure 2-2, except that we have used the Sparling et al. (1997) estimate for the midlatitude diffusion coefficient, $K_M = 0.1\,m^2\,s^{-1}$. Note that the midlatitude boundary layer is now much thinner than in Figure 2-2 b) and that the ages are closely approximated by those from the nondiffusive case.

One of the major advantages of the nondiffusive system of equations is that there is an analytical solution for these equations even when the vertical velocity is a general function of height. Since the local midlatitude downwelling balances the local tropical upwelling, our equations become

$$W_M(Z)\frac{\partial \Gamma_M}{\partial Z} - (1+\varepsilon)\lambda(Z)(\Gamma_T - \Gamma_M) = 1\ , \tag{2.9}$$

$$W_T(Z)\frac{\partial \Gamma_T}{\partial Z} + \frac{\varepsilon\lambda(Z)}{\alpha}(\Gamma_T - \Gamma_M) = 1\ , \tag{2.10}$$

$$W_M(Z) = -\alpha W_T(Z)\ .$$

We can then solve this system for the difference between the tropical and midlatitude age, which is given by

$$\Gamma_M - \Gamma_T = \frac{(1+\alpha)H}{\alpha W_T(Z)} \ .$$

(Note that this is consistent with (2.7) and (2.8) since $\lambda = (\alpha W_T)/H$ when W_T is constant). As in the case with constant ascent rates, the age difference is a function only of the local vertical velocity, and not of the entrainment parameter, ε. In other words, increasing the exchange between the tropics and the surf zones (while the net entrainment maintains the local mass balance) increases the age in each region equally. The age difference does not depend on the path of the air parcels, but only on the local ascent rate.

Age Flux

We can interpret this result more generally by considering the age flux. The steady state equation for age is given by (2.2) or, using (2.1),

$$\frac{1}{\rho} \bigtriangledown \cdot \overrightarrow{F}_\Gamma = 1 \ ,$$

from which it follows, on integration,

$$\int_A \overrightarrow{F}_\Gamma \cdot \vec{n} \ dA = - \int_V \rho \ dZ \ dA \ ,$$

where the area integral is over any surface spanning the globe, $\vec{n}$ is the upward unit normal to that surface, and the volume integral is over the entire atmosphere above the surface. Thus the integrated downward normal flux of age through any global surface equals the total air mass above that surface. (If a net flux with units of mass appears surprising, note that the net flux of a conventional tracer, whose mixing ratio is dimensionless, has dimensions mass per unit time; since age has dimensions of time, its flux has units of mass.)

In the case of the leaky pipe model, we can consider the flux of age through a surface of constant equivalent height (compare to Figure 2-1). The entrainment flux normal to this surface is zero, so that in the absence of cross-isopleth diffusion, the net global flux is purely advective

and is

$$\int_A \vec{F}_\Gamma \cdot \vec{n}\, dA = 2M_M W_M \Gamma_M + M_T W_T \Gamma_T$$
$$= -(M_T W_T)\Delta\Gamma \, .$$

Since we are assuming $\rho \sim \exp(-z/H)$, the mass above the surface is

$$\int_V \rho \, dZ \, dA = H \int_A \rho \, dA$$
$$= H\,(2M_M + M_T)$$
$$= HM_T(1 + \frac{1}{\alpha}) \, .$$

Hence

$$\Delta\Gamma = \frac{(1+\alpha)H}{\alpha W_T(Z)} \, , \tag{2.11}$$

as above.

If we now consider the diffusive age flux as well, we simply need to add the net global diffusive flux F_{DIFF} to the advective flux. We then obtain

$$\Delta\Gamma = \frac{(1+\alpha)H}{\alpha W_T(Z)} + \frac{F_{\mathrm{DIFF}}}{(M_T W_T)} \, .$$

In our model, as well as in observations of age inferred from CO_2 and SF_6 measurements (e.g., Boering et al., 1996; Harnisch et al., 1996), the mean age increases with height throughout the stratosphere, implying that $F_{\mathrm{DIFF}} < 0$; thus the age difference in the nondiffusive limit is an upper bound.

Path Independence

The result that the age difference in the nondiffusive limit depends only on the local ascent rate and not on the path of the air parcels is not an intuitive result. Consider, for example, a situation such as that portrayed schematically in Figure 2-7 a), in which air rises in the tropics with velocity W at altitude Z_0, circulates above, and descends in the extratropics. The age

difference $\Delta\Gamma_0$ at Z_0, between points A and B, is given by (2.11) and reflects the average time taken for the air to circulate above Z_0. Consider now the case of Figure 2-7 b), identical below Z_0, but at which the air moves directly from A to B. By making the jet as narrow as we choose, we can make the time taken to cross from A to B as small as possible, thus making the age difference arbitrarily small. How can this be reconciled with (2.11), which tells us that the age difference is the same as in case a? The answer is that case b is singular. Consider now case c, in which a fraction α of the upwelling air at A is fed into the upper branch and the remaining fraction $1-\alpha$ is fed instantaneously to B. Now, since the mass flux in the upper branch varies as α, the upward velocity immediately above A is αW and so the age difference between B and A in the upper branch flow is $\Delta\Gamma_0/\alpha$. The age difference in the lower branch is zero. The resulting age at B, with respect to A, is simply given by mixing the two air streams together, yielding a net age difference $\alpha\,(\Delta\Gamma_0/\alpha) + (1-\alpha)\,0 = \Delta\Gamma_0$, which is independent of α. Case b is misleading, as the contribution of the upper branch to the age difference is never negligible: Even in the limit $\alpha \to 0$ the upper branch contributes an infinitesimal amount of infinitely old air.

Vertical Structure of Extratropical Age

Observations (e.g., Boering et al., 1996; Harnisch et al., 1996) show that the mean age of stratospheric air increases with altitude both in the tropics and in the extratropics. Within the upwelling tropics, it appears inevitable that the mean age Γ must increase with height, but it is not so clear in the downwelling region of the middle and high latitudes. For example, in a simple advective circulation in which air ascends within the tropics to some height Z, diverges into middle latitudes, and then descends (e.g., as in Figure 2-7 b)), the midlatitude air will become progressively older as it descends below Z; thus Γ would decrease with altitude in the descending region. That it does not, in reality, must be indicative of the injection of young tropical air into the descending branch of the circulation.

If we neglect vertical diffusion, the tropical age budget (2.10) is

$$W_T \frac{d\Gamma_T}{dZ} = \frac{\varepsilon\lambda}{\alpha}\,\Delta\Gamma + 1\,,$$

where $\Delta\Gamma = \Gamma_M - \Gamma_T$. Moreover, since $\Gamma_M = \Gamma_T + \Delta\Gamma$, we have

$$W_T \frac{d\Gamma_M}{dZ} = W_T \frac{d\Gamma_T}{dZ} + W_T \frac{d\Delta\Gamma}{dZ}$$

and so, since $\Delta\Gamma = (1+\alpha)H/\alpha W_T$,

$$\begin{aligned}
\frac{d\Gamma_M}{dZ} &= \frac{1}{W_T} + \frac{(1+\alpha)\varepsilon\lambda}{\alpha^2}\frac{H}{W_T^2} + \frac{d}{dZ}\left(\frac{(1+\alpha)H}{\alpha W_T}\right) \\
&= -\frac{(1+\alpha)H}{\alpha W_T^2} e^{\frac{Z\alpha}{(1+\alpha)H}} \frac{\partial}{\partial Z}\left(W_T\, e^{-\frac{Z\alpha}{(1+\alpha)H}}\right) \\
&\quad -\frac{(1+\alpha)\varepsilon H}{\alpha W_T^2} e^{\frac{Z}{H}} \frac{\partial}{\partial Z}\left(W_T\, e^{-\frac{Z}{H}}\right), \qquad (2.12)
\end{aligned}$$

where we have used

$$\lambda = -e^{\frac{Z}{H}} \frac{\partial}{\partial Z}(\alpha W_T e^{-\frac{Z}{H}}).$$

Thus the midlatitude age profile depends on the vertical structure of the upwelling velocity and on the entrainment coefficient ε. In the limit $\varepsilon \to 0$, Γ_M increases or decreases with height according to whether $W_T\, e^{-Z\alpha/(1+\alpha)H}$ decreases or increases. If the mass flux $W_T\, e^{-Z/H}$ were constant with height, $\partial\Gamma_M/\partial Z < 0$, as noted above. In order to make Γ_M increase with Z when $\varepsilon = 0$, the mass flux must fall off sufficiently quickly with height so that younger tropical air is injected into the older midlatitude air at a sufficient rate. The term in (2.12) involving ε is always positive when the mass flux decreases with altitude (as it must if wave pumping (Holton et al., 1995) is such as to pump air out of the tropics). As noted above, by increasing ε, and thus injecting old air into the tropics, the tropical air becomes older with altitude, and, since $\Gamma_M = \Gamma_T + \Delta\Gamma$ and $\Delta\Gamma$ is independent of ε, the same is true of Γ_M.

2.4 Discussion

Perhaps the most surprising outcome of this work is the result that the age difference across the subtropical edge is insensitive to exchange between the tropics and the surf zones in the limit of negligible cross-isopleth diffusion. In this limit the age difference across the edge depends only on the vertical ascent rates. Further, we have shown that the age difference will always

decrease in the presence of cross-isopleth diffusion. These results have important implications for more complex two- and three-dimensional models. As noted earlier, Figure 5 a) of Hall et al. (1999) suggests that the latitudinal age gradient is smaller than the observed gradient in almost all of the MMII models. While increasing the isolation of the tropics in these models may be necessary to reproduce certain observations, such as the ascent of the water vapor annual cycle in the tropics and the steepness of subtropical tracer gradients, our results suggest that this change will have little impact on the latitudinal age gradient. Reducing vertical ascent rates or vertical diffusion seems to be the most effective way to increase the age difference between the tropics and the midlatitudes.

A second important outcome of this study is the result that increasing the isolation of the tropics, that is, approaching the tropical pipe limit, leads to younger air in both the tropics and midlatitudes. When there is less mixing between the tropics and the midlatitudes, there are fewer opportunities for parcels to make multiple circuits between the two regions. Thus the tail of the age spectrum is reduced, and the mean age is decreased. As discussed in section 2.1, most two- and three-dimensional models produce mean ages that are considerably younger than observed mean ages. Our results suggest that increasing the isolation of the tropics in these models will further reduce the mean age everywhere and that either a less vigorous residual circulation or higher resolution (to decrease vertical diffusion) will be necessary to counteract this effect.

These results are corroborated by more sophisticated models. Figure 9 of Hall et al. (1999) shows the mean age for three versions of the Atmospheric and Environmental Research (AER) two-dimensional model. In the "tropical pipe" version the tropics are isolated from the midlatitudes by setting the latitudinal diffusion coefficient in the tropics to near-zero, while in the "no pipe" version the tropical diffusion coefficient is the same as that in midlatitudes. The "leaky pipe" is an intermediate version. At a given height both the tropical and midlatitude ages are oldest in the "no pipe" version and youngest in the "tropical pipe" version. The age difference between the tropics and midlatitudes, however, changes very little. This supports our result that increasing the mixing between the tropics and midlatitudes increases the age of the air everywhere but has little impact on the tropical - midlatitude age difference. Figure 12 of Hall et al. (1999) shows the mean age from the MONASH1 and MONASH2 three-dimensional

models. These models are identical except for their wind data input: MONASH2 has a more vigorous residual circulation. The mean ages in MONASH1 are older, as we would expect since the transit times are increased for a slower circulation. However, the latitudinal age gradient is also larger in MONASH1 than in MONASH2 despite the fact that the shape of the contours is very similar in the two versions. Thus it seems that the residual circulation plays a major role in determining the latitudinal age gradient.

The solutions presented here provide a powerful demonstration of the usefulness of the leaky pipe model in diagnosing complex transport issues. The model represents the bulk effects of the first-order transport processes of the stratosphere, yet it is simple enough to permit analytical solutions. These solutions have given us a clear understanding of the role of various transport processes in determining the mean age of air in the leaky pipe model, which in turn gives us insight into the role of these processes in more complex models as well as in the real stratosphere. Of course, the coupling between these processes leads to complications that we do not represent in our model. For example, while we constrain the net entrainment out of the tropics, we represent the individual entrainment and detrainment terms as free parameters. In reality, these terms are probably coupled to wave activity, which is coupled to the residual circulation. It seems that comprehensive studies of the role of transport processes in dynamically consistent models will be necessary to determine to what degree these transport processes are coupled and what impact this coupling has on our understanding of what determines the mean age.

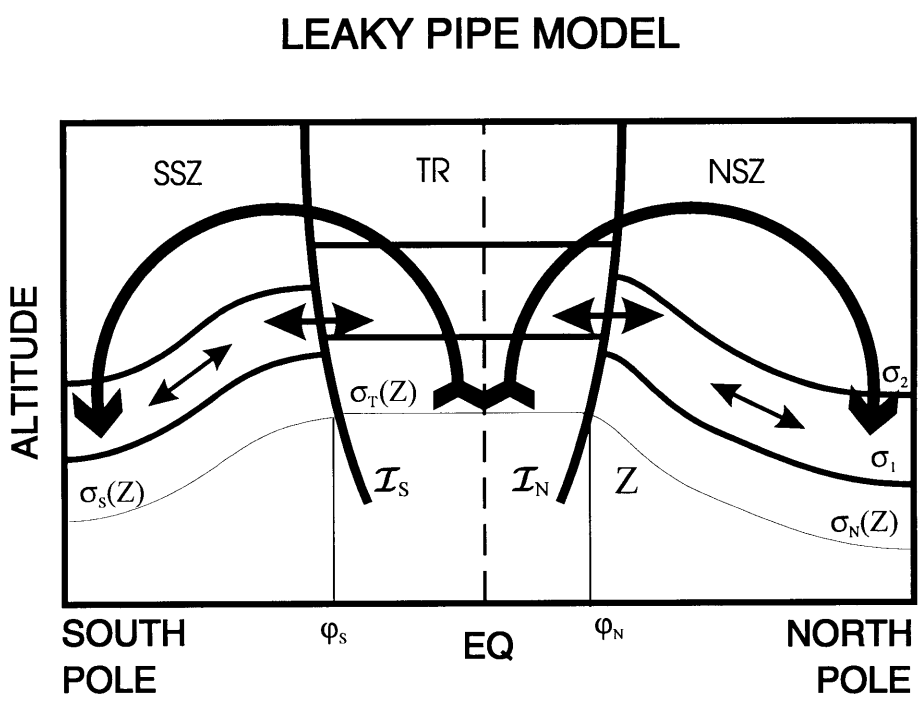

Figure 2-1: Schematic of the leaky pipe model. The large curved arrows represent the residual circulation, while the smaller arrows represent isentropic mixing in the surf zones and quasi-horizontal mixing across the edge of the tropics. The thick lines labeled σ_1 and σ_2 are surfaces of constant mixing ratio. The thin line labeled $\sigma(Z)$ in each region is a surface of constant equivalent height.

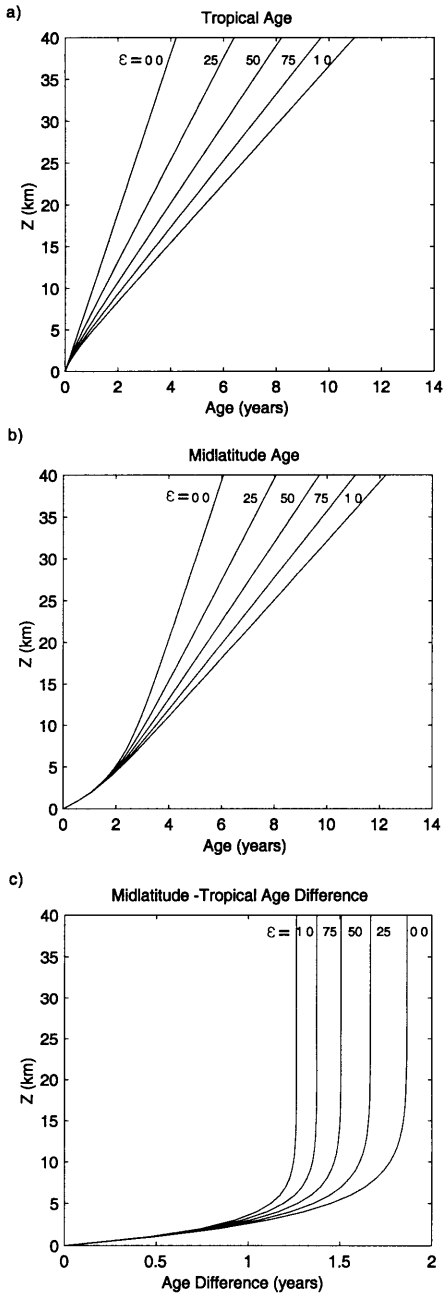

Figure 2-2: Solutions to equations (2.5) and (2.6) for the mean age in (a) the tropics and (b) the midlatitudes, as well as (c) the difference between the midlatitude and tropical age for the parameters given in the text.

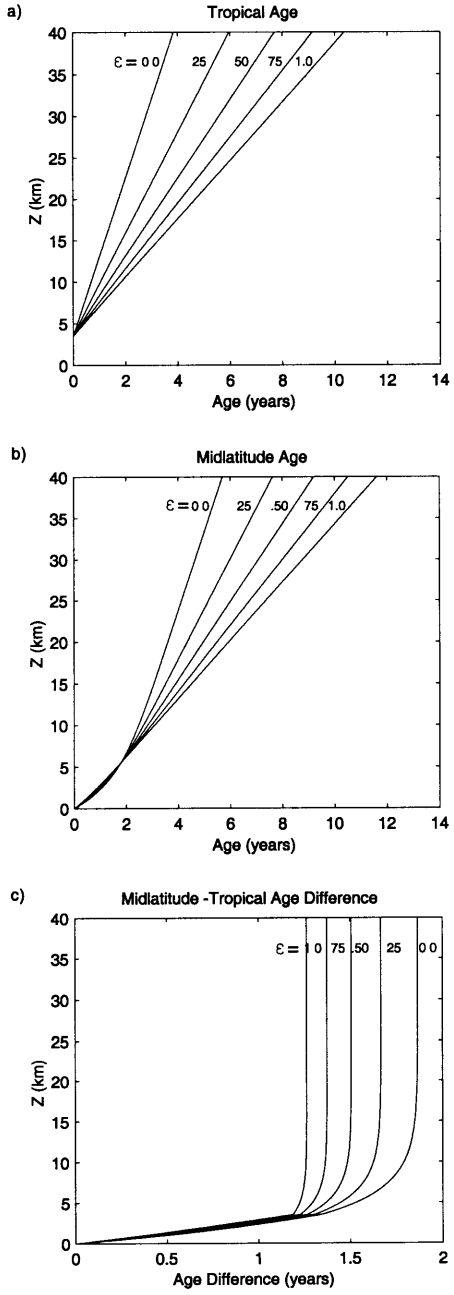

Figure 2-3: Same as Figure 2-2, but for Z_T =3.5 km.

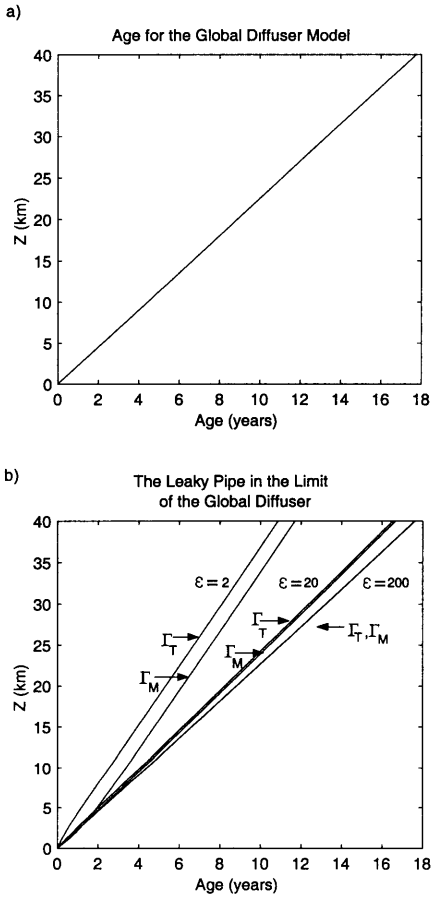

Figure 2-4: Mean age for (a) the global diffuser model of Plumb and Ko (1992) and (b) the leaky pipe model with $K_T = K_M = 0.5$ m^{2}s^{-1}. Other parameters are the same as in Figure 2-2

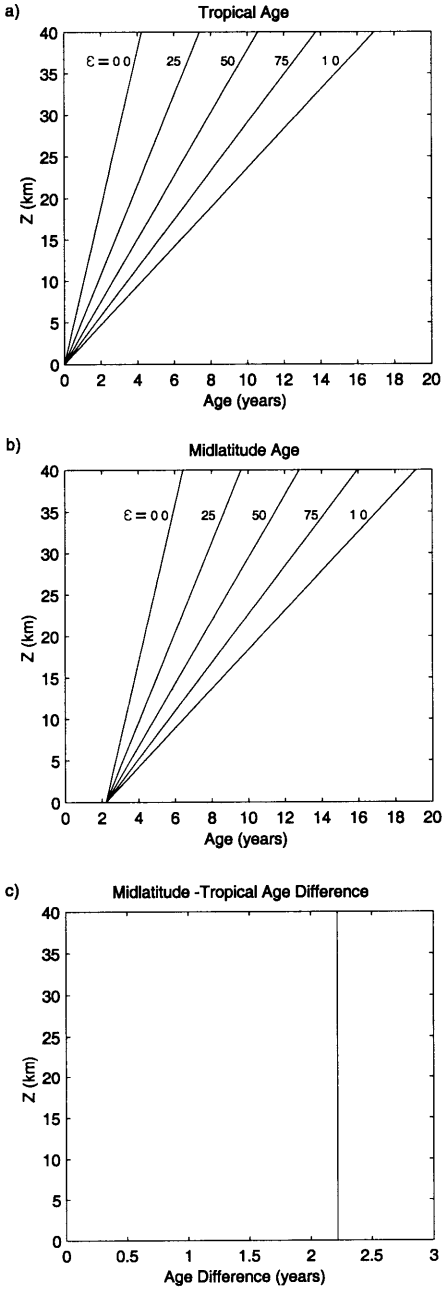

Figure 2-5: Same as Figure 2-2, except that vertical diffusion has been neglected ($K_T, K_M \rightarrow 0$)

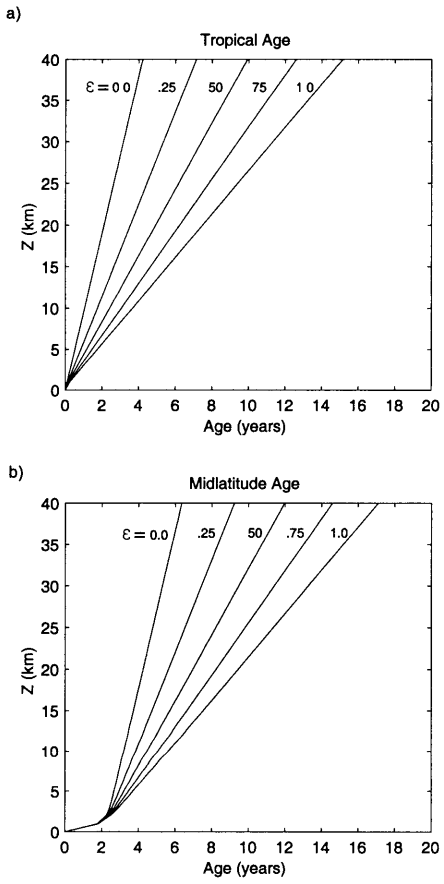

Figure 2-6: Same as Figures 2-2a and 2-2b, except that $K_M = 1.0$ m^{2}s^{-1}.

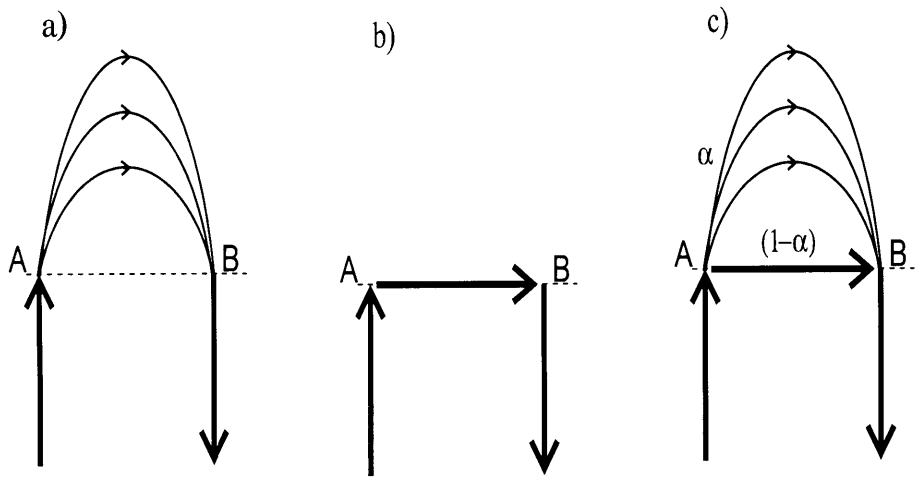

Figure 2-7: Schematic depicting three possible circulations in which air rises in the tropics, moves poleward, and descends in midlatitudes. See text for discussion.

Chapter 3

Seasonal Variability of the Subtropical Edges: Data

3.1 Introduction

While several studies have investigated the seasonal variability of the subtropical tracer gradients that mark the transition between the tropics and midlatitudes in the stratosphere, these studies have been of limited scope and have lacked an objective definition of the subtropical edges. For example, Hitchman et al. (1994) presented aerosol distributions from the Stratospheric Aerosol Measurement (SAM II) and Stratospheric Aerosol and Gas Experiment (SAGE I and SAGE II) instruments and concluded based on subjective analysis of the aerosol distributions that the Northern Hemisphere subtropical tracer gradient is steeper than the Southern Hemisphere gradient during the December-January-February period in the 20 to 25 km altitude range. Luo et al. (1994) showed that in measurements of hydrofluoric acid (HF) from the Halogen Occultation Experiment (HALOE) instrument, the subtropical gradients are sharper for the winter hemisphere than for the summer hemisphere during the latter half of 1993. Roche et al. (1994) examined the latitude range over which the chlorine nitrate ($ClONO_2$) mixing ratio changed from 0.2 to 0.4 x 10^{-9} at 46.4 mb from January, 1992, to April, 1993. They found the range to be quite narrow in the Northern Hemisphere in December and January, broad in July through September, and intermediate during the rest of the year, with the opposite pattern in the Southern Hemisphere. Grant et al. (1996) examined the aerosol

optical thickness during the year following the eruption of Mount Pinatubo. They defined the boundaries of the "tropical stratospheric reservoir" to be the region in which the thickness dropped from 85 percent to 45 percent of the peak value in the tropics, as determined by visual inspection as well as digital analysis of satellite images, and showed the evolution of the boundaries at specific longitudes for the year following the eruption. Here, we attempt to provide a comprehensive analysis of the seasonal variability of the subtropical edges over a wide range of altitudes for a six and a half year time-span using an objective, theory-based definition of the edges.

Sparling (2000) showed that probability distribution functions (PDFs) of long-lived chemical species (chemical "tracers") could be used to identify transport barriers. For a set of observations of a chemical tracer χ at a given pressure level, the equal-area PDF of the tracer, $P(\chi)$, can be approximated as the area-weighted fraction of observations with mixing ratio between χ and $\chi + \delta\chi$. We consider equal-area PDFs because they have the advantage that for sufficiently dense observations, $P(\chi)$ is a good approximation to the fractional area enclosed by the contours χ and $\chi + \delta\chi$. Sparling (2000) showed that PDFs of the chemical tracer nitrous oxide (N_2O) produced from measurements by the Cryogenic Limb Array Etalon Spectrometer (CLAES) satellite instrument (Roche et al., 1994; 1996) are multi-modal, with three modes in the winter hemisphere and two modes in the summer hemisphere. These structures in the PDF indicate that the stratosphere is made up of distinct air masses, corresponding to the maxima in the PDF, separated by mixing barriers, corresponding to minima in the PDF. Since rapid mixing between regions would act to homogenize tracers and eliminate the separation of the modes in the tracer PDF, the minima indicate regions in which mixing is slower than either the advective time-scale or the chemical time-scale. As we shall see, the winter hemisphere modes in the equal-area tracer PDF correspond to the tropical, surf zone, and vortex air masses, and the minima, which coincide with strong gradients in the tracer, correspond to the winter subtropical and vortex edges. The summer hemisphere modes correspond to the tropical and extratropical air masses, and the minimum corresponds to the summer subtropical edge. The "support" of the minima in the PDF, i.e. the spatial region in which the tracer field has mixing ratios corresponding to those in the minima, can be used to identify the most probable latitudes for the subtropical edges.

We use the methods of Sparling (2000) to identify the subtropical edges and determine their position from the latitudinal support as a function of time for eight pressure levels using N_2O measurements from the CLAES instrument as well as methane (CH_4) measurements from the HALOE instrument. The CLAES instrument has an extremely dense sampling pattern, which lends itself to statistical analyses. In addition to determining the position of the subtropical edges, we are able to develop a statistical method to determine their "width", i.e. the area of the hemisphere that they occupy. Unfortunately, the CLAES instrument has a limited data record which does not cover a full year. The HALOE instrument, on the other hand, has a much sparser, non-uniform sampling pattern but a very long data record. In order to justify the use of the HALOE measurements, we extend the analysis of Sparling (2000) which examined the robustness of the PDF of CLAES N_2O under sampling with the HALOE sampling pattern. We present results from this "HALOE-sampled CLAES" data set for the entire CLAES data period. We also present results from the actual HALOE CH_4 data for the same time period, and show that the HALOE sampling is sufficient to reproduce the seasonal variability seen in the CLAES measurements. We then analyze the HALOE measurements over a six-year period and compare the seasonal variability to variability in the zonal winds, residual vertical velocities, and equivalent lengths, which are a measure of contour stretching by large-scale stirring (Nakamura, 1996; Allen and Nakamura, 2000).

We find that there are two separate regimes: a low altitude regime (from 32.2 to 6.8 mb) and a high altitude regime (from 4.6 mb to 2.2 mb). In the low altitude regime, the subtropical edges vary smoothly with season, slowly winding back and forth across the subtropics so that the center of the tropical air mass lies on the summer side of the equator. In the high altitude regime, which is influenced by the semi-annual oscillation in zonal winds (SAO), there is an abrupt shift in the position of the edge at the onset of winter with changes of up to 20^o in a single month. This abrupt shift is more prominent in the Southern Hemisphere where the SAO signal is stronger, and occurs as the SAO westerlies are replaced by the easterlies. We present evidence that in both regimes the winter hemisphere edge is a product of large-scale stirring in the surf zone, while the summer edge is more likely a product of strong upwelling in the tropics and weak downwelling at high latitudes, with some possible contribution from stirring at lower altitudes.

Finally, we examine the interannual variability of the seasonal cycle. We show that there is some evidence for interannual variability in the lower regime and that this variability is related to the quasi-biennial oscillation in zonal winds (QBO), which dominates the lower tropical stratosphere. We also find significant interannual variability at 6.8 mb, which we show to be consistent with modulation of the SAO by the QBO.

3.2 CLAES N_2O

We use version 7, level 3AT CLAES N_2O measurements (Roche et al., 1994, 1996) on eight standard UARS pressure levels between 31.6 mb and 2.2 mb. The pressure levels have a pressure-altitude spacing of 2.67 km. The horizontal resolution of the measurements is approximately 500 km. We use data spanning the time period from July, 1992, to April, 1993, when the instrument ceased operation. Although CLAES was operational before July, 1992, the measurements prior to that time were contaminated by the presence of aerosols from the Mount Pinatubo volcanic eruption. During the 10 month period that we investigate, the instrument underwent eight yaw maneuvers, one roughly every 36 days, in order to keep the Sun on the same side of the instrument. During a northward-facing yaw period, the CLAES measurements cover a latitude range of 35^oS to 80^oN, and during a southward-facing yaw period, they cover a range of 35^oN to 80^oS. The highest confidence range for the N_2O measurements lies between 46 mb and 2 mb, where there are systematic errors of about 15 percent and random errors of about 7 percent (Roche et al., 1996). For more information on the CLAES instrument and its measurements of N_2O, see Roche et al., (1996).

The CLAES instrument has an incredibly dense sampling pattern, which makes its data ideal for statistical analyses. Figure 3-1 shows the coverage of CLAES observations for the northward-facing yaw period spanning December 3, 1992 to January 6, 1993. During this period, there are 40,746 observations of N_2O on each pressure level. We have chosen to use the yaw periods as our data periods, so that we determine a single position for the subtropical barriers at each height during each yaw period. The lifetime of N_2O ranges from several months to decades in the altitude range that we consider (Ko et al., 1991), so that the PDF of the accumulated data during each yaw period can be thought as an average over daily realizations of the PDF which

change with time due to dynamical processes. Obviously, during periods of rapid transition in the large-scale dynamics of the stratosphere, there will be larger variability in the daily PDFs, so that the PDF of the accumulated data will be less representative of the PDF on any given day than during a slowly evolving period. Since we are interested primarily in seasonal, and not shorter, time-scales, we chose the 36 day data periods because they are sufficiently long to average out day-to-day variability but sufficiently short to capture seasonal variability.

The CLAES instrument oversamples at the northern and southern edges of its latitude range. In order to account for the oversampling and to produce equal-area PDFs, we weight each observation so that the sum of the observations in a latitude circle multiplied by the weighting factor is equal to the area of the latitude circle. Figure 3-2 a) is a scatter plot of all of the observed N_2O values on the 6.8 mb pressure surface during the December 3, 1992, to January 6, 1993, yaw period. Figure 3-2 b) is the equal-area PDF of the observations in the Northern Hemisphere, and Figure 3-2 c) is the equal-area PDF of the observations in the Southern Hemisphere. Note that in the particular case shown, the center of the tropical air mass was located approximately at the equator. At other times of the year, this is not necessarily true, and in that situation we use the center of the tropical air mass to divide the atmosphere into the "Northern" and "Southern" Hemispheres so that there is tropical air in both PDFs. We have used a bin size of 2 ppb and smoothed the PDFs with a 2 ppb running average. The PDFs are relatively insensitive to the particular bin size and averaging range, as long as the values are reasonably small.

The Northern (winter) Hemisphere PDF is trimodal, with the most probable N_2O values in the hemisphere corresponding to the tropical, surf zone, and vortex air masses. The subtropical minimum in the PDF, which is "transition region" air that has neither tropical nor surf zone chemical characteristics, lies within N_2O values of about 80 to 100 ppb, and corresponds to the strong gradient in N_2O between the weak gradients in the chemically homogeneous tropics and surf zone. In the Southern (summer) Hemisphere, the PDF is bimodal, with peaks corresponding to the tropical and midlatitude air masses separated by the subtropical minimum in the PDF, which lies between approximately 85 and 115 ppb of N_2O. Figure 3-2 d) shows the latitude support of the N_2O values in the subtropical minima. The distribution of Northern Hemisphere latitudes corresponds to the N_2O values in the Northern Hemisphere subtropical

minimum, and the distribution of Southern Hemisphere latitudes corresponds to the values in the Southern Hemisphere minimum. The bin size is 2^o of latitude, and the PDFs are smoothed with a 2^o running average. The support is not very sensitive to the range of N_2O values that we use to define it, so long as we center the range on the minimum of the PDF. The Northern Hemisphere support is bimodal, with one mode corresponding to air with a most probable latitude of about 16^oN, and another corresponding to a most probable latitude of about 57^oN. The second peak, at 57^oN, can be shown to be tropical air that has been wrapped around the Aleutian anticyclone and transported all the way to the vortex edge (L. C. Sparling, personal communication), as has been observed in other studies (Harvey et al., 1999; O'Neill et al., 1994; Plumb et al., 1994). The most probable latitude for the Southern Hemisphere subtropical minimum is 17^oS. This analysis was repeated for all eight pressure levels for each of the eight yaw periods between June, 1992 and April, 1993.

As in Sparling (2000), we also determine the position of the subtropical edges using the latitudinal gradient of the zonal mode, which is the most probable N_2O mixing ratio at each latitude. Figure 3-3 a) shows the same N_2O measurements as Figure 3-2 a), with both the zonal mean and the zonal mode overplotted. The mean and the mode were calculated at 2^o latitude intervals, and were taken from PDFs of the N_2O measurements at each latitude using a bin size of 4 ppb. Note that the zonal mode is much "sharper" than the zonal mean. The mode emphasizes the striking homogeneity of each air major air mass and the rapid changes in N_2O over narrow latitude regions between the air masses. Figure 3-3 b) shows the latitudinal derivative of the zonal mode. There is a minimum at about 20^oN and a maximum at about 13^oS, corresponding to the latitudes where the zonal mode changes most rapidly, i.e. the transition regions between air masses. Note that these latitude values are close to those determined by the PDF method. In most cases, the two methods yield results within 5^o of each other.

Because the CLAES instrument does not view past 35^o in one hemisphere during each yaw period, it is not always possible to determine a position for the edge in that hemisphere from the PDF. In the example given above, the Southern Hemisphere edge was near the equator, and we were able to see enough of the midlatitude air mass that the Southern Hemisphere PDF was bimodal. In some cases, however, the center of the edge may be located as far poleward as 40^o, in which case the instrument does not observe even the entire edge, much less the midlatitude

air mass. In these cases, we estimate the position of the edge based on its position during the last 10 days of the yaw period before and the first 10 days of the yaw period after the one in question, when the instrument views the opposite coverage pattern. Figure 3-4 shows the CLAES N_2O observations at 10.0 mb (offset by 100 ppb) for the time period of August 17 to September 16, 1992, when the satellite was in its southward viewing configuration. Obviously, the Northern Hemisphere measurements do not cover the entire subtropical edge during this period. The observations for July 31 to August 9, 1992, at the end of the previous yaw period, and for September 25 to October 4, 1992 (offset by 200 ppb), at the beginning of the next yaw period, are overplotted. The edge was found to lie at 33^o during the July 31 to August 9 period and at 34^o during the September 25 to October 4 period. Since the portion of the edge that we can see in the August 17 to September 25 measurements looks very similar to the edge before and after that period, we estimate the position of the edge to be about 34^o. The position of the edge is obviously less certain when determined in this way, and so in our results we indicate which positions are estimated using this method.

There are also situations in which the PDF does not have a subtropical minimum, despite the fact that the measurements cover the entire hemisphere. Figures 3-5 a) and b) show the measurements taken from December 3, 1992, to January 6, 1993, at 31.6 mb and the PDF of the Northern Hemisphere measurements, respectively. There is clearly a strong N_2O gradient in the subtropics, which we expect to coincide with a minimum in the PDF. However, there is also a lot of air in the surf zone which has the same N_2O values as are characteristic of the air in the subtropical gradient, and they prevent the appearance of the minimum in the PDF. As discussed above, this air is tropical air that has been wrapped around the Aleutian anticyclone and transported into the surf zone. In cases in which the PDF does not have a clear subtropical minimum, but there is an obvious subtropical tracer gradient, we use the N_2O values in the subtropical gradient, in this case about 220 ppb to 260 ppb, to define the subtropical air mass and plot the support of that range of N_2O values. The support is generally multi-modal, since the tropical air that has been transported has these same N_2O values. In this case and in others where the support contains a broad range of latitudes, we look at the N_2O observations to help us determine which latitude peak corresponds to the subtropical tracer gradient. Again, we indicate in our results where we have used estimations of this type.

Table A shows the positions of the subtropical edges for each of the eight pressure levels during each of the eight yaw periods. The positions are an average between the latitude determined from the PDFs and the that determined from the zonal mode. Figure 3-6 shows the evolution of the "tropical pipe" over the entire CLAES data period. In July, the tropical region (as defined by chemical composition) is centered in the Northern Hemisphere, with the edge in the Southern Hemisphere lying between about 9^oS and 20^oS, and the edge in the Northern Hemisphere lying between 29^oN and 35^oN. There is little change in the position of the edges until November, when the upper portion of the Northern Hemisphere edge (above about 10 mb) moves rapidly equatorward. The lower portion also moves equatorward, but on a slower timescale. At the same time, the Southern Hemisphere edge slowly begins moving poleward, until April when the tropics are centered in the Southern Hemisphere, with the Northern Hemisphere edge located between 9^oN and 20^oN and the Southern Hemisphere edge located between 25^oS and 35^oS. At high altitudes at the onset of winter, when the winter side edge moves equatorward rapidly and the summer side edge moves only very slowly poleward, the tropical pipe becomes very narrow. Unfortunately, the CLAES data ends in April, 1993, and we are unable to use it to investigate the onset of Southern Hemisphere winter.

3.2.1 Area Enclosed by the Subtropical Edges

In addition to the positions of the subtropical edges, we are interested in whether they are narrow regions with sharp transitions in chemical composition or broad regions with gradual transitions in composition. Zonal maps of tracers show that the winter hemisphere subtropical edge tends to be quite narrow, while the summer hemisphere edge tends to be quite broad. However, the question of how to best quantify these impressions is not an easy one to answer. Sparling (2000) looked at the area of overlap between the tropical and midlatitude air masses, where she defined the tropical air mass as the air equatorward of the most probable latitude of the subtropical barrier, and the midlatitude air mass as the air poleward of that latitude. The tracer values shared by the tropical and midlatitude air masses, however, are not necessarily the tracer values of the bulk of the air in the subtropical edge, if we consider the edge to be defined as the air that makes up the minimum of the tracer PDF. For example, in Figure 5 of Sparling (2000), the peak in the area of overlap lies at considerably higher N_2O values than

the subtropical minimum in the PDF. Thus, while the area of overlap is a good measure of the chemical "distinctness" of the tropical and midlatitude air masses, it is not the most direct definition of the area of the subtropical edge. We choose instead to simply look at the area enclosed by the subtropical minimum in the PDF of N_2O. We define the subtropical edge as air that has an N_2O value less than the value half-way between the tropical peak and the subtropical minimum of the PDF, and an N_2O value greater than the value half-way between the midlatitude peak and the subtropical minimum. Then, since the frequency of a given N_2O value is proportional to the area occupied by air with that value, the integral of the portion of the PDF between these N_2O values compared to the integral over the PDF for the entire hemisphere gives the percentage of the hemisphere occupied by the subtropical edge. We note that this method of determining the area of the edge region does not depend on whether or not the edge is zonally uniform. As long as the tracer values within the edge remain constant, the edge is not "smeared out" as it undulates. However, over the quasi-monthly timescales that we use as our data periods, the tracer values within the edge may change, so that the area that we determine is likely to be somewhat larger than the actual area occupied by the edge at any given time within the data period.

Unfortunately, our method can be complicated by the fact that the PDF does not always have a subtropical minimum, as seen in Figure 3-5 which was discussed above. We overcome this by considering only the measurements which lie within ± 1 standard deviation of the zonal mode at each latitude. The N_2O values in this range are the values that are seen most frequently at a given latitude, and so by restricting ourselves to this range we consider the only the air which can be thought of as typically making up each air mass, and not air which has been transported from one region to another, thereby producing a transient anomaly in the N_2O measurements. Figure 3-7 a) shows the subset of the measurements from Figure 3-5 a) that lie within ± 1 standard deviation of the zonal mode. Figure 3-7 b) shows the PDF of this subset of measurements. The subtropical minimum is now quite clear, because we have eliminated most of the air which was transported from the tropics into the midlatitudes. It should be noted that in almost every set of measurements that we consider, the measurements within ± 1 standard deviation of the zonal mode always produce very clean PDFs with an easily identifiable subtropical minimum. Using the definition given above for the air within the subtropical edge,

we identify that air as having an N_2O range of 232 ppb to 262 ppb in this particular case. This range is shown in Figure 3-7 a). Since this range still includes a small amount of tropical air which has been transported to midlatitudes, we impose a second criterion that the edge lies within the latitudes where the N_2O first takes on the maximum of this range of values and where it first takes on the minimum of this range. In this case, these latitudes are 7^oN and 30^oN, also shown in Figure 3-7 a). The subtropical edge is then composed of all of the measurements within the "box" formed by the minimum and maximum N_2O values and the minimum and maximum latitudes. The PDF of the air within the edge is shown in Figure 3-7 b). Note that the PDF of the edge does not match the PDF of all of the data on the surf zone side. These "missing" measurements correspond to the tropical air that has been transported to midlatitudes. Comparing the integral of the edge PDF to the integral of the hemispheric PDF tells us that the subtropical edge occupies approximately 11% of the hemisphere. Using the previously-determined position of the subtropical edge, 22^oN, as the central latitude of the barrier yields an equivalent latitude range of 18.6^oN to 25.4^oN.

Figure 3-8 shows the central latitude and equivalent latitude range of the subtropical barriers over the CLAES observation period for each of the pressure levels that we consider. Note that only one hemisphere is shown for each yaw period. Since the instrument does not see the entire midlatitude air mass in the opposite hemisphere, we can not define the N_2O value which lies half-way between the subtropical minimum and the midlatitude peak in that hemisphere, and thus can not determine the area occupied by the subtropical edge. The dashed lines connecting the area measurements are merely interpolated from one measurement to the next and are intended purely to aid the viewer in visualizing the edges. Our results show that during the summer, the subtropical edge is indeed very broad, occupying as much as 60 percent of the area of the hemisphere, while in the winter it is quite narrow, occupying as little as 15 percent of the area of the hemisphere. It is interesting to note that the area of overlap between the tropics and midlatitudes defined by Sparling (2000) generally shows the opposite pattern, being larger in the winter than in the summer. During the summer there is a large separation between the N_2O values of the midlatitudes and those of the tropics, while in the winter there is a much smaller separation, thus increasing the possibility of overlap simply due to the edge moving back and forth. In addition, mixing between air masses will tend to increase their area of overlap, and

mixing is generally much stronger in the winter hemisphere than in the summer hemisphere.

3.3 HALOE-sampled CLAES N_2O

The CLAES measurements are ideally suited for statistical analyses because of the instrument's sampling density, but the data record is too short to see a full seasonal cycle, much less investigate the interannual variability of this seasonal cycle. The HALOE instrument also measures long-lived chemical tracers in the stratosphere, but it has a much longer data record, extending from 1991 to the present. However, the HALOE instrument uses a sun occultation technique and therefore samples only at sunrise and sunset, yielding 15 measurements at two latitudes per day. The instrument samples from 80^oS to 80^oN in this way on timescales of about one month. As discussed in Sparling (2000), there are significant questions about whether data sampled by the HALOE instrument is statistically robust, particularly during periods of large departures from stationarity in transport, when an accumulation of daily sparse sampling becomes less representative of the actual state of the atmosphere. However, Sparling (2000) was able to demonstrate that the major features of the PDF of CLAES N_2O measurements at 10 mb taken during the September 25, 1992, to October 25, 1992, yaw period survive under subsampling using the measurements closest in space and time to the HALOE measurements during this time period. We use the same technique, i.e. subsampling of the CLAES data using the HALOE sampling pattern, to produce HALOE-like PDFs over the entire July, 1992 to April, 1993 period. We then use these PDFs to identify the position of the subtropical edges and compare them to the positions identified using the full set of CLAES measurements, in order to determine whether the HALOE data is sufficiently robust to identify the seasonal motions of these edges.

Figure 3-9 shows the HALOE sampling pattern during the September 25, 1992 to October 25, 1992 CLAES yaw period. The CLAES instrument was northward-facing during this period, and made 35,649 measurements of N_2O on each pressure level between 35^oS and 80^oN. During this same period, the HALOE instrument made only 886 measurements on each pressure level, extending from 77^oS to 51^oN. This is a fairly typical example of the discrepancy between the sampling density of the instruments. However, in this case the HALOE instrument happens

to sample most of the globe during the CLAES yaw period. This is not always the case, since the timing of the HALOE global coverage is quite different than the CLAES yaw periods. This was, in fact, the biggest obstacle to identifying the subtropical edges in the HALOE-sampled CLAES data; the HALOE instrument did not always view enough of each hemisphere during the CLAES yaw period to allow for identification of the subtropical edges.

Figure 3-10 a) shows the CLAES N_2O measurements as well as the subsample of those measurements using the HALOE sampling pattern for the November 2 to November 25, 1992 yaw period. Figure 3-10 b) shows the PDF of N_2O in the Southern Hemisphere for both the CLAES and the HALOE-sampled CLAES measurements. There are 16,849 CLAES measurements in the Southern Hemisphere during this yaw period, and only 309 HALOE measurements. It is clear that in this case the features of the PDF of N_2O are remarkably robust under the HALOE subsampling, as was the case for the September 25 to October 25, 1992, period shown in Sparling (2000). However, as in Sparling (2000), the area under each portion of the curve is not preserved. Thus, the HALOE sampling is sufficient in these cases to identify the subtropical edge, but not to calculate quantitative diagnostics such as the width of the edge. Figure 3-11 shows the same information as Figure 3-10, but for the 2.2 mb level during the July 19 to August 9, 1992, yaw period. In this case, the HALOE-sampled CLAES measurements fail to reproduce the bimodality of the PDF of the full set of CLAES measurements. The CLAES observations have a very large spread in this particular case, either due to instrument noise or non-stationarity of the subtropical edge and midlatitude air mass. However, there are enough observations in the full CLAES data set to capture the basic background tracer structure. The HALOE sampling is simply insufficient to overcome the noise in the data, and therefore the PDF shows only the large spread of N_2O values. This result has two possible implications for the use of data from the actual HALOE instrument. If the cause of the measurement spread is instrument noise, then the actual HALOE data would probably provide a better set of measurements for identifying the edge in this case, since HALOE measurements tend to be more precise than CLAES measurements (Park et al., 1996). If, however, the spread results from non-stationarity of the tracer isopleths, then the HALOE instrument would see two incarnations of the tracer structure since it passes through the Southern subtropics twice during this period. If the two incarnations are sufficiently different, the PDF of the actual HALOE measurements

may simply reflect a large spread of values, as the HALOE-sampled PDF does here. Figure 3-12 shows the HALOE measurements of methane (CH_4), a long-lived tracer with a lifetime slightly longer than that of N_2O, during this period. The measurements are "cleaner" than the HALOE-sampled CLAES measurements, but there is still a large spread in the measurements south of 10°S. The PDF of CH_4 in the Southern Hemisphere, shown in Figure 3-12 b), is actually tri-modal, with one mode obviously resulting from the noise in the data rather than an organized structure. This is the major downfall of the HALOE data: the sampling is sometimes insufficient to identify transient disturbances versus background structures. However, this is not always possible in the CLAES data either, and we must sometimes simply provide a "best estimate" based on other information such as the position of the edge at other times and at other pressure levels.

Table B shows the position of the edge determined from the HALOE-sampled CLAES data for each of the eight pressure levels during each of the eight yaw periods. We make no attempt to identify the subtropical edge in cases in which the CLAES instrument does not see far enough into the hemisphere to identify the midlatitude air mass or in which the HALOE sampling pattern does not cover the necessary regions. Figure 3-13 compares the position as determined from CLAES data (in blue) to that determined by the HALOE-sampled CLAES data (in red) for the September 25 to October 25, 1992, as well as March 23 to April 14, 1993, yaw periods. Where a position could be determined from the HALOE-sampled CLAES data, it is very close to the position determined from the full CLAES data, indicating that in most cases the HALOE sampling does indeed provide a data set that is sufficiently statistically robust to identify the seasonal motion of the subtropical edges.

3.4 HALOE CH_4

We use version 19, level 3AT HALOE CH_4 measurements (Russell et al., 1993; Park et al., 1996), which are interpolated from 4.5 km vertical resolution to the 2.67 km vertical resolution of the standard UARS pressure levels. The total (systematic and random) measurement errors are estimated to be between 10 and 20% in the 20 to 30 km altitude range and around 10% in the 30 to 50 km altitude range (Park et al., 1996). We first repeat the analysis of the

CLAES yaw periods using the HALOE CH_4 data in order to determine how well the actual HALOE data reproduces our previous results. Then we analyze the remainder of 1993 and five additional years of data, ending in December, 1998, using data periods chosen to provide as much hemispheric coverage as possible on quasi-monthly timescales. In general, we use a bin size of .02 ppm to produce the PDFs and smooth them with a .02 ppm running smoother. For the PDFs of the latitude support, we generally use 2^o latitude binning, and we smooth them using either a 2^o or 4^o smoother. Again, there are situations in which there are gaps in the data or the subtropical edge is not identifiable directly from the PDFs, and we must estimate its position. As before, we indicate when we have used estimation methods. We do not present an analysis of the edge positions based on the zonal mode, since there was in general very little difference between the position based on the PDF and that based on the zonal mode in the CLAES data. In addition, we do not use the HALOE data to calculate the area enclosed by the subtropical edges. As discussed above, while the general features of the PDFs, i.e. the tropical and midlatitude peaks and subtropical minima, are generally robust under HALOE sampling, the area of the peaks is not preserved because the regions are not fully and equally sampled. Therefore, the HALOE data can not be used for quantitative statistical analyses.

Figure 3-14 a) shows the HALOE CH_4 observations taken at 21.5 mb during the January 13, 1993 to February 5, 1993 CLAES yaw period (we actually use data from January 7, 1993, to February 12, 1993, in order to provide as many HALOE observations as possible). Figures 3-14 b) and c) are the PDFs of the data in the Northern and Southern Hemispheres, respectively, and Figure 3-14 d) shows the latitude support of the subtropical minimum of the PDF for each hemisphere. In this case, the edges are located at 17^oN and 28^oS. The CLAES measurements for the same time period and pressure level gave results of 19^oN and 29^oS, in very good agreement with the results shown here. Table C gives the position of the subtropical edges as determined from the HALOE CH_4 data at each pressure level during the eight CLAES yaw periods, and Figure 3-15 shows the comparison between these results and the results from the CLAES N_2O data which were given in Table A. Note that there are very few HALOE measurements during the December 3, 1992, to January 6, 1993, yaw period, and so we were unable to determine the edge position for this period. At pressure levels below 10 mb, there is extremely good agreement between the results from the CLAES data and those from the HALOE data

throughout the CLAES period. Above 10 mb, there are two major points of disagreement. During the November 2 to November 25, 1992, yaw period, the CLAES data shows that the Northern Hemisphere edge has moved very close to the equator, while the HALOE data shows the position to be much further poleward, near 35^oN, at about the same latitude as during the September 25 to October 25, 1992, yaw period. Unfortunately, there is no HALOE data for the December 3, 1992, to January 6, 1993, yaw period, but during the January 13 to February 5, 1993, period the HALOE data once again agrees very well with the CLAES data, and shows that the Northern Hemisphere edge is located near 20^oN. Figure 3-16 shows the actual CLAES N_2O and HALOE CH_4 measurements at 4.6 mb for September 25, 1992, through February 5, 1993 (slightly longer for the HALOE data), as well as the zonal mode for each period. Unfortunately, the CLAES instrument was southward-facing during the November 2 to November 25 yaw period, and we can not say conclusively that the surf zone has intruded as far into the tropics as it appears to in the zonal mode, although the narrowness of the tropical region during this period is consistent with the next viewing period, December 3, 1992, to January 6, 1993. The HALOE data looks very different from the CLAES data during November. However, if we divide the November CLAES data into two smaller periods, we find that during the first half of November, the N_2O measurements look much more like the HALOE CH_4 measurements, and that the steep cliff in the CLAES N_2O does not develop until the latter half of November. The HALOE instrument views the Northern subtropics in the middle of November, so that it apparently misses this rapid transition. It is unfortunate that there are not enough HALOE measurements during December to determine whether the HALOE instrument sees the edge near the equator during that time, but it is clear that the total change in position from October to January is the same in both data sets. The other major difference between the CLAES data and the HALOE data can be seen at 4.6 and 3.2 mb during the March 23 to April 14, 1993 viewing period. The Northern Hemisphere edge moves equatorward from its February 13 to March 15 position according to the CLAES measurements, while it moves poleward according to the HALOE measurements. It is difficult to say exactly why this disagreement exists, particularly because the CLAES instrument was southward-facing during this period and because there are no CLAES measurements after April 14 to compare to. We do note that at 3.2 mb the CLAES measurements during the latter half of the yaw period agree much better with the

HALOE measurements than those during the first half of the period, and that those at 6.8 mb and 2.2 mb agree quite well with the HALOE data for this period. We will show below that in the six years of HALOE data that we analyze, it seems quite clear that the tropical region does indeed become very wide above 10 mb during the Northern Hemisphere spring, for reasons that will be discussed below.

Tables D-I give the positions of the subtropical edges as determined from HALOE CH_4 measurements for 1993 to 1998, as well as the viewing periods that we use for each year. Figure 3-17 shows the HALOE sampling pattern and the viewing periods for each year. The viewing periods were chosen to give as much coverage as possible on quasi-monthly timescales. In some cases in which there are significant data gaps during a global sweep by the instrument, we combine global sweeps in order to give better coverage. In some cases, particularly during the last three years that we examine, it is impossible to avoid data gaps without expanding the viewing period to cover several months, which would jeopardize our ability to examine the seasonal evolution. Therefore, particularly during 1996, 1997, and 1998, there are several instances in which we must estimate the position of one edge or the other, sometimes for several viewing periods in a row. However, we will show when we examine the interannual variability of the subtropical edges that despite fairly different viewing periods from year-to-year, the results are extremely consistent. We note, however, that there are two issues with the viewing periods which we find impossible to fully address. The first is that while the HALOE instrument generally provides very good coverage at the onset of the Southern Hemisphere winter, it generally provides very poor coverage during December, which we showed in the CLAES data to be crucial to determining how far equatorward the Northern Hemisphere edge moves at the onset of winter. We will show below that we find that in the upper regime, above 10 mb, the Southern Hemisphere edge moves much further equatorward than the Northern Hemisphere edge at the onset of winter. We will present arguments that this hemispheric asymmetry may be real, but we can not say for certain that it exists in the data, since we simply do not have the same data coverage for each hemisphere. However, we note that the CLAES analysis, which has good coverage in November and December, shows the minimum latitude of the Northern Hemisphere edge to be about 10°N. While this is closer to the equator than the Northern Hemisphere winter edge in many of the HALOE years, it is not as close to the equator

as the Southern Hemisphere winter edge in the HALOE analysis, which generally moves to within a few degrees of the equator and occasionally crosses into the Northern Hemisphere. The second issue is that we can not pinpoint the exact timing of changes in the edge position. During viewing periods in which the instrument views the subtropics only once, the edge position determined for that viewing period is only truly representative of the portion of the viewing period in which the instrument views the subtropics. If the dynamics are rapidly evolving, this position may not be particularly representative of the rest of the viewing period. During viewing periods in which the instrument passes through the subtropics twice, it may in fact see two different incarnations of the subtropical edges. In this case we choose one incarnation or the other, based on which sweep through the subtropics is closer to the middle of the viewing period. If, for example, a large change in the edge position occurred during the latter half of a viewing period and we can not see it until the next viewing period, then the timing of the change may be off by a week or more. However, this is an issue in the CLAES data as well, since in that data set the changes in the edge are averaged out over the viewing period, and uncertainties on the order of weeks are not unreasonable when looking at seasonal variability.

Figure 3-18 shows the evolution of the subtropical edges at each of the eight pressure levels that we consider over the entire six year period from January, 1993 to December, 1998. Figure 3-19 shows the superposition of the edge positions for all six years. We note the remarkable consistency of the data from year-to-year, despite fairly large differences in the satellite coverage. Tables D-I give the actual data periods and edge positions, as well as annotations of any estimation methods we use. In the region below 10 mb, the subtropical edges gradually travel back and forth between about 35^o and 15^o, so that the center of the chemically-defined tropics always lies in the summer hemisphere. Above 10 mb, the motion of the edges is much more dramatic; at the onset of winter, the subtropical edge moves rapidly equatorward, changing position by as much as 20^o on timescales of about a month. This rapid evolution is more pronounced in the Southern Hemisphere than the Northern Hemisphere, though as discussed above there is more uncertainty about the onset of Northern Hemisphere winter. Figure 3-20 shows the vertical structure of the subtropical edges for each of the viewing periods of 1993. Again, there is larger variability at the upper levels; in particular, the tropical region becomes very wide during the Southern Hemisphere fall and then the Southern Hemisphere edge moves

rapidly equatorward at the onset of winter.

3.4.1 Comparison to Zonal Winds, Residual Vertical Velocity, and Equivalent Length

The seasonal variability of the subtropical edges results from seasonal variations in stratospheric transport. The winter hemisphere is dominated by breaking planetary-scale waves, which stir material quasi-isentropically in the so-called "surf zone" of the winter midlatitudes (McIntyre and Palmer, 1984), while the summer hemisphere is largely quiescent, particularly in the mid- to upper stratosphere. The large-scale overturning (residual) circulation, which is driven largely by the eddy momentum deposition in the surf zone, is much more vigorous in the winter than the summer hemisphere, though the upwelling branch of the circulation maximizes on the summer side of the equator (Rosenlof, 1995; Eluszkiewicz et al., 1996). Here, we present a brief summary of the dynamics of these large-scale transport mechanisms and then examine their relationship to the subtropical edges diagnosed from the HALOE CH_4 data.

The winter hemisphere surf zone is often thought of as the finite-amplitude equivalent of a nonlinear critical layer (Stewartson, 1978; Haynes, 1985). Quasi-stationary planetary-scale waves propagate upward and equatorward in the winter hemisphere westerlies until they reach this critical layer, where the zonal mean zonal wind speed is close to the phase speed of the wave (which is zero for stationary waves). They then "break" in a highly nonlinear process which results in irreversible deformation of material contours and thus a cascade of potential enstrophy to small scales (McIntyre and Palmer, 1983). This wave breaking is confined to the winter midlatitudes by the high-latitude polar jet, which has high westerly wind speeds that do not match the phase speed of observed planetary-scale waves in the stratosphere (Bowman, 1996), and by the tropical easterlies, which prohibit propagation of planetary-scale waves (Charney and Drazin, 1961). The stirring of the surf zone occasionally pulls material out of the polar vortex and the tropics (e.g. McIntyre and Palmer, 1983, Randel et al., 1993), which has been shown in models to lead to a tightening of gradients in potential vorticity and chemical tracers (Juckes and McIntyre, 1987; Norton, 1994; Polvani et al., 1995). The winter subtropical edge is widely believed to result from this confined stirring in the surf zone, which weakens tracer gradients in the midlatitudes and sharpens them at the edges of the stirring.

The summer hemisphere is generally thought of as very quiescent with respect to wave activity. Since the winds in the summer hemisphere are generally easterly, they do not allow the propagation of planetary-scale waves. Recent studies have shown that there is evidence of large-scale stirring by wave dissipation in the lower summer stratosphere (Haynes and Shuckburgh, 2000, Wagner and Bowman, 1999), but there is no evidence of such stirring in the middle and upper stratosphere. The summer subtropical edge is thus not easily understood in terms of the stirring and consequent sharpening of tracer gradients that occurs in the winter hemisphere. There have, however, been suggestions that the summer edge is merely the remnant of the winter edge, which is preserved because of the lack of mixing (Nakamura and Ma, 1997). We show in Chapter 4 that this is likely not the case, and that the summer subtropical edge forms independently of the winter edge in a shallow water model.

In addition to quasi-horizontal transport by wave breaking, stratospheric transport takes place via the large-scale overturning circulation, which carries air upward in the tropics, poleward, and downward in mid- to high latitudes (Brewer, 1949; Dobson, 1956). This circulation is largely driven by the dissipation of waves in the surf zone, though the precise details of the coupling are not well understood (Haynes et al., 1991; Plumb and Eluszkiewicz, 2000). The circulation is much stronger in the winter hemisphere than in the summer hemisphere, consistent with the difference in wave activity in the two hemispheres. However, the maximum upwelling region lies in the summer hemisphere, so that the circulation cells are highly asymmetric, except for a very brief time at the equinox (Rosenlof, 1995; Eluszkiewicz et al., 1996). The balance between this overturning circulation and the quasi-horizontal mixing by wave breaking control the global distribution of chemical tracers (Plumb and Ko, 1992). Thus, the oppositely-signed vertical velocities in the tropics and midlatitudes are thought to contribute to the steepening of the subtropical tracer gradients (Randel et al., 1998), though it has always been unclear whether the horizontal shear in the vertical velocity is strong enough to produce the observed tracer gradients.

Figure 3-21 shows the monthly mean zonal mean zonal wind for January, 1993, to December, 1998, from the United Kingdom Meteorological Office (UKMO) UARS correlative assimilation, which is a global data assimilation analysis that is interpolated from the assimilation model grid, with a vertical resolution of about 1.6 km, onto the standard UARS pressure levels. The

horizontal resolution is 2.5^o latitude by 3.75^o longitude. Details of the assimilation scheme may be found in Swinbank and O'Neill (1994). The scheme uses observations from a wide variety of sources, but the only observations above 30 km in the tropics come from NOAA polar orbiting satellites, which provide temperature retrievals at low vertical resolution. The subtropical edges diagnosed from the HALOE CH_4 data are overplotted. Figure 3-22 shows the zonal mean zonal wind for June, 1992, to August, 1994, as calculated by Eluszkiewicz et al. (1996) using gradient wind balance with temperatures measured by the Microwave Limb Sounder (MLS). The balanced wind is calculated at latitudes higher than 5^o and is interpolated across the equator. The calculated zonal mean zonal winds are assigned to the center date of the MLS viewing periods, which are given in Eluszkiewicz et al. (1996), and then interpolated between viewing periods. Again, the positions of the subtropical edges are overplotted.

In the "lower regime" (31.6 to 10.0 mb) there is an extremely good correlation between the $\bar{u} = 0$ line and the position of the subtropical edge at the onset of winter. Even when the winds are westerly in the tropics due to the QBO, the subtropical edge corresponds to the subtropical minimum in the winds, which is near the same latitude as the zero wind line during QBO easterlies. This is consistent with the results of Waugh (1996), who showed that the initiation of isentropic transport out of the tropics in the winter corresponds strongly to the appearance of westerlies at 30^o and shows little interannual variability. The agreement with the zero wind line is also consistent with the results of our shallow water model studies presented in Chapter 4, which show that the zero circulation line lies within the PV contours that make up the winter subtropical edge. It is striking that the subtropical edge lies along, rather than equatorward of, the zero zonal wind line. In nonlinear critical layer studies, the critical layer straddles the zero wind line for a wave with zero phase speed, whereas here the *edge* of the "critical layer" lies at the zero wind line. While it is possible that a critical layer is simply not a useful analog for the stratospheric surf zone because it ignores the effects of vertical structure, the fact that the observations agree with our shallow water model results would tend to indicate that vertical structure is not a major issue. Instead, our results seem to highlight the dangers inherent in drawing parallels between weakly nonlinear and highly nonlinear flow. This will be a subject of further study.

At 3.2 and 2.2 mb, the equatorward motion of the edge is delayed relative to the appearance

of the $\bar{u} = 0$ line. We have examined these levels carefully because of the uncertainties in the timing of events that we discussed above. We are confident that in this case, the uncertainty is one-directional; the edge may move equatorward slightly later than we show, but it is highly unlikely that it does so any earlier. However, we note that the measurements show some indication that the edge may be sharpened somewhat when the zero wind line first appears. At these altitudes, the tropical stratosphere is dominated by the SAO in zonal winds, which is an oscillation between westerlies during the equinoxes and easterlies during the solstices (Reed, 1965). The westerlies descend much like the phases of the quasi-biennial oscillation, and appear to result from wave momentum deposition by Kelvin waves and/or gravity waves (Holton, 1975; Hirota, 1978; Salby et al., 1984, Hitchman and Leovy, 1988). The easterlies appear over a large depth nearly simultaneously, and are believed to result from mean advection of the summer easterlies into the tropics (Meyer, 1970; Holton and Wehrbein, 1980) and by easterly eddy momentum deposition by planetary waves ducted into the tropics from the winter hemisphere (Hopkins, 1975). The amplitude of the oscillation is considerably larger during the first half of the year than the second half, and is larger in the Southern Hemisphere than in the Northern Hemisphere (Ray et al., 1998; Belmont and Dartt, 1973; Hopkins, 1975). Ray et al. (1998) presented a comparison between the UKMO zonal winds at the equator and those measured by the high-resolution Doppler imager (HRDI) instrument on the UARS satellite. The HRDI observations do not extend above 3.3 mb, but they clearly show the SAO descending as far 10 mb, while the UKMO analyses show it descending to only 5 mb. In addition, during the westerly phase, the HRDI measurements show westerly winds throughout the tropics at 3.3 mb, while the UKMO winds show that the westerlies do not cross the equator. Thus, it is not unreasonable to believe that the westerlies at these altitudes should be somewhat stronger than those shown in the UKMO analysis and that they should extend across the equator, as they do in 1994 at 2.2 mb and in 1993 and 1994 at 3.2 and 2.2 mb in Figure 3-21. Figure 3-23 shows the UKMO zonal mean zonal winds at 1 mb, which are more consistent with the HRDI observations at 3.3 mb near the equator. The subtropical edges at 2.2 mb are overplotted. The delayed movement of the subtropical edge relative to the appearance of the westerlies and the evidence of some sharpening of the edge when the zero wind line first appears are consistent with a period of weak wave breaking as the winds become westerly and then a period in which

the SAO westerlies in the tropics allow the propagation of planetary-scale waves through the tropics without breaking until the onset of the easterly phase, at which time the subtropical edge is rapidly eroded equatorward. We shall see that the equivalent length calculations, which show regions of contour stretching associated with large-scale stirring, are also consistent with this sequence of events. Since the amplitude of the SAO is larger in the Southern Hemisphere than the Northern Hemisphere and larger in the first half of the year than the second half (Ray et al., 1998), it is possible that the more dramatic movement of the Southern Hemisphere edge compared to the Northern Hemisphere edge is real, and it seems to be consistent with the differences in the wind fields shown here. At 4.6 mb, the timing of the edge motion at the onset of winter is somewhat less certain, though the relationship with the zero wind line is generally consistent with that at 3.2 and 2.2 mb. Note, however, that the subtropical westerlies are weaker at this level and the motion of the edge is generally less delayed than at the upper levels. At 6.8 mb, the subtropical edge in the Southern Hemisphere behaves like the edges of the lower regime during 1993, 1995, and 1997, and like those of the upper regime in 1994, 1996, and 1998. This will be discussed in Section 3.4.2

Figures 3-24 and 3-25 show the residual vertical velocity fields, $\bar{w}^*$, as diagnosed from MLS data by Eluszkiewicz et al. (1996) and as calculated from the UKMO output, respectively. The $\bar{w}^*$ field from the UKMO analyses was calculated from the vertical velocity, meridional wind, and temperature fields using 5-day "snapshots" of the output. The assimilation scheme changed from a single 24-hour assimilation to four six-hourly cycles in October, 1995, and this introduced systematic biases into the vertical velocities (R. Swinbank, personal communication), which are responsible for the very different $\bar{w}^*$ fields in the years after 1995. The $\bar{w}^*$ field from Eluszkiewicz et al. (1996) was diagnosed using MLS temperature, ozone, and water vapor measurements, as well as climatological distributions of other radiatively active gases and aerosols in a highly complex radiative transfer code. As with the $\bar{u}$ shown above, the diagnosed velocities are assigned to the mid-point of the MLS viewing periods, and then interpolated between periods.

At 3.2 and 2.2 mb, the summer subtropical edge moves outward across the upwelling region and in to the downwelling region before being eroded back into the upwelling region by the surf zone stirring. This is particularly the case in the Southern Hemisphere, though the Northern Hemisphere edge behaves similarly. This is particularly visible in the UKMO analysis, which

has more than one Northern Hemisphere summer to winter transition. This behavior is exactly consistent with the seasonal cycle shallow water model simulation shown in Chapter 4. At the other levels shown here, the summer edge moves outward across the upwelling region, but the winter stirring pushes it back equatorward before it really reaches the downwelling region. The motion into the downwelling region is so clear at these upper levels because the surf zone stirring is delayed by the SAO westerlies.

As mentioned above, we present evidence in Chapter 4 that in a shallow water model with relaxation to a seasonally-varying "radiative equilibrium" height field, an enhanced potential vorticity gradient forms in the summer hemisphere purely through the diabatic relaxation, which is equivalent to the vertical gradient of the diabatic heating rate in the real stratosphere, i.e. the convergence and divergence of the mass flux due to the residual circulation. Here, we demonstrate briefly that the residual circulation in the stratosphere is, in fact, capable of producing tracer gradients similar to those observed in the high-altitude summer hemisphere. Figure 3-26 shows the advection of passive tracer particles in the latitude-height plane by the residual circulation of Eluszkiewicz et al. (1996). The tracer particles are initialized on January 9, 1993, on a latitude-height grid, and are advected for 60 days using the circulation interpolated to 2 day intervals. Figure 3-27 shows the zonal mean HALOE CH_4 during February 23 to April 6, 1993, in the altitude region that we have been exploring. A comparison to the last frame of Figure 3-26, which falls within this time frame, shows that the residual circulation does, in fact, produce subtropical tracer gradients in the summer hemisphere that look much like the observed gradients in the region above 10 mb. Below 10 mb, the observed summer subtropical gradients are considerably stronger than those produced by the circulation, which may indicate that high-latitude summer mixing plays a role in steepening the gradients in the lower stratosphere. Surprisingly, the residual circulation also produces a weak midlatitude gradient in the winter hemisphere. The observed weak gradients in the winter hemisphere are generally attributed to mixing in the surf zone, which acts to homogenize tracers. However, the observed winter subtropical gradients are considerably stronger than those produced by the residual circulation, indicating that erosion and sharpening of the gradients by stirring in the surf zone does indeed play a major role in the formation of the winter subtropical edge.

As further evidence for the role of mixing in forming and maintaining the winter subtropical

edge, we present calculations of the normalized equivalent length of an artificial tracer advected by the horizontal winds of the UKMO analysis. These calculations were provided by D. Allen (Allen and Nakamura, 2000). The square of the normalized equivalent length, L_e, is defined by Nakamura (1996) as:

$$L_e^2(A,t) = \left(\frac{\partial q}{\partial A}\right)^{-2} \frac{\partial}{\partial A}\mathcal{A}\left(|\nabla q|^2\right)$$

where q is a tracer whose mixing ratio is governed by the two-dimensional advection-diffusion equation (diffusion in this case referring to microscale diffusion), A is the area enclosed by a contour of q at a given time, and $\mathcal{A}$ is an operator which denotes the integral of any scalar over the area enclosed by the q contour. The equivalent length reduces to the length of the q contour when $|\nabla q|$ is constant on the contour. The advection-diffusion equation may then be written as a one-dimensional diffusion equation

$$\frac{\partial}{\partial t}q(A,t) = \kappa \frac{\partial}{\partial A}\left(L_e^2 \frac{\partial q}{\partial A}\right)$$

where the area enclosed by the q contours is used as the coordinate system and κ is the constant microscale diffusion coefficient. The effects of advection are absorbed into the equivalent length, so that if the advection acts to increase the equivalent length by stretching and folding the contours of q, then it increases the interface available for microscale diffusion. In a region where chaotic advection dominates, the equivalent length will increase exponentially (Ottino, 1989; Pierrehumbert, 1991). The equivalent length is thus a measure of the complexity of the geometry of the tracer contour and can be used as a diagnostic of the efficiency of small-scale mixing.

Figure 3-28 shows calculations of the equivalent length for a tracer that was initialized on 17 October, 1991, with a mixing ratio equal to the sine of latitude (Allen and Nakamura, 2000). The tracer was advected using a Van Leer advection scheme and the horizontal winds from the UKMO assimilation, which were interpolated onto isentropic surfaces. We show the equivalent length on the isentropic surfaces nearest to the standard UARS pressure levels, and the subtropical edge positions are overplotted. While the edge positions are a function of latitude, the equivalent length is a function of equivalent latitude, which is the latitude that encloses the same area as a given tracer contour. In regions where the tracer contours are

highly convoluted, the equivalent latitude will differ significantly from the geometric latitude. However, because tracer contours tend to be fairly zonally symmetric in the tropics, we expect the difference between the equivalent latitude and true latitude to be fairly small. The equivalent length has its maximum values in the winter hemisphere surf zone and its minimum values in the winter hemisphere vortex and the tropics. At lower altitudes, there is evidence of weak mixing in the summer high latitudes. There is generally excellent agreement between the position of the subtropical edge and the transition between the large equivalent lengths in the winter hemisphere midlatitudes and the small equivalent lengths in the tropics. There is good agreement between the timing of the appearance of the large equivalent lengths in the winter hemisphere at 1300 K and 1450 K and the equatorward motion of the edge at 3.2 and 2.2 mb, and there is evidence of a brief period of enhanced mixing rates coincident with the appearance of the zero wind line, which provides further of the sequence of events discussed above. There is also some evidence for the hemispheric asymmetry that we find in the upper regime. Finally, there is evidence in the equivalent length calculations at 960 K for the interannual variability that we discuss below: the "upper regime"-type motion of the edge at 6.8 mb in 1994, 1996, and 1998 and the "lower regime"-type motion in 1993, 1995, and 1997.

3.4.2 Interannual Variability of the Seasonal Cycle

The main source of interannual variability in the lower and middle tropical stratosphere is the QBO in zonal winds, which is characterized by alternately descending easterly and westerly winds over periods ranging from 24 to 32 months. The QBO modulates the SAO (e.g. Ray et al., 1998; Kennaugh et al., 1997), so that it is also the main source of interannual variability in the upper stratosphere. The QBO is believed to result from eddy momentum deposition by various equatorial waves, including Kelvin waves, mixed Rossby-gravity waves, and gravity waves (see review by Dunkerton, 1997). The QBO can potentially affect tracer transport in two ways. It modifies the zonal winds in the tropics, so that it may modify the ability of waves to propagate into and through the tropics, and it induces a secondary meridional circulation since it modifies the thermal structure of the tropics through thermal wind balance (Plumb and Bell, 1982).

Figure 3-29 shows the zonal wind measurements over Singapore for 1993 to 1998, taken from

Marquardt and Naujokat (2000). The alternating regions of easterlies and westerlies are clearly visible. We divide the time period into two categories, one in which there are easterlies overlying westerlies (roughly June, 1993 to July, 1994; August, 1995 to August, 1996; and August, 1997 to July, 1998), which we call easterly shear periods and the other in which there are westerlies overlying easterlies (roughly January, 1993 to June, 1993; July, 1994 to August, 1995; August, 1996 to August, 1997; and July, 1998 to December, 1998), which we call westerly shear periods (shear in this case referring to the bulk shear throughout the lower stratosphere). Figure 3-30 shows the subtropical edges determined from the HALOE data with easterly shear periods in red and westerly shear periods in black. At first glance, it is difficult to see any discernible QBO signal below 10 mb, where the direct effect of the QBO is felt. However, Figure 3-31 shows the subtropical edges at 31.6, 21.5, 14.6, and 10.0 mb divided into years that evolve from westerly to easterly shear (1993, 1995, and 1997) and those that evolve from easterly to westerly shear (1994, 1995, 1998). At 14.6 and 10.0 mb, there is a clear tendency for the edges to be shifted further into the summer hemisphere during the QBO westerly phase. When the westerly phase occurs during Northern Hemisphere winter, the winter edge is closer to the equator and the summer edge is further poleward than during the easterly phase. When the westerly phase occurs during Southern Hemisphere winter, the winter edge is not appreciably shifted toward the equator, but the summer edge is somewhat further poleward, at least at 10.0 mb.

It is not surprising that the QBO has an influence on the subtropical edges. The QBO has been shown to have a distinct impact on the shape of tracer isopleths in the tropics (Trepte and Hitchman, 1992; Grant et al.1996, Jones et al., 1998), including CH_4 as measured by HALOE (Randel et al. 1998). Shuckburgh et al. (2000) showed that during the westerly phase of the QBO there is evidence of enhanced mixing in both the winter and summer subtropics, particularly in early and late winter. However, they showed that some of this enhanced mixing may result from barotropic instability rather than planetary-scale waves, though some planetary-scale waves do appear to propagate through the tropics and break on the summer side. The QBO variability in equivalent length, which is the same diagnostic as used by Shuckburgh et al. (2000), can be seen in Figure 3-28, which shows that the tropical minimum in equivalent length is not as coherent during QBO westerly phases. However, although it is not visible here, the minimum equivalent lengths in the tropics are actually smallest during the QBO westerly

phases (Shuckburgh et al., 2000). The shift of the winter hemisphere edge toward the equator is consistent with enhanced stirring in the subtropics during the westerly phase. It is unclear why this shift is not visible in the Southern Hemisphere winter edge, since Shuckburgh et al. (2000) showed no large interhemispheric differences in the effect of the QBO. The poleward shift of the summer hemisphere edge during the westerly phase could result from enhanced mixing on the summer side of the tropics by the mechanisms discussed above, which would act to erode the edge from the tropics outward. It could also be related to changes in the residual circulation associated with the QBO. The QBO itself drives a secondary meridional circulation, which results in upwelling in the subtropics during the westerly shear phase (Plumb and Bell, 1982). Since, as we shall show below and in Chapter 4, the residual circulation probably plays a key role in the formation of the summer edge, it is likely that changes in the circulation resulting from the QBO secondary circulation affect the position of the edge.

Figure 3-32 shows the subtropical edges at 6.8, 4.6, 3.2, and 2.2 mb, divided into years that evolve from westerly to easterly shear and those that evolve from easterly to westerly shear. The only clearly discernible interannual variability can be seen at 6.8 mb. As mentioned previously, the Southern Hemisphere edge at 6.8 mb behaves like the edges of the lower regime in 1993, 1995, and 1997, while it behaves like those of the upper regime in 1994, 1996, and 1998. We believe that this interannual variability can be explained as QBO modulation of the SAO. Ray et al. (1998) present an analysis of the SAO which includes its interannual variability for the years 1992 to 1996. They show that the SAO westerlies descend further during the easterly phase of the QBO than during the westerly phase, with each successive SAO phase descending further until the onset of the QBO westerlies. In the HRDI observations (which are available only below 3.3 mb), the SAO descends as low as 10 mb during the QBO easterlies, and in 1992 and 1994 the SAO westerlies actually merge with the onset of the QBO westerlies at 10 mb. As noted previously, the SAO in the UKMO winds is weak compared to the HRDI measurements and the lowest pressure level that the signal descends to is 5 mb. However, the interannual variability of the UKMO winds is consistent with the HRDI measurements. Both data sets show that the SAO descends to low altitudes in the latter half of 1993 and 1995 and the first half of 1994 and 1996. Since the amplitude of the SAO is larger in the Southern Hemisphere and larger in the first half of the year, and since we see the large differences at 6.8 mb only in the

Southern Hemisphere, we concentrate on the westerly phases during the first half of the year. We can find indirect evidence of the descent of the SAO signal in the HALOE CH_4 observations. Figures 3-33 and 3-34 show the observations from late February to mid-July for 1993 and 1994 at 6.8, 4.6, 3.2, and 2.2 mb. The "double-peak" structure in the data was first observed by Jones and Pyle (1984) in CH_4 and N_2O measurements from the Stratospheric and Mesospheric Sounder and has been shown to be consistent with local vertical motions induced by the SAO. The temperature perturbations associated with the SAO changes in the zonal winds have peak amplitudes of about 2-3^{o}K and are centered on the equator. These temperature perturbations induce secondary meridional circulations in the tropics (Meyer, 1970). Figure 3-35 is a schematic of this circulation for the descending westerly phases of the SAO. During the descent of the westerlies, there is induced descent at the equator and upwelling in the subtropics, which lead to the double-peaked structure in Figures 3-33 and 3-34. During the easterly phase, the induced circulation is in the same sense as the large-scale mean residual circulation, and there is no double-peaked structure. In 1993, the amplitude of the double peak is larger at 3.2 and 2.2 mb than in 1994, but the double peak signal descends further, down to 6.8 mb, in 1994. This is consistent with a strong SAO signal confined to high altitudes in 1993 and a weaker SAO signal that propagates to lower altitudes in 1994, which is what Ray et al. (1998) show in the UKMO data. The fact that the Southern Hemisphere edge behaves as though it feels the SAO in years in which the high-altitude QBO winds switch from easterly to westerly (which are the same as our easterly to westerly shear years) is consistent with this modulation of the SAO by the QBO.

3.5 Summary

We have provided an extensive analysis of the seasonal variability of the subtropical edges using an objective, theory-based definition of the edges as the minima in the PDFs of long-lived tracers. We have also shown that the subtropical minima and their latitude supports are robust enough to survive sparse, uneven sampling, which greatly extends the potential applications of these methods.

We find that during the winter, the edge is eroded equatorward and becomes quite narrow

as the westerlies appear. The winter edge coincides with the zero wind line as well as with the transition between the large equivalent lengths in the surf zone and the small equivalent lengths in the tropics. In the upper regime, the motion of the winter edge and the appearance of large equivalent lengths in the midlatitudes are delayed relative to the appearance of the zonal wind line, perhaps by the SAO westerlies allowing waves to propagate all the way through the tropics. This delay and the subsequent rapid erosion are more pronounced in the Southern Hemisphere, which is consistent with the variability in the amplitude of the SAO. The winter edge tends to be located near the edge of the tropical upwelling region, and we will show in Chapter 4 that the upwelling acts to balance the erosion by the surf zone. During the summer, the edge moves poleward across the upwelling region and becomes quite broad in the altitude range that we explore. The summer edge at these levels is not associated with a transition between large and small equivalent lengths, though the fact that there are relatively large equivalent lengths in the summer hemisphere at the lowest levels that we examine could mean that stirring plays a role in limiting how broad the edge can become at those levels. Above 10.0 mb, the residual circulation appears to be capable of producing tracer gradients in the summer hemisphere similar to those observed in the satellite measurements.

There is evidence of QBO-related variability in the subtropical edges in the lower regime that is consistent with QBO westerlies allowing enhanced wave stirring in the subtropics. There is a clear QBO signal in the summer edge as well, which could be related to stirring within the tropics or to changes in the meridional circulation associated with the QBO. In the upper regime, there is variability that is consistent with QBO modulation of the SAO.

While the analyses presented here are purely diagnostic, they have provided us with a great deal of insight into the relationship between the seasonal variability in the transport mechanisms of the stratosphere and the seasonal variability of the subtropical edges, and provide us with many clues about the mechanisms of edge formation during each season. We can use this insight to test the consistency of mechanistic studies such as the one presented in Chapter 4.

TABLE A

	1	2	3	4	5	6	7	8
Northern Hemisphere								
31.6 mb	33	26*	31	24*	22^	21	19	21
21.5 mb	35	30*	33	27*	23	19	19	18
14.7 mb	35	34*	35	27*	16	16	16	15
10.0 mb	33	34*	35	27+	17	22^	18	13^
6.8 mb	31	31*	34	15+	18	25	22	23#
4.6 mb	31	26*	34	13*	14	22	25	12^
3.2 mb	31	28*	33	10*	14^	18	25	10#
2.2 mb	28	30*	35	12#	19^	16	26	32#
Southern Hemisphere								
31.6 mb	-20^	-22	-15	-21	-24*	-25	-27*	-29
21.5 mb	-25*	-22	-17	-19	-25*	-29	-29*	-33
14.7 mb	-17^	-15	-15	-13	-29*	-30	-30*	-35
10.0 mb	-9	-9	-12	-13	-16	-29	-30*	-31
6.8 mb	-11	-8	-8	-9	-14	-23	-25*	-30
4.6 mb	-9	-11	-6	-6	-16^	-23	-20*	-22
3.2 mb	-13^	-12	-9	-5	-14	-20	-21^	-24
2.2 mb	4	-20^#	-13#	-19^	-7^	-18	-21^	-31

*CLAES instrument does not view midlatitudes sufficiently - used data before and after the yaw period

^considered additional information

#fairly uncertain latitude determination

Uars Month			
1	Jul 19-Aug 9, 1992	5	Dec 3, 1992-Jan6, 1993
2	Aug 17-Sep 16, 1992	6	Jan 13 - Feb5, 1993
3	Sep 25-Oct 25, 1992	7	Feb 13-Mar15, 1993
4	Nov 2-Nov 25, 1992	8	Mar 23-Apr 14, 1993

TABLE B

	1	2	3	4	5	6	7	8
Northern Hemisphere								
31.6 mb	-	*	33	*	-	25	20ˆ	**
21.5 mb	-	*	37	*	-	19	21	16
14.7 mb	-	*	43	*	-	**	14	17
10.0 mb	-	*	39	*	-	19	19	16
6.8 mb	-	*	34	*	-	22	22	*
4.6 mb	-	*	35	*	-	23	23	9
3.2 mb	-	*	37	*	-	**	**	**
2.2 mb	-	*	37	*	-	**	**	-
Southern Hemisphere								
31.6 mb	*	**	-13^{+}	-20	-	-	-	-
21.5 mb	*	-25	**	-22	-	-	-	-
14.7 mb	-11	-14	-14^{+}	-10	-	-	-	-39
10.0 mb	-12	-8	-13^{+}	-11	-	-	-	-30ˆ
6.8 mb	-12	-8	-14^{+}	-12	-	-	-	-30ˆ
4.6 mb	**	-9	-13^{+}	-9ˆ	-	-	-	-25ˆ
3.2 mb	**	**	-14^{+}	-9ˆ	-	-23	-	-34
2.2 mb	**	**	*	-19ˆ	-	-	-	-

$^{+}$all observations within the edge come from two latitudes

ˆused raw data to help define range of CH_4 values in the subtropical minimum

*CLAES does not observe midlatitudes

-HALOE sampling pattern does not sufficiently overlap with CLAES

**unable to determine a latitude from HALOE-sampled CLAES

Table C

	1	2	3	4	5	6	7	8
Northern Hemisphere								
31.6 mb	36^	30**	31	25+	-	20	23	17
21.5 mb	36^	32**	30*	19+	-	17	15	13
14.7 mb	32^	34**	35*	22+	-	17	16	15
10.0 mb	34	37**	40*	30+	-	22	19	17
6.8 mb	34	35**	37	35+	-	24	23	32^
4.6 mb	34	32**	38	37+	-	20	23	37
3.2 mb	33	32**	38	39+	-	19	23	39**
2.2 mb	40^	38**	40^	35+	-	17	29	40**
Southern Hemisphere								
31.6 mb	-22	-22	-16	-20	-	-25	-25**	-25
21.5 mb	-21	-22	-16	-14	-	–28	-28**	-27
14.7 mb	-12	-18	-15	-15	-	-33	-28**	-35**
10.0 mb	-11	-10	-11	-16	-	–30	-30**	-35**
6.8 mb	-11	-11	-11	-13	-	-30**	-28**	-37^
4.6 mb	-13^	-13	-9	-9	-	-33**	-30**	-37**
3.2 mb	-13^	-13	-19	-14	-	-34**	-28**	-35**
2.2 mb	-13^	-10**	-20*	-23	-	-25	-30**	-35**

^used raw data to help define range of CH_4 values in the subtropical minimum

**purely estimated - satellite does not see midlatitudes or objective methods unclear

+no well-defined peak in latitude support - used raw data to help determine latitude

-HALOE sampling pattern does not sufficiently overlap with CLAES

TABLE D

	1	2	3	4	5	6	7	8	9
Northern Hemisphere									
31.6	21	19	18	19	20	27	31^	31	30
21.5	17	17	17	15	19	25	31^	23^	23
14.7	17	18	17	15	23	25	30^	31^	25
10.0	21	21	21**	30	27^	26	31^	31^	27
6.8	25	23	30	33	35	33	31	31^	27&
4.6	21	19	23	39	35	40	34	31**	28**#
3.2	21	19	27^	38	35	37	35	43**#	25**#
2.2	20	19	35	40	38	38	35	43**#	23**#
Southern Hemisphere									
31.6	-28	-25	-22	-22^	-20	-18^	-19	-17	-17
21.5	-32	-33^	-35	-22	-19	-20	-20	-18	-19
14.7	-32	-35	-37	-25^	-20	-22^	-19	-18	-19
10.0	-28	-35	-37	-30	-20	-19^	-19	-18	-21
6.8	-23	-31^	-37	-30^	-25**	-17^	-22	-20	-20
4.6	-23	-30	-37^	-35	-38**	1	0&#	-20**	-21
3.2	-23	-29	-38^	-38**	-40**	-7^	-1	-1	-27&
2.2	-26	-28	-32	-40**	-43**	-3^	-1	-15	-27&

^used raw data to help define range of CH_4 values in the subtropical minimum

&used raw data alone to define range of CH_4 values in the subtropical minimum

**purely estimated - satellite does not see midlatitudes or objective methods unclear

fairly uncertain latitude determination

Viewing Period

1	Jan 1-Jan 24, 1993	6	Jun 24-Jul 24, 1993
2	Jan 24-Feb 23, 1993	7	Jul 24-Sep 25, 1993
3	Feb 23-Apr 6, 1993	8	Sep 25-Oct 27, 1993
4	Apr 6-May 13, 1993	9	Oct 27-Dec 22, 1993
5	May 13-Jun 24, 1993		

TABLE E

	1	2	3	4	5	6	7	8	9	10
Northern Hemisphere										
31.6	17	23	19	21	25	22	21	30	26	26
21.5	20	22	21	24	27	26	23	29	23	26
14.7	22	30^	21	27	27^	28	27	35^	25	20&#
10.0	27	31	27	31	28	31	36^	39	30&	20&#
6.8	18^	19	31	33	31	30	39	40	33&	29&
4.6	19^	17	21	35	31	33	35	41	35&	30
3.2	18	15	19	33	33	31	32	38	35**	30**#
2.2	19	16^	30	35	33	33	34	39	37&	30&#
Southern Hemisphere										
31.6	-26	-27	-27	-23	-24	-23	-23	-19	-21	-17
21.5	-22	-21	-27	-21	-27	-20	-19	-18	-17	-15
14.7	-23	-19	-27	-23^	-27	-27^	-23	-17	-17	-15
10.0	-23	-24	-27	-29	-25&	-20**#	-17&	-18	-16	-15
6.8	-25	-26	-32	-31	4&	-3^	-12^	-11	-12	-13
4.6	-29^	-26&	-32	-31	7&	-5^	-6	-11	-11	-13
3.2	-27	-30	-40	-33**	10&	-4	-10	-9	-13	-11
2.2	-33	-29	-42	-40**#	-15&#	-5	-6	-13	-26	-25

^used raw data to help define range of CH_4 values in the subtropical minimum

&used raw data alone to define range of CH_4 values in the subtropical minimum

**purely estimated - satellite does not see midlatitudes or objective methods unclear

fairly uncertain latitude determination

Viewing Period

1	Jan 1-Jan 20, 1994	6	Jun 20-Jul 19, 1994
2	Jan 20-Feb 21, 1994	7	Jul 19-Aug 22, 1994
3	Feb 21-Apr 2, 1994	8	Aug 22-Sep 30, 1994
4	Apr 2-May 9, 1994	9	Sep 30-Nov 6, 1994
5	May 9-Jun 20, 1994	10	Nov 6-Dec 31,1994

TableF

	1	2	3	4	5	6	7	8	9
Northern Hemisphere									
31.6	20	19	17	23	25**	30^	35^	30^	24
21.5	19	17	19	17	25**	22**	35^	35^	25
14.7	17	17^	15	15	19**	17^	32^	35^	25^
10.0	17	17	19	20	22**	22	22^	29	25&
6.8	23	17	19	27^	37**	21	30	31	35&
4.6	17^	17	32	29	40**	36	39	29	35&#
3.2	17	19	25^	39	40**	43	40^	35	30**#
2.2	17	17	40**#	39	43**	43	43	-	31**#
Southern Hemisphere									
31.6	-25	-26	-27	-28	-21	-11	-11	-16	-16
21.5	-21	-26	-25	-25	-21^	-12^	-11	-12	-15
14.7	-27	-30	-28^	-21^	-21&	-17**#	-16	-19	-18
10.0	-26	-26^	-35&	-25^	-25^	-31^	-19	-20	-19
6.8	-25	-25	-38^	-26^	-21	-38**	-28	-26	-22
4.6	-26	-30	-35	-30^	-30	-40**	-5&#	-21**	-23
3.2	-23	-23	-35	-40^	-35	1	-7	-26**	-24
2.2	-16	-23	-34	-38^	-36	0	-7	-14	-30**#

^used raw data to help define range of CH_4 values in the subtropical minimum

&used raw data alone to define range of CH_4 values in the subtropical minimum

**purely estimated - satellite does not see midlatitudes or objective methods unclear

fairly uncertain latitude determination

Viewing Period

1	Jan 1-Jan 15, 1995	6	Jun 3-Aug 14, 1995
2	Jan 15-Feb 13, 1995	7	Aug 14-Sep 27, 1995
3	Feb 13-Mar 28, 1995	8	Sep 27-Nov 1, 1995
4	Mar 28-May 4, 1995	9	Nov 1-Dec 31, 1995
5	May 4-Jun 3, 1995		

TABLE G

	1	2	3	4	5	6	7	8	9
Northern Hemisphere									
31.6	24	18	20	23	22	18	27^	27	27
21.5	15	18	22	23	21	23	21	25	25
14.7	15^	21	26	29	24	35**	31**	37**	22**
10.0	13	23	27	31	37^	40**	40**	40**	26&
6.8	5^	23	28	29	36	35**	40**	40**	30**
4.6	8	21	30	29	31	33**	42**	40**	24#
3.2	6	25	34	32	32	33**	40**	40**	30**#
2.2	9	14	34	33	28**	35**	42**	45**	27**#
Southern Hemisphere									
31.6	-23^	-31^	-26	-27	-19	-19	-17	-19	-21
21.5	-23	-30	-25	-25	-19	-17	-16	-24	-21
14.7	-20	-22	-25	-25	-20	-17	-17	-25	-23
10.0	-26	-23	-23	-25	-23**	-21	-15	-22	-22
6.8	-23	-30^	-26	-28^	-5&	-9^	-12	-13	-16
4.6	-26	-35^	-34	-35&	-4&	-13	-11	-10	-10
3.2	-27	-40^	-36&	-42**#	-5&	-13^	-11	-15	-20
2.2	-27	-43	-38&	-42**#	-1&	-10	-20**	-24	-22

^used raw data to help define range of CH_4 values in the subtropical minimum

&used raw data alone to define range of CH_4 values in the subtropical minimum

**purely estimated - satellite does not see midlatitudes or objective methods unclear

fairly uncertain latitude determination

Viewing Period

1	Jan 1-Feb 1, 1996	6	Jul 9-Aug 8, 1996
2	Feb 1-Mar 23, 1996	7	Aug 8-Sep 20, 1996
3	Mar 23-Apr 29, 1996	8	Sep 20-Oct 26, 1996
4	Apr 29-May 27, 1996	9	Oct 26-Dec 31, 1996
5	May 27-Jul 9, 1996		

TABLE I

	1	2	3	4	5	6	7	8	9	10
Northern Hemisphere										
31.6	21	27	27	27**	25**	27**	30**	27&	23	29^
21.5	23	29	25	28**	27**	27**	30**	28&	29&	25
14.7	26	28	25	32**	30**	30**	35**	28&	32**	16^
10.0	25^	34	30	35**	35**	33**	35**	41&	33**	19
6.8	31^	30	37	35**	36**	34**	37**	42&	29&	25
4.6	27	28	35	35**	37**	35**	38**	37&	29^	23
3.2	17	27	37	33**	37**	35**	40**	38&	29^	21^
2.2	15	12	38#	33**	35**	40**	40**	38^	30^	15
Southern Hemisphere										
31.6	-28**	-35**	-31	-23^	-20	-21	-21	-18	-21	-29**
21.5	-30**	-35**	-28	-25^	-20	-19	-21	-18	-19	-25
14.7	-28**	-30**	-28	-25^	-20	-21	-21	-17	-18	-27
10.0	-20**	-30**	-26	-25^	-14^	-19&	-21	-21	-17	-32**
6.8	-17	-30**	-25	-25^	-5	-3	-8	-11	-15	-33**
4.6	-17	-30**	-25^	-25^	-5	-1	-8	-10	-10	-30**
3.2	-19	-35**	-40**	-25**	-5&	1	-13	-12	-11	-25**
2.2	-21	-37**	-40**	-27**	1^	2	-13	-10^	-17	-25**

^used raw data to help define range of CH_4 values in the subtropical minimum

&used raw data alone to define range of CH_4 values in the subtropical minimum

**purely estimated - satellite does not see midlatitudes or objective methods unclear

fairly uncertain latitude determination

Viewing Period

1	Jan 1-Feb 13, 1998	6	Jul 1-Jul 29, 1998
2	Feb 13-Mar 14, 1998	7	Jul 29-Sep 11, 1998
3	Mar 14-Apr 19, 1998	8	Sep 11-Oct 17, 1998
4	Apr 19-Jun 2, 1998	9	Oct 17-Nov 14, 1998
5	Jun 2-Jul 1, 1998	10	Nov 14-Dec 31,1998

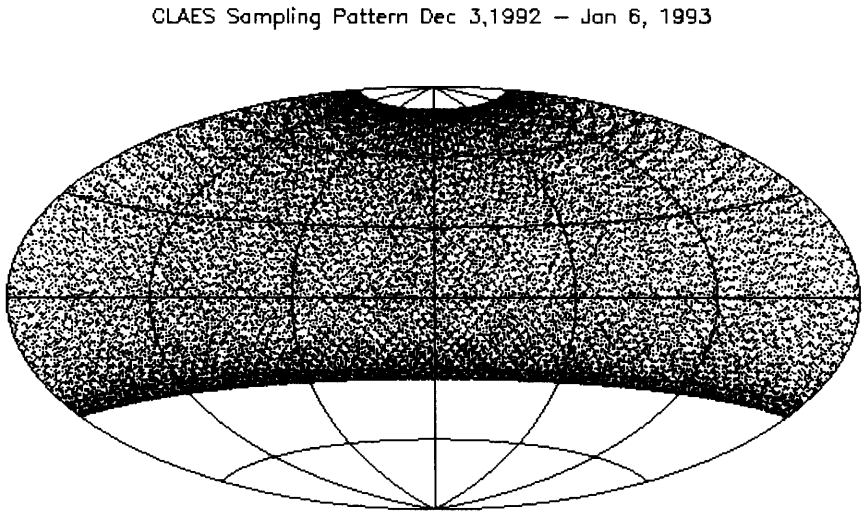

Figure 3-1: The CLAES sampling pattern for December 3, 1992, to January 6, 1993. Each symbol represents a single sounding.

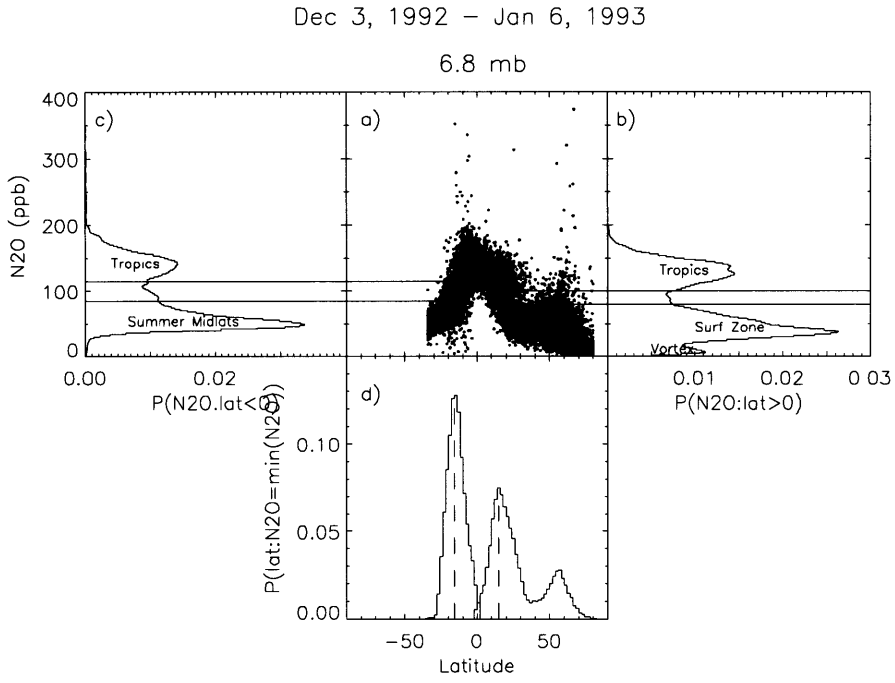

Figure 3-2: The CLAES N_2O observations for December 3, 1992, to January 6, 1993, at 6.8 mb, the PDFs of those observations in each hemisphere, and the PDF of the latitude support of the subtropical minima of the PDFs of N_2O. Frame a) is a scatter plot of all of the N_2O measurements at 6.8 mb during this period. Frame b) is the PDF of the N_2O measurements in the Northern (winter) Hemisphere, with the normalized frequency along the x-axis and the N_2O mixing ratio along the y-axis. Peaks in the PDF correspond to weak N_2O gradients in the tropics, surf zone, and vortex. The minimum in the PDF between the tropics and the surf zone, shown by the horizontal lines, corresponds to the strong N_2O gradient in the subtropics. There is also a minimum between the surf zone and the vortex, which corresponds to the strong N_2O gradient at the vortex edge. Frame c) shows the PDF of the N_2O measurements in the Southern (summer) Hemisphere. The subtropical minimum, which lies between the modes corresponding to the tropical and summer midlatitude air masses, is again indicated by the horizontal lines. Frame d) shows the PDF of the latitudes of the observations for the N_2O measurements within each subtropical minimum. We define the most probable latitude in each hemisphere as the latitude of the subtropical edge.

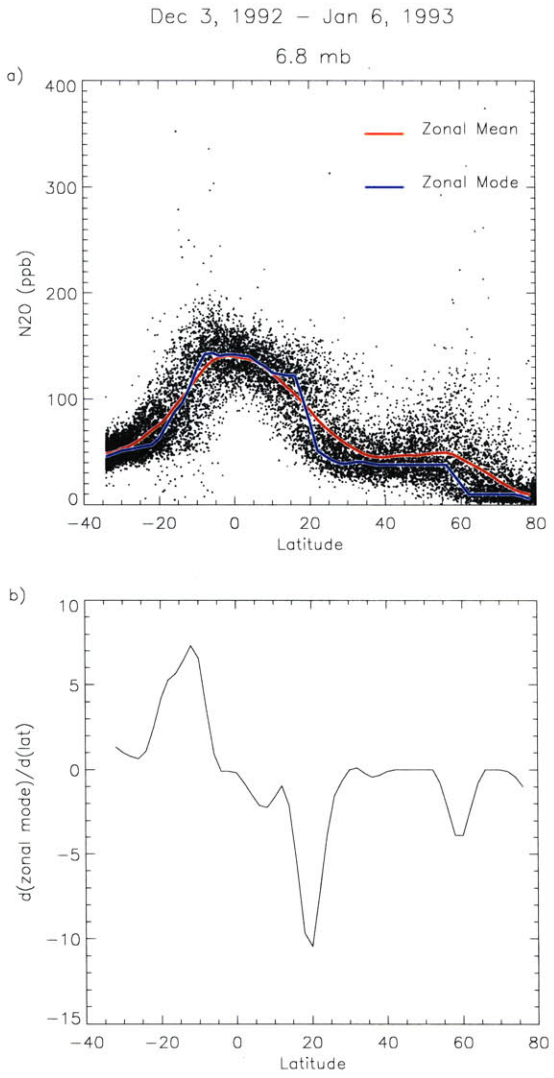

Figure 3-3: a) The CLAES N_2O measurements at 6.8 mb during the December 3, 1992, to January 6, 1993, yaw period. The zonal mean and the zonal mode (the most probable N_2O value at each latitude) are overplotted. b) The latitudinal gradient of the zonal mode. Maxima and minima in this gradient correspond to sharp transitions in chemical composition.

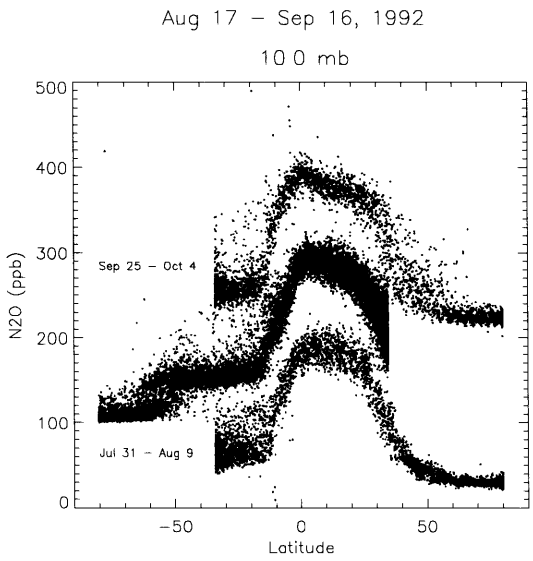

Figure 3-4: CLAES N_2O measurements from the August 17, 1992, to September 16, 1992, yaw period (offset by 100 ppb), as well as observations from the last 10 days of the previous yaw period (July 31, 1992, to August 9, 1992,) and the first 10 days of the next yaw period (September 25, 1992, to October 4, 1992) (offset by 200 ppb). The latitude of the Northern Hemisphere subtropical edge is estimated using the data from the adjacent yaw periods.

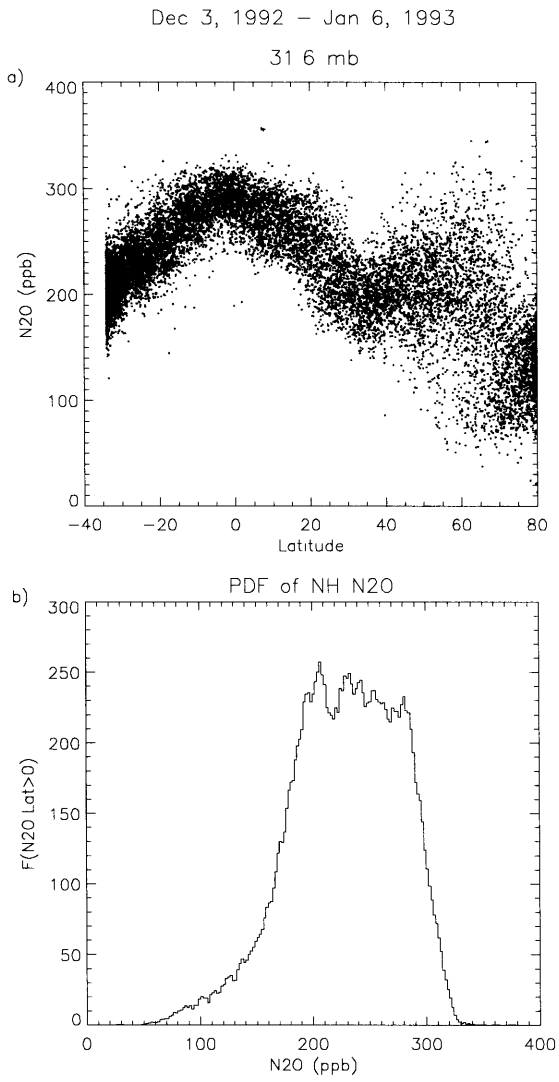

Figure 3-5: a) The CLAES N_2O measurements from Decmeber 3, 1992, to January 6, 1993, at 31.6 mb. b) The PDF of the N_2O measurements in the Northern Hemisphere. The subtropical minimum is absent because of the large amount of air in the surf zone with tropical N_2O values.

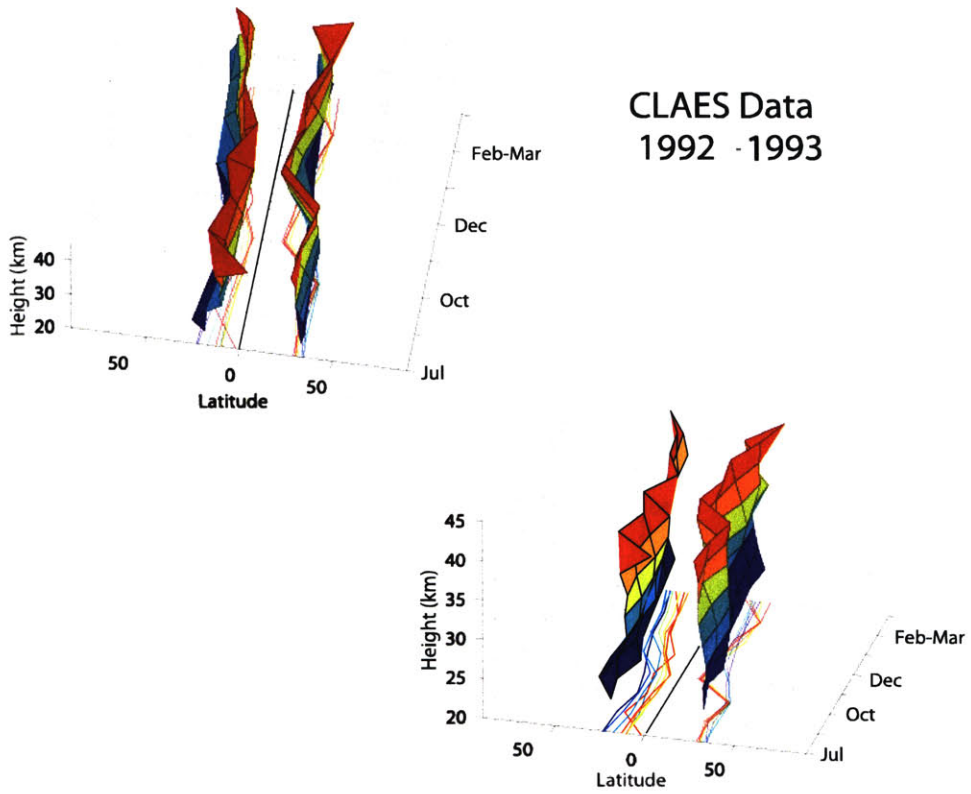

Figure 3-6: The "tropical pipe" as determined from the CLAES N_2O measurements, viewed from two different angles.

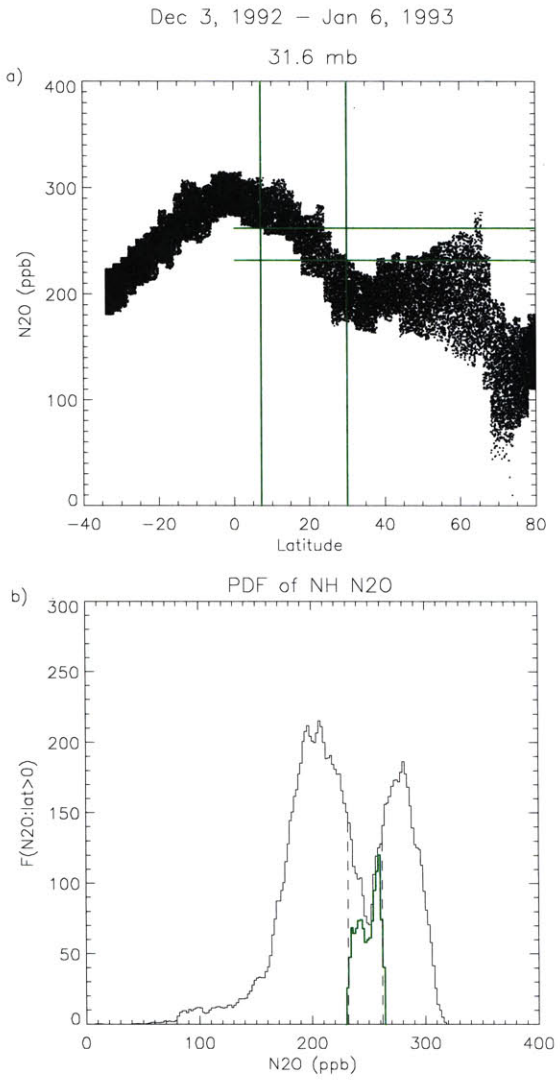

Figure 3-7: a) The CLAES N_2O measurements at 31.6 mb for December 3, 1992, to January 6, 1993, within ± 1 standard deviation of the zonal mode. The subtropical edge air, as defined in the text, lies within the "box" of N_2O values and latitudes. b) The frequency of the Northern Hemisphere measurements plotted in the top frame (in black), the range of N_2O values within the subtropical edge (dashed lines), and the PDF of the observations within the "box" in the top frame (in green).

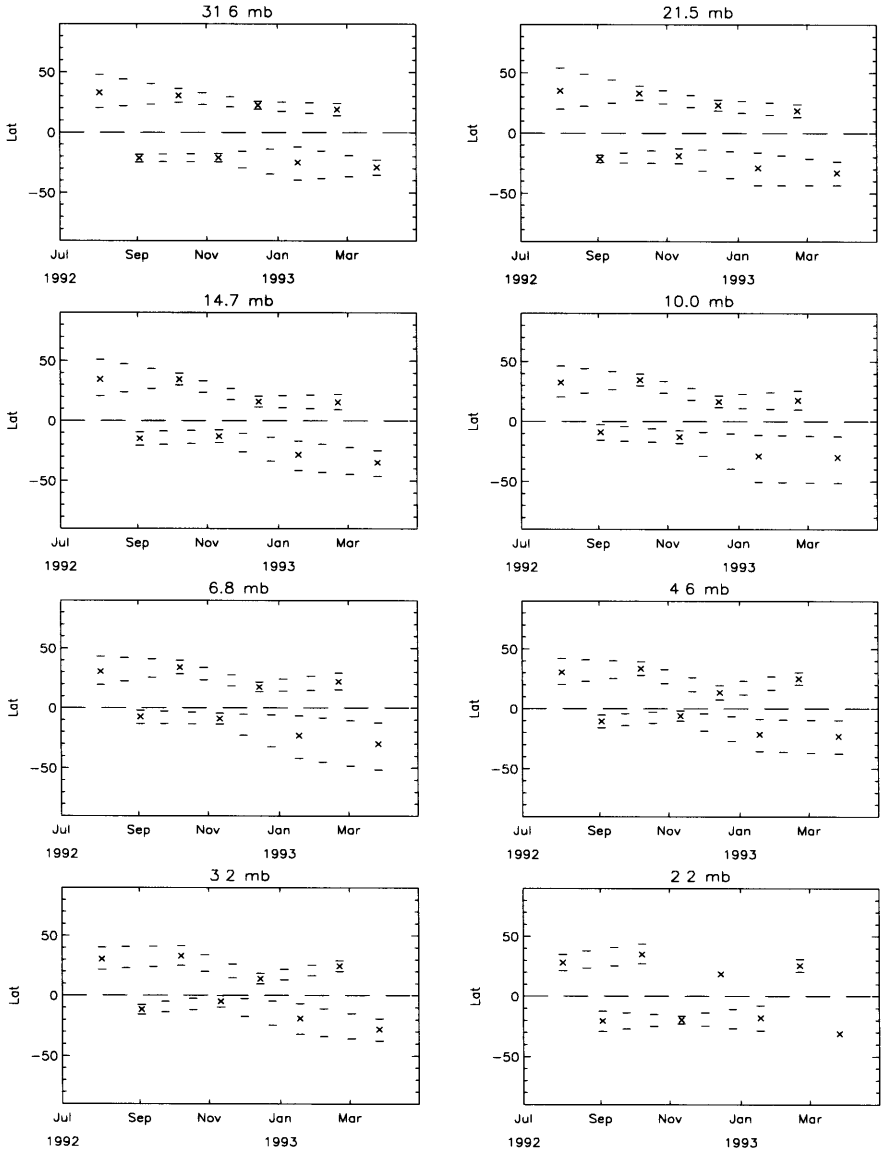

Figure 3-8: Position and latitudinal extent of the subtropical edges at each pressure level during the CLAES data period. The x's mark the most probable latitude of the edge, while the lines mark the equivalent latitude range corresponding to the area of the hemisphere occupied by the edge. Lines between the observation periods are interpolated, and are merely intended to guide the eye.

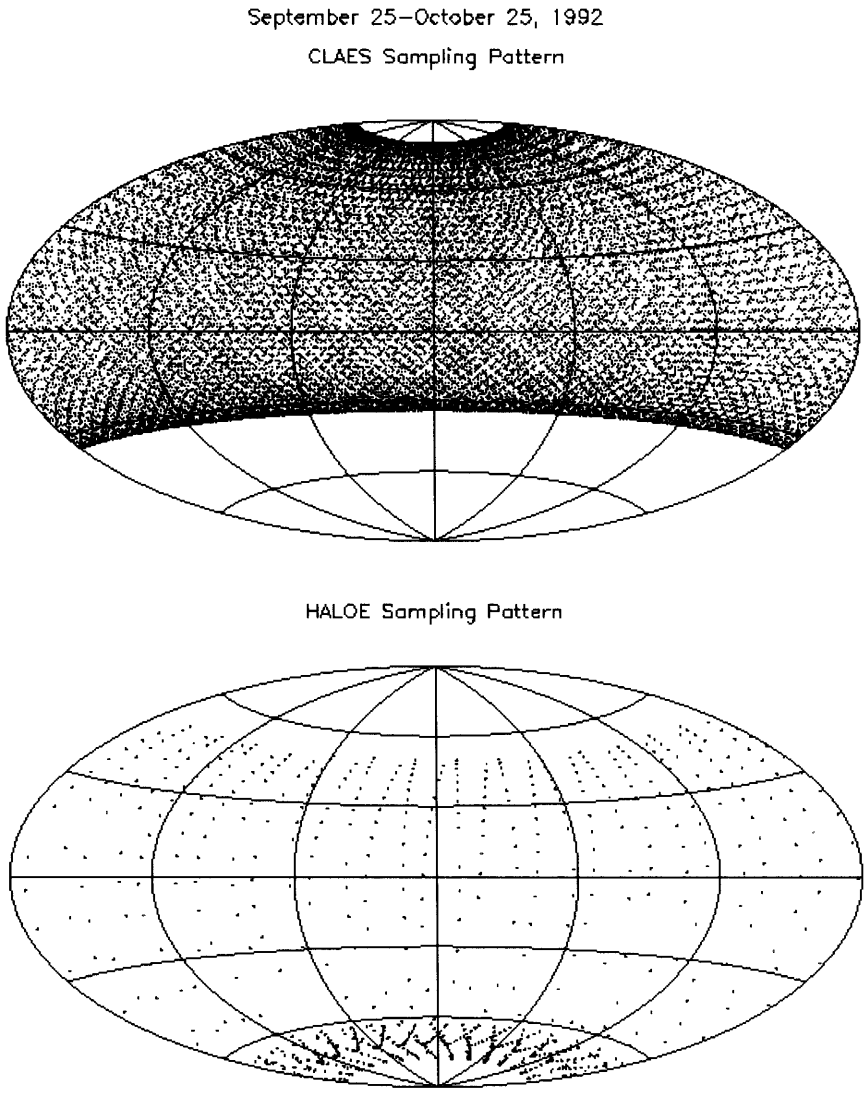

Figure 3-9: The CLAES sampling pattern for September 25, 1992, to October 25, 1992, (top) as well as the HALOE sampling pattern for the same time period (bottom). Each symbol represents a single sounding.

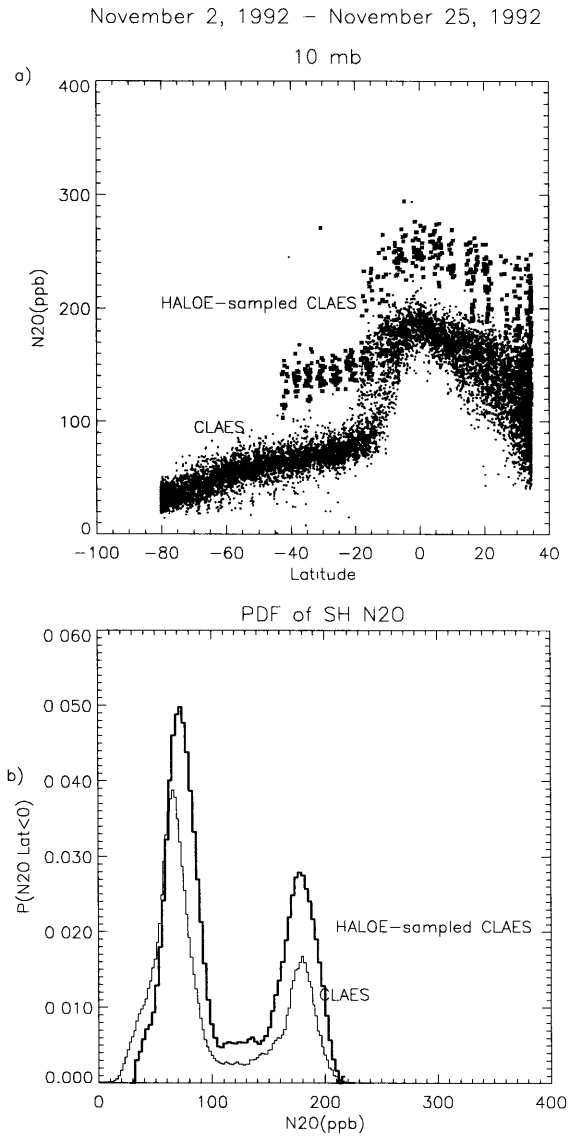

Figure 3-10: a) The CLAES N_2O measurements for November 2, 1992, to November 25, 1992, at 10 mb, as well as the CLAES measurements corresponding to the HALOE sampling pattern during this period (offset by 70 ppb). b) The PDF of the CLAES data in the Southern Hemisphere as well as the PDF of the HALOE-sampled CLAES data

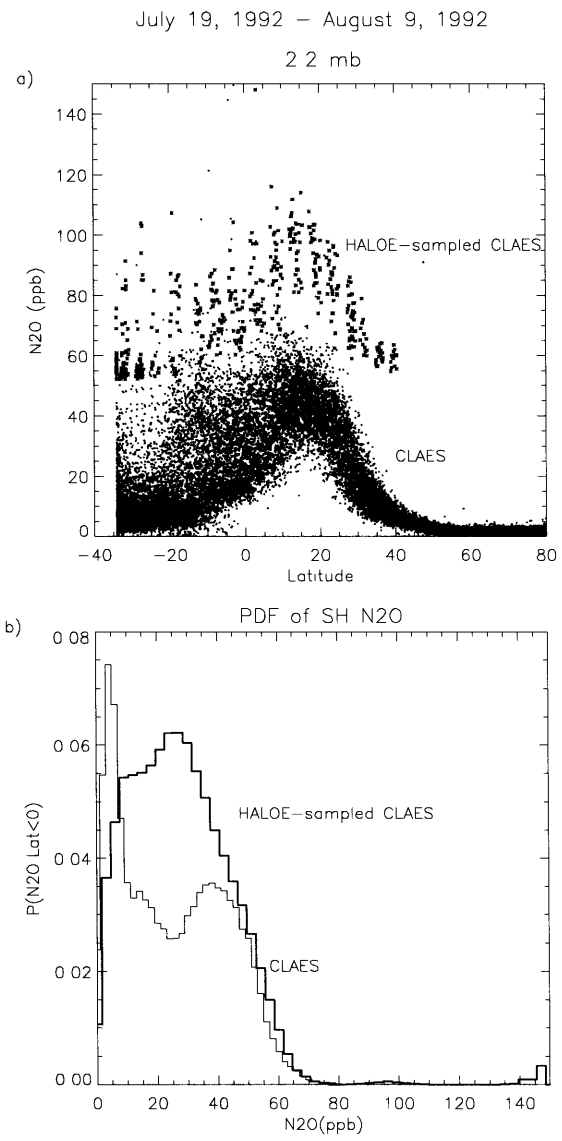

Figure 3-11: The same as Figure 3-10, but for July 19, 1992, to August 9, 1992, at 2.2 mb.

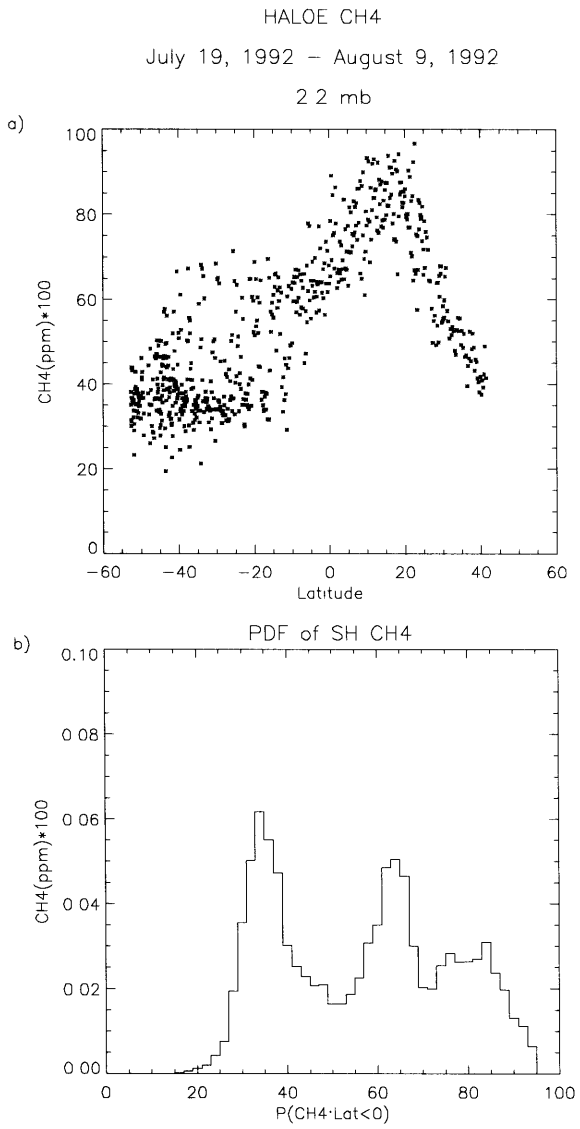

Figure 3-12: a) The HALOE CH_4 measurements for the same period and pressure level as Figure 3-11. The bottom frame shows the PDF of the measurements in the Southern Hemisphere.

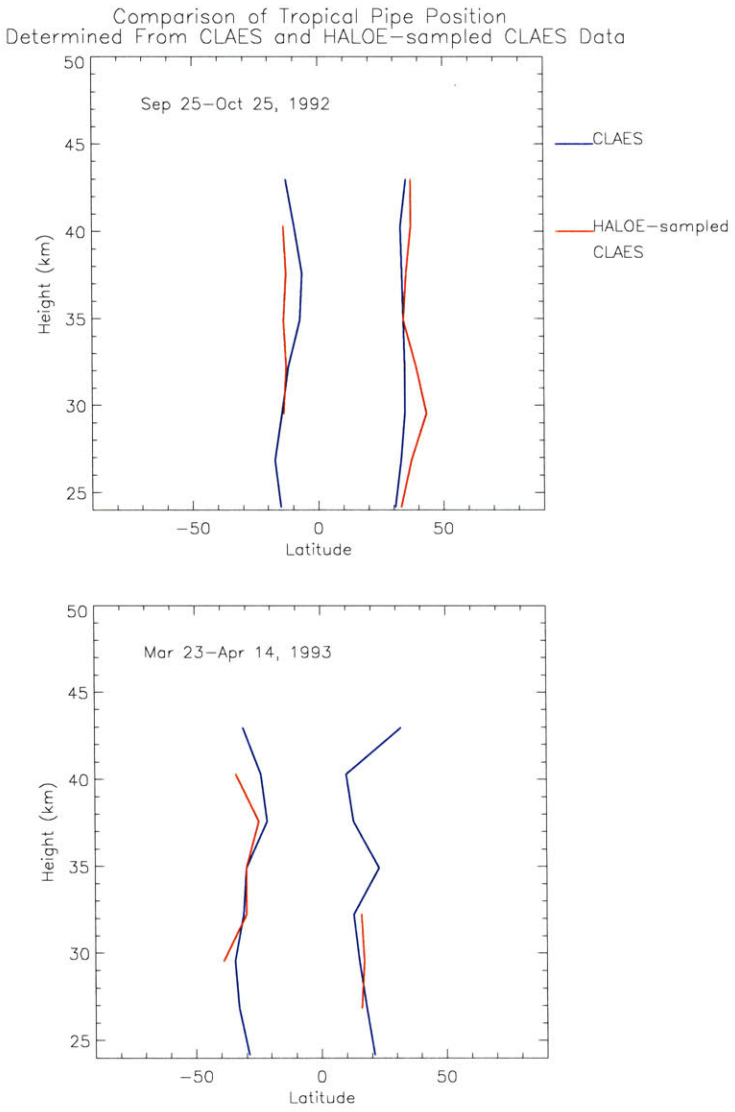

Figure 3-13: A comparison of the positions of the subtropical edges as determined from the CLAES data to the positions as determined from the HALOE-sampled CLAES data for the September 25, 1992, to October 25, 1992, (top frame) and March 23, 1993, to April 14, 1993, (bottom frame) viewing periods.

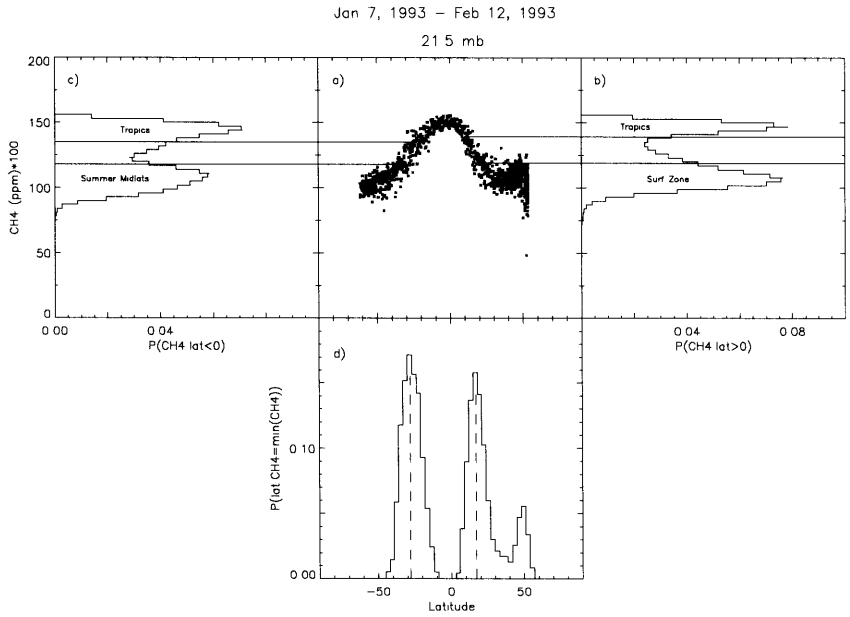

Figure 3-14: The same as Figure 3-2, but for HALOE CH_4 measurements taken from January 7, 1993, to February 12, 1993, at 21.5 mb.

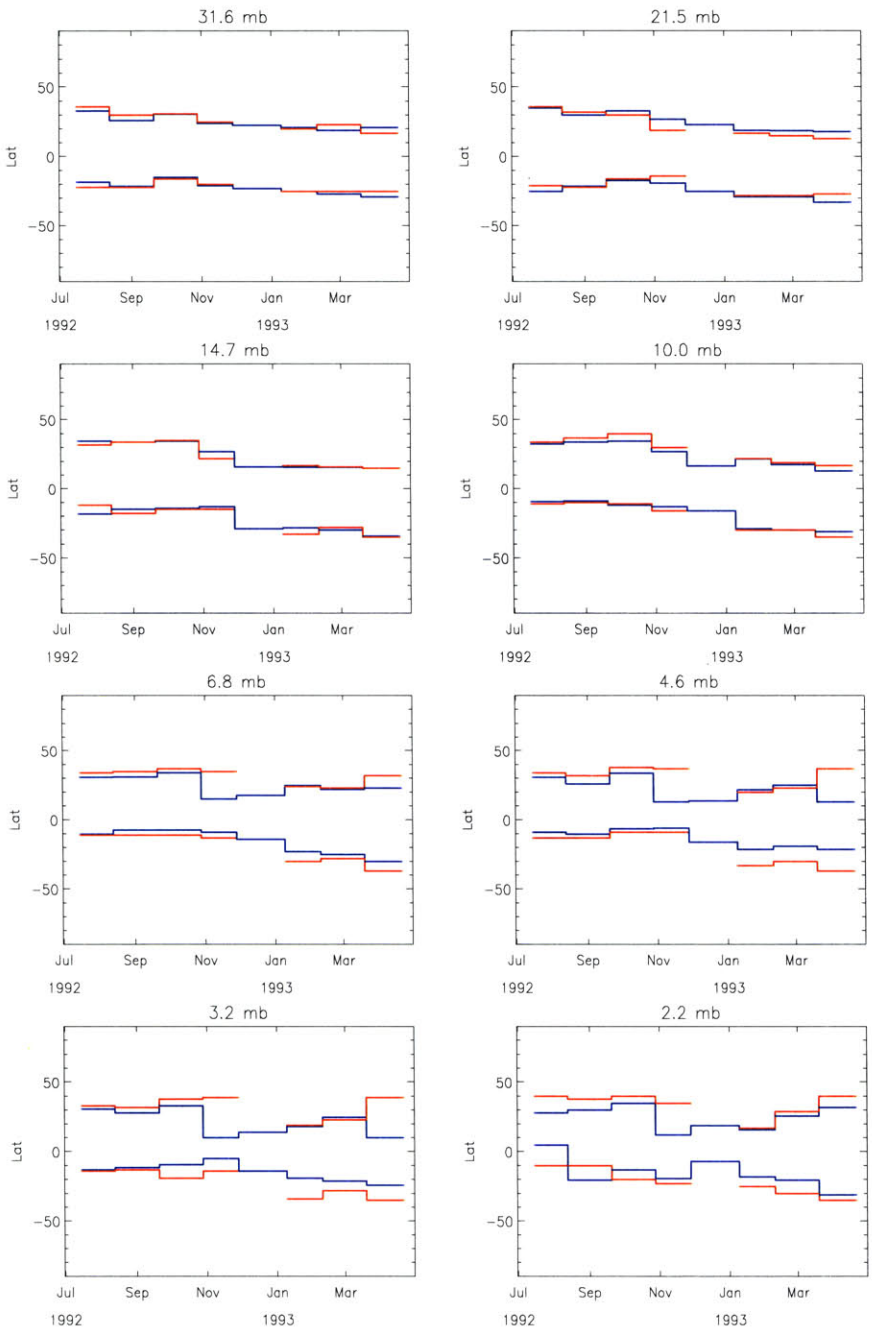

Figure 3-15: A comparison of the subtropical edge positions at each pressure level as determined from the CLAES N_2O data (in blue) to those determined from the HALOE CH_4 data (in red) for the CLAES yaw periods.

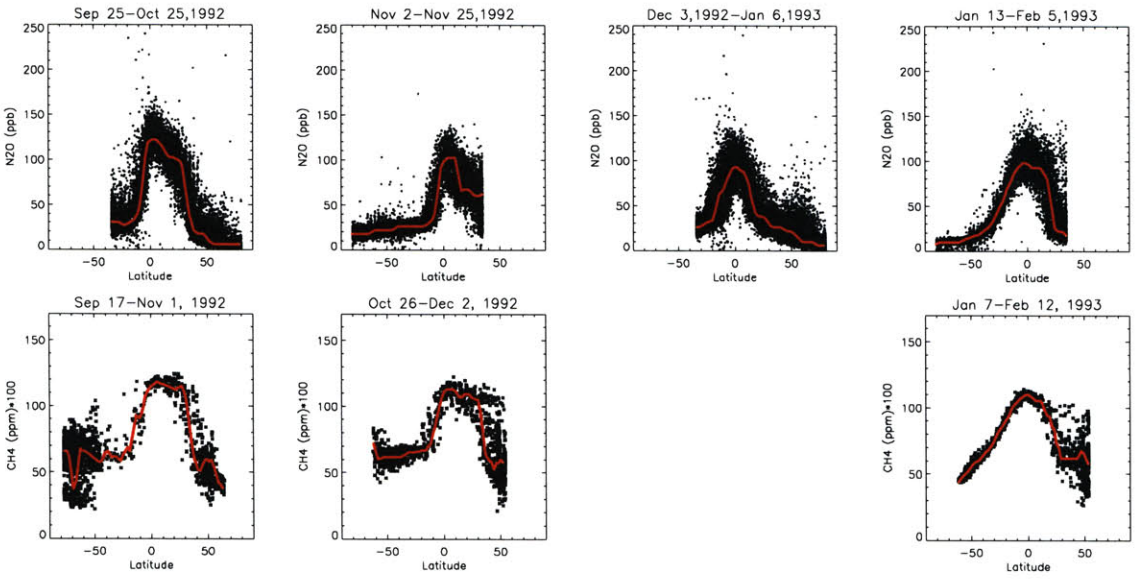

Figure 3-16: A comparison of the CLAES N_2O measurements during the transition to the 1992-1993 Northern Hemisphere winter and the HALOE CH_4 measurements during the same period. The zonal mode of each set of measurements is overplotted in red.

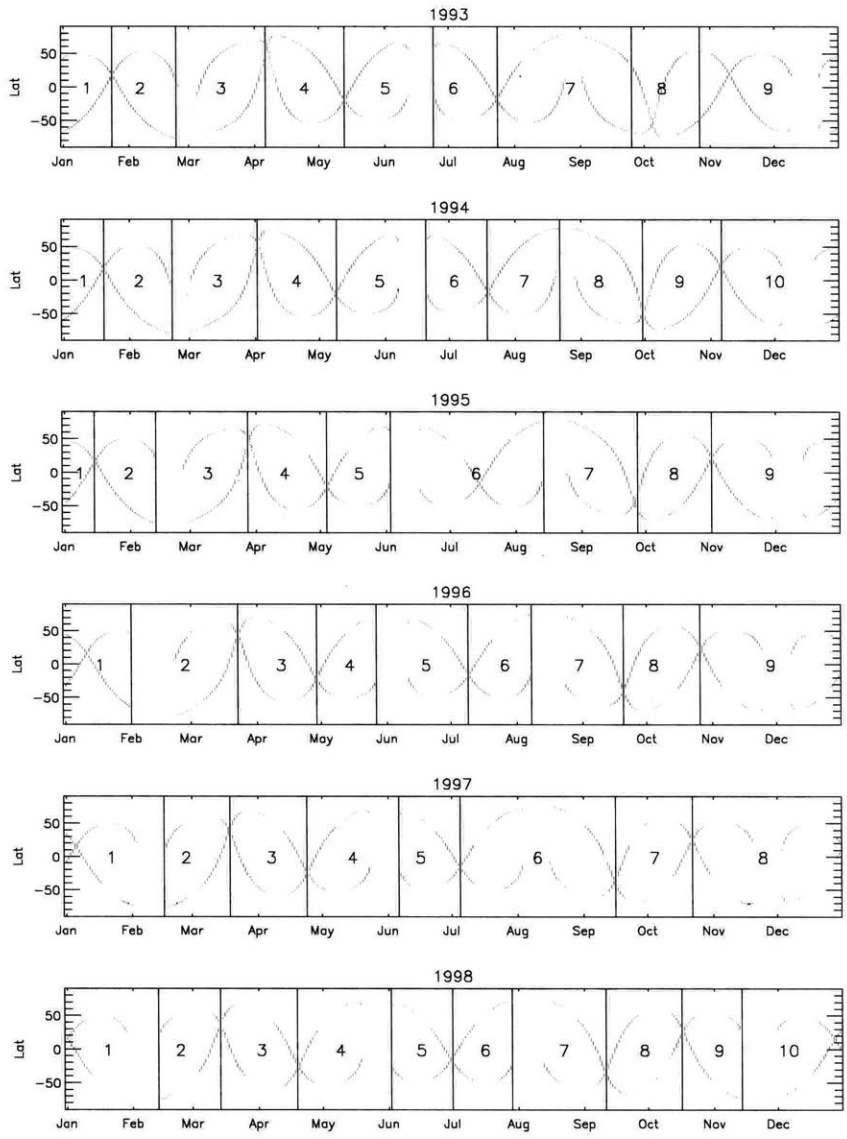

Figure 3-17: The HALOE sampling pattern for each year from 1993 to 1998. The vertical lines indicate the data periods used for each year, and the numbers correspond to the viewing period numbers in Tables D-I.

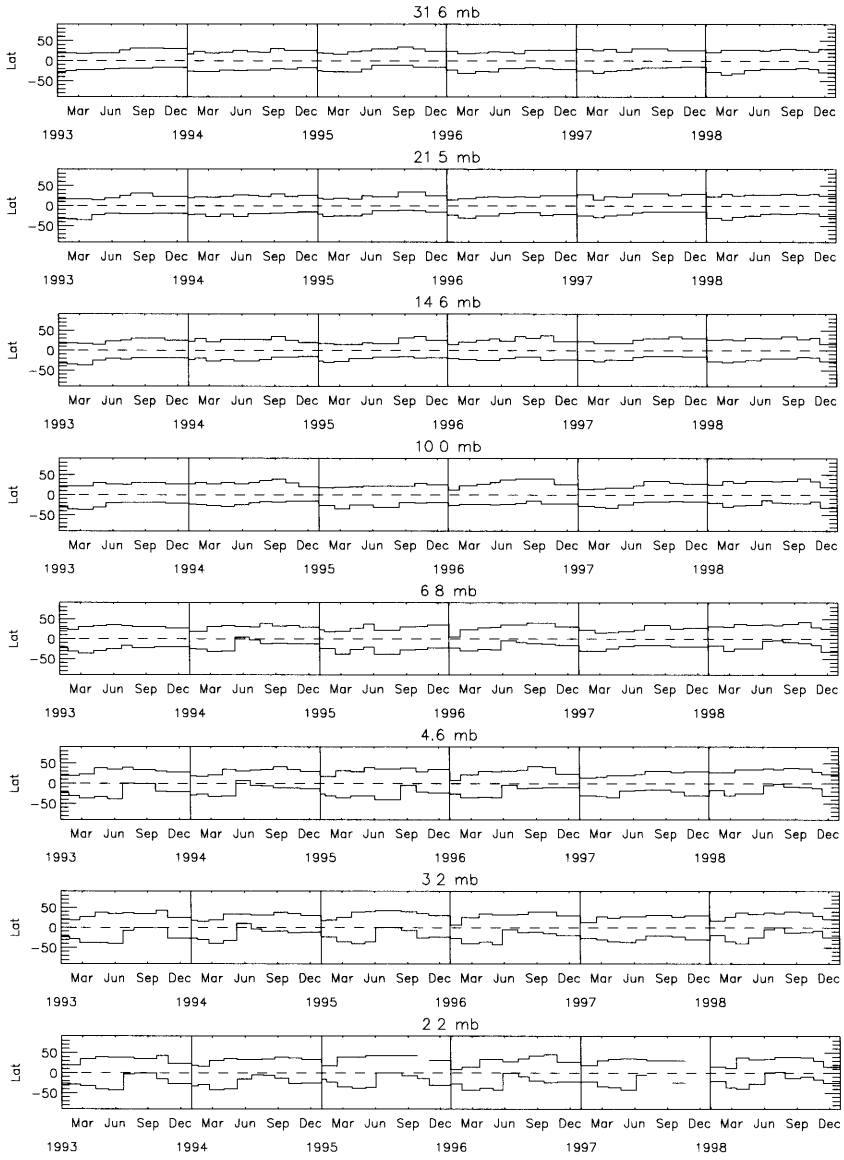

Figure 3-18: The evolution of the subtropical edges at each pressure level as determined from the HALOE data.

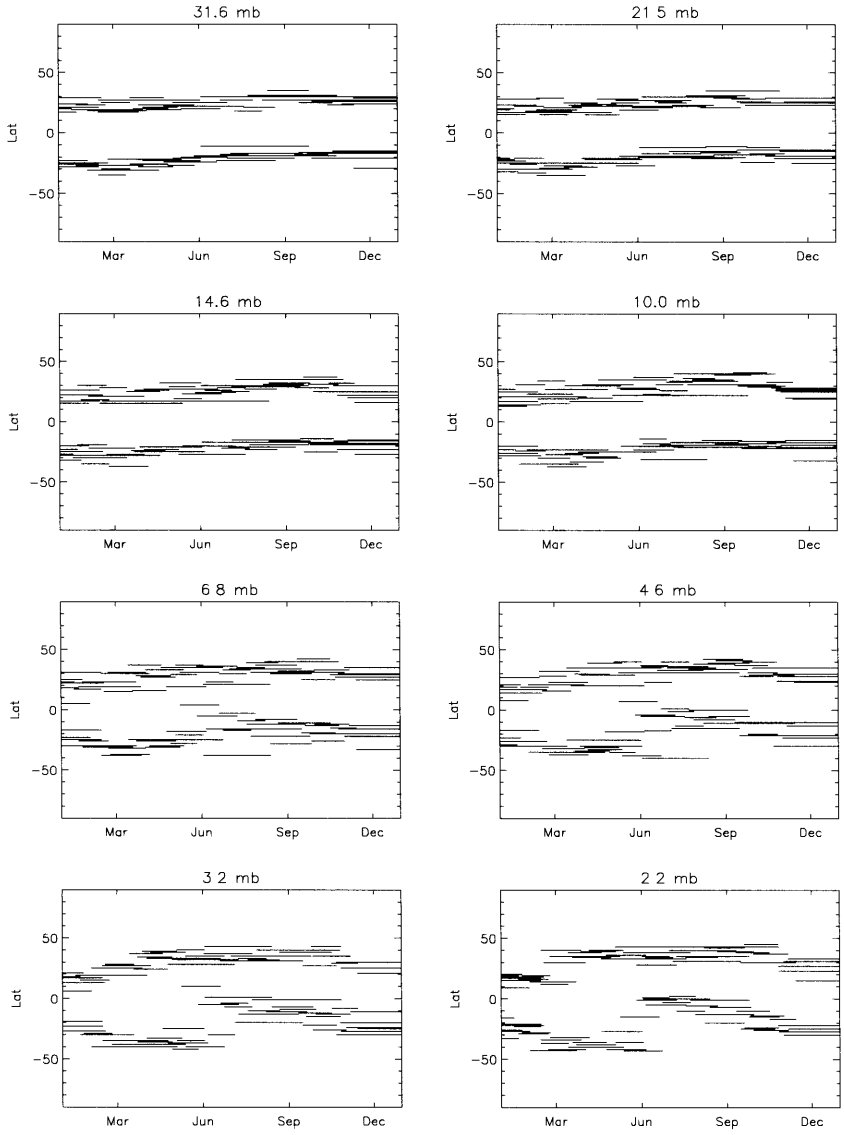

Figure 3-19: The subtropical edges as determined from the HALOE data. The results for all of the years from 1993 to 1998 are plotted.

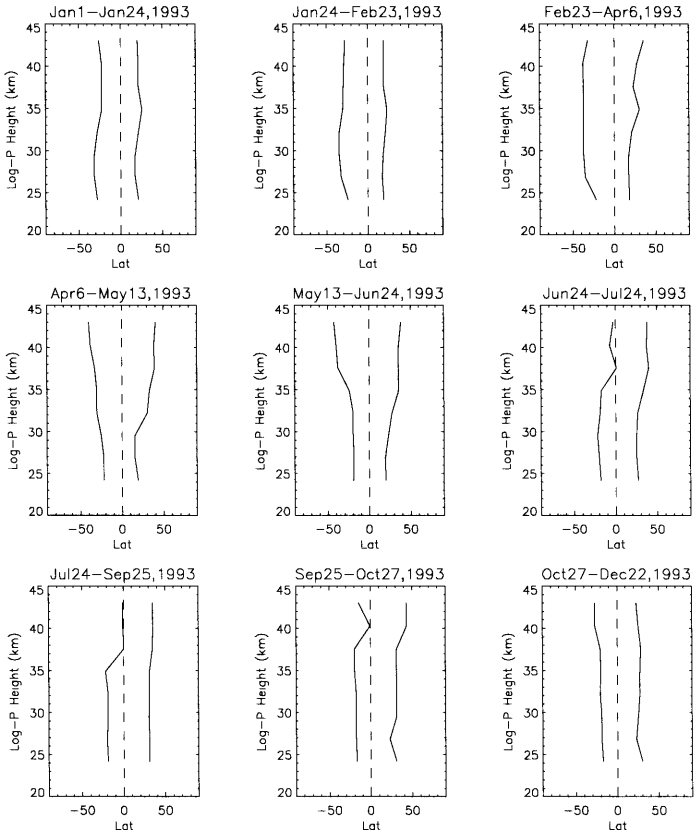

Figure 3-20: The vertical structure of the "tropical pipe" as determined from the HALOE CH_4 measurements for each of the viewing periods in 1993.

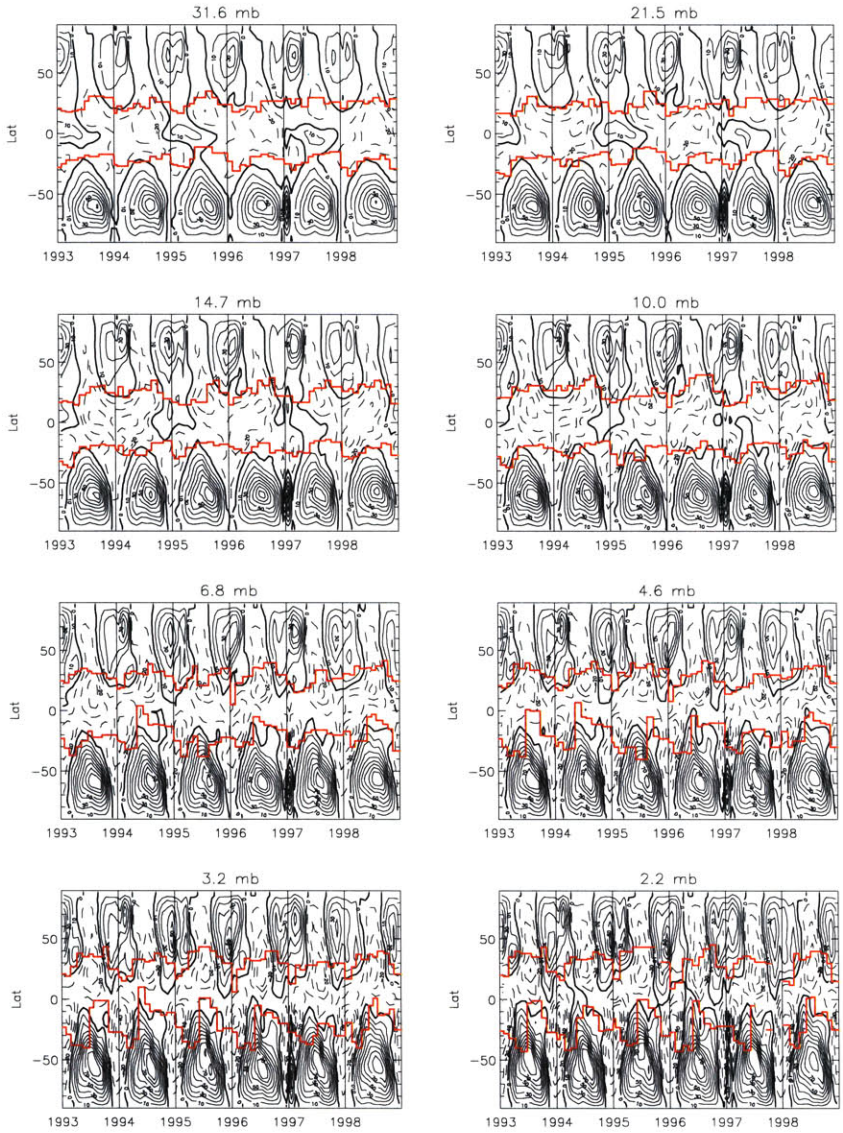

Figure 3-21: The subtropical edge positions as determined from the HALOE data overplotted on zonal mean zonal winds from the UKMO UARS correlative analyses. The contour interval is 10 ms^{-1}. Solid lines are positive values and dashed lines are negative values. The zero contour is in bold.

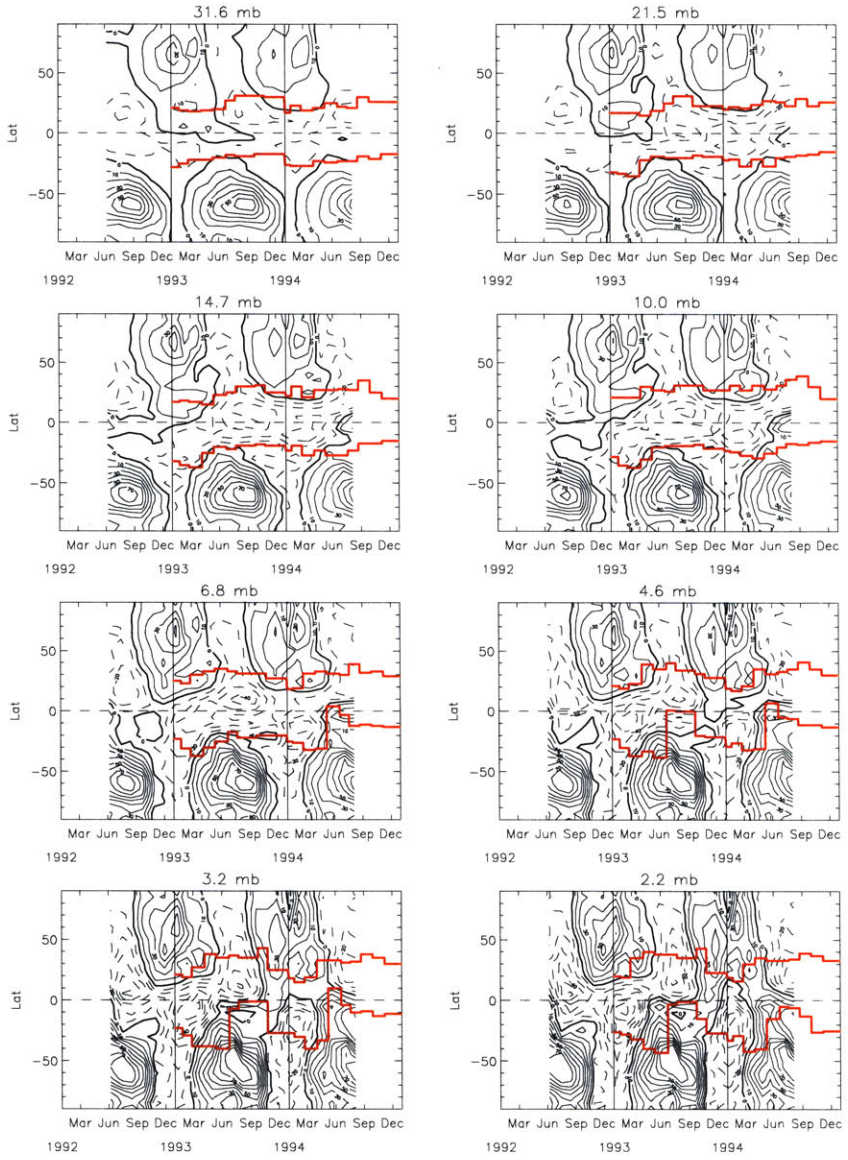

Figure 3-22: The same as Figure 3-21, but for the zonal mean zonal wind derived from gradient wind balance by Eluszkiewicz et al. (1996).

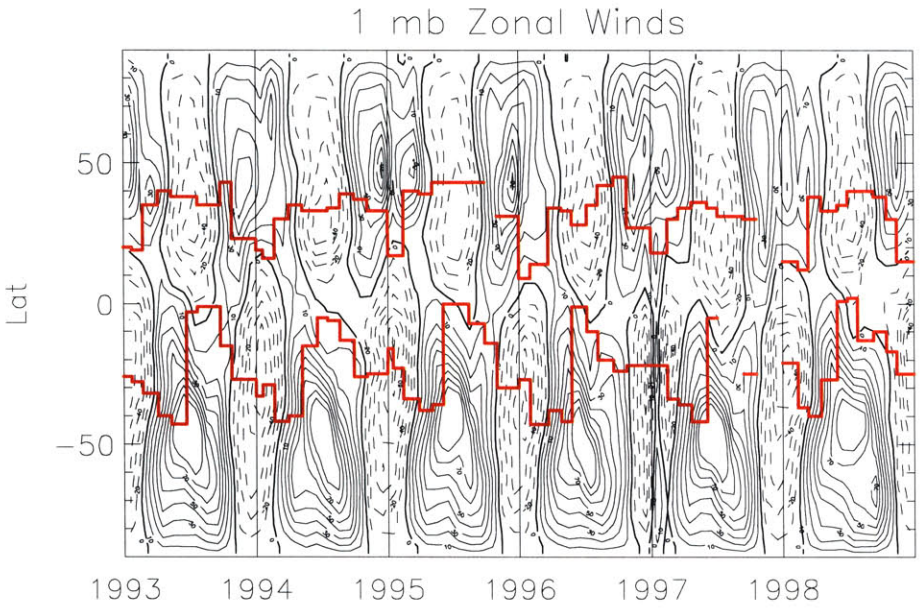

Figure 3-23: The zonal mean zonal winds at 1 mb from the UKMO analysis. The subtropical edge positions at 2.2 mb are overplotted.

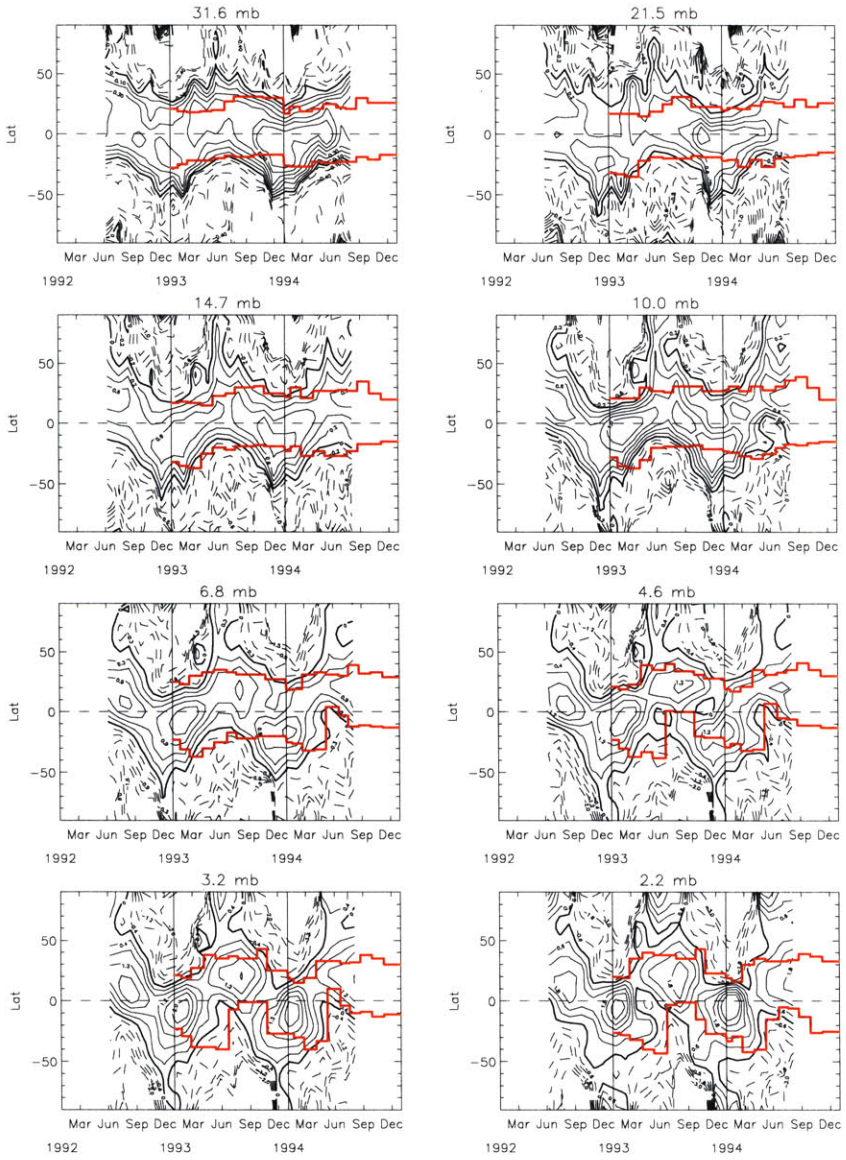

Figure 3-24: The subtropical edge positions overplotted on the residual vertical velocity derived by Eluszkiewicz et al. (1996). The contour interval is different in each frame. Solid lines are positive values and dashed lines are negative values. The zero contour is in bold.

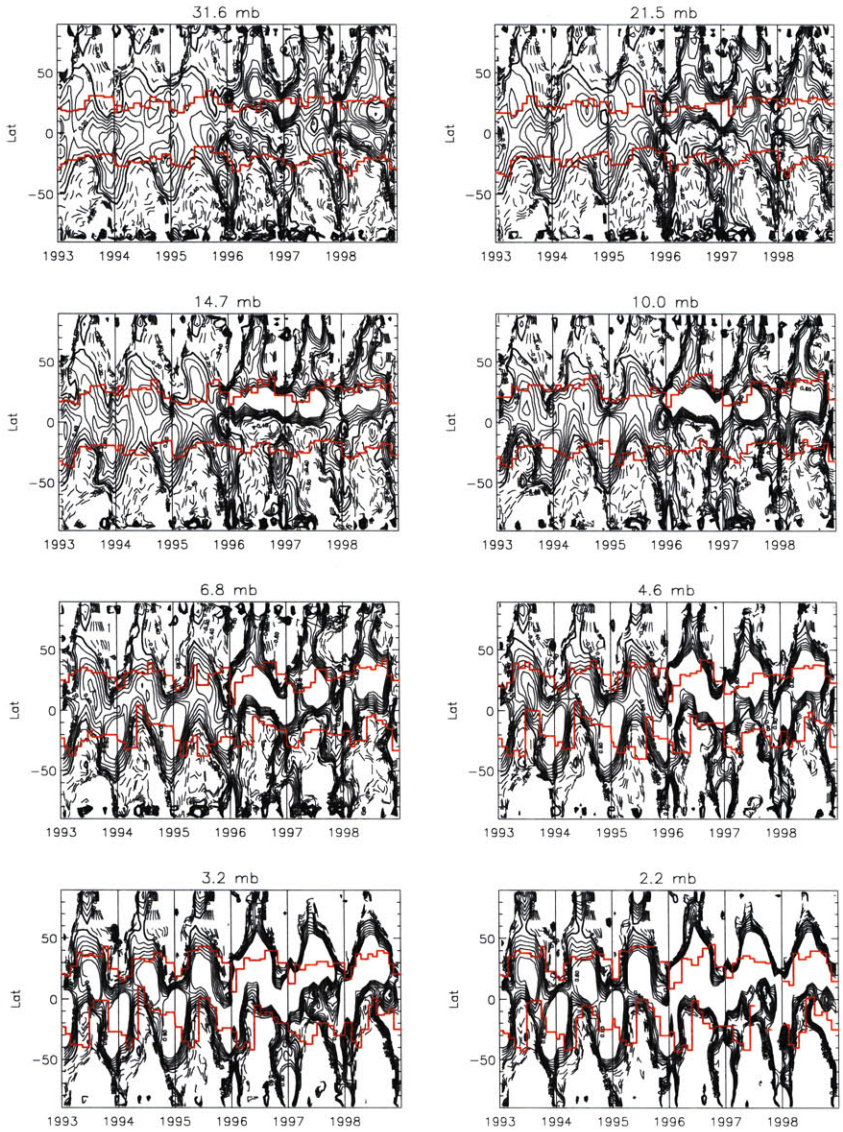

Figure 3-25: The same as Figure 3-24, but for the residual vertical velocity derived from 5-day snapshots of the UKMO UARS correlative analysis.

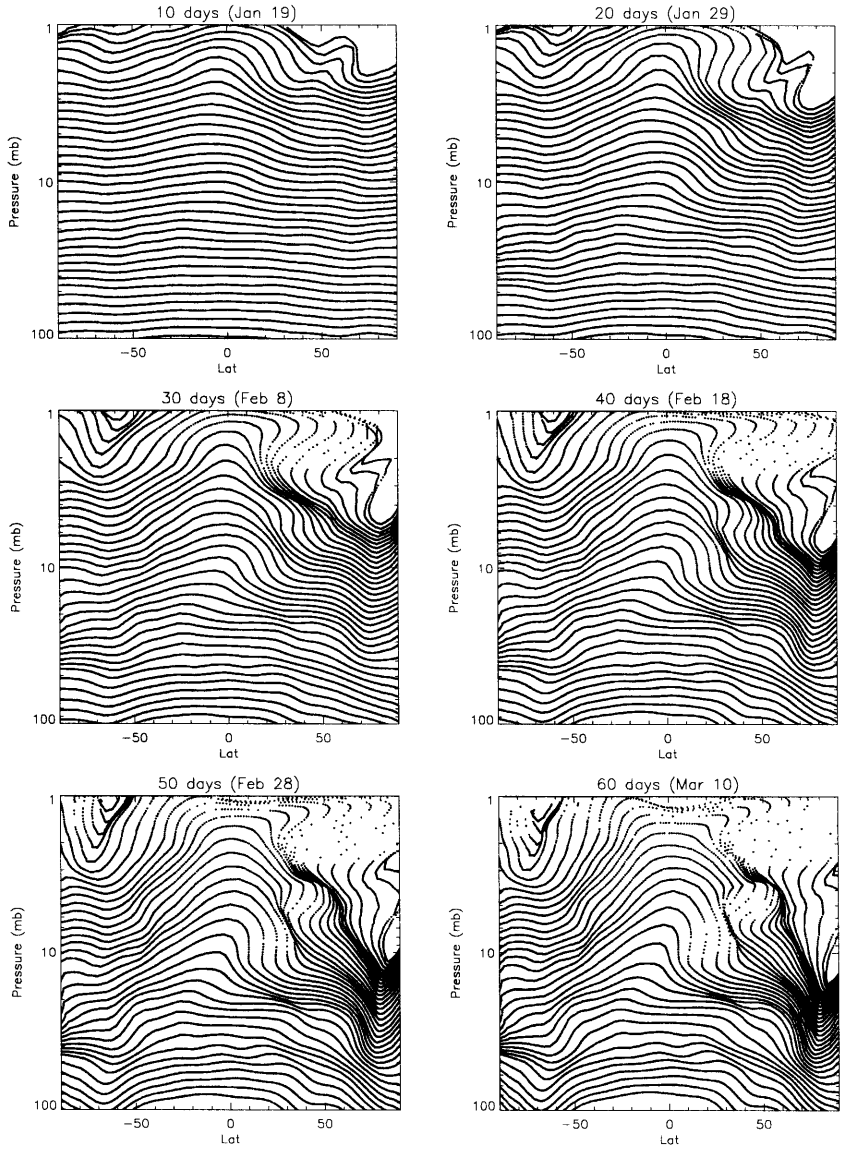

Figure 3-26: The evolution of particles advected by the residual circulation of Eluszkiewicz, et al. (1996). The particles were initialized on a log-pressure, latitude grid on January 9, 1993.

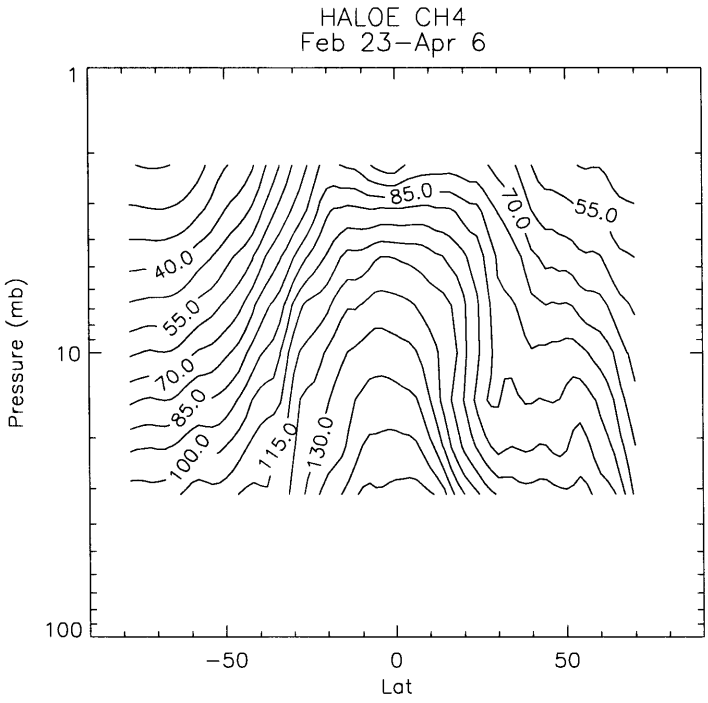

Figure 3-27: The latitude - height cross section of zonal mean HALOE CH_4 measured during the period February 23, 1993 to April 6, 1993. Compare to the last frame of Figure 3-26.

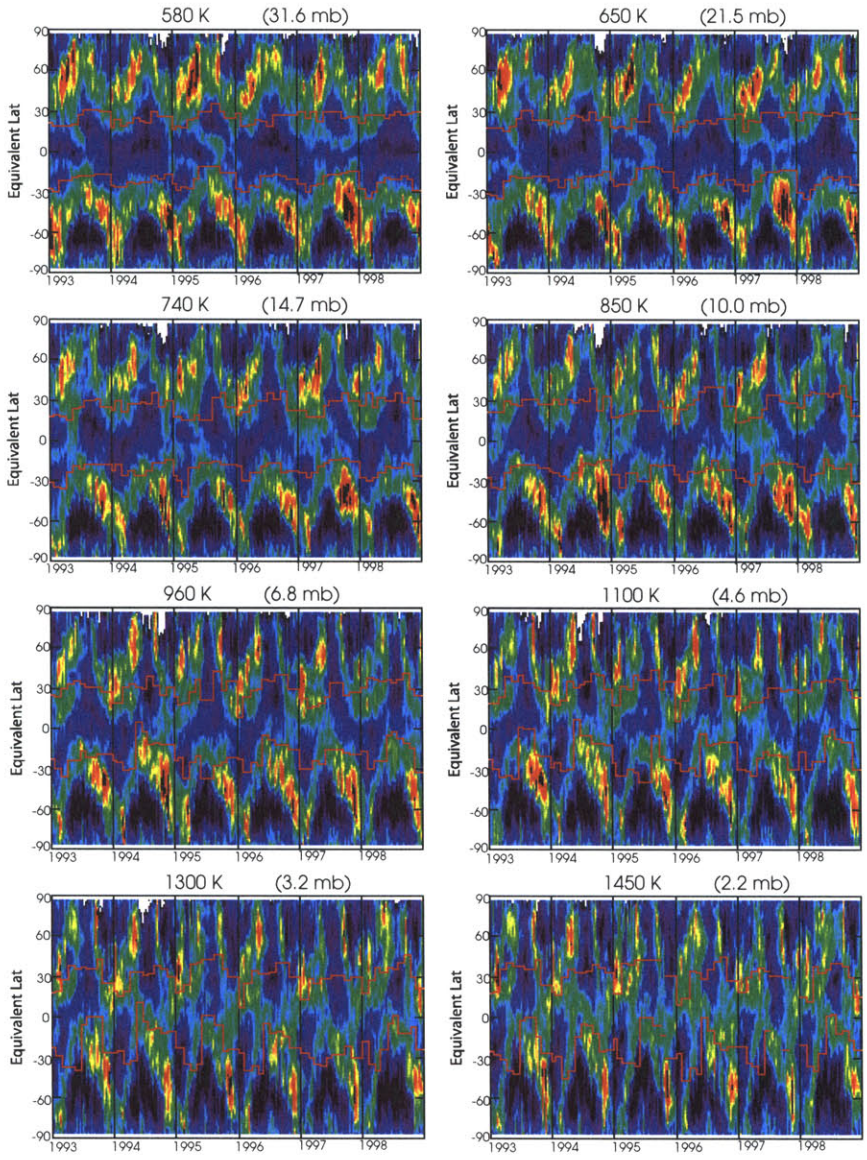

Figure 3-28: The subtropical edge positions overplotted on the Normalized Equivalent Length, calculated by D. Allen (Allen and Nakamura, 2000). The isentropic level of the calculation and the pressure level of the edges are given for each frame. The y-axis is equivalent latitude for the equivalent length calculations and latitude for the edge positions. Dark colors are low equivalent lengths, bright colors are high equivalent lengths.

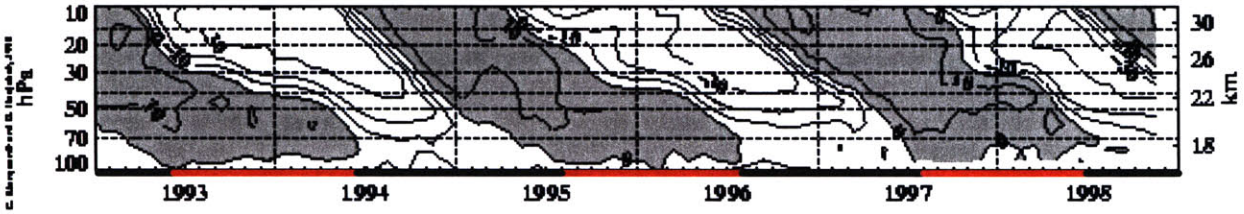

Figure 3-29: The time-height cross section of the zonal wind over Singapore (Marquardt and Naujokat, 2000). The contour interval is 10 m $s^{-1}$and shading indicates positive values (westerlies).

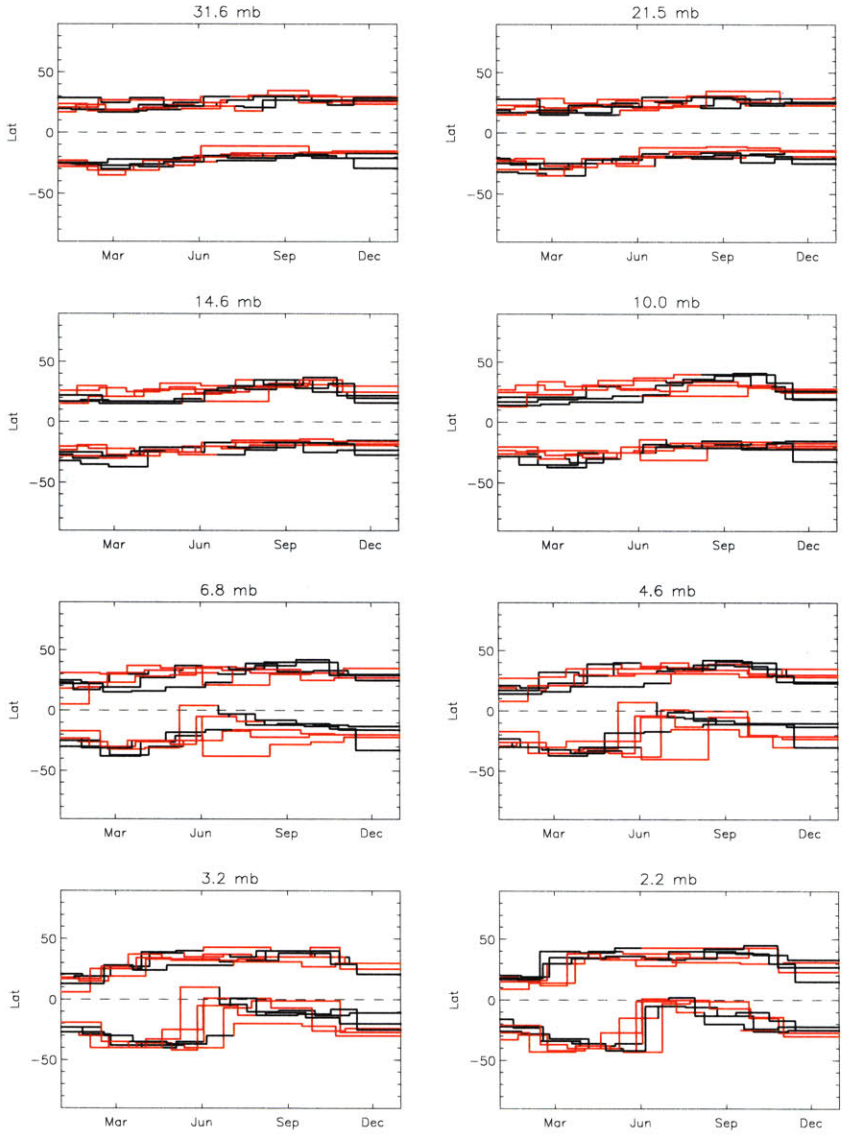

Figure 3-30: The subtropical edges as determined from the HALOE measurements, for all years, 1993-1998. Time periods of bulk easterly shear (over the layer from 100 to 10 mb) are in red, and time periods of bulk westerly shear are in black.

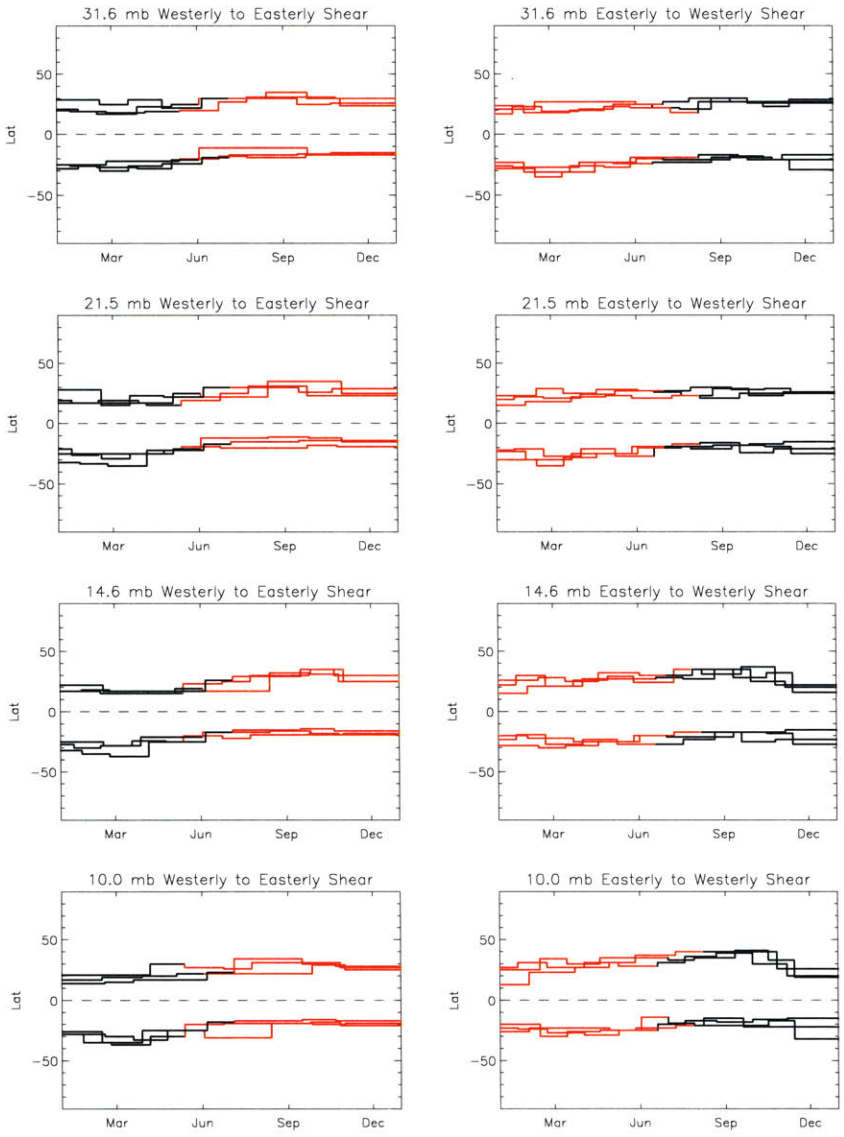

Figure 3-31: The subtropical edge as determined from the HALOE data, for 31.6 to 10.0 mb, separated into years in which the bulk shear changed from westerly to easterly (1993, 1995, and 1997) and years in which it changed from easterly to westerly (1994, 1996, 1998).

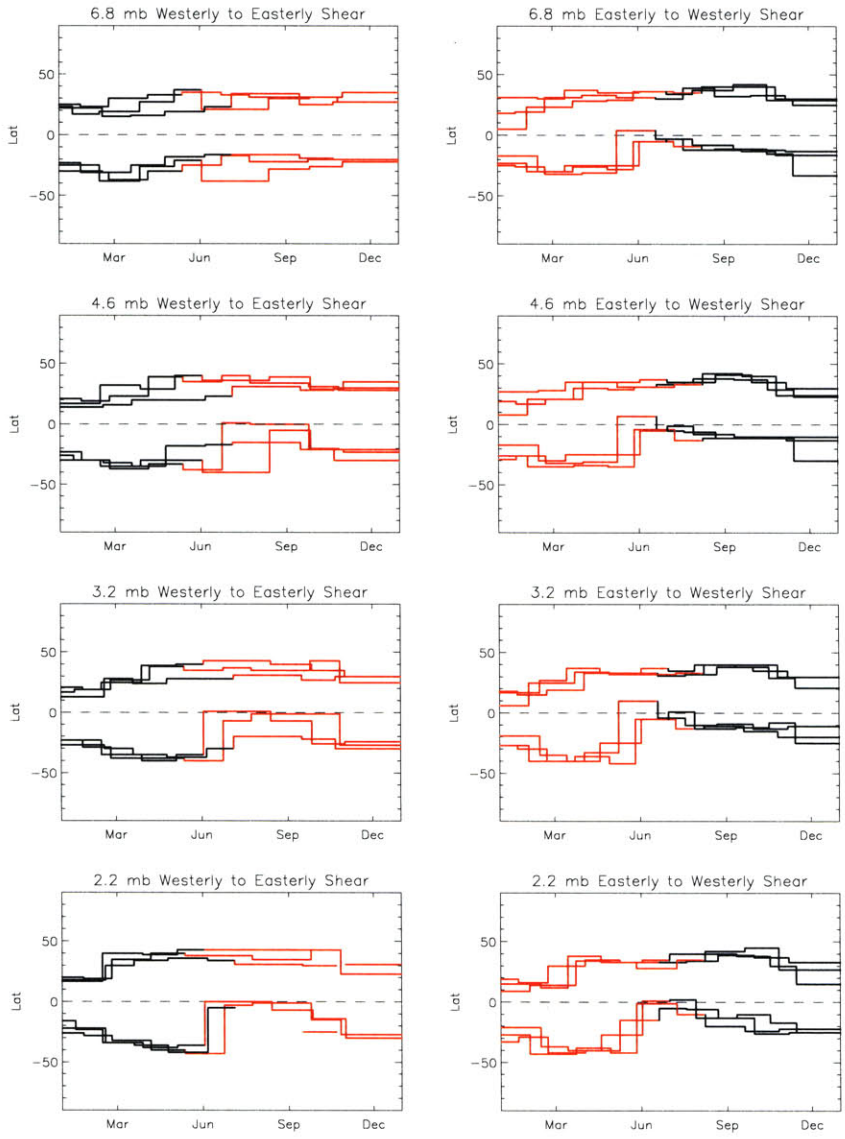

Figure 3-32: The same as Figure 3-31, but for 6.8 to 2.2 mb.

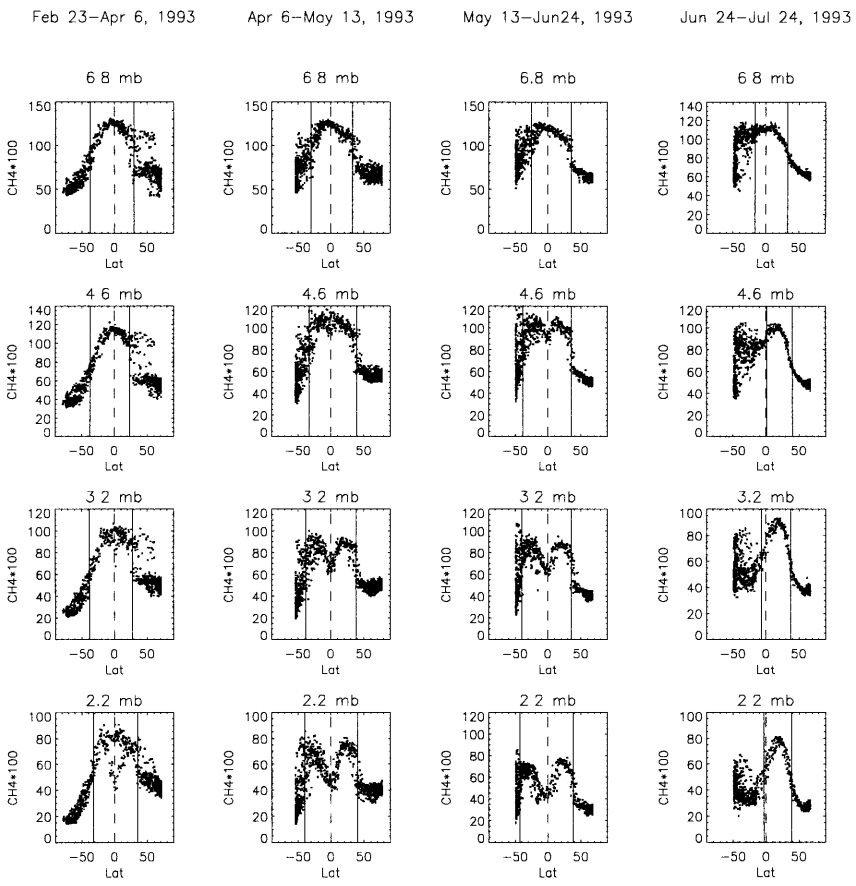

Figure 3-33: HALOE CH_4 measurements during Southern Hemisphere fall and early winter of 1993. See the text for discussion.

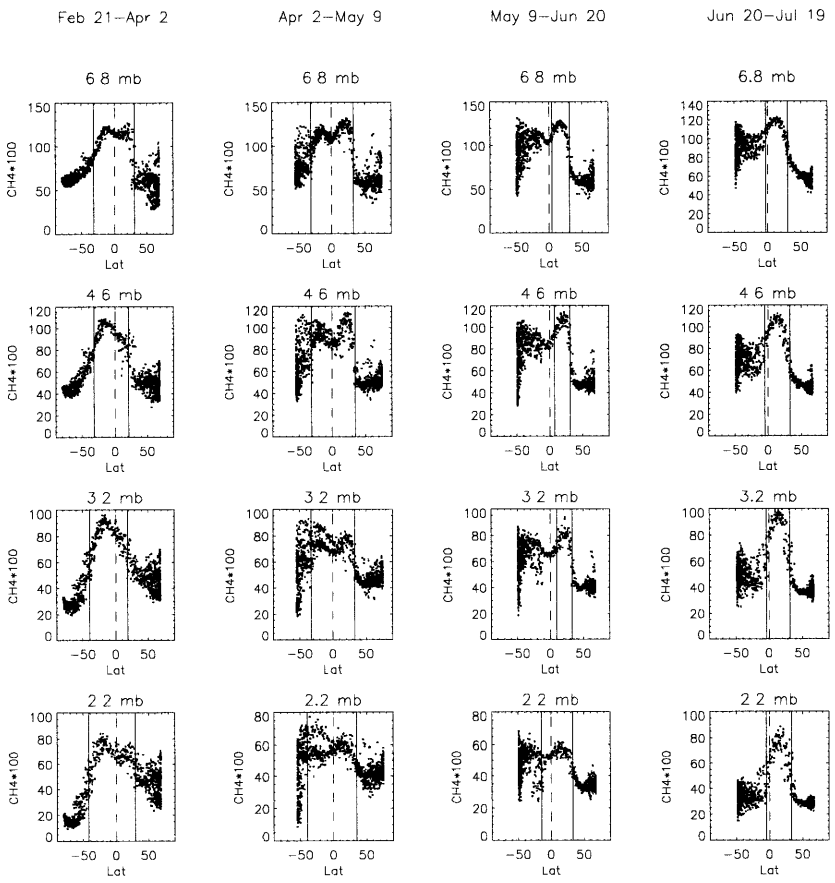

Figure 3-34: The same as Figure 3-33, but for 1994.

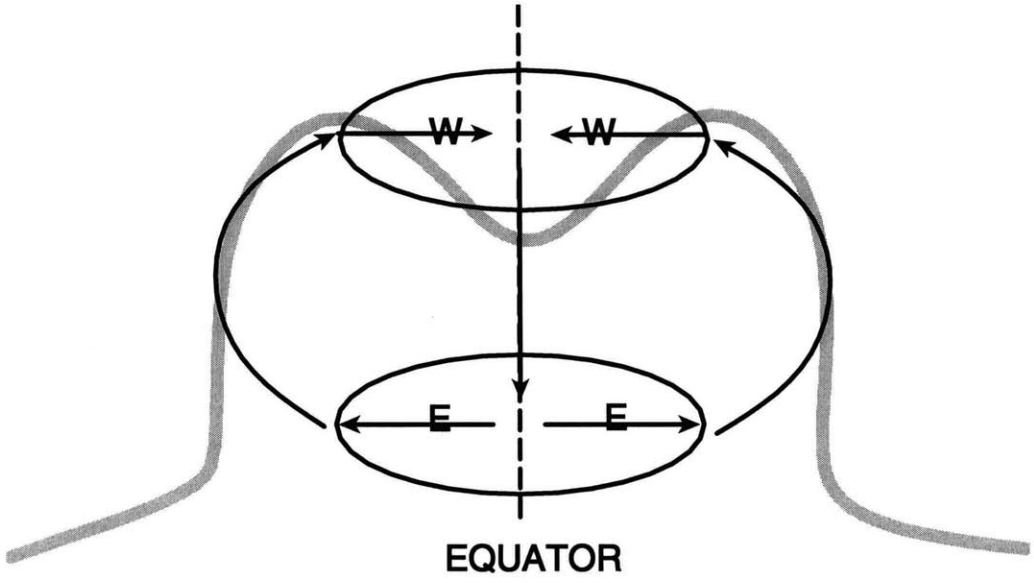

Figure 3-35: Schematic representing the meridional circulation induced during the descending westerly phase of the SAO. Ovals represent regions of wave drag and arrows represent the induced circulation. The gray line represents a mixing ratio isopleth advected by the induced circulation.

Chapter 4

Seasonal Variability of the Subtropical Edges: Shallow Water Model

4.1 Introduction and Motivation

The shallow water system of equations is the simplest system of equations that includes a representation of the processes that we believe to be important in the formation and maintenance of the subtropical edges: stirring by planetary-scale wave breaking and diabatic heating and cooling. Here, we present both "perpetual solstice" and seasonal cycle simulations and examine the role of these processes in irreversible mass transport out of the subtropical edge regions during each season.

The shallow water system can be thought of as representing the flow within a thin isentropic layer, assuming that there is no variation of the flow with height. Since the large-scale wave motions in the stratosphere are largely isentropic, shallow water models have proven extremely useful for high-resolution studies of wave breaking. Topography is used to represent the undulation of isentropic surfaces as waves propagate upward through the stratosphere, and for zonal wind profiles similar to those of the winter hemisphere, this undulation results in wave breaking much like that observed in the surf zone (e.g. Juckes and McIntyre, 1987; Juckes,

1989). In addition, a mass source can be used to represent the effects of diabatic processes on the thickness of the isentropic layer. The shallow water layer thickness, h, can be thought of as the thickness of a layer of constant density fluid that contains the same mass per unit area as an isentropic layer of depth $\Delta\theta$ with density $\sigma = -\frac{1}{g}\frac{\partial p}{\partial \theta}$. The heating rate, Q, is the vertical velocity in isentropic coordinates, so that the isentropic mass continuity equation is given by:

$$\frac{\partial \sigma}{\partial t} = -\nabla_H \cdot (\mathbf{u}\sigma) - \frac{\partial(\sigma Q)}{\partial \theta}$$

For a thin isentropic layer in which the variation of σ with height is negligible, h is proportional to σ, and we can write the shallow water continuity equation as:

$$\frac{\partial h}{\partial t} = -\nabla_H \cdot (\mathbf{u}h) + H$$

where H, which is a mass source, is equivalent to the vertical gradient of the mass-weighted heating rate across the isentropic layer:

$$H = -\frac{\Delta(\sigma Q)}{\Delta\theta} \tag{4.1}$$

Thus, by including a mass source in the shallow water system, we do not actually represent diabatic heating and cooling, but we represent the effects of the vertical convergence and divergence of the mass flux associated with the heating rate on the mass in the layer.

Since potential vorticity (PV) "substance", which can be thought of as a tracer whose mixing ratio is ρP, where P is Ertel's PV, can only be concentrated or diluted between isentropic surfaces (and not advected across them) by diabatic heating and cooling (Haynes and McIntyre, 1987), the inclusion of a mass source in the shallow water equations represents the effects of diabatic processes on PV in an isentropic layer despite the fact that there is no vertical velocity associated with this mass source in the shallow water equations. This PV impermeability theorem also implies that the local effects of stirring by breaking Rossby waves upon the global distribution of PV can be thought of solely in terms of PV rearrangement along isentropic surfaces. Thus, a shallow water model can capture the response of the vertically integrated isentropic potential vorticity to Rossby wave propagation and diabatic heating and cooling,

so that the results are meaningful in the context of the behavior of an isentropic layer in the stratosphere that is subject to these processes. However, in reality, the wave-induced departure from radiative equilibrium drives the meridional circulation and associated diabatic heating and cooling non-locally (Haynes et al., 1991), and thus an isentropic layer is sensitive to the wave dissipation in the layers above it, which can not be represented in a shallow water model.

Shallow water models have been used to study wave breaking under both adiabatic and nonadiabatic conditions (e.g. Juckes and McIntyre, 1987; Juckes, 1989; Polvani et al., 1995; Thuburn and Lagneau, 1999; Sobel and Plumb, 1999). These studies have focused almost entirely on the winter hemisphere, particularly on the surf zone and the polar vortex, which are separated by the vortex edge, a semi-permeable barrier to mixing. The surf zone behaves in many ways like a nonlinear critical layer, with stationary Rossby waves stirring material isentropically as they break in the weak winds of the winter midlatitudes. The vortex is shielded from this stirring by the strong westerly winds of the polar jet, and a strong PV gradient, the vortex edge, forms as the stirring occasionally manages to pull material out of the vortex, thus decreasing the mass between PV contours. Since the tropical winds are easterly, and thus prevent propagation of stationary waves, a similar mechanism should result in a tightening of the subtropical PV gradient. This was first observed by Norton (1994), and extensively studied by Polvani et al. (1995), hereafter referred to as PWP, who demonstrated that representing diabatic processes in a shallow water model can confine the equatorward encroachment of the surf zone, preventing strong mixing from reaching into the tropics and leading to a sharpening of the PV gradient in the subtropics. They found that the representation of diabatic processes led to a larger difference between the midlatitude and tropical winds, so that transient waves generated by wave breaking in the surf zone were unable to propagate into the tropics. Here, we examine not only the enhanced PV gradient that forms in the winter subtropics as a result of surf zone stirring, but also an enhanced PV gradient that forms in the summer subtropics when diabatic processes are represented.

The summer subtropical edge has long been a matter of debate in the stratospheric community. It is clear that long-lived tracers show strong gradients between the tropics and midlatitudes throughout the summer (e.g. Grant et al., 1994), and correlations of these tracers, which are compact in regions where there is rapid mixing (Mahlman, 1985; Plumb and Ko,

1992; Thuburn and McIntyre, 1997) have distinctly different curvatures in the tropics and midlatitudes, indicating a lack of communication between these regions (Murphy et al., 1993). In addition, as shown in Chapter 3, the probability distribution functions (PDFs) of such tracers are bimodal throughout the summer, again indicating that the tropics and midlatitudes are isolated from one another. The mechanism behind the summer subtropical edge, however, has always been unclear, since the winter subtropical edge is associated with strong mixing in the surf zone, and wave propagation is strongly inhibited during the summer, particularly in the middle stratosphere. There have been suggestions that the winter subtropical edge is simply "frozen" in the tracer field due to a lack of mixing in the summer hemisphere (e.g. Nakamura and Ma, 1997), that the summer subtropical tracer gradients result entirely from differential vertical velocities, which carry the tracers upward in the tropics and downward in midlatitudes (e.g. Randel et al., 1998), and that, for certain tropical zonal wind profiles, the summer edge results from waves that manage to propagate through the tropics and break on the summer side, thus tightening PV gradients in the subtropics (O'Sullivan and Chen, 1996; Chen, 1996). It has also been unclear whether the summer subtropical edge can be considered a mixing barrier; since there is little mixing in the summer hemisphere, it is difficult to say whether the edge resists and is sharpened by mixing in the same way as the winter subtropical edge or whether the edge exists only because there is no mixing that would act to destroy it. Recent studies, however, have shown that there is, in fact, evidence of mixing in the summer lower stratosphere (Wagner and Bowman, 1999; Haynes and Shuckburgh, 2000), which would tend to indicate that the subtropical edge is at least somewhat effective as a barrier to mixing since it is not destroyed over the course of the summer.

We demonstrate here that by including relaxation to a radiative equilibrium height field in their shallow water model, PWP not only formed the winter subtropical edge by confining wave breaking to the winter midlatitudes, they also formed a summer subtropical edge purely through the radiative forcing. We then show that the summer edge can act as an efficient barrier to mixing (i.e., that if we force waves in the summer midlatitudes, the breaking region does not extend into the tropics) and that the winter and summer subtropical edges are inherently different, the former being formed and maintained by a balance between radiative heating throughout the edge region and mixing into the surf zone, and the latter being located at the

transition between heating in the tropics and cooling at high latitudes, even when there is mixing in the summer hemisphere. We also present seasonal cycle simulations, in which the radiative equilibrium height field is varied to produce both a Northern and a Southern winter, and show that the summer subtropical edge is not formed merely from remnants of the winter edge. In fact, in the absence of mixing in the summer hemisphere, the subtropical edge forms mainly from air that was in the surf zone and the vortex edge. Many of the features of the seasonal cycle simulations, including the migration of the tropical air mass toward the summer hemisphere, the formation of a very narrow winter subtropical edge near the equator and a very broad summer subtropical edge further toward the midlatitudes, are in excellent agreement with the tracer data shown in Chapter 3.

We use two very powerful tools to aid in our interpretation of these simulations. The first is modified Lagrangian mean (MLM) theory (McIntyre, 1980; Nakamura, 1995; 1996). In shallow water MLM theory, a quasi-conserved tracer, in this case PV, is used as the horizontal coordinate (in three dimensions a second tracer, usually potential temperature, is used for the vertical coordinate). MLM diagnostics are thus much more powerful than classical Eulerian mean diagnostics for identifying long-term, irreversible changes in the PV structure of a flow. While Eulerian means can not distinguish, for example, between changes in the PV structure resulting from the action of large-scale eddies versus those resulting from nonconservative processes, MLM diagnostics follow the PV contours themselves, so that any changes in the PV structure in the MLM framework result only from nonconservative processes such as irreversible mixing and diabatic heating (represented in the shallow water model by a mass source). Advection plays no direct role in the MLM framework since it merely acts to move the coordinate system. We also use a related diagnostic tool, the PDF of PV. In Chapter 3, we used equal-area PDFs of the satellite observations of long-lived tracers, in which each observation represents an equal area of the globe so that the frequency is directly related to the area occupied by a certain tracer value, to identify the subtropical edges. Here, we use the equal-mass PDF of PV, which is proportional to the gradient of the MLM mass. We can thus calculate the contributions of the nonconservative processes in the model to the MLM mass budget and interpret the role of these processes in the formation and maintenance of the subtropical edge regions, which are identified by minima in the PDF of PV.

We present results from three simulations, two perpetual solstice simulations and a seasonal cycle simulation. The first perpetual solstice simulation is almost identical to the thermal relaxation simulation of PWP; it uses a Northern Hemisphere winter radiative equilibrium profile and Northern Hemisphere topographic forcing. In the second perpetual solstice simulation, we add topographic forcing in the Southern Hemisphere in order to look at the effects of mixing on the summer subtropical edge. The seasonal cycle experiment has seasonally dependent topographic forcing, so that the forcing is confined to the winter hemisphere.

4.2 The Model

4.2.1 Formulation

We use the same shallow water model as used by PWP and Sobel and Plumb (1999), hereafter referred to as SP, which solves the following dynamical equations for a one-layer incompressible fluid on a sphere:

$$\begin{aligned}
\frac{\partial \zeta}{\partial t} &= -\boldsymbol{\nabla} \cdot (\mathbf{u}\zeta_a) + G \\
\frac{\partial \delta}{\partial t} &= -\frac{1}{2}\nabla^2(\mathbf{u}\cdot\mathbf{u}) + \mathbf{k}\cdot\boldsymbol{\nabla}\times(\mathbf{u}\zeta_a) - g\nabla^2(h+h_B) \\
\frac{\partial h}{\partial t} &= -\boldsymbol{\nabla}\cdot(\mathbf{u}h) + H,
\end{aligned}$$

where ζ is the relative vorticity, ζ_a the absolute vorticity, $\mathbf{u}$ the fluid velocity, G the vorticity forcing, δ the divergence, h the layer thickness, h_B the bottom topography, and H the mass source. As in PWP and SP, H is represented by relaxation to a zonally symmetric "radiative equilibrium" state, $h_r(x)$, over timescale τ_R,

$$H = \tau_R^{-1}[h_r - h],$$

and the vorticity forcing is represented by a sixth order hyperdiffusion,

$$G = \nu\nabla^6\zeta.$$

For all of the simulations shown here, τ_R =10 days and ν =5x10^{26} m^{6}s^{-1}. These are the same values as those used in PWP[1] and for the "low resolution" run of SP. Both PWP and SP found that the large scale flow evolution was largely independent of the hyperdiffusion coefficient, and SP found little difference in quantitative transport rates across the vortex edge when ν was reduced by a factor of 50. The model is initialized with a zonally symmetric flow in gradient wind balance with the initial height field, which has a global mean layer thickness of 8 km. This initial condition, shown in Figure 4-1, is the same as that used by PWP and SP. The model equations are solved using a spectral code at T85 resolution. Details of the code, except the topographic and radiative forcing, may be found in Browning et al. (1989).

4.2.2 Radiative Equilibrium Profiles

The perpetual solstice simulations use a radiative equilibrium height profile that is identical to the one used in the thermal relaxation run shown in Figure 8 of PWP and diagnosed using transport calculations in SP, except that the profile is specified to have the same global mean thickness as the initial height field, so that there is no net mass source. From equation 4.1, it can be shown that for Newtonian cooling, the radiative equilibrium height field is equivalent to $\frac{\Delta(\sigma\theta_r)}{\Delta\theta}$, where σ is the isentropic density and θ_r is the relaxation potential temperature field. Thus, the radiative equilibrium height field, shown in Figure 4-1, mimics the latitudinal profile of $\frac{\partial(\sigma\theta_r)}{\partial\theta}$ that is consistent with the Fels-Schwarzkopf radiative equilibrium temperature distribution in the middle stratosphere during northern winter (with the exception of gradients in the distribution near the equator, which have been eliminated in order to avoid generating a Hadley circulation). This radiative equilibrium temperature distribution can be seen in Figure 1.2 of Andrews et al. (1987).

The seasonal cycle simulation uses the following radiative equilibrium height profile:

$$\begin{aligned} h_r(\varphi,t) &= h_{rNH}\sin\left(\frac{\pi t}{182.5}\right) \qquad 0<t<182.5;\ 365<t<547.5\ days \\ &= h_{rSH}\sin\left(\frac{\pi(t-182.5)}{182.5}\right) \quad 182.5<t<365;\ 547.5<t<730\ days \end{aligned}$$

where h_{rNH} is the same as the profile used in the perpetual solstice simulations and h_{rSH} is

[1] The hyperdiffusion coefficient, ν, was incorrectly given as 1x10^{26}m^{6}s^{-1} in PWP.

its mirror in latitude. Thus, the simulations are initialized with a flat radiative height profile, representing a northern fall equinox. The relaxation profile then evolves so that one-quarter of the way through a 365 day period it is the same as in the perpetual solstice simulation, representing northern winter. The profile continues to evolve through a northern spring and summer, which is exactly opposite to northern winter, and back to the fall equinox. This evolution is then repeated for a second year-long period.

4.2.3 Topographic Forcing

As discussed in Section 4.1, topography is used in the shallow water system to represent the undulation of the bottom of an isentropic layer as planetary-scale waves propagate upward through the stratosphere. The topographic forcing used here is of the same form as in PWP and SP, but we have added the option for topography in the Southern Hemisphere so that the bottom boundary is now given by

$$h_B(\varphi, \lambda, t) = H_B \cos(\lambda)[T_{NH}(t)\Phi_{NH}(\varphi) + T_{SH}(t)\Phi_{SH}(\varphi)]$$

where H_B is a constant amplitude, λ is longitude, $T(t)$ is of the form described below, and $\Phi(\varphi)$ is of the form $\Phi = e^{-[(\varphi-\varphi_0)/\Delta\varphi]^2}$ where φ_0 is the central latitude of the topography in each hemisphere. For the constant forcing runs, in which the topography is introduced gradually and then held constant in either the Northern Hemisphere alone or both the Northern and Southern Hemispheres, the time dependence is:

$$T(t) = 1 - e^{-\frac{t}{\tau}}.$$

For the seasonal forcing run, in which the topographic forcing is present only during the "winter" (actually, fall equinox to spring equinox) in each hemisphere, the time dependence is:

$$\begin{aligned}
T_{NH}(t) &= 1 - e^{\frac{-t}{\tau}} - e^{\frac{t-182.5}{\tau}} \qquad 0 < t < 182.5 \; days \\
&= 0 \qquad\qquad\qquad\qquad 182.5 < t < 365 \; days \\
&= 1 - e^{\frac{-(t-365)}{\tau}} - e^{\frac{(t-547.5)}{\tau}} \qquad 365 < t < 547.5 \; days \\
&= 0 \qquad\qquad\qquad\qquad 547.5 < t < 730 \; days
\end{aligned}$$

$$
\begin{aligned}
T_{SH}(t) &= 0 && 0 < t < 182.5\ days \\
&= 1 - e^{\frac{-(t-182\ 5)}{\tau}} - e^{\frac{(t-365)}{\tau}} && 182.5 < t < 365\ days \\
&= 0 && 365 < t < 547.5\ days \\
&= 1 - e^{\frac{-(t-547.5)}{\tau}} - e^{\frac{(t-730)}{\tau}} && 547.5 < t < 730\ days
\end{aligned}
$$

so that the topography is introduced gradually at the fall equinox, held constant, and then decreased gradually to zero at the spring equinox. In all of the simulations shown here, H_B =1500 m, φ_0 =45^o in the winter hemisphere and 60^o in the summer hemisphere (when topography is present there), $\Delta\varphi$ =14^o, and τ =5 days. These are the same values as used by PWP[2] and SP for their Northern Hemisphere topography. We discuss the choice of φ_0 in the summer hemisphere in Section 4.4.2

4.3 Diagnostics

We examine the flow evolution using MLM diagnostics as in SP and Thuburn and Lagneau (1999) as well as equal-mass PDFs of PV, which are related to the gradient of the MLM mass. In regions where the MLM mass converges with time, PV gradients are irreversibly sharpened, and a local minimum develops in the PDF of PV. These are the "edge" regions, which separate air masses that do not have rapid communication with one another through mixing. The MLM mass budget, which depends only on nonconservative processes (in this case, small-scale mixing by the hyperdiffusion and radiative forcing), can be used to identify the mechanisms that lead to such irreversible PV gradient formation.

4.3.1 Modified Lagrangian Mean Theory

The MLM framework was developed for 3-dimensional flow by Nakamura (1995) and adapted to shallow water flow in SP and Thuburn and Lagneau (1999). Here, we merely summarize the relevant results of these papers. We focus on the MLM mass and use PV as the tracer coordinate.

[2]In PWP, $\Delta\varphi$ was incorrectly listed as 15^o.

In a shallow water model, the mass enclosed by a given PV contour, which we label q, is given by

$$m(q,t) = \iint\limits_{A(q' \geq q,t)} h dA,$$

where h is the layer thickness and the integral is taken over the area where the PV is greater than q. Strictly, this is a volume integral. However, in the context of a shallow water model, we may assume a uniform unit density. Since PV increases northward, the MLM mass is the integrated mass north of the contour, even in the Southern Hemisphere. The mass at a given PV value is summed over all contours with that value so that isolated "blobs" or filaments of PV are included in the mass until they are dissipated nonconservatively. Thus, only irreversible transport is accounted for in the MLM framework.

The evolution equation for $m(q,t)$ can be written

$$\frac{\partial m}{\partial t} = \iint\limits_{A(q' \geq q,t)} H dA - \frac{\partial}{\partial q} \iint\limits_{A(q' \geq q,t)} h\dot{q}' dA,$$

where H is the source term in the shallow water model mass budget and $\dot{q} = \frac{Dq}{Dt}$. The first term on the right hand side is simply the integrated mass source within the PV contour. The second term on the right hand side can also be written as

$$-\frac{\partial}{\partial q} \iint\limits_{A(q' \geq q,t)} h\dot{q}' dA = \oint\limits_{q'=q} h\dot{q}' \frac{dl}{|\boldsymbol{\nabla} q'|},$$

where dl is an infinitesimal segment of the contour q, and $|\boldsymbol{\nabla} q|$ is the magnitude of the local PV gradient. SP addresses the issue of whether or not the line integral remains finite everywhere and shows that, if we assume that ∇q vanishes only at isolated maxima and minima, the contour length will shrink to zero linearly as ∇q does, so that the integral remains finite. This term may also be written as a cross-contour mass flux, $V(q)$,

$$\oint\limits_{q'=q} h\dot{q}' \frac{dl}{|\boldsymbol{\nabla} q|} = V(q) = \oint\limits_{q'=q} h(\mathbf{u} - \mathbf{u}_c) \cdot \mathbf{n}\, dl,$$

where $\mathbf{u}$ is the fluid velocity, $\mathbf{u}_c$ is the velocity of the PV contour, and $\mathbf{n}$ is the outward unit

vector normal to the contour. Thus, the mass enclosed by a given PV contour changes only as a result of either mass sources or sinks within the contour or mass fluxes across the contour due to non-conservation of PV. In this case, where the non-conservative terms of the PV budget are

$$\dot{q} = \frac{G - qH}{h}$$

the mass continuity equation becomes

$$\frac{\partial m}{\partial t} = \oint\limits_{q'=q} G \frac{dl}{|\nabla q'|} - q \oint\limits_{q'=q} H \frac{dl}{|\nabla q'|} + \iint\limits_{A(q' \geq q, t)} H dA$$

where $\oint\limits_{q'=q} G \frac{dl}{|\nabla q'|}$ is the mass flux across the contour due to the hyperdiffusion, $-q \oint\limits_{q'=q} H \frac{dl}{|\nabla q'|}$ is the mass flux due to diabatic processes, and $\iint_{A(q' \geq q, t)} H dA$ is the mass source or sink within the contour. Note that for a tracer other than PV, the mass source/sink term would be identical to that given here, while the mass flux terms would depend on the sources and sinks of that particular tracer. The fact that the diabatic forcing appears in not only the mass source/sink term, but also the mass flux, is a consequence only of the non-conservation of PV in the presence of diabatic heating and cooling.

The MLM mass budget is a non-local budget. It describes the change in the total mass everywhere north of a given q contour. In order to obtain a "local" MLM mass budget, we must consider instead $\frac{\partial(\delta m)}{\partial t}$, where δm is the mass between two q contours spaced δq apart. The mass between the contours changes as a result of convergence or divergence of the mass flux, $V(q)$, or a local mass source or sink, $\iint_{A(q_0 \leq q' \leq q_0 + \delta q, t)} H dA$. For infinitesimally small δq,

$$\frac{\partial}{\partial t}\left(-\frac{\partial m}{\partial q}\right) = -\frac{\partial V}{\partial q} + \oint\limits_{q'=q} H \frac{dl}{|\nabla q'|}$$

so that the gradient of the MLM mass increases or decreases with time (i.e. the mass between PV contours increases or decreases and PV gradients are irreversibly sharpened or weakened) if there is a gradient in the mass flux or a local mass source or sink. The negative sign arises from the fact that the MLM mass decreases northward, while q increases northward.

4.3.2 Probability Distribution Functions

The equal-mass probability distribution function of PV, which has the property that the probability of a range of PV values is proportional to the mass enclosed by the contours in that range, is directly related to the gradient of the MLM mass. The probability of a given PV value, q, that lies between q_0 and $q_0 + \delta q$ is simply proportional to δm,

$$P(q_0 < q < q_0 + \delta q, t) = \frac{\iint_{A(q' \geq q_0, t)} h dA - \iint_{A(q' \leq q_0 + \delta q, t)} h dA}{\iint_{A(q' \geq q_{\min}, t)} h dA} = \frac{\delta m}{m_{tot}}$$

where m_{tot} is the MLM mass contained by the minimum q contour.

4.3.3 Application

To compute the MLM mass budget, we archived the quantities

$$\begin{aligned} m(q,t) &\approx \sum_{q_i \geq q} h_i \Delta A_i \\ \iint_{A(q' \geq q, t)} H dA &\approx \frac{1}{\tau_r} \sum_{q_i \geq q} (h_{ri} - h_i) \Delta A_i \\ -q \oint_{q'=q} H \frac{dl}{|\nabla q|} &\approx \frac{\partial}{\partial q} \frac{1}{\tau_r} \sum_{q_i \geq q} q_i (h_{ri} - h_i) \Delta A_i \end{aligned}$$

every 24 hours for 64 values of PV in the perpetual solstice simulations and 87 values of PV in the seasonal cycle simulations. We computed the area integrals by simply counting the grid boxes where PV is greater than the bin value. The hyperdiffusion term, $\oint_{q'=q} G \frac{dl}{|\nabla q'|}$, was calculated as the residual of the mass budget since it contains contributions due to numerical mixing. Both SP and Thuburn and Lagneau (1999) found that this method was the most reliable for determining the hyperdiffusion term. The equal-mass PDFs of PV were produced for these experiments by calculating $(m(q,t)_{n+1} - m(q,t)_n)/m_{tot}$ for each of the PV bins and assigning that value to the midpoint of the bin.

4.4 Perpetual Solstice Simulations

4.4.1 Northern Hemisphere Constant Topographic Forcing

This simulation is almost identical to the thermal relaxation simulation of PWP, which was then used by SP as their "low resolution" simulation to test transport rate calculations. The only differences are that the radiative equilibrium height profile is specified to have the same global mean thickness as the initial condition, so that there is no net mass source, and that the simulation is run for 170 days rather than 100 days in PWP and 150 days in SP. PWP focused on the formation of the surf zone and the subsequent tightening of PV gradients in the winter subtropics and at the vortex edge using zonal mean diagnostics and contour advection, and SP looked at transport rates across the vortex edge based on the hyperdiffusion term of the MLM mass budget as well as an algorithm called "local gradient reversal". Here, we investigate the balance of forces that form and maintain PV structures in both the winter and the summer hemisphere using the MLM mass budget as well as equal-mass PDFs of PV. Since H represents the effects of diabatic processes on the mass in an isentropic layer, we refer to $H > 0$ as radiative heating and $H < 0$ as radiative cooling throughout the discussion[3].

Formation of PV structures

Figure 4-2 shows the evolution of PV during the simulation, and Figure 4-3 shows the evolution of the zonal mean zonal wind, the zonal mean layer thickness, and the zonal mean potential vorticity. We focus first on the first 60 days of the run. The Northern Hemisphere surf zone forms by day 20 of the simulation, as seen in Figure 4-2, and the stirring in the surf zone leads to PV homogenization in the midlatitudes and enhanced zonal mean PV gradients in the Northern subtropics and at the vortex edge, as seen in Figure 4-3 c). The zonal mean PV gradient in the Southern subtropics also increases during the first 60 days of the simulation, despite the fact that the Southern Hemisphere PV contours remain largely zonally symmetric. The high latitudes of both hemispheres approach radiative equilibrium, as seen in Figure 4-3

[3] As discussed in Section 4.1, H is actually analagous to the vertical gradient of the mass-weighted diabatic heating in isentropic coordinates. However, given the vertical structure of the diabatic mass flux, regions of diabatic heating are generally regions of vertical mass convergence, while regions of diabatic cooling are generally regions of vertical mass divergence.

b), which is accompanied by an acceleration of the westerly jet in the Northern high latitudes and a deceleration of the easterlies in the Southern high latitudes, as seen in Figure 4-3 a). The dissipation of small-scale filaments in the surf zone and the diabatic heating and cooling produce mass transport across the PV contours, as required by the MLM mass budget. The balance between this mass transport and the diabatic mass source/sink results in the formation of four air masses, where PV is homogenized, separated by three "edge regions", where PV gradients are tightened. While these changes in the PV structure can be seen in the zonal mean PV in Figure 4-3 c), it is impossible to say whether the zonal mean reflects long-term, irreversible changes in the PV field. However, these PV features are clearly visible in Figure 4-4, which shows the MLM mass as a function of time, as well as Figure 4-5, which shows the evolution of the PDF of PV. The air masses and edge regions, which develop during the first 60 days of the simulation and then evolve slowly over the next 110 days, are labeled in the final frame of Figure 4-5.

We are interested in the balances between the mass transport and the mass sources and sinks that result in increased mass in the vortex, surf zone, tropics, and summer polar region and decreased mass in the vortex edge and the winter and summer subtropics. Figure 4-6 a) shows the equal-mass PDF of PV on day 60 of the simulation, with each of the edges and the air masses labeled. Figure 4-6 b) shows the mass tendency, $\frac{\partial m}{\partial t}$, the mass flux across the PV contours, $\oint\limits_{q'=q} h(\mathbf{u}-\mathbf{u}_c)\cdot\mathbf{n}\,dl$, and the integrated mass source within the PV contours, $\iint_{A(q'\geq q,t)} H dA$, averaged over the first 60 days of the simulation and plotted as a function of PV. Figure 4-6 c) shows the mass flux divided into its two components: the diabatic mass flux, $-q\oint\limits_{q'=q} H\frac{dl}{|\nabla q'|}$, and the hyperdiffusive mass flux, $\oint\limits_{q'=q} G\frac{dl}{|\nabla q'|}$. Figures 4-6 d) and e) show the gradient of the mass tendency, the mass flux, and the mass source with respect to PV, so that we can investigate the local mass budget in each region. Figure 4-7 is a schematic which summarizes the information in Figure 4-6.

A detailed examination of Figure 4-6 is left to the reader, and we concentrate on the schematic representation in Figure 4-7. In the summer subtropics, there is a strong divergence of the diabatic mass flux, and only a very weak net mass source. Thus, the mass between PV contours, δm, decreases over the first 60 days of the simulation in this region, leading to an irreversible increase in the PV gradient and a minimum in the PDF of PV. This is the summer

subtropical edge. It is formed simply because there is diabatic cooling at high latitudes, which acts to decrease PV values there, and diabatic heating in the tropics, which acts to increase PV values there. The diabatic forcing thus leads to mass transport out of the subtropical PV contours and into the tropics and high latitudes. In both the tropics and the summer high latitudes, the diabatic mass flux converges. In the high latitudes, this convergence of the mass flux is not balanced by the weak mass sink, while in the tropics, it is augmented by the strong mass source. Thus, δm in the high latitudes increases slightly over the first sixty days of the simulation, while δm in the tropics increases greatly. In the winter subtropics, the mass flux is divergent; there is a large hyperdiffusive mass flux across the PV contours on the surf zone side of the winter subtropics. This hyperdiffusive mass flux results from transport of air out of the subtropics by the large-scale stirring in the surf zone and the subsequent cascade of transported filaments to small scales, which leads to their eventual elimination by the hyperdiffusion. The divergence of the mass flux in the winter subtropics completely overwhelms the mass source there, and the PV gradient increases rapidly. There is a net transport of mass into the surf zone by the hyperdiffusive mass flux from both the winter subtropical edge and the outer vortex edge. The details of the balance between the hyperdiffusive mass flux and the diabatic mass flux within the surf zone are quite interesting, but are not addressed here. We note only that despite the fact that there is net transport of mass out of the surf zone and into the vortex edge due to the diabatic forcing, the net mass flux, i.e. the sum of the hyperdiffusive and diabatic contributions, is convergent throughout the surf zone. This net convergence is not balanced by the mass sink in the surf zone, and δm in the surf zone increases with time. At the outer vortex edge, the outward hyperdiffusive mass flux is somewhat balanced by the inward diabatic mass flux. The diabatic mass flux gradually increases toward the pole, while the hyperdiffusive mass flux is non-zero only at the outer vortex edge. Thus, the total mass flux is divergent in the vortex edge region, and it is augmented by the weak mass sink there, so that δm decreases and the minimum in the PDF at the vortex edge deepens. The diabatic mass flux converges near the winter pole, so that δm increases and the vortex air mass grows with time.

In regions where there is no hyperdiffusive mass flux and the PV evolution depends only on the diabatic forcing (the entire summer hemisphere as well as the tropical and vortex air masses), the flow evolves slowly and smoothly, with gradual convergence and divergence of the

PV contours (see Figure 4-4 as well as Figure 4-5). In regions where the hyperdiffusive mass flux dominates the PV evolution (the winter subtropics, surf zone, and vortex edge), however, the flow evolves much more rapidly during this period of the simulation. In fact, as seen in Figure 4-4 and Figure 4-5, the winter subtropical edge, surf zone, and vortex edge are initially formed in a single large mixing event between day 15 and day 20 of the simulation. In the subtropics during this time period, a very narrow structure forms in the .25x10^{-8}m^{-1}s^{-1} PV contour, which is on the flank of a developing "cat's eye" in the midlatitudes. What remains of this structure on day 20 can be seen in the first frame of Figure 4-2. Figure 4-5 shows that between days 15 and 20, mass is lost at PV values between about .1x10^{-8}m^{-1}s^{-1} and .4x10^{-8}m^{-1}s^{-1} and gained between about .4x10^{-8}m^{-1}s^{-1} and .6x10^{-8}m^{-1}s^{-1}, indicating that air from the narrow feature has been irreversibly mixed into the anticyclone. In fact, a more detailed look at the evolution between day 15 and day 20 (not shown here) reveals that a large filament is cut off from the .25x10^{-8}m^{-1}s^{-1} contour on day 19 and is mixed down in the surf zone by day 20. In a single large event, the initial winter subtropical air mass is split into a tropical air mass and a surf zone air mass. The vortex edge also develops quite rapidly between days 15 and 20. Unlike the subtropics, the simulation is initialized with a strong PV gradient in the winter polar region. However, that gradient is not a mixing barrier in the sense that it separates two air masses until day 20, when mass is lost from about 1.2x10^{-8}m^{-1}s^{-1} to 1.7x10^{-8}m^{-1}s^{-1} and is gained at about 1.0x10^{-8}m^{-1}s^{-1}, resulting in a small minimum, the vortex edge, in the PDF. Figure 4-2 shows that air between the 1.25x10^{-8}m^{-1}s^{-1} and 1.75x10^{-8}m^{-1}s^{-1} contours is wrapped around an anticyclone on day 20, and more detailed analysis again shows a cut-off filament which is mixed into the surf zone. Notice also that in Figure 4-10, which shows the mass budget for individual contours, there is a large spike in the mass flux due to hyperdiffusion at contour 25 in the subtropics and contour 31 in the vortex edge during these five days.

Mechanisms maintaining PV structures

We focus now on days 100 to 170 of the simulation. As seen in Figure 4-2, the surf zone is active throughout this period and remains confined to the winter midlatitudes. PWP showed that this confinement is largely a consequence of the acceleration of the westerly jet by the diabatic forcing, which results in the formation of few transient waves that are capable of penetrating

the tropical easterlies. Note, however, that the periodic deformations of the PV contours in the subtropics that result from wave breaking events now extend all the way across the subtropical PV gradient. We shall show below that air is being transported out of the tropics and into the surf zone. The tropics, winter subtropics, and the surf zone are still far from radiative equilibrium, as seen in Figure 4-3 c). As in the real stratosphere, the wave breaking in the surf zone continually drives the flow away from radiative equilibrium, which results in a stress-driven circulation (of course, unlike the real stratosphere, there is no vertical velocity associated with the diabatic heating and cooling in the model). However, the departure from radiative equilibrium extends into the summer subtropics, where as we shall see, there is no wave-induced stress. It is possible that this extensive departure from radiative equilibrium results from the interaction of a Hadley cell-type circulation with the stress-induced circulation. However, this is beyond the scope of the current investigation.

Figure 4-8 shows the same information as Figure 4-6, but the PDF shown is for day 150 of the simulation, and the terms of the mass budget are averaged over days 100 to 170. A comparison between Figures 4-8 b) and 4-6 b) shows that the simulation is much closer to steady state during this period than during the first 60 days, but the departures from steady state are not negligible in the tropics, winter subtropics, and surf zone. However, it is clear from Figures 4-3 and 4-5 that the flow is evolving very slowly. Figure 4-9 is a schematic of the information contained in Figure 4-8. As seen in Figure 4-9, the mass source/sink is now near-zero in the summer high latitudes and summer subtropical edge as well as in the vortex and vortex edge, since these regions are close to radiative equilibrium. In the summer subtropics, there is still a weak divergence of the diabatic mass flux, so that mass is transported out of the subtropics and the PV gradient continues to slowly increase. The mass flux into the summer pole is much weaker than at the beginning of the simulation, and the local MLM mass tendency there is very small. As discussed above, the hyperdiffusive mass flux into the surf zone now penetrates all the way into the tropics, so that the mass flux is now divergent in the tropics, the outward hyperdiffusive flux on the winter side of the tropics being larger than the inward diabatic flux on the summer side of the tropics. However, the mass source is still larger than the divergence of the mass flux, so that δm in the tropics continues to increase. Inspection of Figures 4-8 d) and e) shows that, as discussed above, the diabatic heating in the tropics

extends into the summer subtropics, while the hyperdiffusive mass flux that results from the wave breaking only reaches into the winter side of the tropics. We leave this for future study. In the winter subtropical edge, the divergence of the hyperdiffusive mass flux is nearly balanced by the mass source, and δm is almost steady. The winter edge is thus maintained by a balance between the mass transport into the surf zone and the tropical mass source. In the surf zone, the net mass flux is still convergent. However, inspection of Figure 4-8 d) reveals that the maximum convergence of the mass flux is at higher PV values than the maximum of the mass sink, so that the net mass tendency is actually negative for the lower PV values in the surf zone. Thus, it seems likely that the peak in the PV PDF corresponding to the surf zone air mass will continue to shift toward slightly higher PV values as more and more mass is mixed into the surf zone and the PV contours are packed into the subtropics. At the outer vortex edge, the inward diabatic mass flux is slightly larger than the outward hyperdiffusive mass flux, so that there is a small net mass flux into the vortex edge. However, this mass flux is almost exactly balanced by the small mass sink term, so that δm is almost steady. Figure 4-8 e) shows that in the vortex, there is a small positive mass tendency, which comes from the convergence of the hyperdiffusive mass flux. It is not clear whether this is a real feature. SP's results do not agree exactly with ours in the vortex, probably because they use a finer grid resolution in calculating their mass budgets. There is no evidence of filamentation in the vortex, so that if this is a real feature, it probably results from the hyperdiffusion acting on the strong PV gradient in the vortex edge.

In Chapter 3, we showed that there is excellent agreement between the central latitude of the subtropical edge and the zero zonal wind line during winter. The equivalent of the zonal wind in the MLM formalism is the relative circulation along PV contours, $\oint_{q'=q} \mathbf{u} \cdot \, dl$. Figure 4-11 shows the evolution of the relative circulation as well as the diabatic heating and cooling along the PV contours, $\oint_{q'=q} H dl$, throughout the simulation. The approximate minimum and maximum values of PV in the summer and winter subtropical edges are also shown. It is striking that the circulation vanishes within the winter subtropical edge. Under linear scaling, this would imply that the zero zonal wind line lies within the subtropical edge, in agreement with the results of Chapter 3, as well as Waugh (1996), who demonstrated that the onset of isentropic transport out of the tropics coincides strongly with the appearance of the zero zonal wind line

at the beginning of winter, and Haynes and Shuckburgh (2000), who showed that the tropical minimum in effective diffusivity coincides with the zero zonal wind line. However, this is in sharp contrast to studies of nonlinear critical layers such as Stewartson (1978) and Warn and Warn (1978), in which the critical layer straddles the zero zonal wind line, as well as the work of Plumb and Mahlman (1987) which showed that in a general circulation model with weak eddy amplitudes, the maximum eddy diffusivity lies along the zero zonal wind line. Figure 4-3 shows that on days 60 and 170 of the simulation, the zonal mean zonal wind actually vanishes at the latitude of the transition between the enhanced subtropical zonal mean PV gradient and the relatively weak surf zone gradient, rather than near the center of the subtropical edge. In fact, at other times during the simulation, the zero zonal wind line drifts poleward toward the center of the surf zone, though it always eventually returns to the subtropical edge. It is perhaps because of this asymmetry that, unlike the vortex edge, the entire winter subtropical edge acts as an entrainment zone in this simulation, with persistent episodic mass transport out of the tropics and into the surf zone. In contrast, the vortex is highly isolated from the surf zone in the model, with episodic transport occurring mainly along the outer flank of the vortex edge. Figure 4-11 b) shows that the winter subtropical edge lies entirely within the diabatic heating region, so that the mass that is lost through transport into the surf zone is replenished by the diabatic source.

As discussed above and shown in Figure 4-11 b), the summer subtropical edge is gradually formed and then maintained by the divergence of the diabatic mass flux in the summer subtropics. As the summer polar region approaches radiative equilibrium, the mass flux toward the pole decreases, and the PV gradient is sharpened mainly from the equatorward side by the equatorward mass flux which results from the diabatic heating in the tropics. It is interesting to note that the summer polar region is subject to the same mass balance as the winter vortex, and that in both cases the convergence of the diabatic mass flux at the pole and the adjustment toward radiative equilibrium sharpen the PV gradients of their respective edge regions from the poleward side. Figure 4-10 shows that the MLM mass budget at contour 55, on the poleward side of the vortex edge, is almost identical to the mass budget at contour 3, on the poleward side of the summer subtropical edge. Clearly, if the summer subtropical edge is formed purely by diabatic processes as it is in this simulation, the summer edge can only be considered a

mixing barrier in the sense that there is no communication between the tropical and summer high latitude air masses. However, we will show below that if we force stationary waves in the summer hemisphere, they effectively mix material, and that the summer subtropical edge acts as an efficient barrier to this mixing.

4.4.2 Northern and Southern Hemisphere Constant Topographic Forcing

Since the zonal mean zonal wind in the Southern Hemisphere is actually westerly (though very weakly so) from about 45^o S to the South pole in the simulation discussed above, one may ask what would happen if stationary waves were to propagate in the summer hemisphere. There is, in fact, evidence of mixing by large-scale waves in the summer midlatitudes of the lower stratosphere (Wagner and Bowman, 1999; Haynes and Shuckburgh, 2000), so that the behavior of the summer subtropical edge under these conditions is of considerable interest. This simulation examines the effects of mixing in the summer hemisphere through the addition of topography that is of the same form and amplitude as that in the winter hemisphere. However, as noted in Section 4.2.3, the summer hemisphere mountain is centered at 60^o South, rather than at 45^o as in the winter hemisphere. We have chosen this latitude because it is located within, rather than at the edge of, the Southern Hemisphere westerlies in the previous simulation and because Haynes and Shuckburgh (2000) showed that where there is considerable summer mixing (below about 500 K), the maximum stretching rates are located at a higher latitude in the summer hemisphere than in the winter hemisphere. This evidence of high-latitude mixing is also consistent with tracer observations in the lower stratosphere, which show very flat tracer gradients in the summer hemisphere poleward of about 50^o.

Formation of PV structures

Figure 4-12 shows the evolution of PV during the simulation, and Figure 4-13 shows the evolution of the zonal mean zonal wind, surface height, and PV. The flow in the winter hemisphere is very similar to the previous simulation, and will not be discussed here. However, we do note that the fact that the winter hemisphere flow is mostly unchanged despite large differences in the summer hemisphere flow indicates that the hemispheres exert minimal influence on each other. Figure 4-12 shows evidence of stirring in the high Southern latitudes, accompanied by

the occasional formation of small-scale PV features (note that the contour interval has been increased from that in Figure 4-2 so that these small scale features are visible). The summer subtropical PV gradient is now considerably stronger than in the previous case, though the range of PV within the gradient is nearly the same. Figure 4-13 shows that the PV gradient has been sharpened almost exclusively from the poleward side, i.e. the transition between the tropics and the subtropical edge occurs at the same latitude as in the non-mixing case, while that between the subtropical edge and the high latitude air mass occurs considerably further equatorward. The evolution of the zonal mean surface height is also strikingly different from the previous simulation; the mixing prevents the Southern high latitudes from approaching radiative equilibrium, as can be seen in Figure 4-13 b). Figures 4-14 and 4-15, the MLM mass and the evolution of the PDF of PV, show that the summer subtropical edge contains considerably less mass, and the high latitude air mass contains considerably more mass, than in the simulation without summer mixing.

Figure 4-16 a) shows the equal-mass PDF of PV on day 60 of the simulation, with each of the edges and the air masses labeled. Figure 4-16 b) shows the mass tendency, the mass flux across the PV contours, and the integrated mass source within the PV contours averaged over the first 60 days of the simulation and plotted as a function of PV. Figure 4-16 c) shows the mass flux divided into its two components: the diabatic mass flux and the hyperdiffusive mass flux, and Figures 4-6 d) and e) show the gradient of the mass tendency, the mass flux, and the mass source with respect to PV. A comparison of Figure 4-16 and Figure 4-6 shows that the first 60 days of this simulation are quite similar to the previous simulation. The divergence of the diabatic mass flux is still the primary mechanism behind the formation of the summer subtropical edge, and the hyperdiffusive flux plays only a secondary role. In fact, during this early stage, the hyperdiffusive flux actually opposes the tendency of the diabatic flux to increase the mass in the summer high latitudes. The hyperdiffusive flux is instead convergent at the boundary between the summer subtropical edge and the summer mixed zone, and we shall see that the summer subtropical edge eventually shifts toward slightly higher PV values. The convergence of the diabatic mass flux in the summer high latitudes is stronger in this simulation because the diabatic forcing acts on the layer thickness, rather than the free surface height. The zonal mean height of the mountain is zero, so that the zonal mean forcing is the same as in the

previous case, but since the PV contours are not zonally symmetric, they experience stronger diabatic forcing in the region of the "peak" of the topography. The fact that the hyperdiffusion plays only a minor role during the initial 60 days of the simulation is also evident in Figure 4-15, which shows that the summer subtropical edge and summer polar air mass develop gradually, rather than in a rapid mixing event like the winter subtropical edge and the surf zone.

Mechanisms maintaining PV structures

Figure 4-17 shows the same information as Figure 4-16, but the PDF shown is for day 150 of the simulation, and the mass budget terms are averaged over days 100 to 170. In contrast to Figure 4-8, both the mass source/sink term and the diabatic mass flux are still quite large in the summer hemisphere since, as discussed above, the mixing prevents adjustment toward radiative equilibrium. As in the vortex edge, and in strong contrast to the winter subtropical edge, the diabatic mass flux nearly balances the hyperdiffusive mass flux in the summer subtropical edge, though in this case they are both divergent in the edge region, so that the mixing in the summer hemisphere tightens the subtropical PV gradient both by erosion of material into the mixed region and by preventing adjustment to radiative equilibrium, thereby allowing the divergence of the diabatic mass flux to remain large throughout the simulation.

Figure 4-18 shows the evolution of the relative circulation and the diabatic heating and cooling along the PV contours for this simulation, as well as the minimum and maximum PV values of the summer and winter subtropical edges. Both edges are located in a region of zero circulation (though the westerly circulation in the summer hemisphere is obviously very weak). The contrast between Figure 4-18 b) and Figure 4-11 b) is striking; as discussed above, the radiative forcing on the contours South of the summer subtropical edge persists throughout the simulation in this case.

The result that the divergence of the diabatic mass flux plays a key role in the formation and maintenance of the summer subtropical edge even in the presence of mixing indicates that the summer edge is very different from the winter subtropical edge, where the diabatic mass flux plays a relatively minor role. This is also evidenced by the fact that the summer subtropical edge is sharpened by the stirring of the mixed zone, but is inherently the same edge as in the radiative forcing-only case. In fact, we have also run a simulation with the topography

centered at 45^o in the Southern Hemisphere, and the subtropical edge in that case forms in the same latitude band as it does here, indicating that the radiative forcing, and not the mixing, ultimately determines the position of the edge. This is not the case for the winter subtropical edge. In a simulation (not shown here) without topography in either hemisphere, both the summer edge and a single, broad winter hemisphere edge are formed. The winter hemisphere edge is located between 35^o and 50^o, far poleward of the winter subtropical edge that forms in the presence of stirring.

4.5 Seasonal Cycle simulation

In the seasonal cycle simulation, the radiative equilibrium height profile is varied throughout a 365 day time period in order to mimic the seasonal cycle in radiative forcing and the topography is modulated by the seasonal time dependence described in section 4.2.3, so that waves are forced in each hemisphere only from the fall equinox to the spring equinox. The simulation is initialized with the same initial height field as the perpetual solstice simulations and is run for two years, so that there are two Northern Hemisphere and two Southern Hemisphere winters. As we shall see in Figure 4-20 and Figure 4-22, the initial condition influences only the first 50 days or so of the simulation. Since the forcing is symmetric, the evolution of the third and fourth winter periods are identical to that of the second (Southern Hemisphere) winter.

Figure 4-19 shows the evolution of PV during the first year of the simulation, Figure 4-20 shows the evolution of the MLM mass over the full two year period, and Figure 4-21 shows the evolution of the PDF of PV during the first year. During each half-year (equinox to equinox), the flow develops the same PV structures as in the perpetual solstice simulation discussed in Section 4.4.1: the vortex, surf zone, tropical, and summer polar air masses separated from one another by the vortex and winter and summer subtropical edges; these are labeled in Figure 4-21.

The initial evolution in the winter (Northern) hemisphere is only slightly different than in the perpetual solstice simulation. Figure 4-21 shows that the mass of the polar vortex begins to increase before the first mixing event which leads to the formation of the surf zone. In addition, the surf zone air mass is formed more slowly than in the perpetual solstice simulations; air

that is mixed out of the tropics and the vortex slowly merges into a single air mass. The summer (Southern) hemisphere initially evolves in much the same way as the perpetual solstice simulation, though the summer polar air mass is formed more slowly, as we expect given that the radiative forcing is weaker than in the perpetual solstice simulation except at the solstice itself. During each half-year thereafter, the winter side of the PDF evolves quite rapidly after the equinox. This can be seen in the transition to Southern Hemisphere winter in Figure 4-21, where air is mixed out of the polar and tropical air masses and by day 250 has merged into the surf zone. On the summer side, there is a rapid change at high latitudes as the vortex "breaks down" (compare day 190 and day 200 in Figure 4-21), and then the tropical air mass slowly pushes northward until it merges with air that was in the surf zone during the winter. The subtropical edge then forms where the tropical and polar air masses meet. Interestingly, it is not remnants of the winter subtropical edge that form the summer subtropical edge. Rather, the summer subtropical edge is made up mostly of potential vorticity values that were formerly in the surf zone air and the vortex edge. This is most clear in Figure 4-20, which shows that a PV contour that was in the surf zone during the winter becomes the meeting point for tropical and polar air in the summer, i.e., the center of the subtropical edge, and that the vortex edge maintains a strong gradient as it moves southward, while the subtropical edge is spread out into the tropics. If this is true in the real stratosphere, then the transition from winter to summer may represent a very significant mechanism for transport of midlatitude air into the tropics.

Figures 4-22 a) and b) show the circulation and the diabatic forcing along the PV contours over the two year period, as well as the range of PV values that comprise the bulk of each subtropical edge during each season. Comparison to Figure 4-11 shows that the mechanisms behind the formation of the subtropical edges are basically the same as those in the perpetual solstice simulation, if we consider the average effect of the surf zone mixing and the diabatic heating and cooling over each season. The circulation is, on average, zero within the winter subtropical edge and there is diabatic heating on average throughout the edge, as is the case in the perpetual solstice simulation. During the initial summer period, there is diabatic cooling at the pole and throughout the subtropical edge during early and late summer, and diabatic heating in the tropics and throughout much of the edge during mid-summer, so that there is a net divergence of the diabatic mass flux in the subtropical edge over the season. The subsequent

summers are somewhat different, since there is strong heating in the high latitudes during early summer, as the vortex "warms up" and the westerly jet decelerates. The polar region does not experience diabatic cooling until after the solstice, when the radiative equilibrium height begins decreasing and the polar region, which has warmed to near-radiative equilibrium, suddenly becomes warmer than equilibrium. Thus, there is a net divergence of the diabatic mass flux only from the solstice to the equinox. Figures 4-20 and 4-21 show that the summer subtropical edge does, in fact, develop mostly during this solstice to equinox period.

4.6 Discussion

We have shown that in a shallow water model with radiative relaxation, it is possible to form not only a strong PV gradient on the subtropical flank of the surf zone, but also an enhanced summer subtropical PV gradient that is generated by the radiative forcing alone. The summer edge is not, as often proposed, simply the remnant of the winter subtropical edge. It is formed in the perpetual solstice simulations, which are initialized without a strong PV gradient in the summer subtropics. Even in seasonal cycle simulation, where the summer season begins with the winter subtropical edge still intact, the summer edge forms mainly from surf zone and vortex edge air, with the winter subtropical edge air being absorbed into the tropical air mass as the diabatic heating region shifts into the summer hemisphere. Despite the fact that the summer edge can form in the absence of mixing, we have shown that it is eroded and sharpened by mixing much like the winter edge, even though the divergence of the diabatic mass flux still plays a crucial role in the edge formation and maintenance. Mixing can act to sharpen the summer edge in toward the tropics, but the edge position is ultimately determined by the latitude of the transition between the diabatic heating in the tropics and diabatic cooling at the pole. However, the relationship between the edge position and the diabatic forcing is more complicated in the seasonal cycle simulation, when it is the net forcing over the season that matters, and we cannot simply expect to find the summer edge at the edge of the tropical upwelling region throughout the summer.

The winter subtropical edge is inherently different from the summer subtropical edge. It is rapidly formed at the onset of winter as the surf zone becomes active. It is then maintained

by a balance between the transport of air into the surf zone and the diabatic mass source in the tropics. The zero wind line lies near or within the winter subtropical edge, and the entire edge acts as an entrainment zone, often being deformed into small scale features which are then wrapped around and irreversibly mixed into the anticyclones of the surf zone. PWP showed that the winter subtropical edge can form in the absence of diabatic forcing, as long as the difference between the midlatitude and tropical winds is sufficiently large. This, along with our result that in the absence of mixing, the winter edge would be quite broad and located much further poleward than it is in these simulations, indicates that it is the mixing of the surf zone that is the crucial mechanism in the winter edge formation. We do note, however, that the diabatic forcing prevents the edge from being eroded completely, as it eventually balances the mass flux out of the edge by providing a constant supply of mass.

We must, of course, be mindful of the inherent limitations of single-layer models when interpreting our results in the context of the real stratosphere. The two limitations likely to be most relevant here are the lack of tropical dynamics, particularly the quasi-biennial oscillation (QBO), and the differences between our thermal relaxation and real diabatic heating and cooling. There is evidence that the QBO modulates transport rates between the tropics and midlatitudes (O'Sullivan and Dunkerton, 1998; Shuckburgh et al., 2000), and we showed in Chapter 3 that it has some effect on the position of the subtropical edges in the middle stratosphere. Thus, our results are most applicable to the easterly phase of the QBO, given our initial wind profile. Since our results indicate that the formation and maintenance of the summer edge depends critically on the radiative forcing, our biggest concern is with the relationship of this forcing to real diabatic heating. As discussed in Section 4.1, for a thin isentropic layer, H is analogous to $-\frac{\partial(\sigma Q)}{\partial\theta}$, where $\sigma = -\frac{1}{g}\frac{\partial p}{\partial\theta}$ is the isentropic density and Q is the heating rate. The isentropic PV equation is

$$\frac{DP}{Dt} = \frac{1}{\sigma}\left[\frac{\partial \mathbf{u}}{\partial\theta}\cdot\nabla_H Q\right] - Q\frac{\partial P}{\partial\theta} + P\frac{\partial Q}{\partial\theta} + \frac{1}{\sigma}\mathbf{k}\cdot\boldsymbol{\nabla}_H\times\mathcal{F}$$

where $P = \frac{\zeta+f}{\sigma}$ is the isentropic potential vorticity and $\mathcal{F}$ represents the body force terms. For

vertically coherent flow, this reduces to

$$\frac{DP}{Dt} = \frac{P}{\sigma}\frac{\partial}{\partial\theta}(\sigma Q) + \frac{1}{\sigma}\mathbf{k}\cdot\boldsymbol{\nabla}_H \times \mathcal{F},$$

so that the shallow water PV is forced by H in the same way as the isentropic PV is forced by $-\frac{\partial(\sigma Q)}{\partial\theta}$ under these assumptions. Thus, we realistically represent the effects of diabatic processes on the PV distribution in an isentropic layer to the extent that the layer is thin enough that the static stability is constant across it, the flow is vertically coherent within the layer, and our choice of h_r realistically mimics the latitudinal distribution of the convergence of the mass-weighted radiative equilibrium potential temperature field.

A related issue is whether or not the processes that lead to the formation of PV gradients also lead to the formation of gradients in chemical tracers. Numerous studies (e.g. Juckes, 1989; Grose et al., 1987; Norton, 1994) have shown that in shallow water models, passive tracers form strong gradients that coincide with the enhanced PV gradients at the subtropical and vortex edges of the winter hemisphere surf zone. This is not surprising, since the winter hemisphere is dominated by mixing, which erodes and sharpens tracer gradients in the same way as PV gradients. In the summer hemisphere, however, the situation is more complicated. Since diabatic heating and cooling affect tracers in a fundamentally different way than PV, it is unclear whether formation of a PV gradient by radiative processes necessarily implies the formation of a tracer gradient. The diabatic circulation advects tracers through isentropic surfaces, so that the effect of this circulation on tracer gradients will depend on the vertical structure of the tracer as well as the vertical structure of the mass flux, since H in our model implies only a convergent or divergent mass flux. Figures 4-23 a) and 4-23 b) are schematic representations of the residual circulation through an isentropic layer in the middle stratosphere (above about 40 mb) during early and late summer, respectively (see Eluszkiewicz et al. (1996) for a discussion of the seasonal evolution of the residual circulation). Since $\partial(\sigma Q)/\partial\theta$ decreases with height, the vertical mass flux in the tropics is always convergent, while in the extratropics the vertical mass flux is convergent in early summer and divergent in late summer, consistent with the pattern of H. For a tracer with a tropospheric source and stratospheric sink, so that the mixing ratio falls off with height, the early summer circulation will act to increase the

extratropical tracer mixing ratio, particularly near the pole, while the late summer circulation will act to decrease the mixing ratio, thus maintaining a gradient between the tropics and extratropics. This behavior is, in fact, observed in the N_2O measurements from the CLAES instrument. Figure 4-24 shows the CLAES N_2O measurements in the Southern Hemisphere at 4.6 mb for the viewing periods between August 17, 1992, and April 14, 1993. Figure 4-25 shows the PDFs of the data for the southern-viewing yaw periods. Between the August 17 to September 16, 1992, viewing period and the November 2 to November 25, 1992, viewing period, the high-latitude tracer values increase, and the vortex and surf zone peaks of the PDF merge into a single peak. Note that this time frame falls between the equinox and the solstice. By the January 13 to February 5, 1993, viewing period, after the solstice, the high-latitude tracer values have decreased, and the edge has become "summer-like". The PDF shows that the summer edge now has tracer values typical of a portion of the surf zone/vortex peak from the previous period. This is extremely consistent with the results of the shallow water model seasonal cycle simulation. As was seen in Figure 4-22, the mass source/sink term acts as a mass source in the high latitudes between the spring equinox and the summer solstice in this simulation, which is consistent with the convergent vertical mass flux implied by the increase in mixing ratio at high latitudes during this time in Figures 4-24 and 4-25. After the solstice, there is a weak mass sink at high latitudes, consistent with the weak divergent mass flux implied by the gradual decrease in high latitude mixing ratios during this time in Figures 4-24 and 4-25. Finally, while there is some overlap in the data between the mixing ratios of the winter edge and those of the summer edge, the summer edge is largely composed of mixing ratios that were typical of the surf zone during winter, and the tropical air is partially composed of mixing ratios that were typical of the winter subtropical edge, which is consistent with the potential vorticity distributions in the shallow water model simulation. As additional evidence that the diabatic circulation can, in fact, produce enhanced tracer gradients in the summer subtropics, we showed in Chapter 3 that advecting a passive tracer with the observed residual circulation results in tracer gradients in the summer hemisphere that are broadly consistent with observed tracer gradients. It seems likely, then, that mixing via Rossby wave breaking is the dominant mechanism behind the formation of the winter subtropical edge, while the residual circulation, which is related to diabatic heating and cooling, plays a major role in the formation of the

summer subtropical edge. However, we note that the residual circulation is, in part, wave-driven, so that the two processes should not be thought of completely independently of one another.

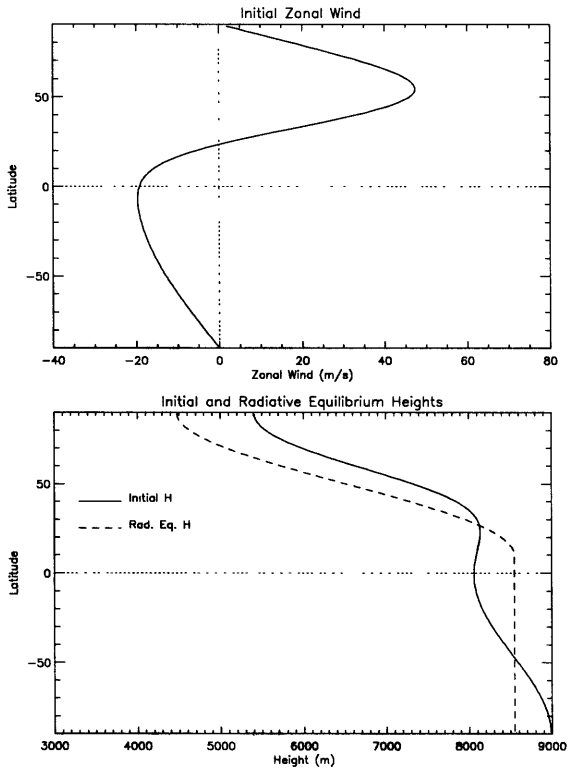

Figure 4-1: The initial zonal wind and height profiles (solid lines) as well as the radiative equilibrium height profile (dashed line) for the perpetual solstice simulations.

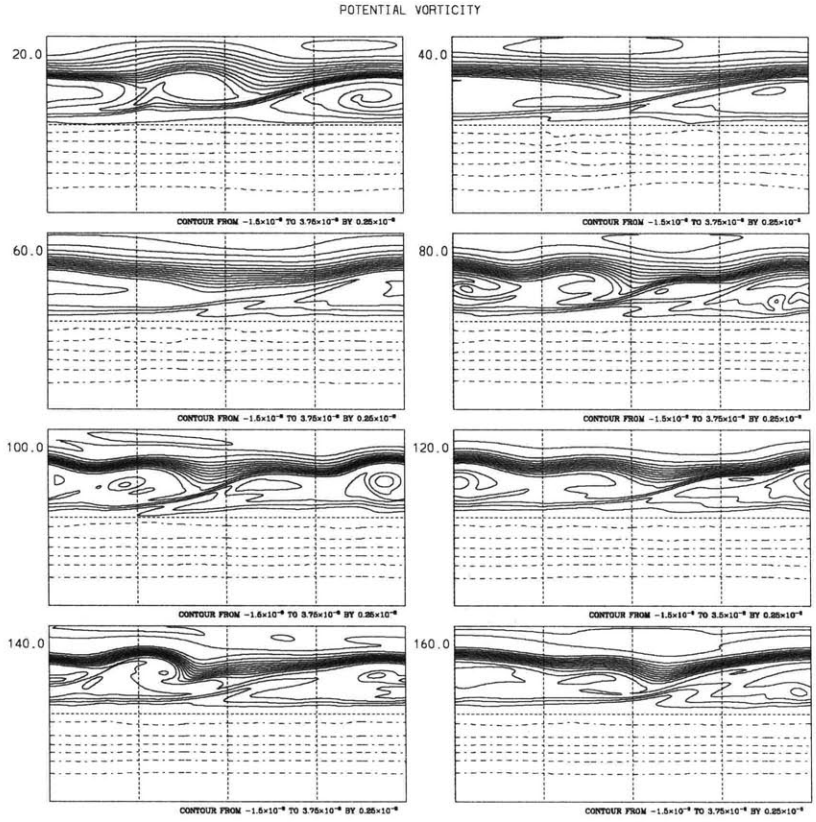

Figure 4-2: The potential vorticity in intervals of $0.25\text{x}10^{-8}$ m^{-1} s^{-1} for the perpetual solstice simulation with Northern Hemisphere topographic forcing. Time, in days, is given in the upper left corner of each frame. This is a cylindrical longitude/latitude projection with 0^o longitude at the center of the frame. Solid lines are positive PV contours, dash-dot lines are negative PV contours.

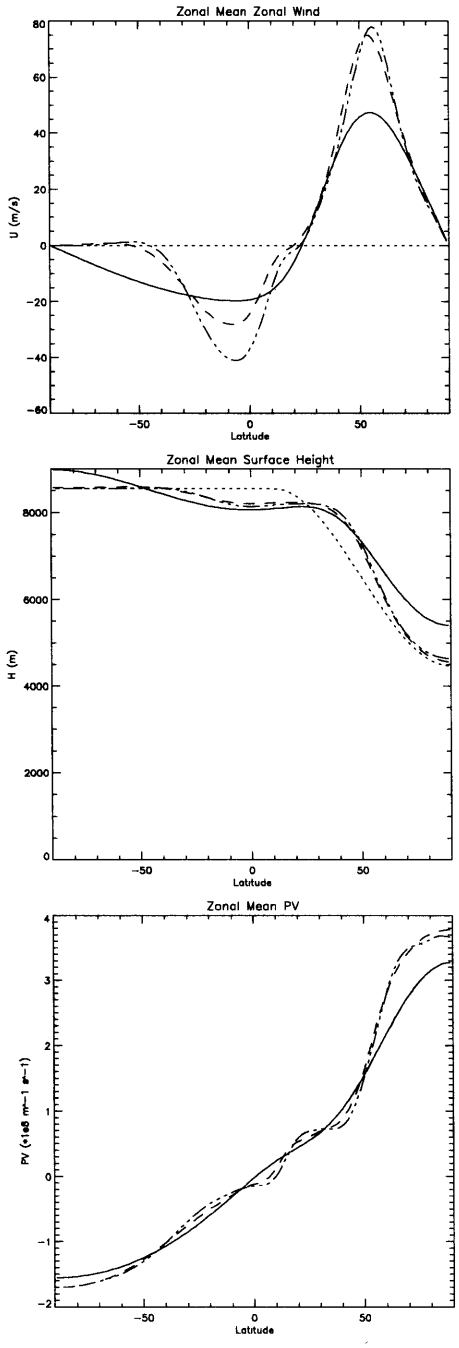

Figure 4-3: The a) zonal mean zonal wind, b) zonal mean surface height, and c) zonal mean potential vorticity on day 0 (solid line), day 60 (dashed line), and day 150 (dash-dot line).

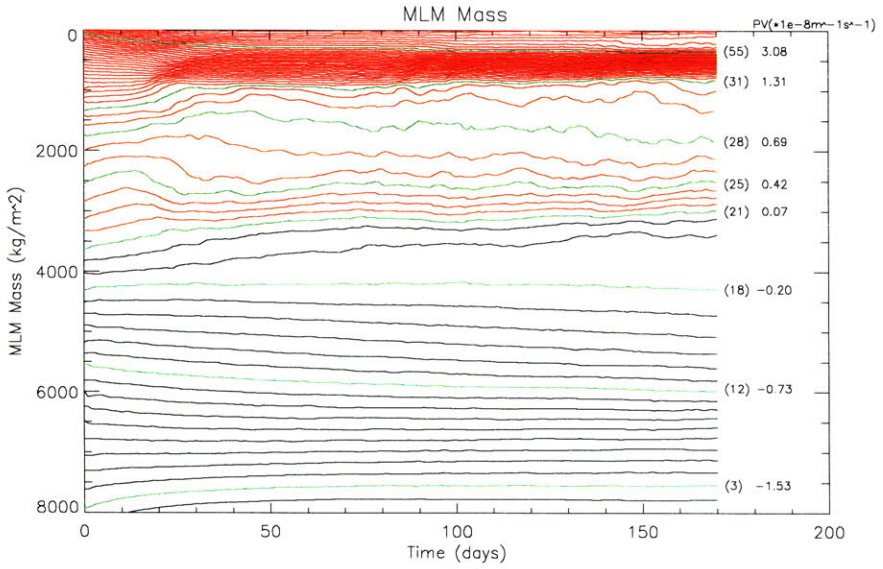

Figure 4-4: The Modified Lagrangian Mean Mass (mass per unit area enclosed by PV contours assuming unit density) as a function of time for the simulation shown in Figure 4-2, for 64 evenly spaced values of PV. Negative PV contours are in black, positive PV contours in red. Selected contours, which are numbered and shown in green, are discussed in the text. The PV values for these contours are given on the far right of the plot.

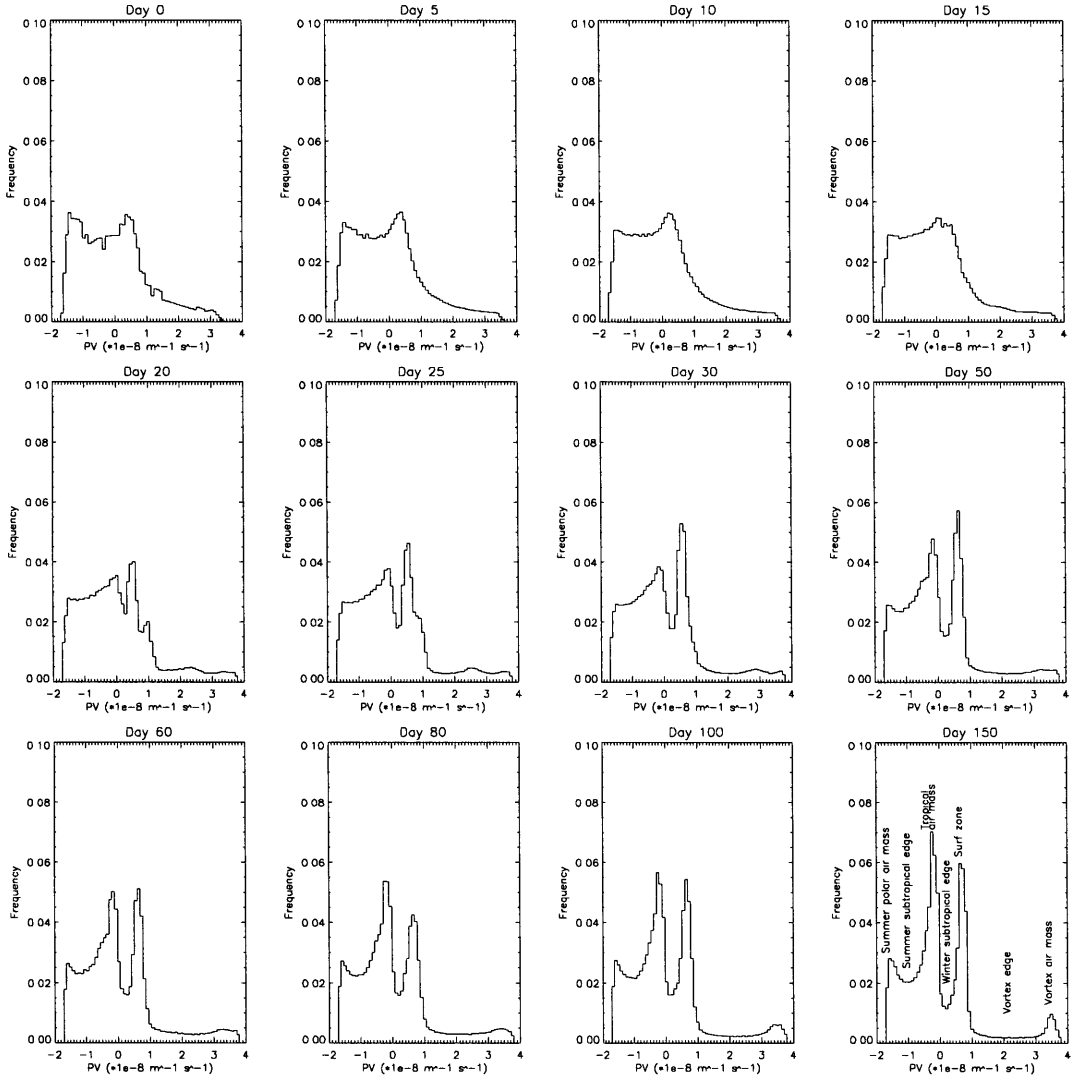

Figure 4-5: The PDFs of PV for selected days of the simulation shown in Figure 4-2. The day is given at the top of each frame. The PV features discussed in the text are indicated on the PDF for day 150.

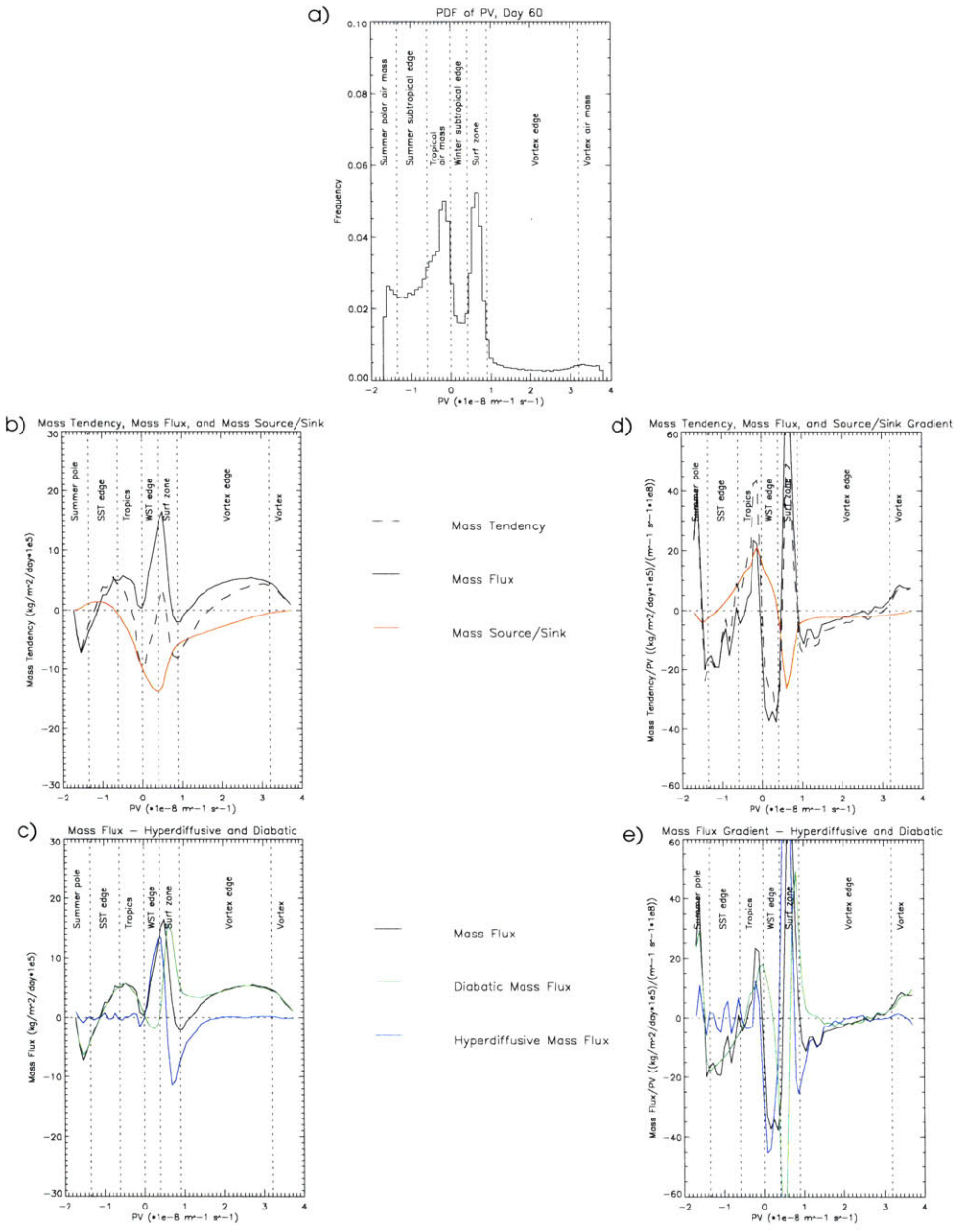

Figure 4-6: a) The PDF of PV on day 60 for the simulation shown in Figure 4-2, with the approximate boundaries of the air masses and edge regions marked by the dashed lines. b) The mass tendency (dashed line), mass flux (solid line), and mass source/sink term (red line) as a function of PV. c) The total mass flux (black line), the mass flux due to diabatic processes (in green), and the mass flux due to hyperdiffusion (in blue) as a function of PV. d) The local mass tendency, the local mass flux, and the local mass source/sink, as a function of PV. e) The local mass flux, the local diabatic mass flux, and the local hyperdiffusive mass flux, as a function of PV. See text for a full definition of each term.

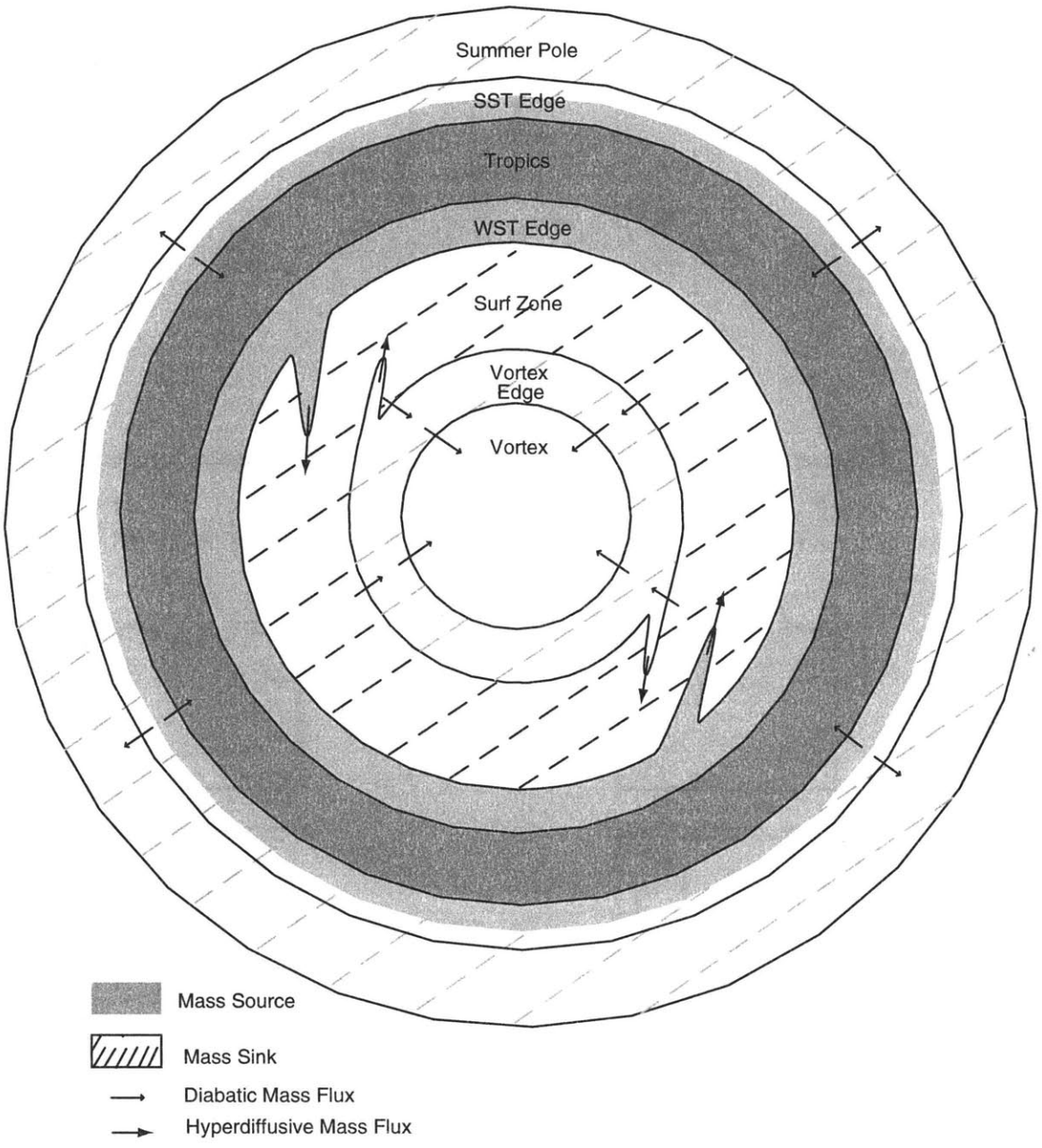

Figure 4-7: A schematic representing the balance between the horizontal mass fluxes and the mass source/sink in each region during the first 60 days of the simulation. Shaded areas represent the mass source and hatched areas represent the mass sink, with the darkness proportional to the magnitude of the source/sink term. Arrows with small heads represent the diabatic mass flux and arrows with large heads represent the hyperdiffusive mass flux. See the text for discussion.

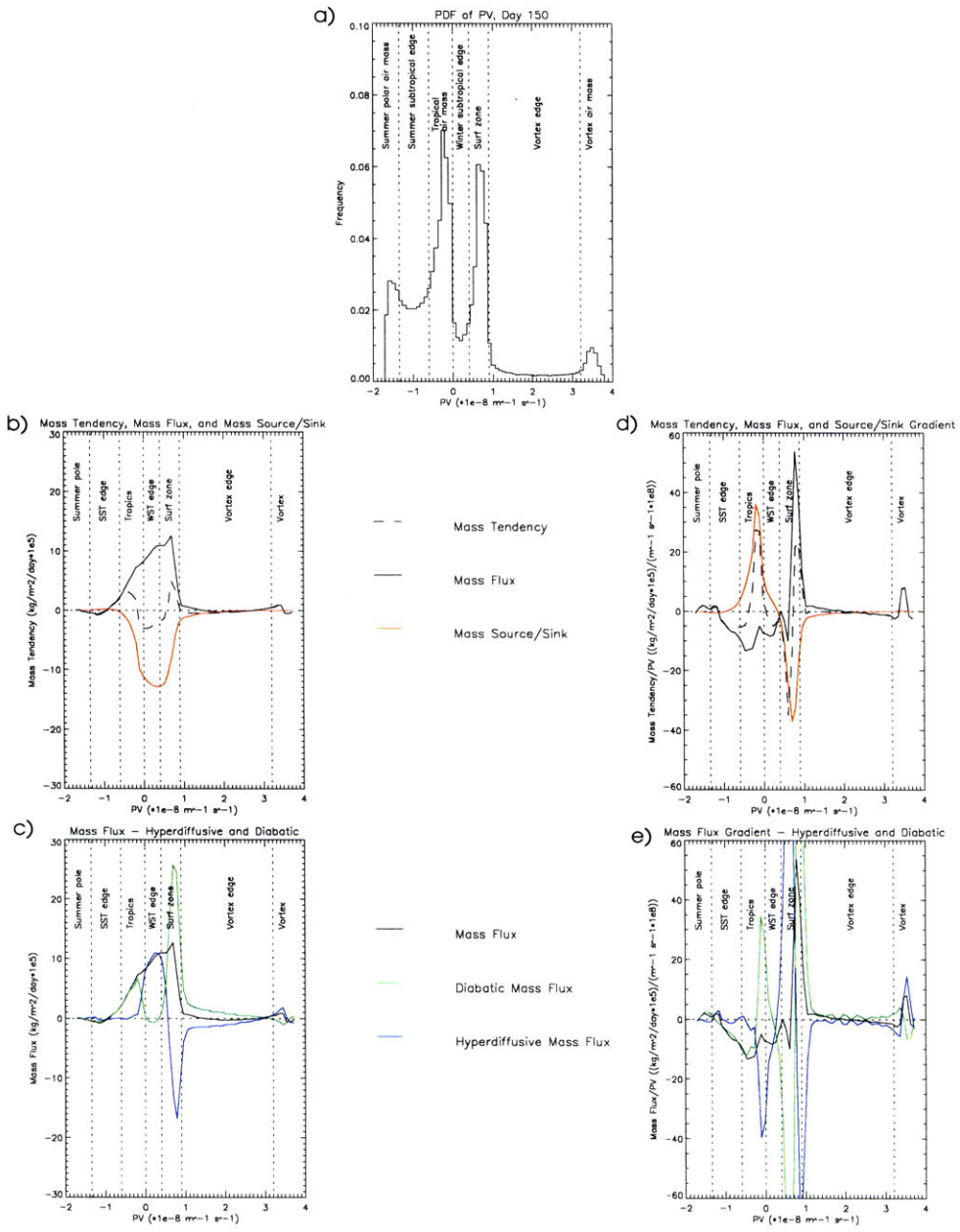

Figure 4-8: Same as Figure 4-6, but for day 150 of the simulation.

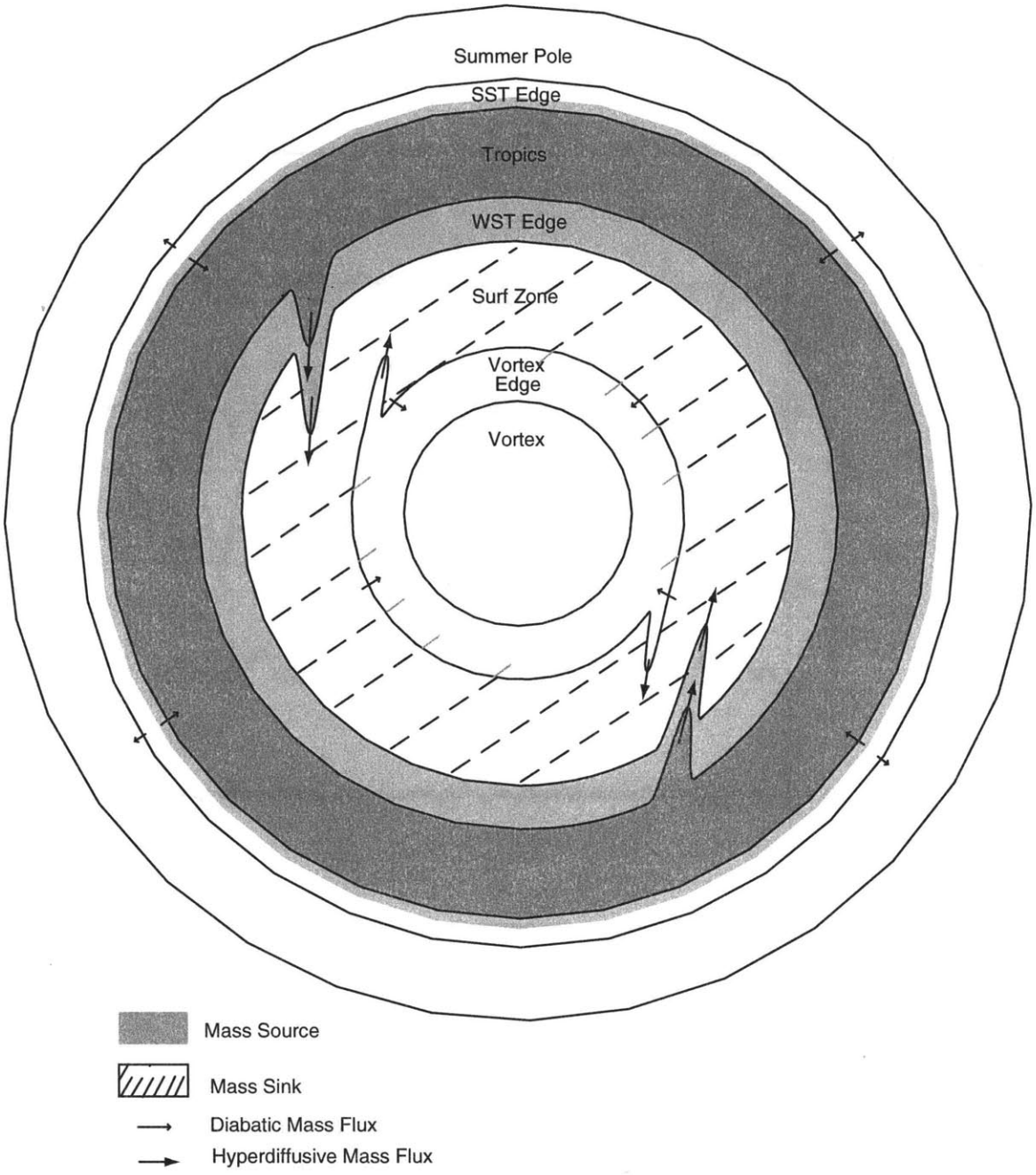

Figure 4-9: Same as Figure 4-7, but representing the balances during days 100 to 170 of the simulation.

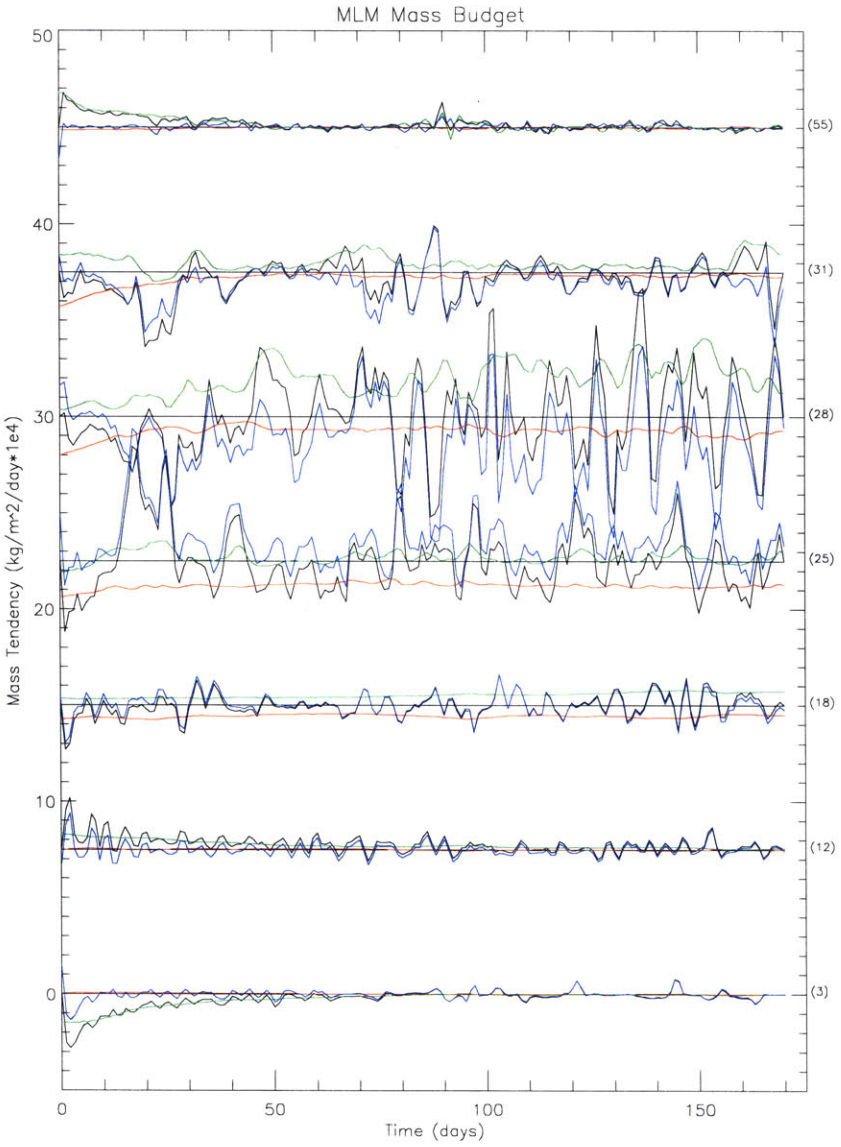

Figure 4-10: The MLM mass budget for selected PV contours, shown in Figure 4-4, as a function of time, offset along the y-axis. The dashed line is the zero line for each contour, and the contour number is given to the far right. Black lines are the mass tendency, green lines are the diabatic mass flux, red lines are the mass source/sink term, and blue lines are the hyperdiffusive flux.

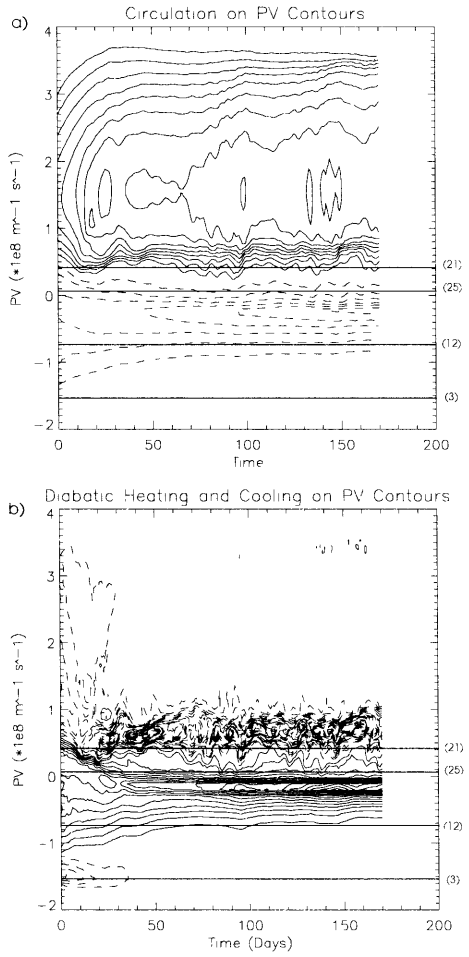

Figure 4-11: a) The relative circulation, calculated along each of the 64 PV contours, as a function of time. Contour interval is 5 m^2s^{-1}. Negative values are dashed, positive values are solid. Zero is not plotted. b) The diabatic heating and cooling along PV contours as a function of time. Contour interval is .25 m^2s^{-1}. Negative values are dashed, positive values are solid. The horizontal lines in each plot mark the approximate boundaries of the winter and summer subtropical edges. The numbers along the right-hand side correspond to the numbered contours in Figure 4-4.

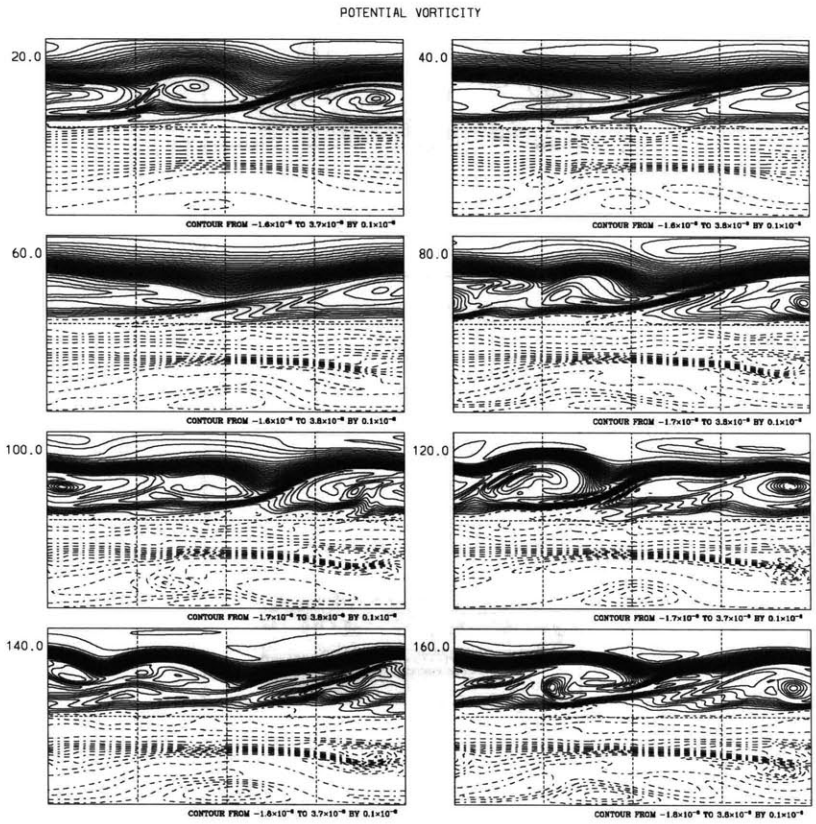

Figure 4-12: Same as Figure 4-2, but for the perpetual solstice simulation with Northern and Southern Hemisphere topographic forcing. The contour interval is much finer, .01x10^{-8} m^{-1} s^{-1}, to allow the reader to see the filamentary structures in the Southern Hemisphere mixed zone.

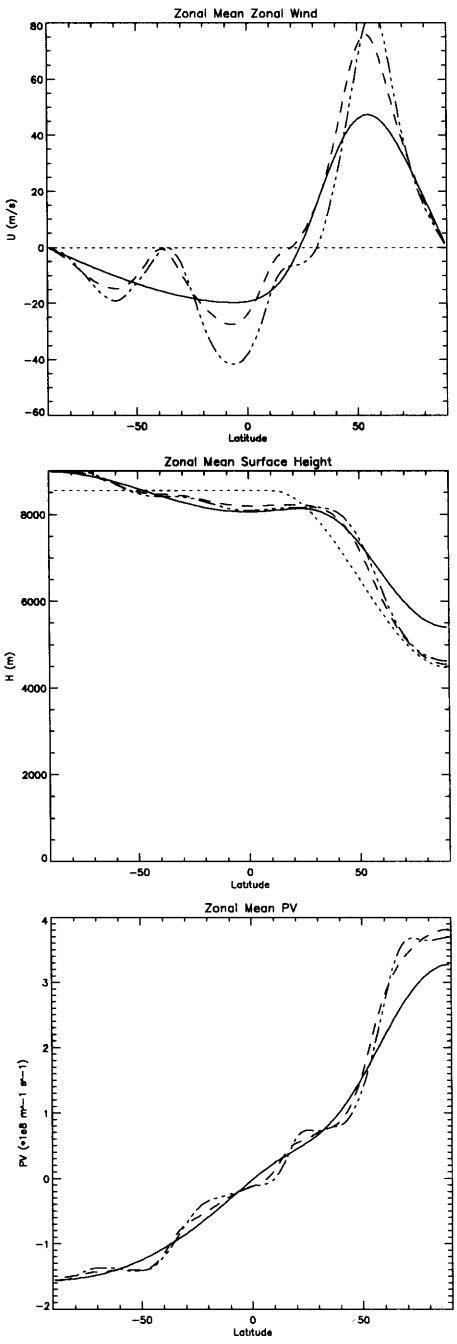

Figure 4-13: Same as Figure 4-3, but for the simulation shown in Figure 4-12.

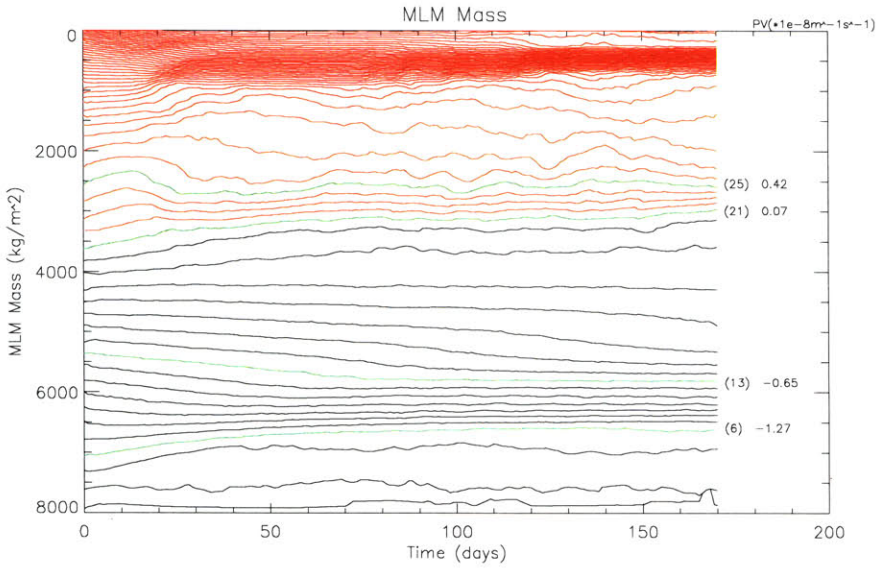

Figure 4-14: Same as Figure 4-4, but for the simulation shown in Figure 4-12.

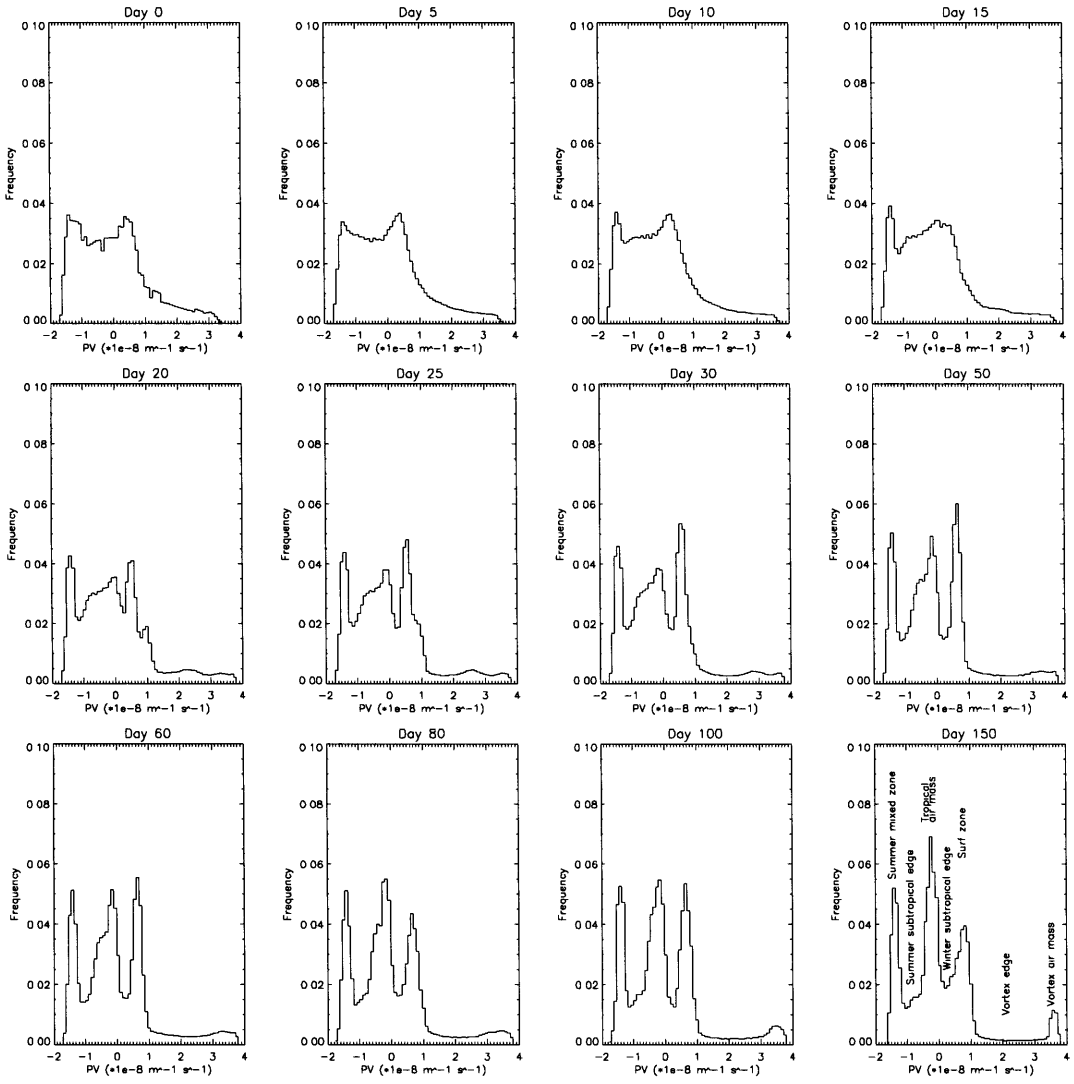

Figure 4-15: Same as Figure 4-5, but for the simulation shown in Figure 4-12.

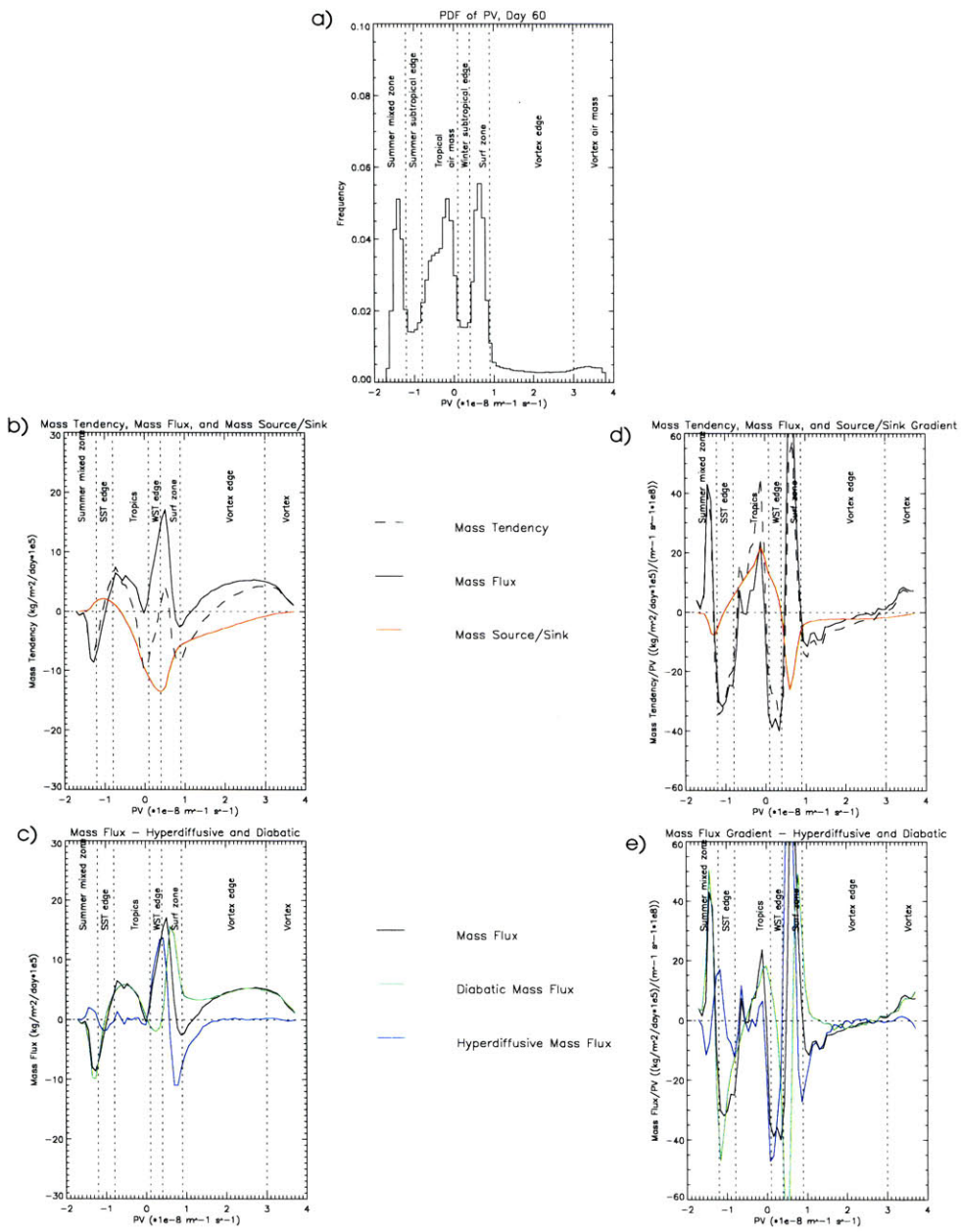

Figure 4-16: Same as Figure 4-6, but for the simulation shown in Figure 4-12.

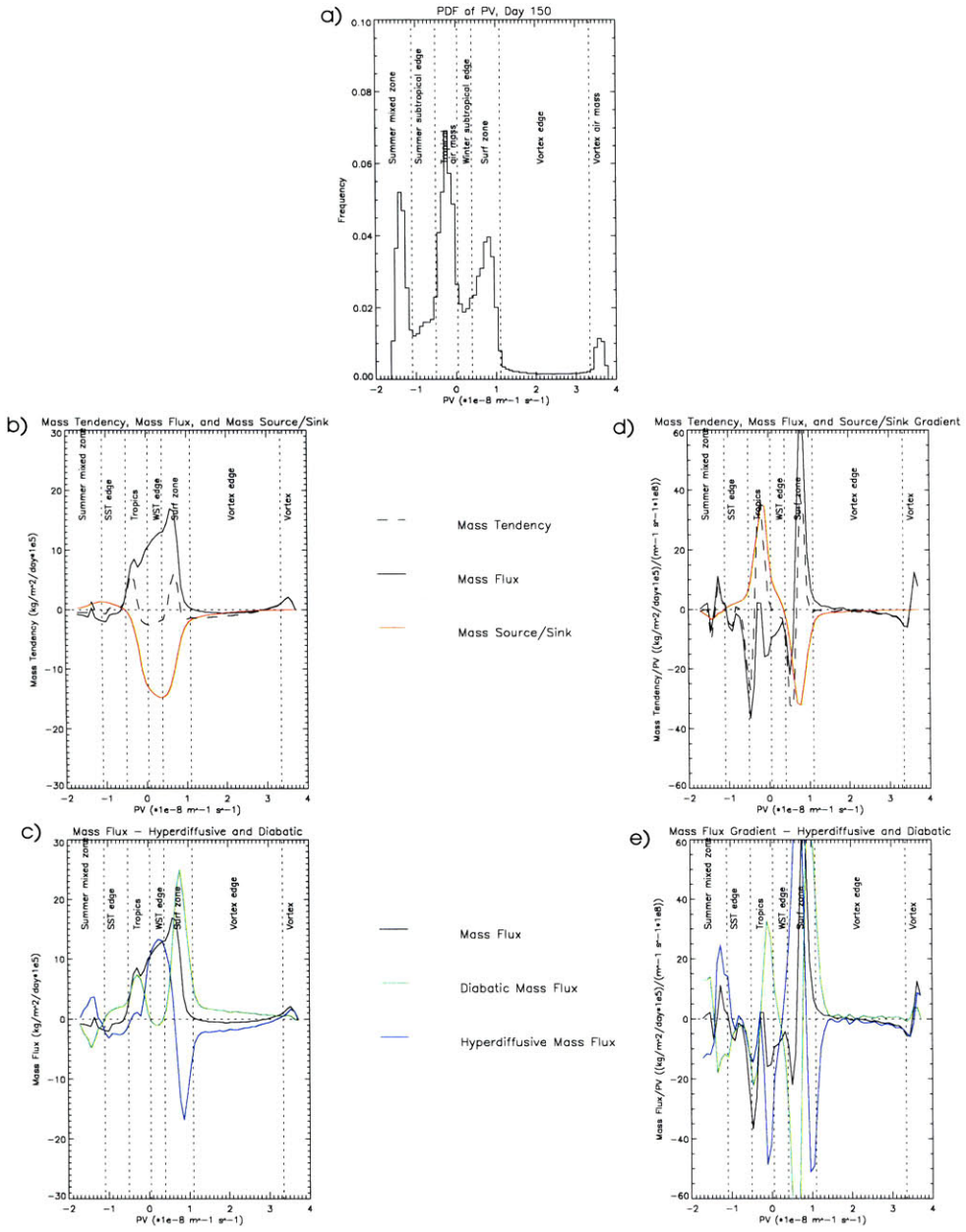

Figure 4-17: Same as Figure 4-8, but for the simulation shown in Figure 4-12.

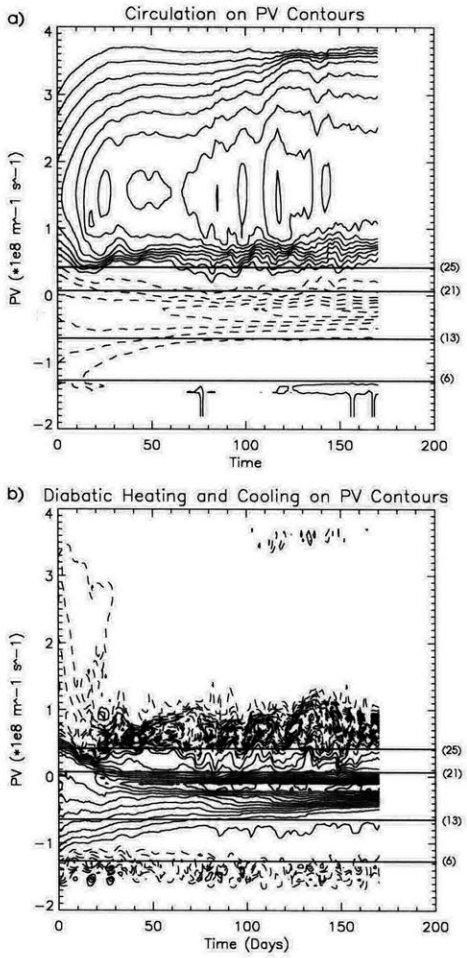

Figure 4-18: Same as Figure 4-11, but for the simulation shown in Figure 4-12.

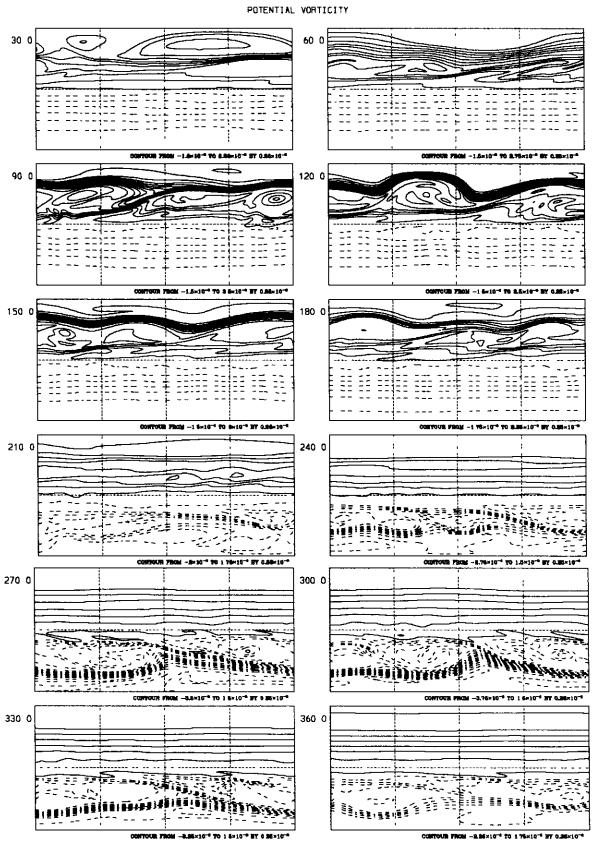

Figure 4-19: Same as Figure 4-2, but for the first year of the seasonal cycle simulation.

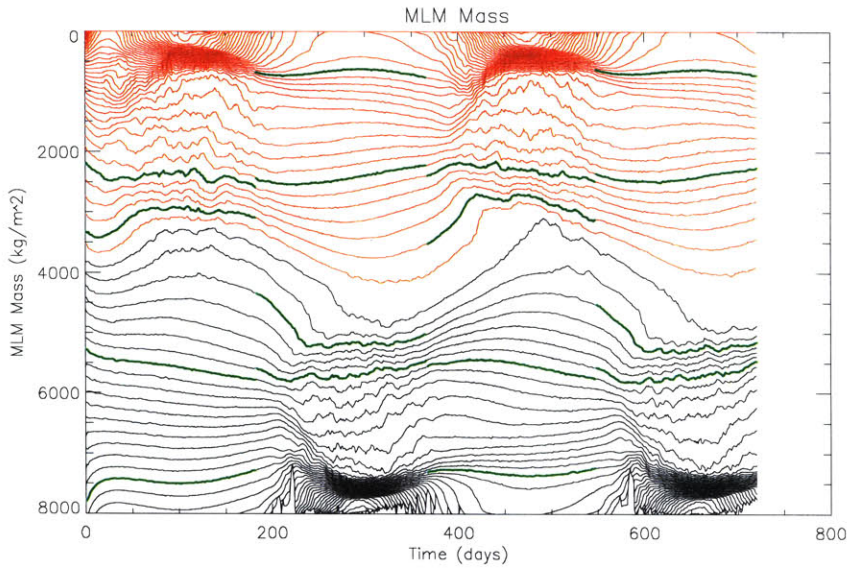

Figure 4-20: Same as Figure 4-4, but for the full two years of the simulation shown in Figure 4-19, and using 87 rather than 64 values of PV. The contours in green mark the approximate boundaries of the subtropical edges (c.f. Figure 4-22)

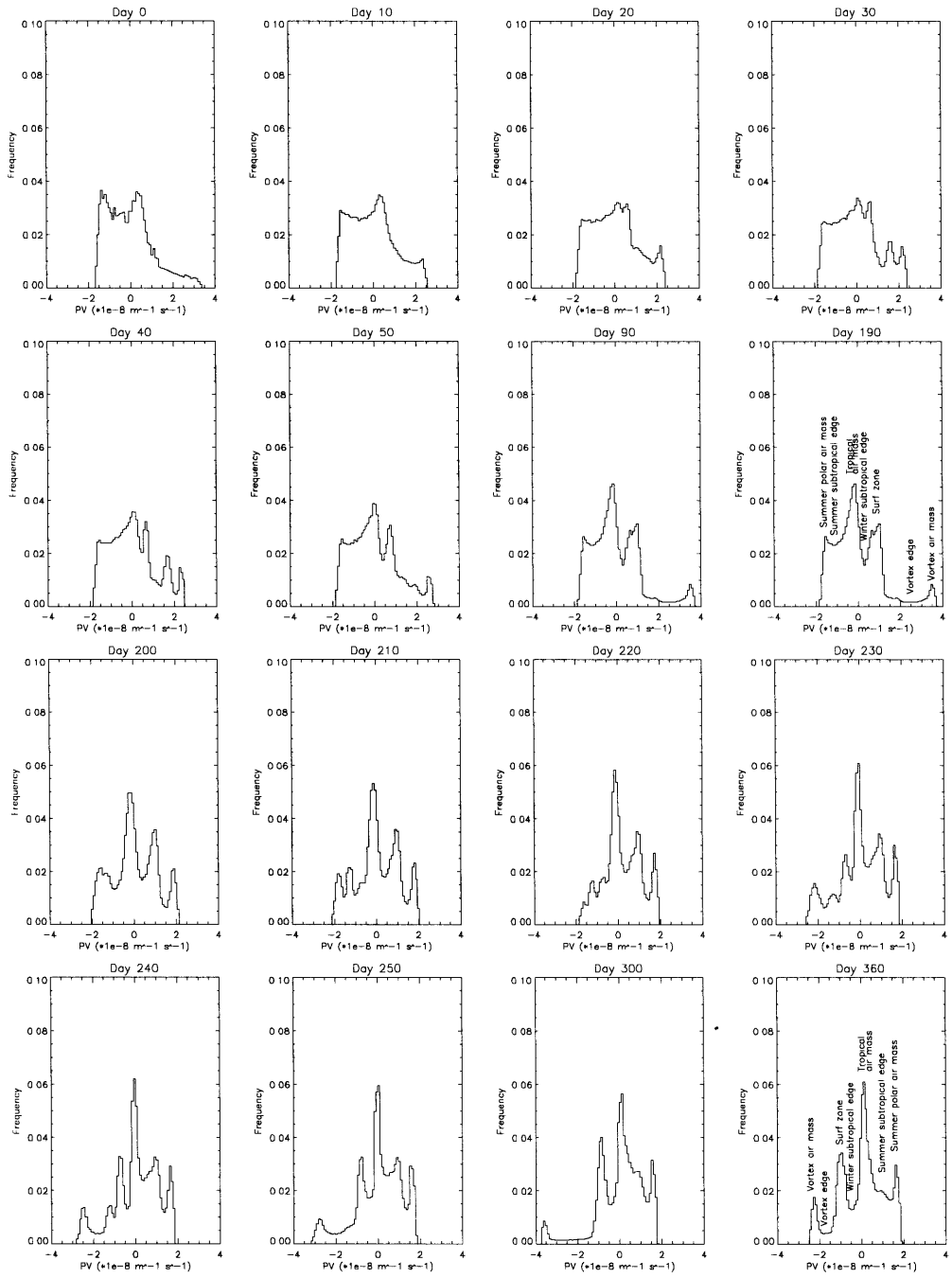

Figure 4-21: Same as Figure 4-5, but for the first year of the simulation shown in Figure 4-19.

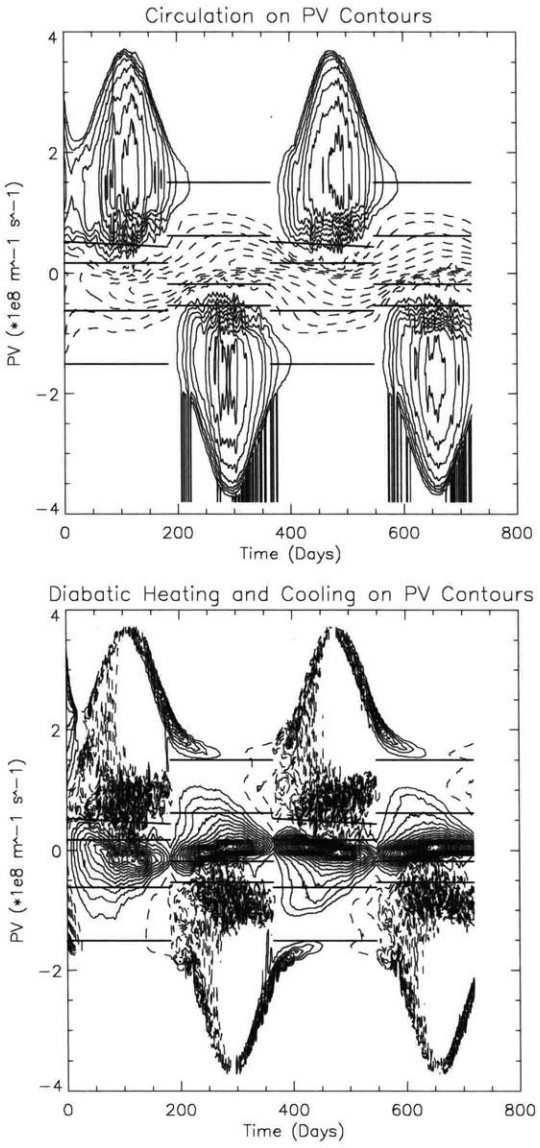

Figure 4-22: Same as Figure 4-11, but for the full two years of the simulation shown in Figure 4-19. The horizontal lines representing the PV values of the subtropical edge correspond to the green contours in Figure 4-20.

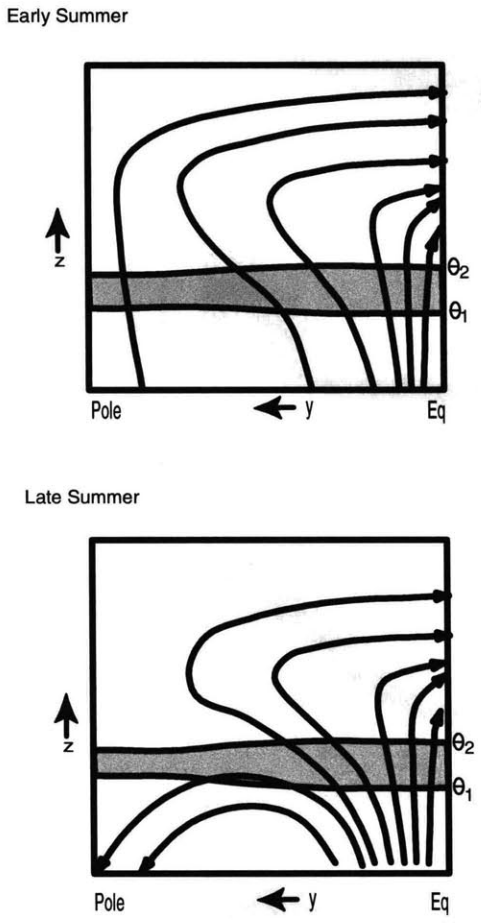

Figure 4-23: Schematic representing the flow through an isentropic layer in the stratosphere in a) early summer and b) late summer. See the text for discussion.

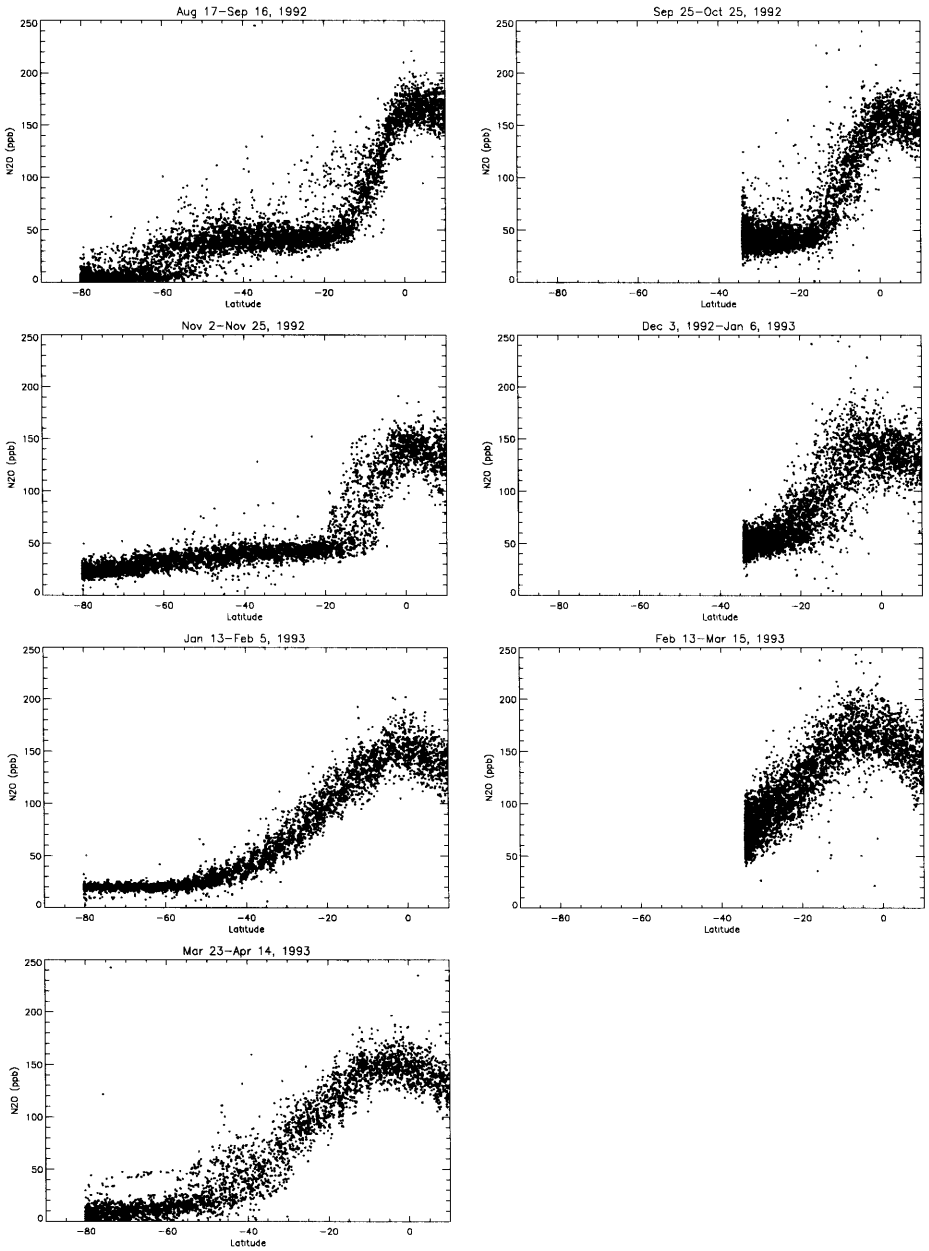

Figure 4-24: CLAES N_2O measurements during each viewing period from July, 1992, to April, 1993, at 6.8 mb.

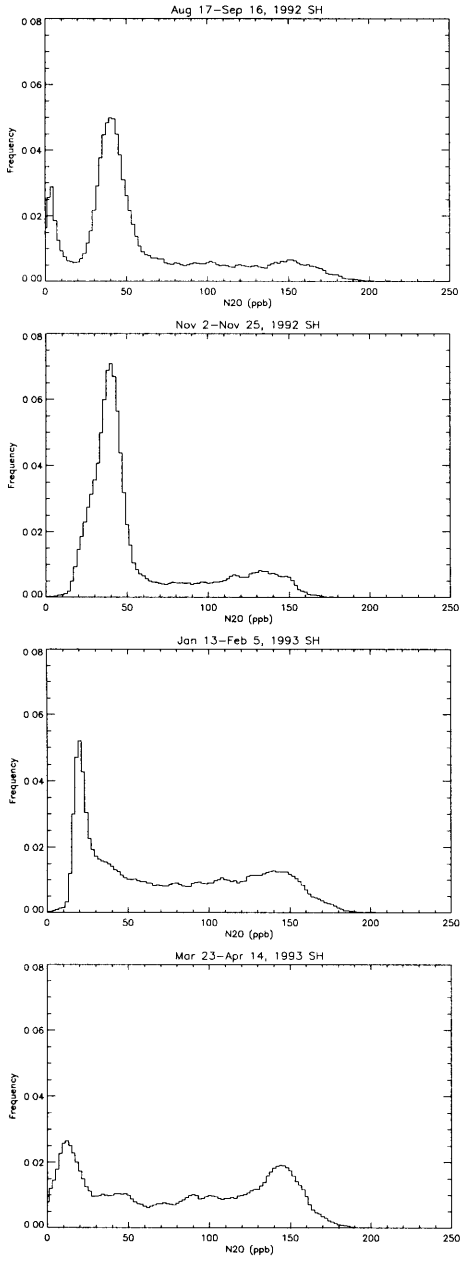

Figure 4-25: PDFs of the CLAES N_2O measurements for the southern-viewing periods in Figure 5-1.

Chapter 5

Implications for Tracer Transport

The seasonal variability of the subtropical edges discussed in Chapters 3 and 4 is indicative of seasonal variability in transport between the tropics and midlatitudes of the stratosphere. The edge moves equatorward during winter as tropical air is entrained into the surf zone. During summer, surf zone air becomes subtropical edge air and winter subtropical edge air is transported into the tropics as the edge moves poleward and becomes quite broad and the weak residual circulation becomes the dominant transport mechanism. A simple model such as the "leaky pipe" model is directly applicable only to the winter hemisphere (though it may apply to the summer hemisphere in the lower stratosphere as well), where the edge is narrow enough that transport across the edge can be represented as entrainment across a discontinuity in mixing ratio. However, if the edge is assumed to be stationary during the winter, such models will underestimate the mass transport out of the tropics and into the surf zone since they ignore the change in the area of these regions that occurs when the edge moves.

We can estimate the contribution of the edge motion to the mass budget in each region using the edge positions determined in Chapter 3. The time-dependent continuity equation for each region is given by:

$$\begin{aligned}
\frac{\partial M_T}{\partial t} &= -\frac{\partial (M_T W_T)}{\partial Z} - 2\pi a\rho(v_N - v_{EN}) + 2\pi a\rho(v_S - v_{ES}) \\
\frac{\partial M_N}{\partial t} &= -\frac{\partial (M_N W_N)}{\partial Z} + 2\pi a\rho(v_N - v_{EN}) \\
\frac{\partial M_S}{\partial t} &= -\frac{\partial (M_S W s)}{\partial Z} - 2\pi a\rho(v_S - v_{ES})
\end{aligned}$$

where the subscripts T, N, and S refer to the tropics, Northern midlatitudes, and Southern midlatitudes, respectively. The variables M, W, and Z are defined in the same way as in Chapter 2, a is the radius of the earth, and ρ is the density in log-pressure coordinates. The horizontal velocities v_N and v_S are given by $\bar{v}^* \cos\varphi$ at the latitude of the Northern and Southern subtropical edges (assuming that the local vertical slope of the subtropical edge is small), and v_{EN} and v_{ES} are the velocities of the edges themselves (multiplied by $\cos\varphi$). Changes in the mass of each region are thus associated with the convergence or divergence of the vertical mass flux, horizontal transport by the residual circulation, and movement of the subtropical edges. The net horizontal mass transport now depends on the difference between $\bar{v}^*$ and the velocity of the edge. If, for example, $\bar{v}^*$ is poleward, so that it acts to transport mass from the tropics to the midlatitudes, then equatorward motion of the edge will further decrease the mass in the tropics and increase the mass in midlatitudes. Poleward motion of the edge in this case will reduce the impact of $\bar{v}^*$on the mass of each region, and could even result in increased mass in the tropics and decreased mass in the midlatitudes if the velocity of the edge is greater than $\bar{v}^*$.

Unfortunately, if we define the tropics, as they are defined in the leaky pipe model, as a region in which the tracer mixing ratios are horizontally uniform, then estimating the contribution of the edge motion to the mass budget is not as simple as determining the velocity of the edge from the change in edge position. The reason for this is that the edges have a finite width. As we showed in Chapter 3, the winter edge may occupy up to 20 percent of the area of the hemisphere, and the summer edge may occupy as much as 60 percent of the area of the hemisphere (in the altitude region that we explore). Thus, particularly in the summer hemisphere, the edge of the tropics, if we define the tropics as having a uniform tracer distribution, is different than the center of the subtropical edge. Figure 5-1 is a schematic which clarifies this difference. Figure 5-1 a) is a schematic of the PDF of a tracer whose value monotonically increases with latitude (such as the sin(latitude) tracer which is often used in modelling studies). The PDF shown is similar to observed PDFs during Northern Hemisphere winter (we have excluded the vortex edge and vortex air mass). If we use our latitudes for the subtropical edges as the boundaries of the tropics, so that any air equatorward of those latitudes is tropical air and any air poleward of those latitudes is midlatitude air, then the "tropical air mass" will be all of the air enclosed by

the blue line, the surf zone air mass will be the air enclosed by the green line, and the summer midlatitude air mass will be the air enclosed by the red line (the area of overlap between these air masses is one of the quantities defined by Sparling (2000)). Clearly, the "tropics" in this case do not have a horizontally uniform tracer distribution, since they contain a significant portion of the subtropical edge air (mostly on the summer side). If, however, we define the tropical air mass to be the tropical mode of the tracer distribution, so that it is chemically homogeneous, then as shown if Figure 5-1 b), the edges become finite, with their own tracer distributions (note that for N_2O, it is often impossible to completely resolve the tropical and surf zone peaks since the range of N_2O values in the winter subtropical edge is quite small). Since the edges are represented as discontinuities in the leaky pipe model, they are assumed to contain zero mass. For the winter edge, this is probably a reasonable representation since the edge is a small portion of the hemispheric area. For the summer edge, this is probably not a reasonable representation since the edge itself occupies a significant portion of the hemisphere. Thus, the only way to formulate the leaky pipe model so that it applies in the summer hemisphere is to define the summer midlatitude air as both the summer edge and the summer midlatitude air mass. Figure 5-1 c) shows the distribution in the context of the leaky pipe paradigm. The edges of the tropics, which are the winter subtropical edge and the boundary between the summer subtropical edge and the tropical air mass, contain zero mass. The tropics and surf zone have relatively homogeneous tracer distributions, and the mixing ratio of these regions in the model tracer budget may be taken as the most probable value from the tracer PDF. It is unclear what mixing ratio should be used for the summer midlatitudes in order to correctly represent the effects of transport between the tropics and the summer hemisphere, since the summer air contains a large range of mixing ratios. However, given the area of the subtropical edge, it is unlikely that there is transport between the actual summer midlatitude air mass and the tropics, so that the mixing ratio should probably be taken as some value within the summer subtropical edge.

Figure 5-2 illustrates the difference in the transport that is implied by assuming that both the winter and summer subtropical edges are discontinuities and that implied by assuming that the summer midlatitude air includes the air within the summer edge. In Figure 5-2 a), the edge is a discontinuity. The boxes represent measurements for the edge positions on quasi-monthly

timescales such as those determined from the HALOE data. In this case, the poleward motion of the edge during the summer implies that there has been transport of first surf zone and then the summer midlatitude air into the tropics. The equatorward motion of the edge at the onset of winter implies that there has been transport from the tropics into the surf zone. In Figure 5-2 b), the discontinuity lies at the edge of the tropics, as in Figure 5-1 c). In this case, the motion of the edge implies transport between the surf zone and the tropics during winter and implies transport between the summer subtropical edge and the tropics during summer. For the same subtropical edge positions, shown by the boxes, the implied transport is much less than in Figure 5-2 a), and would have a very different impact on the tracer budgets since the mixing ratio of the summer midlatitude air is quite different than that of the edge air.

Unfortunately, we do not have a great deal of information about the boundary between the tropics and the summer subtropical edge. The area calculations from the CLAES data, however, can provide an estimate of the latitudinal extent of the edge. Figure 5-3 shows the positions of the edges for 1993 as determined from the HALOE data in red. In black we show an approximation of the extent of the summer edge. This approximation was produced by using the area of the summer edge in each hemisphere at each level as determined from the CLAES data and shown in Chapter 3 (in the Southern Hemisphere we use the average area from the two summer viewing periods, while in the Northern Hemisphere there is only one purely summer month in the CLAES data) and the latitude of the center of the edge from the HALOE data. We chose to use the HALOE edge positions rather than simply using the CLAES data because we wanted to examine a full year of data and because the residual circulation calculations that we will use seem to be most consistent during 1993. A subjective comparison to the raw HALOE measurements shows that the latitudes seen here agree quite well with the boundaries between the subtropical air and the tropical and summer midlatitude air masses. The choice of "summer" months is somewhat subjective, and is based on the magnitude of the latitudinal tracer gradient. However, we note that our choice of summer months corresponds quite well to the periods in which there are easterlies in the subtropics.

In most cases, the edge of the tropics, as defined in the leaky pipe context, actually moves equatorward at the beginning of summer, poleward during the summer, and then poleward at the onset of winter. This implies that tropical air is transported into the subtropical edge at

the transition to summer, and that subtropical edge air is transported into the tropics over the course of the summer and at the onset of winter. The tracer PDFs indicate that the winter and summer subtropical edges share some range of mixing ratios (see Figure 4-25), so that it is likely that air is actually exchanged between the winter subtropical edge and the tropics and summer subtropical edge at the transitions to summer and winter, which we can not represent since we assume that the winter edge is a discontinuity. The shallow water model simulations actually show that the exchange is exclusively between the winter edge and the tropics, but this is probably an oversimplification.

Figure 5-4 shows the velocity of the edge of the tropics (the winter subtropical edge and the boundary between the summer subtropical edge and the tropics) compared to $\bar{v}^*$. The velocity of the edge was taken as the difference in edge position between two viewing periods divided by the total length of the viewing periods. The $\bar{v}^*$ values are the Eluskiewicz et al. (1996) $\bar{v}^*$ values interpolated to the edge positions, averaged over each viewing period and then averaged between viewing periods, so that they are applicable to the same time period as the edge velocities. The Northern Hemisphere velocities are in black, the Southern Hemisphere velocities in red, and the velocities of the edges are the dashed lines. In most cases, and particularly at upper levels, the velocity of the edge is not negligible compared to $\bar{v}^*$. In some cases, the edge is located inside the winter circulation cell during the summer, so that the velocity is equatorward across the summer subtropical edge. Unfortunately, it is impossible to say whether this is the case in reality, since the details of the residual velocities are not well known. Figure 5-5 shows the mass transport by $\bar{v}^*$ compared to the change in mass associated with the velocity of the edge, expressed as a percentage of the total mass in the tropics (which changes with time according to the edge motion). Figure 5-6 shows the total change in mass resulting from $\bar{v}^*$ and the velocity of the edge, again expressed as a percentage of the tropical mass. Again, it is difficult to draw any sweeping conclusions because of the uncertainties of $\bar{v}^*$, but in most cases, there are not drastic differences in the outward transport when we include the velocity of the edge in the lower altitude regime, but there are very large differences in the upper regime. There are also significant differences in the mass transport into the tropics during the summer at many levels.

While it is possible to formulate time-dependent tracer budgets for a seasonally-varying leaky pipe model, which allows for advection only in the summer hemisphere (see Appendix B),

it is not clear that doing so is particularly reasonable, given that it is unclear what mixing ratios are transported from the summer hemisphere and that the transition between the tropics and the summer edge should not necessarily be represented as a discontinuity. However, the mass budget analysis presented above does indicate that if the steady-state tropical tracer budget is used to determine an in-mixing timescale for transport of midlatitude air into the tropics from the winter hemisphere, as is done in Volk et al., (1996), Hall and Waugh (1997), Mote et al. (1998), and many other studies, then the assumption that all midlatitude air comes from the surf zone may not be valid, since there may be advection into the tropics from the summer hemisphere. As noted, however, it is difficult to say what contribution this makes to tropical mixing ratios since it is unclear what mixing ratios are being advected in.

Since most exchange between the tropics and midlatitudes takes place during the winter, the annual mean advection by the residual circulation is poleward, and the mixing ratios of the summer edge are much the same as those of the surf zone, the steady-state leaky pipe model is probably a reasonable representation of the annual mean transport between the tropics and midlatitudes. However, the annual mean entrainment rates between the tropics and the midlatitudes contain some contribution from processes other than entrainment: the motion of the edges and advection during the summer.

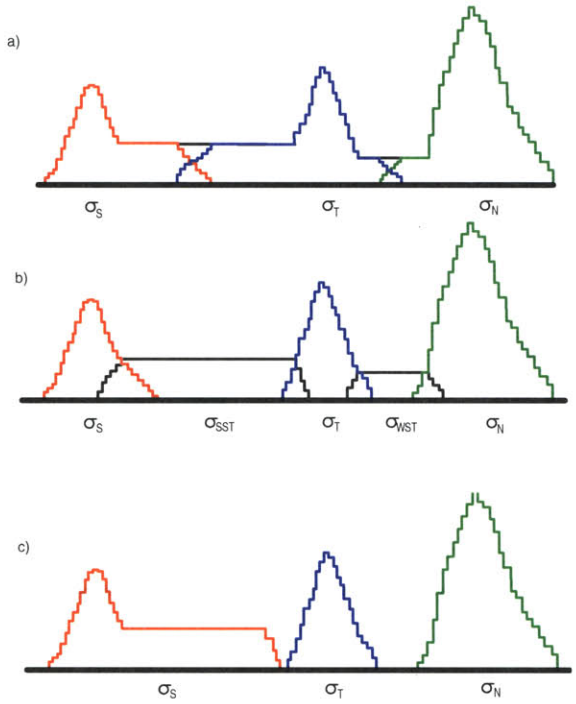

Figure 5-1: Schematic illustrating different ways of defining the tropical and midlatitude air masses. See text for discussion.

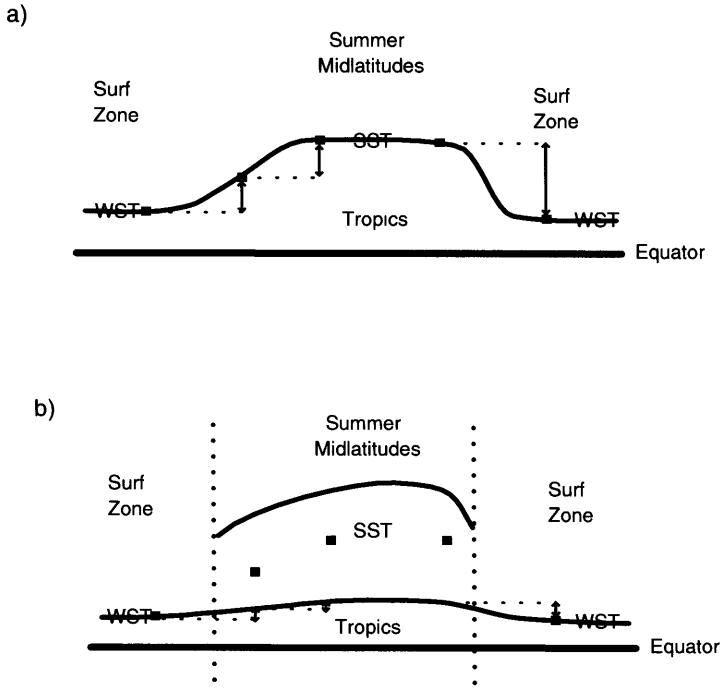

Figure 5-2: Schematic illustrating transport across a) a discontinuous summer edge and b) a finite-width summer edge. See text for discussion.

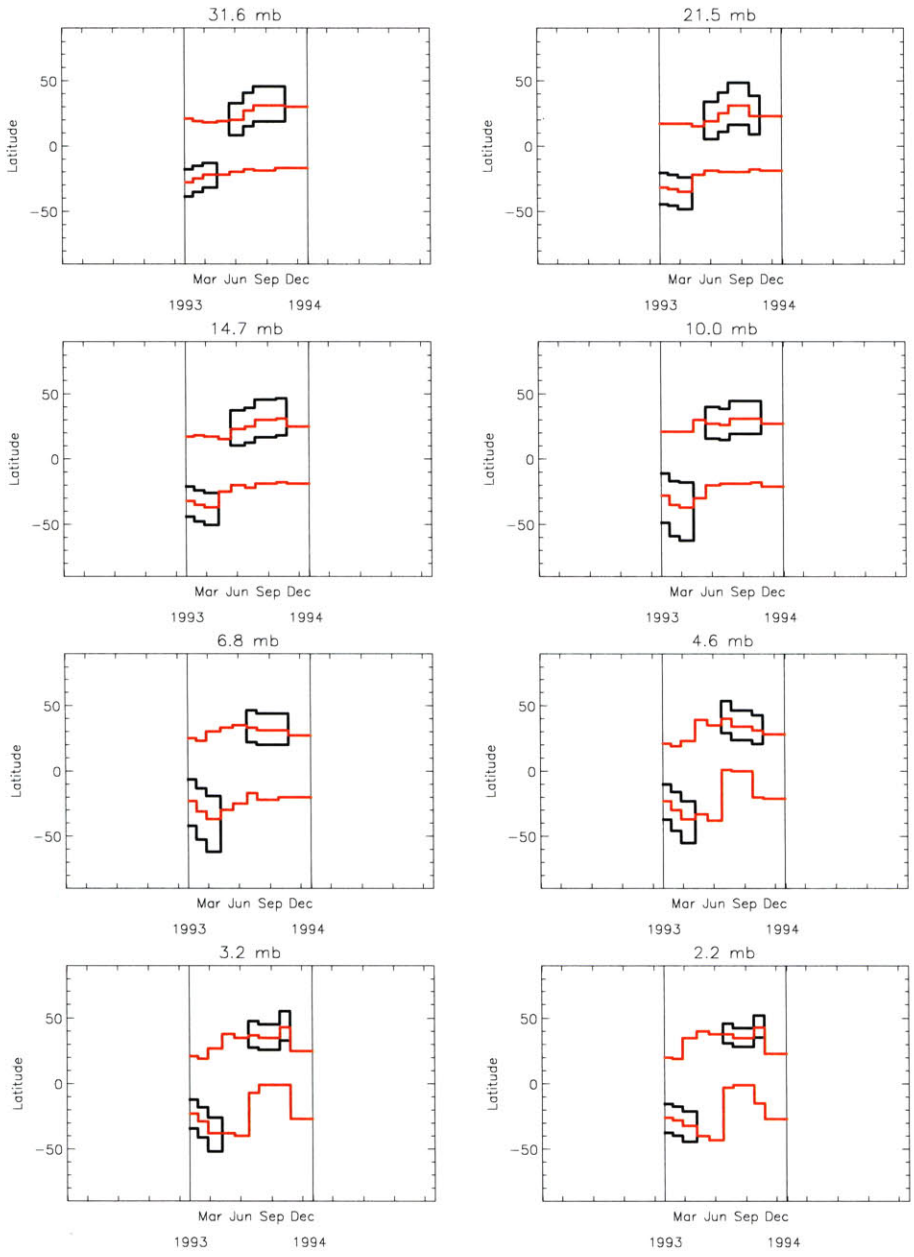

Figure 5-3: Positions for the subtropical edges as determined from the HALOE data for 1993 (in red) as well as an estimate of the width of the summer edge (in black). See text for discussion.

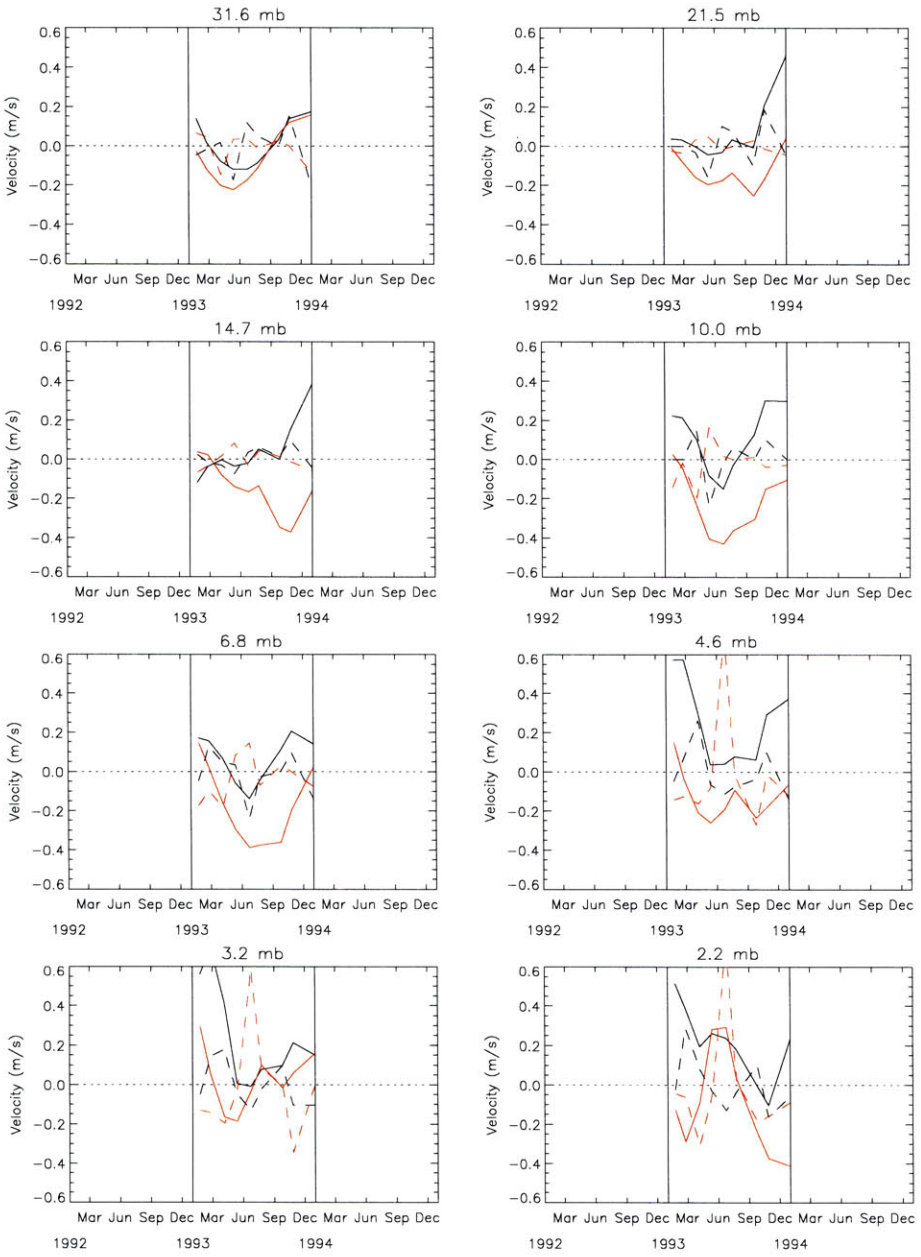

Figure 5-4: Residual meridional velocity (solid lines) at the edge of the tropics and velocity of the edge of the tropics (dashed lines) at each level. Southern Hemisphere data is in red, Northern Hemisphere data is in black.

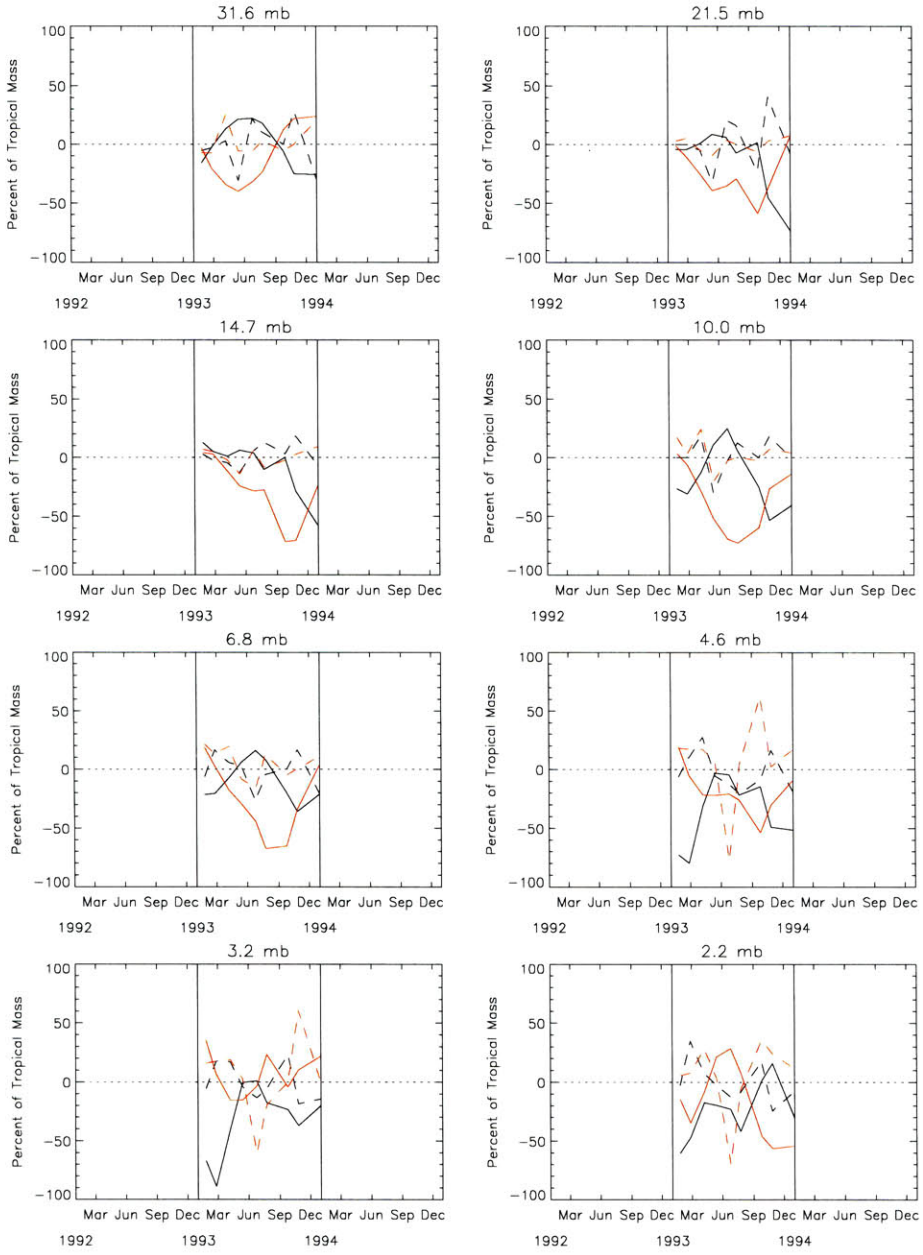

Figure 5-5: Mass transport across the edge of the tropics by the residual meridional circulation (solid lines) and mass transport associated with the motion of the edge of the tropics (dashed lines), as a percentage of total mass in the tropics. Southern Hemisphere data is in red, Northern Hemisphere data is in black.

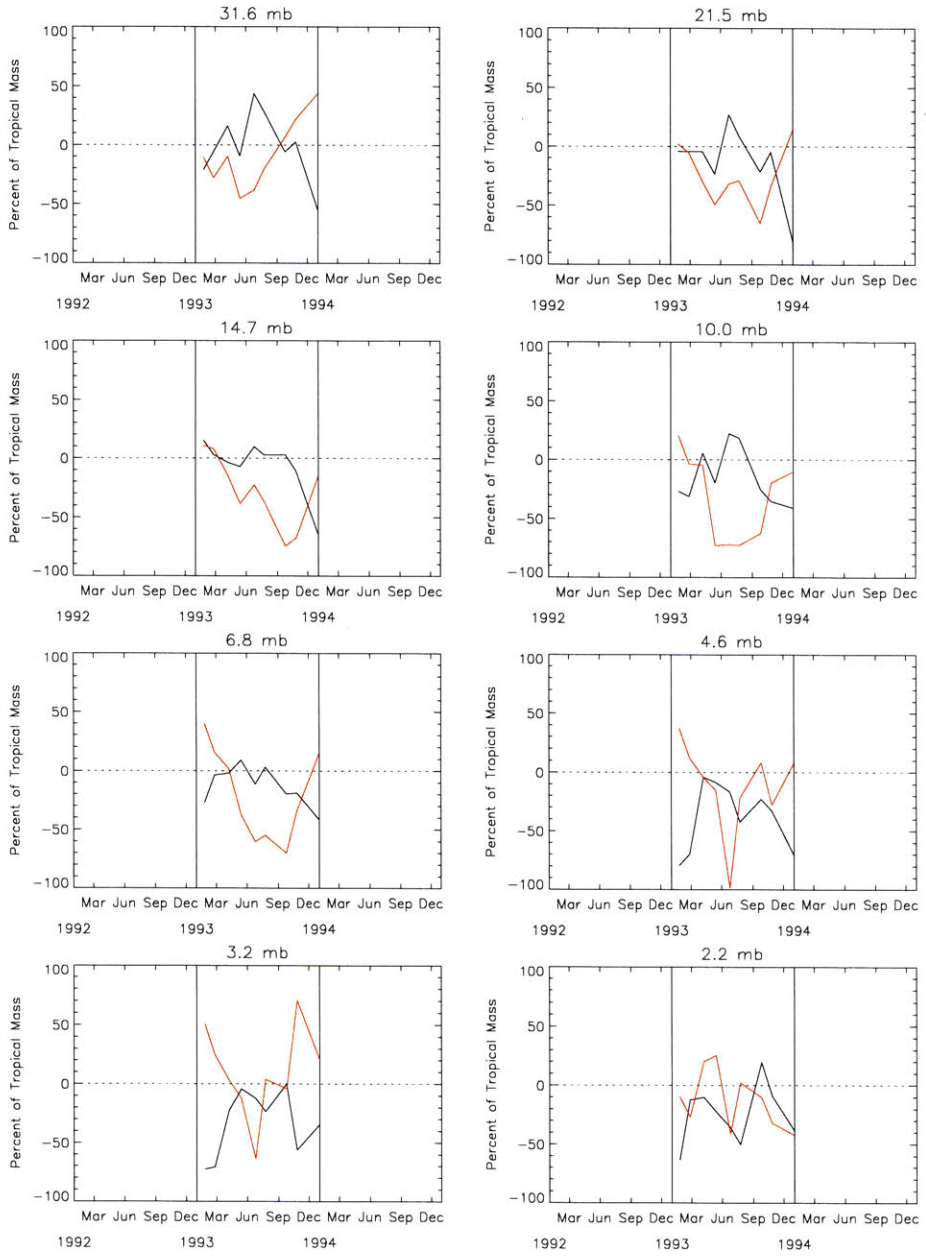

Figure 5-6: Total horizontal mass transport across the tropical edges. Southern Hemisphere data is in red, Northern Hemisphere data is in black.

Chapter 6

Summary

Chapters 3 and 4 represent an extensive investigation of the seasonal variability of the subtropical edges from both a diagnostic and a mechanistic standpoint. In Chapter 3, we extend the findings of Sparling (2000) by showing that the PDFs of long-lived tracers provide an objective and unambiguous method of defining the subtropical edges throughout the year over a wide range of altitudes. The fact that there are well-defined subtropical minima in the PDFs of long-lived tracers throughout the year indicates that there is, in fact, a perennial lack of rapid communication between the tropics and the midlatitudes, in the sense that the timescale for mixing across the edges is slow relative to other transport timescales. We provide an extensive diagnosis of the seasonal variability of the subtropical edges as well as their relationship to various transport parameters. In Chapter 4, we examine the mechanisms of edge formation in a shallow water model, which is the simplest system that includes isentropic stirring by stationary waves and a representation of diabatic processes, and show that the degree of tropical isolation and the processes that lead to edge formation are very different during the winter than during the summer. In Chapter 5, we attempt to assess the importance of the seasonal variability of the subtropical edges in determining global mass and tracer budgets in the context of the simple conceptual model presented in Chapter 2. Here, we summarize the main results of the thesis.

6.1 The Winter and Summer Subtropical Edges: Observations

The data analysis of Chapter 3 indicates that in the middle and upper stratosphere, the winter subtropical edge is centered closer to the equator and is much narrower than the summer subtropical edge, which can occupy 35 to 60 percent of the area of the summer hemisphere. There appear to be two distinct altitude regimes, with much less seasonal variability in the central latitude of the edge below 6.8 mb than above that level. The difference between these regimes is consistent with the influence of the SAO at the upper levels, which we identify through the "double-peak" structure of the tracer field.

The winter edge in the lower regime coincides almost exactly with the zero zonal wind line in the subtropics during the QBO easterly phase and with near-zero zonal winds in the subtropics during the westerly phase, and is eroded inward as the zero wind line appears at the onset of winter. In the upper regime, the equatorward movement of the winter edge is delayed relative to the appearance of the zero zonal wind line, but once the tropical SAO westerlies weaken, the edge is rapidly eroded inward, in some cases crossing the equator. There is some indication that the edge may be sharpened, but not moved, by weak stirring when the zonal wind line first appears at these levels. The influence of the SAO westerlies is much stronger in the Southern Hemisphere than in the Northern Hemisphere, as expected, given the difference in the amplitude of the first and second cycles of the oscillation. In both regimes there is excellent correspondence between the edge as determined from the tracer PDFs and the transition between very large equivalent lengths in the winter hemisphere and very small equivalent lengths in the tropics, which indicates that the winter tracer gradient does, indeed, coincide with a mixing barrier.

The center of the summer edge tends to move outward across the tropical upwelling region and, in the upper regime, where the erosion of the edge at the onset of winter is delayed, into the downwelling region. The center of the summer edge lies within a region of very small equivalent lengths, so that stirring does not seem to play a role in its formation. However, in the lowest levels that we examine, 31.6 and 21.5 mb, there are relatively large equivalent lengths in the summer hemisphere as compared to 14.6 mb and above, and stirring may play a role in determining how far into midlatitudes the broad edge region extends. Above about 10 mb, the residual circulation alone appears to be capable of producing tracer gradients similar to those observed in the summer hemisphere on seasonal timescales.

6.2 Interannual Variability

There is evidence of some interannual variability in the seasonal behavior of the edges, which is consistent with variability in the tropical winds associated with the QBO. Below 10 mb, there is evidence that the edges are shifted toward the Southern Hemisphere during Northern Hemisphere winter when the QBO phase is westerly. This is consistent with surf zone stirring penetrating further into the tropics in the winter hemisphere. The difference in the summer edge position could be consistent with either some stirring within the tropics, which could erode the edge from the tropical side, or with changes in the residual circulation associated with either the enhanced wave breaking in the winter hemisphere or the secondary meridional circulation of the QBO itself. It is difficult to distinguish any difference in Southern Hemisphere winter associated with the QBO. Above 10 mb, the interannual variability is consistent with QBO modulation of the SAO.

6.3 The Mechanisms of Edge Formation

The modeling studies of Chapter 4 indicate that the subtropical edges are regions in which there is a divergence of the irreversible mass transport along isentropic surfaces, which is not balanced by replenishment of mass through the convergence of the vertical mass flux (which we represent as a mass source in the shallow water model). The winter edge in the model forms as air is pulled out of the tropics by stirring in the surf zone. At the edge of the tropics, the convergence of the mass flux is too weak to balance this transport, and the mass between material contours decreases. The edge is eroded equatorward and sharpened by the stripping of edge material. The material contours throughout the entire edge are often deformed into filaments by the surf zone stirring, so that tropical air, not just edge air, is transported into the surf zone. Thus, more and more tropical air becomes edge air until the edge has been pushed far enough into the tropics that the mass source can balance the horizontal mass divergence, and the mass tendency within the edge nears steady-state. We find that the winter edge coincides with the zero circulation line, in good agreement with the data analysis.

We demonstrate that it is possible to form a summer-like edge, i.e. a broad region of enhanced potential vorticity gradient, purely through a representation of diabatic processes. In

the perpetual solstice simulations, the divergence of the vertical mass flux (represented as a mass sink) associated with adjustment toward radiative equilibrium at high latitudes acts to decrease the potential vorticity in that region, while the convergence of the vertical mass flux (represented as a mass source) in the tropics acts to increase the potential vorticity there. The diabatic forcing thus leads to irreversible mass transport across the PV contours, which is not balanced by the vertical mass flux in the subtropics, and the subtropical PV gradient increases. Interestingly, the tropics do not adjust toward radiative equilibrium on the summer side of the equator, beyond the direct influence of the stress-driven mass flux in the winter hemisphere. Thus, while the mass transport out of the subtropics and into the high latitudes becomes very weak as the high latitudes adjust toward radiative equilibrium, the mass transport from the subtropics into the tropics persists throughout the 170 day simulation. In the seasonal cycle simulation, the vertical mass flux is actually convergent throughout the hemisphere after the spring equinox, as the vortex "warms" toward equilibrium. The high latitudes are not "cooled" until after the solstice, and the summer edge is then formed from air with potential vorticity values that were found in the surf zone and the vortex edge during winter. This is the first evidence that has been found that the summer subtropical tracer gradient may not be just a remnant of the winter edge. Finally, we demonstrate that stirring in the weak winds of the summer high latitudes can act to strengthen the subtropical potential vorticity gradient both through erosion and sharpening and through increasing the horizontal diabatic mass flux by preventing adjustment toward radiative equilibrium.

As we discuss in detail in Section 4.6 of Chapter 4, the tracer observations are consistent with the mechanisms of edge formation seen in the shallow water model simulations. The winter subtropical tracer gradient is likely formed by the stripping of material out of the subtropics by the large-scale stirring in the surf zone. The summer subtropical tracer gradient in the middle and upper stratosphere, on the other hand, is likely formed by the residual circulation. For long-lived tracers with tropospheric sources and photochemical sinks, the residual circulation acts during early summer, as the high latitudes adjust toward radiative equilibrium, to increase the tracer values in both the tropics and high latitudes. Then, as the stress-driven circulations of the winter stratosphere, mesosphere, and summer lower stratosphere form, the residual circulation acts to decrease the tracer values in the high latitudes while it continues to increase the values

in the tropics, thus leading to mass transport across the tracer contours and the enhancement of the tracer gradient in the subtropics. It is likely that stirring plays a role in the formation of the summer subtropical tracer gradient in the lower stratosphere.

6.4 Tracer Transport

Above 10 mb, the motion of the subtropical edges contributes significantly to the mass budgets of the tropics and the extratropics in "leaky pipe"-type models. Below this level, the contribution of the edge motion is much smaller, and the mass budgets are dominated by the residual circulation. These models are not particularly applicable to the summer hemisphere, and we find that it is difficult to determine the contribution of the edge motion to tracer budgets because of the large range of tracer values in the summer hemisphere. However, we find that throughout the middle and upper stratosphere, advection from the summer hemisphere into the tropics may contribute significantly to the mass and tracer budgets in the tropics, so that estimates of in-mixing from the winter hemisphere must be considered as an upper limit to the actual transport across the winter subtropical edge.

6.5 Further Research

There are many results of this work that are ripe for further study. In particular, we are interested in the relationship between the zero zonal wind line and the subtropical edge. As discussed in the thesis, a weakly nonlinear critical layer view of the surf zone would imply that the region of strong stirring straddles the zero wind line, rather than ends at the zero wind line. The surf zone is far from the parameter range covered by nonlinear critical layer simulations, so that it is likely that the discrepancy results from finite amplitude effects. This could imply that breaking is actually *more* dependent on the zero wind line than linear theory would predict. We have briefly examined the relationship between the subtropical edge and the PDF of the latitude support of the near-zero zonal wind speeds in the UKMO analysis. Preliminary analysis indicates that there is a relationship between the latitude of the *vortex* edge of the surf zone and the latitude of non-zero frequency of near-zero zonal wind. Poleward of that latitude, the polar jet is so strong that there are no appearances of the zero wind line.

The subtropical edge of the surf zone tends to coincide with a large increase in the frequency of near-zero zonal winds, which are frequent enough that the zonal mean zonal wind speed is zero. Thus, it is possible that most wave breaking occurs during appearances of the zero wind line in the midlatitudes, rather than where the zonal mean wind speed is zero. We plan to further study the relationship between the zero zonal wind line and the subtropical edge in the shallow water model used in this thesis.

There are many interesting details about the relationship between the edges and the transport parameters shown in Chapter 3 that we could not address in this thesis. In particular, the interaction between the SAO, extratropical wave propagation, and the subtropical edge appears to be an interesting avenue of investigation, as does the dependence of the summer edge on the phase of the QBO. We note that we have begun a preliminary examination of PDFs of N_2O as simulated by the NCAR MATCH three-dimensional chemical transport model, which is driven with analyzed winds, and that these PDFs exhibit many of the characteristics of the data presented in Chapter 3. It may therefore be possible to use this model to investigate the mechanisms of edge formation and their role in transport in a fully three-dimensional system.

Appendix A

Leaky Pipe Model Formulation

A.1 Surf Zones

As done by Plumb (1996), we assume that long-lived tracers are in slope equilibrium (Plumb and Ko, 1992) in the surf zones. Thus the slope of mixing ratio isopleths in the surf zones is determined by a balance between the residual circulation and quasi-horizontal mixing. The equilibrium slope of a mixing ratio isopleth in NSZ or SSZ is given by

$$\gamma = \frac{-a}{\kappa \cos\varphi} \int^{\pi/2} (W^* - \langle W^* \rangle) \cos\varphi' d\varphi' , \tag{A.1}$$

where φ is latitude, a is the radius of the Earth, κ is the isentropic diffusivity, W^* is the vertical component of the residual circulation, and $\langle W^* \rangle$ is the mean descent in the region, averaged along the tracer isopleth (Plumb, 1996). This expression is derived under the assumption that the isopleth slope is small compared to the aspect ratio of the transport coefficients,

$$\gamma << \frac{H}{L} , \tag{A.2}$$

where H and L refer to the minimum height and length scales of the stream function of the residual circulation χ and the diffusive flux $\kappa (1/a) [(\partial\sigma)/(\partial\varphi)]$. It is also assumed that the

vertical kink in the isopleth at the tropical interface is small compared to the height scale,

$$\frac{\Delta\sigma}{\partial\sigma/\partial z} << H \ , \tag{A.3}$$

where σ is the mixing ratio, z is the log-pressure height, and $\Delta\sigma$ is the change in mixing ratio across the tropical interface. As long as conditions (A.2) and (A.3) are met, the slope of the mixing ratio isopleths in the surf zones depends only on transport properties.

Using an equivalent height coordinate Z, which is the height of a given mixing ratio isopleth at the tropical interface (see Figure 2-1), we define our one-dimensional variables for the surf zones in the same way as Plumb (1996):

$$M(Z) = \int \sigma\rho \frac{\partial z}{\partial Z} dA \ ,$$

$$W(Z) = M^{-1} \int \sigma\rho \overrightarrow{v} \cdot \widehat{n} dA \ ,$$

$$K(Z) = M^{-1} \int \sigma\rho K_{\perp} \frac{\partial Z}{\partial n} dA \ ,$$

$$S(Z) = \int \sigma s \frac{\partial z}{\partial Z} dA \ ,$$

where $\int\sigma$ denotes the integral along a given mixing ratio isopleth, ρ is the log-pressure density, z is the log-pressure height, $\overrightarrow{v} = (V^*, W^*)$ is the residual circulation, s is the source term from the tracer continuity equation, and $K_{\perp}$ is the diffusivity across the mixing ratio isopleth, which is given by

$$K_{\perp} = \gamma^2 \kappa \tag{A.4}$$

in the small slope limit.

The tracer continuity equation can be integrated over $\delta\sigma$, the volume between two adjacent mixing ratio isopleths, to give

$$\frac{\partial\sigma}{\partial t} \int_{\delta\sigma} \rho dA dz - \int_{\delta\sigma} s dA dz = -\delta \left\{ \int \sigma \overrightarrow{F} \cdot \widehat{n} dA \right\} + \int_{\delta I} \overrightarrow{F} \cdot \widehat{n} dA' \ ,$$

where

$$\overrightarrow{F} = \rho \overrightarrow{v} \sigma - \rho \kappa \cdot \bigtriangledown \sigma \ ,$$

so that $-\delta \left\{ \int \sigma \overrightarrow{F} \cdot \widehat{n} dA \right\}$ is the difference in the tracer mass flux across the two isopleths and $\int_{\delta I} \overrightarrow{F} \cdot \widehat{n} dA'$ is the tracer mass flux across the tropical interface, where dA' is the area element on I. It is the flux across the tropical interface that distinguishes the leaky pipe model from the tropical pipe model. In the tropical pipe model this term represented the outward flux of tracer from the tropics into the surf zones. Here it represents the net flux of tracer out of the tropics: the difference between the outward and inward tracer fluxes. We define $\mu_{M\text{en}}\sigma_T$ to be the entrainment flux of tracer per unit equivalent height outward from the tropics into the midlatitudes and $\mu_{M\text{de}}\sigma_M$ to be the detrainment flux of tracer per unit equivalent height inward from the midlatitudes into the tropics. The symbols σ_T and σ_M represent the tropical and midlatitude mixing ratios, respectively. The subscript M here is used as a generic symbol for either surf zone and the following equations will apply separately but equally to both. Using our one-dimensional quantities defined above, the integrated continuity equation becomes

$$M_M \frac{\partial \sigma_M}{\partial t} - S_M = -\frac{\partial}{\partial Z}(M_M W_M \sigma_M - M_M K_M \frac{\partial \sigma_M}{\partial Z}) + \mu_{M\text{en}}\sigma_T - \mu_{M\text{de}}\sigma_M \ .$$

Mass continuity within $\delta\sigma$ tells us that

$$\mu_{M\text{en}} - \mu_{M\text{de}} = \mu_{M\text{net}} = \frac{\partial}{\partial Z}(M_M W_M) \ ,$$

so that the continuity equation becomes

$$M_M \frac{\partial \sigma_M}{\partial t} - S_M = \frac{\partial}{\partial Z}(M_M K_M \frac{\partial \sigma_M}{\partial Z}) - M_M W_M \frac{\partial \sigma_M}{\partial Z} + \mu_{M\text{en}}(\sigma_T - \sigma_M) \ .$$

We now define the parameters

$$\lambda = \frac{\mu_{M\text{net}}}{M_M} = \frac{1}{M_M} \frac{\partial (M_M W_M)}{\partial Z} \ ,$$

the effective rate coefficient for net entrainment, and

$$\varepsilon = \frac{\mu_{M\mathrm{de}}}{\mu_{M\mathrm{net}}} ,$$

the ratio of detrainment into the tropics to the net entrainment. Using these parameters, the equations for NSZ and SSZ become

$$M_N \frac{\partial \sigma_N}{\partial t} - S_N = \frac{\partial}{\partial Z}\left(M_N K_N \frac{\partial \sigma_N}{\partial Z}\right) - M_N W_N \frac{\partial \sigma_N}{\partial Z} + M_N \left(1+\varepsilon_N\right)\lambda_N \left(\sigma_T - \sigma_N\right) ,$$

$$M_S \frac{\partial \sigma_S}{\partial t} - S_S = \frac{\partial}{\partial Z}\left(M_S K_S \frac{\partial \sigma_S}{\partial Z}\right) - M_S W_S \frac{\partial \sigma_S}{\partial Z} + M_S \left(1+\varepsilon_S\right)\lambda_S \left(\sigma_T - \sigma_S\right) ,$$

where the subscripts N and S refer to NSZ and SSZ, respectively.

A.2 Tropics

The equation for the tropics is considerably more complicated than that derived in Plumb (1996) because we now include entrainment of midlatitude air into the tropics. We also include a term for vertical diffusion in the tropics. Since we assume that long-lived tracers are horizontally uniform in the tropical region, the terms M, W, K, and S now represent a horizontal average across TR:

$$M_T(Z) = \int_{\mathrm{TR}} \rho dA ,$$

$$W_T(Z) = M_T^{-1} \int_{\mathrm{TR}} \rho W^* dA ,$$

$$K_T(Z) = M_T^{-1} \int_{\mathrm{TR}} \rho K_Z dA ,$$

$$S_T(Z) = \int_{\mathrm{TR}} s dA .$$

The integrated continuity equation is

$$M_T \frac{\partial \sigma_M}{\partial t} - S_T = -\frac{\partial}{\partial Z}(M_T W_T \sigma_T - M_T K_T \frac{\partial \sigma_T}{\partial Z}) + \mu_{N\mathrm{de}}\sigma_N + \mu_{S\mathrm{de}}\sigma_S - \mu_{N\mathrm{en}}\sigma_T - \mu_{N\mathrm{en}}\sigma_T .$$

Mass continuity gives

$$\frac{\partial(M_T W_T)}{\partial Z} = \frac{\partial(M_N W_N)}{\partial Z} + \frac{\partial(M_S W_S)}{\partial Z}$$

$$= \mu_{N\text{net}} + \mu_{S\text{net}} ,$$

so that the continuity equation for the tropics becomes

$$M_T \frac{\partial \sigma_T}{\partial t} - S_T = \frac{\partial}{\partial Z}\left(M_T K_T \frac{\partial \sigma_T}{\partial Z}\right) - M_T W_T \frac{\partial \sigma_T}{\partial Z}$$

$$-M_T \varepsilon_N \lambda_N \frac{M_N}{M_T}(\sigma_T - \sigma_N) - M_T \varepsilon_S \lambda_S \frac{M_S}{M_T}(\sigma_T - \sigma_S) ,$$

A.3 Scaling

We can show that the equations of the leaky pipe model are dominated by the advective terms. Since the diffusive flux, $\kappa\,(1/a)\,[(\partial\sigma)/(\partial\varphi)]$, at the tropical interface must balance the net entrainment flux, $V^*(\sigma_T - \sigma_N) \sim V^* \Delta\sigma$, we have

$$\kappa\gamma \sim V^* \frac{\Delta\sigma}{\partial\sigma/\partial Z} \sim \frac{W^* L}{H} \frac{\Delta\sigma}{\partial\sigma/\partial Z} ,$$

and the condition (A.3) that the vertical kink in the isopleths must be small compared to the height scale of the circulation gives

$$\kappa\gamma << W^* L .$$

Now, using (A.4), we have

$$\frac{K_\perp}{W^* L} << \gamma ,$$

and condition (A.2) gives

$$\frac{K_\perp}{H} << W^* .$$

Since $K \sim K_\perp(\text{area})$ and $W \sim W^*(\text{area})$ we have

$$\frac{K}{H} << W .$$

This result is less rigorous in the midlatitudes than in the tropics since we have neglected the contribution of V^* to W in assuming that $W \sim W^*(\text{area})$. The contribution of V^* should be small, however, given the small slope assumption.

Appendix B

Seasonally-Varying Leaky Pipe Model Formulation

Figure B-1 is a schematic representing a seasonally-varying formulation of the leaky pipe model, in which the latitudes of the tropical interfaces vary with time, the winter hemisphere communicates with the tropics through entrainment and detrainment across the tropical interface, and air is advected across the interface between the summer subtropical edge and the tropics.

Integrating the mass continuity equation over $\delta\sigma$, the volume between two adjacent mixing ratio isopleths, gives

$$\begin{aligned}
\frac{\partial M_T}{\partial t} &= -\frac{\partial (M_T W_T)}{\partial Z} - 2\pi a\rho(v_N - v_{EN}) + 2\pi a\rho(v_S - v_{ES}) \\
\frac{\partial M_N}{\partial t} &= -\frac{\partial (M_N W_N)}{\partial Z} + 2\pi a\rho(v_N - v_{EN}) \\
\frac{\partial M_S}{\partial t} &= -\frac{\partial (M_S W_S)}{\partial Z} - 2\pi a\rho(v_S - v_{ES})
\end{aligned}$$

where M, W, and Z are as defined in Appendix A, a is the radius of the earth, ρ is density, $v = \bar{v}^* \cos\varphi$, and v_E is the edge velocity multiplied by $\cos\varphi$. The subscripts N and S refer to the Northern and Southern midlatitudes, and T refers to the tropics.

B.1 Winter Midlatitudes

The winter midlatitudes are formulated in the same way as in Appendix A, including 2-way mixing across the subtropical edge and diffusion across the mixing ratio isopleths. We assume that mixing in the winter hemisphere is rapid enough to maintain slope equilibrium, even when the edge motion is included. For simplicity, we present the equations for Northern Hemisphere winter. The integrated tracer continuity equation is now:

$$M_N\frac{\partial\sigma_N}{\partial t}+\sigma_N\frac{\partial M_N}{\partial t}-S_N=-\frac{\partial}{\partial Z}(M_NW_N\sigma_N-M_NK_N\frac{\partial\sigma_N}{\partial Z})+\mu_{N\mathrm{en}}\sigma_T-\mu_{N\mathrm{de}}\sigma_N$$

where, as in Appendix A, $\mu_{N\mathrm{en}}$ is the entrainment flux of tracer per unit equivalent height outward from the tropics into the midlatitudes and $\mu_{N\mathrm{de}}$ is the detrainment flux of tracer per unit equivalent height inward from the midlatitudes into the tropics. Using mass continuity gives:

$$M_N\frac{\partial\sigma_N}{\partial t}-S_N=\frac{\partial}{\partial Z}(M_NK_N\frac{\partial\sigma_N}{\partial Z})-M_NW_N\frac{\partial\sigma_N}{\partial Z}-2\pi a\rho(v_N-v_{EN})\sigma_N+\mu_{N\mathrm{en}}\sigma_T-\mu_{N\mathrm{de}}\sigma_N$$

We now re-define the net entrainment flux as

$$\mu_{N\mathrm{net}}=\mu_{N\mathrm{en}}-\mu_{N\mathrm{de}}=2\pi a\rho(v_N-v_{EN})$$

Substituting,

$$\begin{aligned}M_N\frac{\partial\sigma_N}{\partial t}-S_N &= \frac{\partial}{\partial Z}(M_NK_N\frac{\partial\sigma_N}{\partial Z})-M_NW_N\frac{\partial\sigma_N}{\partial Z}+\mu_{N\mathrm{en}}(\sigma_T-\sigma_N)\\ &= \frac{\partial}{\partial Z}(M_NK_N\frac{\partial\sigma_N}{\partial Z})-M_NW_N\frac{\partial\sigma_N}{\partial Z}+M_N(1+\varepsilon_N)\lambda_N(\sigma_T-\sigma_N)\end{aligned}$$

as before (see Appendix A), where λ, the effective rate coefficient for the net entrainment, is now given by

$$\lambda_N=\frac{2\pi a\rho(v_N-v_{EN})}{M_N}$$

B.2 Summer Midlatitudes

As discussed in the text, the leaky pipe formalism does not lend itself particularly well to the summer hemisphere. However, it is possible to include communication between the summer subtropical edge air and tropical air through advection across the edge of the tropics. The small slope assumption does not apply in the summer hemisphere, so that it is not straightforward to choose the mixing ratio to use at the tropical interface.

The integrated tracer continuity equation for the summer hemisphere, assuming that the only important processes are advection and the motion of the tropical interface, is given by:

$$M_S\frac{\partial \sigma_S}{\partial t} + \sigma_S\frac{\partial M_S}{\partial t} - S_S = -\frac{\partial}{\partial Z}(M_S W_S \sigma_S) + \mu_{S\text{net}}\sigma_T$$

Substituting from the mass continuity equation,

$$\begin{aligned} M_S\frac{\partial \sigma_S}{\partial t} - S_S &= -M_S W_S\frac{\partial \sigma_S}{\partial Z} + M_S\lambda_S(\sigma_T - \sigma_S) && ;\lambda_S > 0 \\ &= -M_S W_S\frac{\partial \sigma_S}{\partial Z} && ;\lambda_S < 0 \end{aligned}$$

where

$$\lambda_S = \frac{-2\pi a\rho(v_S - v_{ES})}{M_S}$$

Thus, the communication between the tropics and the summer midlatitudes is one-directional, and depends on the net advection by the residual circulation.

B.3 Tropics

The integrated continuity equation in the tropics is given by

$$M_T\frac{\partial\sigma_T}{\partial t}+\sigma_T\frac{\partial M_T}{\partial t}-S_T=-\frac{\partial}{\partial Z}(M_TW_T\sigma_T-M_TK_T\frac{\partial\sigma_T}{\partial Z})+\mu_{N\text{de}}\sigma_N-\mu_{N\text{en}}\sigma_T-\mu_{S\text{net}}\sigma_S$$

Substituting, we have

$$\begin{aligned}M_T\frac{\partial\sigma_T}{\partial t}-S_T&=\frac{\partial}{\partial Z}(M_TK_T\frac{\partial\sigma_T}{\partial Z})-M_TW_T\frac{\partial\sigma_T}{\partial Z}\\&\quad-M_T\varepsilon_N\lambda_N\frac{M_N}{M_T}(\sigma_T-\sigma_N)+M_T\lambda_S\frac{M_S}{M_T}(\sigma_T-\sigma_S)\qquad;\lambda_S0\\&=\frac{\partial}{\partial Z}(M_TK_T\frac{\partial\sigma_T}{\partial Z})-M_TW_T\frac{\partial\sigma_T}{\partial Z}-M_T\varepsilon_N\lambda_N\frac{M_N}{M_T}(\sigma_T-\sigma_N)\quad;\lambda_S>0\end{aligned}$$

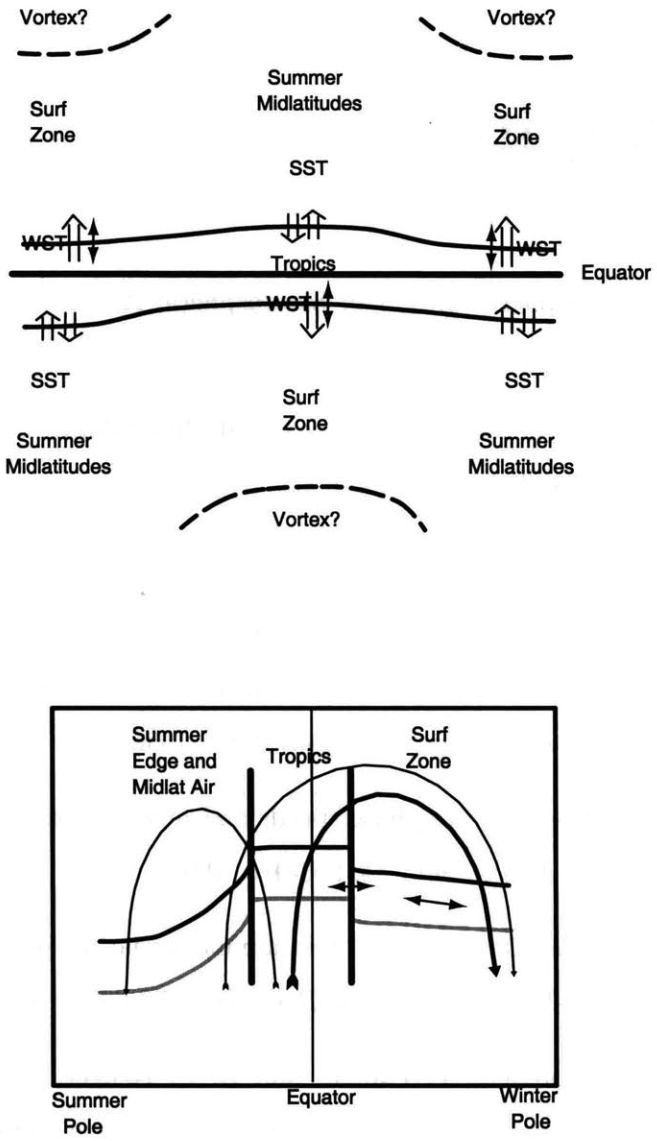

Figure B-1: Schematic representation of the seasonally varying leaky pipe model. The tropical interfaces represent the subtropical edge in the winter and the boundary between the tropics and the subtropical edge in the summer. In the top frame, the large arrows represent the net advection by the residual circulation, which may be in to the tropics during the summer. The small arrows represent 2-way exchange across the interface during winter, which must add up to the net outward flow. Compare the bottom frame to Figure 2-1.

Bibliography

[1] AESA, The Atmospheric Effects of Stratospheric Aircraft: A Third Program Report, *NASA Publ. 1313*, 1994.

[2] Allen, D. R., and N. Nakamura, A seasonal climatology of effective diffusivity in the stratosphere, *J. Geophys. Res., 2000, submitted.*

[3] Andrews, D., J. R. Holton, and C. B. Leovy, *Middle atmosphere dynamics*, Orlando, Academic Press, 1987.

[4] Avallone, L. M., and M. J. Prather, Photochemical evolution of ozone in the lower tropical stratosphere, *J. Geophys. Res., 101*, 1457-1461, 1996.

[5] Bowman, K. P., Rossby wave phase speeds and mixing barriers in the stratosphere. Part I: Observations, *J. Atmos. Sci., 53*, 905-916, 1996.

[6] Belmont, A. D. and D. G. Dartt, Semiannual variation in zonal wind from 20 to 65 kilometers at 80^oN-10^oS, *J. Geophys. Res., 78,* 6373-6376, 1973.

[7] Bischof, W., R. Borchers, P. Fabian, and B. C. Kruger, Increased concentration and vertical distribution of carbon dioxide in the stratosphere, *Nature, 316*, 708-710, 1985.

[8] Boering, K. A., S. C. Wofsy, B. C. Daube, H. R. Schneider, M. Loewenstein, J. R. Podolske, and T. J. Conway, Stratospheric mean ages and transport rates from observations of carbon dioxide and nitrous oxide, *Science, 274*, 1340-1343, 1996.

[9] Brewer, A. W., Evidence for a world circulation provided by the measurements of helium and water vapor distribution in the stratosphere. *Quart. J. Roy. Meteor. Soc., 75*, 351-363, 1949.

[10] Browning, G. L., J. J. Hack, and P. N. Swarztrauber, A comparison of three numerical methods for solving the shallow water equations on the sphere, *Mon. Wea. Rev., 117*, 1058-1075, 1989.

[11] Bryan, F., and W. R. Holland, A high resolution simulation of the wind- and thermohaline-driven circulation in the North Atlantic Ocean, in *Aha Huliko'a Hawaiin Workshop, University of Hawaii, Parameterization of Small-Scale Processes: Proceedings*, edited by P. Muller and D. Henderson, pp. 99-115, Hawaii Inst. of Geophys., Honolulu, 1989.

[12] Chen, P., The influences of zonal flow on wave breaking and tropical-extratropical interaction in the lower stratosphere, *J. Atmos. Sci., 53*, 2379-2392, 1996.

[13] Charney, J. G. and P. G. Drazin, Propagation of planetary-scale disturbances from the lower into the upper atmosphere, *J. Geophys. Res., 66*, 83-110, 1961.

[14] Dickinson, R. E., Analytic model for zonal winds in the tropics. I. Details of the model and simulation of the gross features of the zonal mean troposphere. *Mon. Wea. Rev., 99,* 501-510, 1971

[15] Dobson, G. M. B., Origin and distribution of the polyatomic molecules in the atmosphere. *Proc. Roy. Soc. London, 236A*, 187-193, 1956.

[16] Dunkerton, T. J., The role of gravity waves in the quasi-biennial oscillaiton, *J. Geophys. Res., 102*, 26053-26076, 1997.

[17] Eluszkiewicz, J., et al., Residual Circulation in the Stratosphere and Lower Mesosphere as Diagnosed from Microwave Limb Sounder Data, *J. Atmos. Sci., vol. 53, 2*, 217-240,1996

[18] Feely, H. W., and J. Spar, Tungsten 185 from nuclear bomb tests as a tracer for stratospheric meteorology, *Nature, 188,* 1062-1064, 1960.

[19] Goldan, P. D., W. C. Kuster, D. L. Albritton and A. L. Schmeltkopf, Stratospheric $CFCl_3$, CF_2Cl_2, and N_2O height profile measurements at several altitudes, *J. Geophys. Res., 85*, 413-423, 1980.

[20] Grant, W. B., et al., Aerosol-associated changes in tropical stratospheric ozone following the eruption of Mount Pinatubo, *J. Geophys. Res., 99,* 8197-8211, 1994.

[21] Grant, W. B., E. V. Browell, C. S. Long, L.L. Stowe, R. G. Grainger and A. Lambert, Use of volcanic aerosols to study the tropical stratospheric reservoir, *J. Geophys. Res., 101,* 3973-3988, 1996.

[22] Grose, W. L., J. E. Nealy, R. E. Turner, and W. T. Blackshear, Modeling the transport of chemically active constituents in the stratosphere. In: *Transport Processes in the Middle Atmosphere*, edited by G. Visconti and R. R. Garcia. Dordrecht, Reidel, 229-250, 1987.

[23] Hall, T. M., and R. A. Plumb, Age as a diagnostic of stratospheric transport, *J. Geophys. Res., 99*, 1059-1070, 1994.

[24] Hall, T. M., and D. W. Waugh, Tracer transport in the tropical stratosphere due to vertical diffusion and horizontal mixing, *Geophys. Res. Lett., 24*, 1383-1386, 1997.

[25] Hall, T. M., D. W. Waugh, K. A. Boering, and R. A. Plumb, Evaluation of transport in stratospheric models, *J. Geophys. Res., 104,* 18815-18839, 1999.

[26] Harnisch, J., R. Borchers, P. Fabian, and M. Maiss, Tropospheric trends for CF_4 and C_2F_6 since 1982 derived from SF_6 dated stratospheric air, *Geophys. Res. Lett., 23*, 1099-1102, 1996.

[27] Harvey, V. L., M. H. Hitchman, R. B. Pierce, and T. D. Fairlie, Tropical aerosol in the Aleutian High, *J. Geophys. Res., 104*, 6281-6290, 1999.

[28] Haynes, P. H., Nonlinear instability of a Rossby-wave critical layer. *J. Fluid Mech., 161*, 493-511, 1985.

[29] Haynes, P. H. and M. E. McIntyre, On the evolution of vorticity and potential vorticity in the presence of diabatic heating and frictional or other forces, *J. Atmos. Sci., 44*, 828-841, 1987.

[30] Haynes, P. H., C. J. Marks, M.E. McIntyre, T. G. Shepard, and K. P. Shine, On the "downward control" of extratropical diabatic circulations by eddy-induced mean zonal forces, *J. Atmos. Sci., 48,* 651-678, 1991.

[31] Haynes, P. H. and E. Shuckburgh, Effective diffusivity as a diagnostic of atmospheric transport. Part I: stratosphere, *J. Geophys. Res., to appear.*

[32] Hirota, I., Equatorial waves in the upper stratosphere and mososphere in relation to the semiannual oscillation of the zonal wind, *J. Atmos. Sci., 35*, 714-722, 1978.

[33] Hitchman, M. H., M. McKay, and C. R. Trepte, A climatology of stratospheric aerosol, *J. Geophys. Res., 94*, 16779-16794, 1994.

[34] Hitchman, M. H. and C. B. Leovy, Estimation of the Kelvin wave contribution to the semiannual oscillation, *J. Atmos. Sci., 45*, 1462-75, 1988.

[35] Holton, J. R., *The Dynamic Meteorology of the Stratosphere and Mesosphere, Meteorol. Mongr. Ser., 37*, 216 pp., Am. Meteorol. Soc., Boston, Mass., 1975.

[36] Holton, J. R., P. H. Haynes, M. E. McIntyre, A. R. Douglass, R. B. Rood, and L. Pfister, Stratosphere-troposphere exchange, *Rev. Geophys., 33*, 403-439, 1995.

[37] Holton J. R. and W. M. Wehrbein, A numerical model of the zonal mean circulation of the middle atmosphere, *Pure Appl. Geophys., 118*, 284-306, 1980.

[38] Hopkins, R. H., Evidence of polar-tropical coupling in upper stratospheric zonal wind anomalies, *J. Atmos. Sci., 32*, 712-719, 1975.

[39] Hyson, P., Stratospheric water vapour over Australia, *Quart. J. Roy. Meteor. Soc., 109*, 285-294, 1983.

[40] Jones, D. B. A., H. R. Schneider, and M. B. McElroy, Effects of quasi-biennial oscillation on the zonally averaged transport of tracers, *J. Geophys. Res., 103*, 11235-11249; 1998.

[41] Jones, R. L., and J. A. Pyle, Observations of CH_4 and N_2O by the Nimbus-7 SAMS: a comparison with in situ data and two-dimensional numerical model calculations, *J. Geophys. Res., 89,* 5264-5279, 1984.

[42] Juckes, M. N., A shallow water model of the winter stratosphere, *J. Atmos. Sci., 46,* 2934-2955, 1989.

[43] Juckes, M. N. and M. E. McIntyre, A high-resolution, one-layer model of breaking planetary waves in the winter stratosphere, *Nature, 328*, 590-596,1987.

[44] Kennaugh, R., S. Ruth, and L. J. Gray, Modelling quasi-biennial variability in the semi-annual double peak, *J. Geophys. Res., 102*, 16169-16187, 1997.

[45] Ko, M. K. W., N. D. Sze, and D. K. Weisenstein, Roles of dynamical and chemical processes in determining the stratospheric concentration of ozone in one-dimensional and two-dimensional models, *J. Geophys. Res., 94*, 9889-9896, 1989.

[46] Ko, M. K. W., N. D. Sze, and D. K. Weisenstein, Use of satellite data to constrain the model-calculated atmospheric lifetime for N_2O: Implications for other trace gases, *J. Geophys. Res., 96,* 7547-7552, 1991.

[47] Luo, M., R. J. Cicerone, J. M. Russell III, and T. Y. W. Huang, Observations of stratospheric hydrogen flouride by halogen occultation experiment, *J. Geophys. Res., 99*, 16691-16705, 1994.

[48] Mahlman, J. D., Mechanistic interpretation of stratospheric tracer transport, in *Climate Dynamics, Adv. Geophys.*, vol. 28A, edited by B. Saltzman, pp. 301-320, Academic, San Diego, Calif., 1985.

[49] Marquardt, C. and B. Naujokat, http://tao.atmos.washington.edu/data_sets/qbo

[50] McCormick, M. P. and R. E. Veiga, SAGE II measurements of early Pinatubo aerosols, *Geophys. Res. Lett., 19*, 155-158, 1992.

[51] McIntyre, M. E., Towards a Lagrangian-mean description of stratospheric circulations and chemical transports, *Philos. Trans. Roy. Soc. London, 296A*, 129-148,1980.

[52] McIntyre, M. E. and T. N. Palmer, Breaking planetary waves in the stratosphere, *Nature, 305*, 593-600, 1983.

[53] McIntyre, M. E. and T. N. Palmer, The "surf zone" in the stratosphere, *J. Atmos. Terr. Phys., Vol. 46, 9*, 825-849, 1984.

[54] Meyer, W. D., A diagnostic numerical study of the semiannual variation of the zonal wind in the tropical stratosphere and mesosphere, *J. Atmos. Sci., 27*, 820-830, 1970.

[55] Michelsen, H. A., G. L. Manney, M. R. Gunson, and R. Zander, Correlations of stratospheric abundances of NO_y, O_3, N_2O, and CH_4 derived from ATMOS measurements, *J. Geophys. Res., 103*, 28347-28359, 1998.

[56] Minschwaner, K., A. E. Dessler, J. W. Elkins, C. M. Volk, D. W. Fahey, M. Loewenstein, J. R. Podolske, A. E. Roche, and K. R. Chan, Bulk properties of isentropic mixing into the tropics in the lower stratosphere, *J. Geophys, Res., 101*, 9433-9439, 1996.

[57] Mote, P. W., et al., An atmospheric tape recorder: The imprint of tropical tropopause temperatures on stratospheric water vapor, J. *Geophys. Res., 101,* 3989-4006, 1996.

[58] Murphy, D. M., et al., Reactive nigrogen and its correlation with ozone in the lower stratosphere and upper troposphere, *J. Geophys. Res., 98*, 8751-8773, 1993.

[59] Nakamura, N., Modified Lagrangian-Mean diagnostics of the stratospheric polar vortices. Part I: formulation and analysis of GFDL SKYHI GCM, *J. Atmos. Sci., 52*, 2096-2108, 1995.

[60] Nakamura, N., Two-dimensional mixing, edge formation, and permeability diagnosed in an area coordinate, *J. Atmos. Sci., 53,* 1524-1537, 1996.

[61] Nakamura, N. and J. Ma, Modified Lagrangian mean diagnostics of the stratospheric polar vortices. Part II: nitrous oxide and seasonal barrier migration in the cryogenic limb array etalon spectrometer and SKYHI general circulation model, *J. Geophys. Res., 102*, 25721-25735, 1997.

[62] Norton, W. A., Breaking Rossby waves in a model stratosphere diagnosed by a vortex-following coordinate system and a technique for advecting material contours, *J. Atmos. Sci., 51*, 654-673, 1994.

[63] O'Neill, A., W. L. Grose, V. D. Pope, H. Maclean, and R. Swinbank, Evolution of the stratosphere during northern winter 1991/1992 as diagnosed from U.K. Meterological Office Analyses, *J. Atmos. Sci., 51*, 2800-2817, 1994.

[64] O'Sullivan, D. and P. Chen, Modeling the quasi-biennial oscillation's influence on isentropic tracer transport in the subtropics, *J. Geophys. Res., 101*, 6811-6821, 1996.

[65] O'Sullivan, D. and T. J. Dunkerton, The influence of the quasi-biennial oscillation on global consitituent distributions, *J. Geophys. Res., 102,* 21731-21743, 1997.

[66] Ottino, J. M., *The kinematics of mixing: stretching, chaos, and transport*, Cambridge Univerisity Press, 364 pp., 1989.

[67] Park, J. H., et al., Validation of Halogen Occulatation Experiment CH_4 measurements from the UARS, *J. Geophys. Res., 101*, 10183-10203, 1996.

[68] Pierrehumbert, R. T., 1991: Large-scale horizontal mixing in planetary atmospheres, *Phys. Fluids, 3A*, 1250-1260.

[69] Plumb, R. A., A "tropical pipe" model of stratospheric transport, *J. Geophys. Res., 101*, 3957-3972, 1996.

[70] Plumb, R. A., et al., Intrusions into the lower stratospheric Arctic vortex during the winter of 1991-1992, *J. Geophys. Res., 99*, 1089-1105, 1994.

[71] Plumb, R. A. and R. C. Bell, A model of the quasi-biennial oscillation on an equatorial beta-plane, *Quart. J. Roy. Meteor. Soc.*, 108, 335-352, 1982.

[72] Plumb, R. A. and J. Eluszkiewicz, The Brewer-Dobson circulation: dynamics of the tropical upwelling, *J. Atmos. Sci., 56*, 868-890, 1999.

[73] Plumb, R. A. and J. D. Mahlman, The zonally averaged transport characteristics of the GFDL general circulation/transport model, *J. Atmos. Sci., 44*, 298-327, 1987.

[74] Plumb, R. A. and M. K. W. Ko, Interrelationships between mixing ratios of long-lived stratospheric constituents, *J. Geophys. Res., 97*, 10145-10156, 1992.

[75] Plumb, R. A., D. W. Waugh, and M. P. Chipperfield, The effects of mixing on tracer relationships in the polar vortices, *J. Geophys. Res., 105*, 10047-10062, 2000.

[76] Polvani, L. M., D. W. Waugh, and R. A. Plumb, On the subtropical edge of the surf zone, *J. Atmos. Sci., 52*, 1288-1309, 1995.

[77] Randel, W. J., et al., Stratospheric transport from the tropics to middle latitudes by planetary-wave mixing, *Nature, 365*, 533-535, 1993.

[78] Randel, W. J., F. Wu, J. M. Russell III, A. Roche, and J. W. Waters, Seasonal cycles and QBO variations in stratospheric CH_4 and H_2O observed in UARS HALOE data, *J. Atmos. Sci., 55*, 163-185, 1998.

[79] Ray, E. A., M. J. Alexander, J. R. Holton, An analysis of the structure and forcing of the equatorial semiannual oscillation in zonal wind, *J. Geophys. Res., 103,* 1759-1774, 1998.

[80] Reed, R. J., The quasi-biennial oscialltion fo the atmosphere between 30 and 50 km over Ascension Island, *J. Atmos. Sci,.22*, 331-333, 1965.

[81] Roche, A. E., et al., Observations of lower-stratospheric ClONO2, HNO3, and aerosol by the UARS CLAES experiment between January, 1992, and April 1993, *J. Atmos. Sci., 51*, 2877-2902, 1994.

[82] Roche, A. E., et al., Validation of CH4 and N2O measurements by the Cryogenic Limb Array Etalon Spectrometer instrument on the Upper Atmosphere Research Satellite, *J. Geophys. Res., 101,* 9679-9710, 1996.

[83] Rosenlof, K. H., Seasonal cycle of the residual mean meridional circulation in the stratosphere, *J. Geophys. Res., 100*, 5173-5191, 1995.

[84] Russell, J. M. III, et al., The Halogen Occultation Experiment, *J. Geophys. Res., 98*, 10777-10797, 1993.

[85] Salby, M. L., D. L. Hartmann, P. L. Bailey, and J. C. Gille, Evidence for equatorial Kelvin modes in Nimbus-7 LIMS, *J. Atmos. Sci., 41*, 220-235, 1984.

[86] Semeniuk, K. and T. G. Shepard, Mechanisms for tropical upwelling in the stratosphere, *J. Atmos. Sci., to appear.*

[87] Shuckburgh, E., W. Norton, A. Iwi, P. Haynes, The influence of the quasi-bienniel oscillation on isentropic transport and mixing in the tropics and subtropics, *J. Geophys. Res., submitted,* 2000.

[88] Sobel, A. H. and R. A. Plumb, Quantitative diagnostics of mixing in a shallow water model of the stratosphere, *J. Atmos. Sci., 56*, 2811-2829, 1999.

[89] Sobel, A. H., R. A. Plumb, and D. W. Waugh, Methods of calculating transport across the Polar Vortex Edge, *J. Atmos. Sci., 54*, 2241-2260, 1997.

[90] Sparling, L. C., Statistical perspectives on stratospheric transport, *Rev. Geophys.*, 38, 417-436, 2000.

[91] Sparling, L. C., J. A. Kettleborough, P. H. Haynes, M. E. McIntyre, J. E. Rosenfield, M. R. Schoeberl, and P. A. Newman, Diabatic cross-isentropic dispersion in the lower stratosphere, *J. Geophys. Res., 102*, 25,817-25,829, 1997.

[92] Stewartson, K., The evolution of the critical layer of a Rossby wave. *Geophys. Astrophys. Fluid Dyn., 9*, 185-200, 1978.

[93] Strahan, S. E., M. Loewenstein, and J. R. Podolske, Climatology and small-scale structure of lower stratospheric N_2O based on in situ observations, *J. Geophys. Res., 104*, 2195-2208, 1999.

[94] Swinbank, R. and A. O'Neill, A stratosphere-troposphere data assimilation system, *Mon. Wea. Rev., 122*, 686-702, 1994.

[95] Thuburn, J. and V. Lagneau, Eulerian mean, contour integral, and finite-amplitude wave activity diagnostics applied to a single-layer model of the winter stratosphere, *J. Atmos. Sci., 56*, 689-710, 1999.

[96] Thuburn, J. and M. E. McIntyre, Numerical advection schemes, cross-isentropic random walks, and correlations between chemical species, *J. Geophys. Res., 102*, 6775-6797, 1997.

[97] Trepte, C. R. and M. H. Hitchman, Tropical stratospheric circulation deduced from satellite aerosol data, *Nature, 355*, 626-628, 1992.

[98] Trepte, C. R., R. E. Veiga, and M. P. McCormick, The poleward dispersal of Mount Pinatubo volcanic aerosol, *J. Geophys. Res., 98*, 18563-18573, 1993.

[99] Volk, C. M., et al., Quantifying transport between the tropical and mid-latitude lower stratosphere, *Science, 272*, 1763-1768, 1996.

[100] Wagner, R. and K. P. Bowman, Wave breaking and mixing in the Northern Hemisphere summer stratosphere, *J. Gephys. Res., submitted*, 1999.

[101] Warn, T, and H. Warn, The evolution of a nonlinear critical level. *Stud. Appl. Math., 59*, 37-71, 1978.

[102] Waugh, D. W., et al., Mixing of polar vortex air into middle latitudes as revealed by tracer-tracer scatterplots, *J. Geophys. Res., 102*, 13119-13134, 1997.

[103] Waugh, D. W., Seasonal variation of isentropic transport out of the tropical stratosphere, *J. Geophys. Res., 101*, 4007-4023, 1996.